Radiation Hard Hybrid Pixel Detectors, and a $b\bar{b}$ Cross-Section Measurement at the CMS Experiment

by

Jennifer A. Sibille

Submitted to the graduate degree program in Physics and the Graduate Faculty of the University of Kansas in partial fulfillment of the requirements for the degree of Doctor of Philosophy

Committee:

Dr. Alice Bean, Chairperson

Dr. Philip Baringer

Dr. Stephen Sanders

Dr. Kyoungchul Kong

Dr. Cindy Berrie

Dr. Tilman Rohe

Date defended: April 19, 2013

The Dissertation Committee for Jennifer A. Sibille certifies that this is the approved version of the following dissertation:

Radiation Hard Hybrid Pixel Detectors, and a $b\bar{b}$ Cross-Section Measurement at the CMS Experiment

Committee:

Dr. Alice Bean, Chairperson

Dr. Philip Baringer

Dr. Stephen Sanders

Dr. Kyoungchul Kong

Dr. Cindy Berrie

Dr. Tilman Rohe

Date approved: April 22, 2013

Abstract

Measurements of heavy flavor quark production at hadron colliders provide a good test of the perturbative quantum chromodynamics (pQCD) theory. It is also essential to have a good understanding of the heavy quark production in the search for new physics. Heavy quarks contribute to backgrounds and signals in measurements of higher mass objects, such as the Higgs boson. A key component to each of these measurements is good vertex resolution. In order to ensure reliable operation of the pixel detector, as well as confidence in the results of analyses utilizing it, it is important to study the effects of the radiation on the detector.

In the first part of this dissertation, the design of the CMS silicon pixel detector is described. Emphasis is placed on the effects of the high radiation environment on the detector operation. Measurements of the charge collection efficiency, interpixel capacitance, and other properties of the pixel sensors as a function of the radiation damage are presented.

In the second part, a measurement of the inclusive $b\bar{b}$ production cross section using the $b \to \mu D^0 X, D^0 \to K\pi$ decay chain with data from the CMS experiment at the LHC is presented. The data were recorded with the CMS experiment at the Large Hadron Collider (CERN) in 2010 using unprescaled single muon triggers corresponding to a total luminosity of 25 pb^{-1}. The differential cross section is measured for $p_{\mathrm{T}}^{D^0\mu} > 6$ GeV/c and $|\eta| < 2.4$ corresponding to a total cross section of $4.36 \pm 0.54(stat.)^{+0.28}_{-0.25}(sys.) \pm 0.17(\mathcal{B}) \pm 0.23(\mathcal{L})$ μ b.

Acknowledgements

I can not thank every person who helped me on this journey, but I would like to take this opportunity to mention a few of those people who were instrumental for this dissertation.

First and foremost I would like to thank Dr. Alice Bean, my advisor, for all of her help over the years. She has been encouraging and patient through the ups and downs of my studies, and given me so many opportunities that led me to where I am today. I would also like to thank Dr. Michael Murray for my first introduction into CERN and the CMS experiment. In addition I thank Dr. Philip Baringer, Dr. Stephen Sanders, Dr. K. C. Kong, and Dr. Cindy Berrie for agreeing to serve on my committee.

I am equally grateful to Dr. Tilman Rohe, my supervisor at the Paul Scherrer Institut (PSI). He spent countless hours with me both in the office and in the lab, and never tired of answering my questions. My thanks also to Prof. Dr. Roland Horisberger and the entire CMS Pixel group at PSI, for accepting me into the group as one of their own.

The work for this PhD was funded by the Marie Curie Initial Training Network - PArticle Detectors (MC-PAD). I want to thank Dr. Christian Joram and the entire Marie Curie - Particle Detectors (MC-PAD) Initial Training Network. The opportunites, connections, and training that I received in this network are what made me into the scientist I am today. Thank you also to the National Science Foundation, who also supported this work with the PIRE grant OISE-0730173.

Of course, a huge "thank you" goes to my family, who have supported me through all the years of school and hard work that led up to this point, especially my parents, Mark and Kim Sibille, and my sister, Michelle Sibille, who have never wavered in their belief in me. A special thanks also goes to my fiancé, Thomas Pöhlsen, who has been my sounding board, my cheer leader, and my shoulder to cry on especially in these last difficult months.

Without all of you, none of this would have been possible.

Contents

List of Tables

List of Figures

1 Introduction

The Standard Model (SM) of particle physics attempts to describe the structure of matter and the interactions between the elementary particles and forces which make up the universe. In 1961, Sheldon Glashow suggested a unification of the electromagnetic and weak forces [16]. The addition of the Higgs mechanism by Steven Weinberg and Abdus Salam in the late 1960's completed the current version of the theory [17, 18]. Since then, the Standard Model has done a remarkably good job of describing a large number of experimental results, as well as correctly predicting the existence of several particles before they were experimentally observed (c [19, 20, 21], b [22, 23], t [24, 25, 26], ν_τ [27, 28], W/Z bosons, gluon [29]).

In the SM there are 12 spin-$\frac{1}{2}$ fermions and 4 spin-1 gauge bosons. The bosons act as the carriers of the forces. The SM incorporates three of the four fundamental forces: the electromagnetic, the weak, and the strong force. Gravity, which is only relevant at macroscopic distances, is not included in the theory.

The 12 fermions are divided into the 6 quarks (u, d, s, c, b, t) and the 6 leptons $(e, \mu, \tau, \nu_e, \nu_\mu, \nu_\tau)$. They are further divided into 3 generations, and have a wide range in masses. The lighest quarks (u, d) have a mass on the order of a few MeV, while the t has a mass of about 172 GeV. Each of the particles also has a charge-conjugate partner, called its "anti-particle."

The b quark is one of the third-generation quarks, together with the t (or top) quark. The b has a bare mass around 4 GeV/c^2 and a charge of $-\frac{1}{3}e$. It was first predicted in 1972 by Kobayashi and Maskawa to explain CP-violation, and was discovered in 1977 at Fermilab [22, 23]. The b-quark decays via the weak interaction to a u or c quark, but the decay is suppressed by the CKM matrix. It is the heaviest quark which can hadronize, with a mean lifetime of approximately $10^{-12}s$.

Heavy flavor physics is described theoretically by perturbative Quantum Chromodynamics (pQCD). The b production cross section at the LHC is very large, which makes

it a perfect opportunity to study how well the theory describes the strong interaction. In addition, b-quarks make up a large background to many other measurements which will be performed at the LHC. As such, the production mechanisms should be well understood.

Despite the many successes of the Standard Model, it is still incomplete. The search for the Higgs boson was one of the main motivations for the Large Hadron Collider (LHC). Recently, the ATLAS and CMS experiments at the LHC have published the discovery of a new boson with a mass of approximately 125 GeV, which is so far consistent with the Higgs boson [30, 31]. In addition, the Standard Model offers no explanation for the nature of dark matter, or for the matter-antimatter asymmetry. Many additional theories, such as Supersymmetry, have been developed in attempts to answer these questions. Many of these theories predict effects which should manifest at the LHC.

In hadron collider experiments the collisions produce very dense events. The tracking detector is essential in order to reconstruct the interesting events. Strip and pixel detectors provide the necessary granularity and resolution to reliably reconstruct vertices. Due to the long lifetime of b mesons, they are able to travel distances on the order of 500 μm before decaying, and these decay vertexes can then be reconstructed using the information from the tracking detector. This makes the identification of b mesons relatively easy.

In this work, a measurement of the $b\bar{b}$ cross section in pp collisions at a center-of-mass energy $\sqrt{s} = 7$ TeV using data from the CMS experiment is presented. The data were collected using unprescaled single muon triggers during 2010. The cross section is measured using the decay $b \to \mu D^0 X, D^0 \to K\pi$. This analysis takes advantage of the pixel detector, as it requires reconstructing both secondary and tertiary vertexes.

The collisions also produce a very harsh radiation environment. The radiation damages the detectors and degrades the performance of the detector. These effects must be studied and understood, both for the operation of the current experiments and for the

development of future detectors.

In order to assess the radiation hardness of the current CMS barrel pixel sensors, and their viability for use in the upcoming Phase 1 Upgrade of the pixel detector, several measurements were performed on irradiated samples. The charge collection efficiency, detection efficiency, and interpixel capacitance are measured and compared to those same properties in unirradiated sensors. In addition, a possible alternative sensor to reduce cost is investigated.

A brief overview of the LHC and the Compact Muon Solenoid (CMS) experiment are given in Chapter 2. The CMS pixel detector is described in more detail in Chapter 3. In Chapter 4 the main mechanisms and results of radiation damage in silicon are discussed. The various measurements that were performed in order to assess the effect of radiation damage on the macroscopic properties of the silicon sensors are presented in Chapter 5. In Chapter 6 the heavy flavor production mechanisms are discussed, and a few previous b-quark production cross section measurements are reviewed. In Chapter 7 a $b\bar{b}$ cross section measurement at the CMS experiment at the LHC is presented.

2 The LHC and CMS

2.1 The Large Hadron Collider

The Large Hadron Collider is located at the European Organization for Nuclear Research (CERN) in Switzerland. It has a circumference of 27 km and is an average of 100 m underground. It is a proton-proton collider, with a design center of mass energy of 14 TeV. The machine can also run in heavy ion mode, where it can collide lead ions and protons with lead ions. There are four main experiments at the LHC: ALICE [32], ATLAS [33], CMS [34, 3], and LHCb [35]. CMS and ATLAS are general purpose detectors, LHCb is designed to study b physics, and ALICE is designed for heavy ion physics.

The LHC accelerator complex is shown in Figure 1. The protons are obtained by stripping the electrons from hydrogen atoms. The protons travel through the linear accelerator LINAC2, the PS Booster, the Proton Synchrotron (PS), and the Super Proton Synchrotron (SPS) before being injected into the main LHC ring with an energy of 450 GeV. The LHC is designed to accelerate the protons to an energy of 7 TeV per beam. For the heavy ion running, lead ions are obtained from a source of vaporized lead. They pass through the LINAC3 linear accelerator and are collected in the Low Energy Ion Ring (LEIR) before being injected into the PS, at which point they follow the same path as the protons to the LHC where they are accelerated to a center of mass energy of 2.76 TeV per nucleon [36].

During the first running period the energy is limited to 3.5 TeV per beam. This is as a precaution following the events of September 2008 [37]. During a long shutdown in 2013 the remaining repairs to the magnets will be performed. The running period following this shutdown is expected to be at the design energy of 7 TeV per beam.

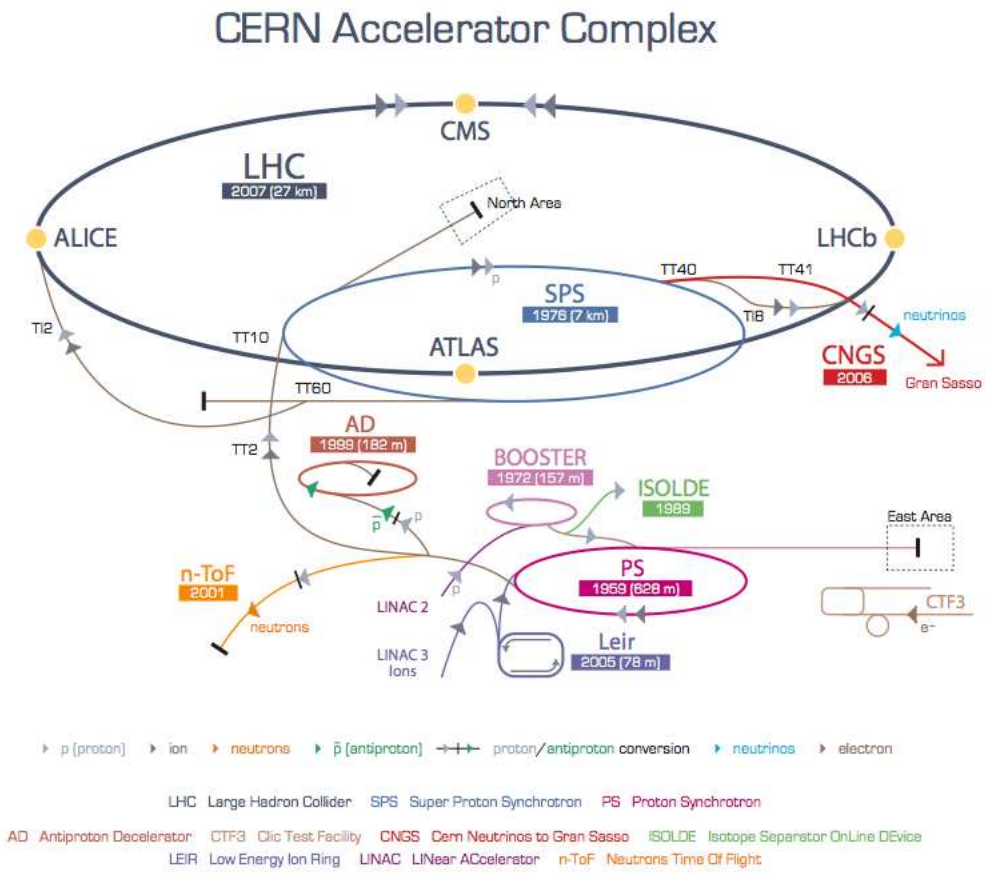

Figure 1: The LHC accelerator complex, showing the locations of the 4 experiments [2].

2.2 The Compact Muon Solenoid Experiment

The central feature of the Compact Muon Solenoid (CMS) apparatus is a superconducting solenoid. The silicon tracker, the electromagnetic calorimeter (ECAL), and the hadron calorimeter (HCAL) are contained within the solenoid. Muon detectors are embedded in the steel return yoke. The CMS apparatus has an overall length of 22 m, a diameter of 15 m, and weighs 12 500 tons. In addition to the barrel and endcap detectors, CMS has extensive forward calorimetry. Figure 2 shows a cutaway view of the CMS detector.

CMS uses a right-handed coordinate system, with the origin at the nominal interaction point, the x-axis pointing to the center of the LHC, the y-axis pointing up

(perpendicular to the LHC plane), and the z-axis along the counterclockwise-beam direction. The polar angle, θ, is measured from the positive z-axis and the azimuthal angle, ϕ, is measured in the x-y plane. Pseudorapidity is defined as $\eta = -\ln\left[\tan\left(\frac{\theta}{2}\right)\right]$.

In the following sections the different subdetectors are described. A much more detailed description of CMS can be found elsewhere [3].

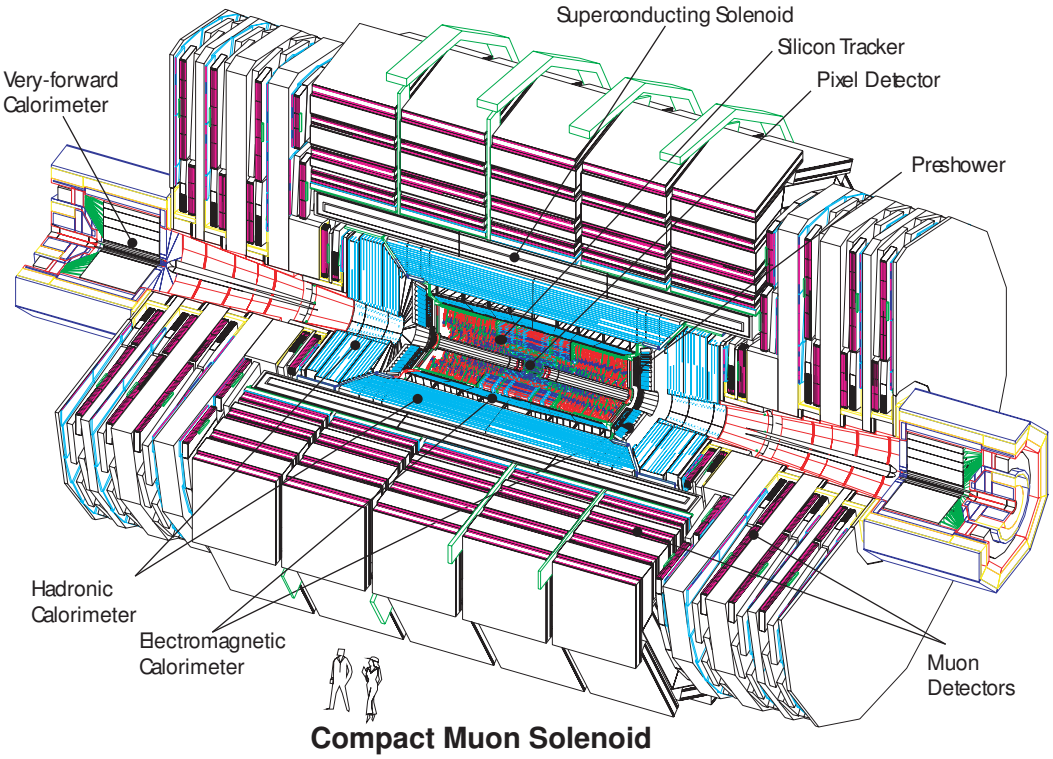

Figure 2: The CMS Detector [3].

2.2.1 The Solenoid

The superconducting solenoid provides a magnetic field of 3.8 T. This high magnetic field provides the bending power to accurately measure the momentum of high energy charged particles. The solenoid has an internal diameter of 6 m, a length of 12.5 m, and contains the tracking and calorimeter detectors. The solenoid has the capacity to store 2.6 GJ of energy at full current and weighs 220 tons. The flux is returned through an

iron return yoke, which consists of 5 wheels and 2 endcaps, composed of 3 disks each, and weighs 10,000 tons. The muon chambers are integrated within the return yoke.

2.2.2 The Silicon Tracker

The silicon tracker consists of a pixel detector in the center, surrounded by a strip tracker. The pixel detector consists of 3 barrel layers and 2 endcap disks on each side, with 65 million channels. The strip tracker is divided into the Tracker Inner Barrel (TIB), the Tracker Inner Disks (TID), the Tracker Outer Barrel (TOB), and the Tracker EndCaps (TEC), with a total of 10 million channels. The layout of the tracker is shown in Figure 3.

The sensors used in the strip tracker are single-sided p-on-n type float zone silicon microstrip sensors. In the TIB, TID, and the four inner rings of the TECs thin sensors with a thickness of 320 μm are used. Thicker sensors with a thickness of 500 μm are used in the TOB and the outer three rings of the TECs. There are "double sided modules" where two modules are mounted back-to-back with a stereo angle of 100 mrad.

The TIB consists of 4 layers, at radii of 255.0 mm, 339.0 mm, 418.5 mm, and 498.0 mm, respectively from the beam axis. They extend from -700 mm to +700 mm along the z axis. The two inside layers have double sided modules with an 80 μm strip pitch, while the two outer layers have single sided modules with a strip pitch of 120 μm. The TID consists of two sets of three disks, on either end of the TIB. The three disks range in distance from 800-900 mm in z, and cover a range of radii from 200-500 mm. The mean strip pitch varies from 100 μm to 141 μm. The two inner rings have double sided modules, while the outer disk has single sided modules.

The TOB consist of 6 layers, placed at radii of 608, 692, 780, 868, 965, and 1080 mm from the beam axis. They cover the range from -1090 mm to +1090 mm along the z axis. The strip pitch of the inner four layers is 183 μm, and 122 μm for the outer two layers. The inner two layers have double sided modules, while the outer four layers have single sided modules. Each TEC has nine disks, covering a range of radii from 220-1135 mm

and placed between 1240 mm and 2800 mm in z. The modules are arranged in seven rings around the beam axis. The mean strip pitch varies from 97 μm to 184 μm. The outer six disks have a slightly larger inner radius than the first three in order to leave space for the insertion of the pixel detector.

The pixel detector is discussed in much more detail in Chapter 3.

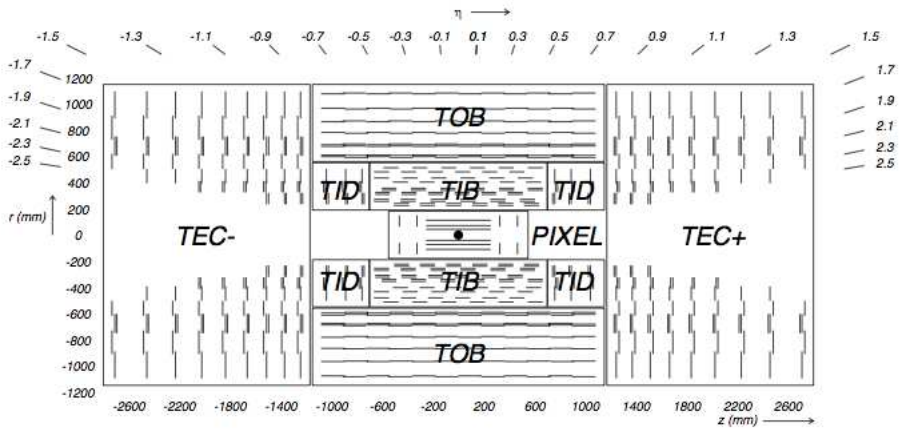

Figure 3: Layout of the tracker, showing the pixel detector, TIB, TID, TOB, and TEC [3].

The main tasks of the silicon detector are tracking and vertexing. The silicon strip tracker measures charged particles within the $|\eta| < 2.5$ pseudorapidity range. The pixel detector provides 3 space points for each track up to $|\eta| < 2.4$. The strip tracker inner barrel and disks provide up to 4 $r - \phi$ measurements, while the outer barrel provides another 6 $r - \phi$ measurements. The strip tracker end caps give up to 9 ϕ measurements. This layout ensures at least 9 strip tracker hits for each track, with at least 4 of those being two dimensional. Figure 4 shows the number of strip tracker hits per track as a function of $|\eta|$.

The tracker provides an impact parameter resolution of $\sim$15 μm and a transverse momentum (p_{T}) resolution of about 1.5 % for 100 GeV/c particles [3].

The vertexing and tracking performance has been studied during the early data taking period at $\sqrt{s} = 7$ TeV [4]. The primary vertex resolutions for vertices with more

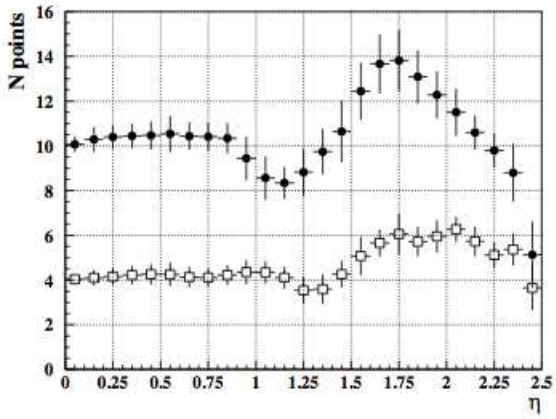

Figure 4: Number of measurement points in the strip tracker as a function of pseudorapidity . Filled circles show the total number (back-to-back modules count as one) while open squares show the number of stereo layers [3].

than 30 tracks are found to be around 25 μm in x and y, and around 20 μm in z. Figure 5 shows the primary vertex resolutions in x, y, and z as a function of the number of tracks in the vertex.

The resolution of the track impact parameter depends on the p_{T} and η of the track. The impact parameter resolution improves for tracks with higher p_{T} since they are less affected by multiple scattering. Tracks at higher values of $|\eta|$ travel through more material, and so the multiple scattering effects are increased, leading to a degradation in the impact parameter resolution. The measured impact parameter resolutions as a function of the track p_{T} are shown in Figure 6, while they are shown as a function of η in Figure 7. The dip in the longitudinal impact parameter resolution at $|\eta| = 0.5$ is due to the fact that at this angle, the particle deposits its charge in more than one pixel. The position is then determined by the charge barycenter, improving the resolution.

2.2.3 The Electromagnetic Calorimeter

The electromagnetic calorimeter (ECAL) is made of scintillating lead tungstate ($PbW0_4$) crystals. The signal is read out by avalanche photodiodes in the barrel section (EB)

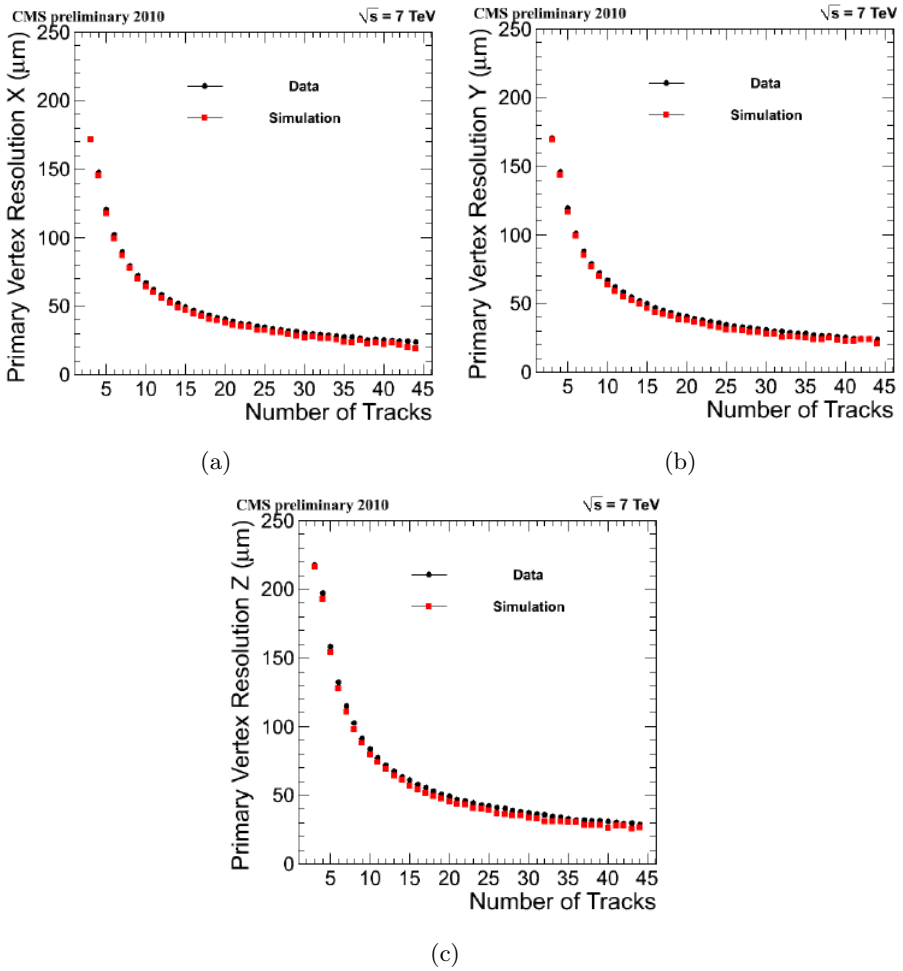

Figure 5: Primary vertex resolution in x (a), y (b), and z (c) as a function of the number of tracks [4].

and vacuum phototriodes in the endcaps (EE). The ECAL provides coverage in pseudorapidity $|\eta| < 1.479$ in the EB and $1.479 < |\eta| < 3.0$ in the EE. A preshower detector consisting of two planes of silicon sensors interleaved with a total of $3\,X_0$ of lead is located in front of the EE, where X_0 is the radiation length. The ECAL has an energy resolution of better than 0.5 % for unconverted photons with transverse energies above 100 GeV. The layout of the ECAL is shown in Figure 8.

The EB is made up of 61,200 crystals formed into 36 "supermodules", each containing 1700 crystals, and two endcaps, made up of almost 7,324 crystals each. Each

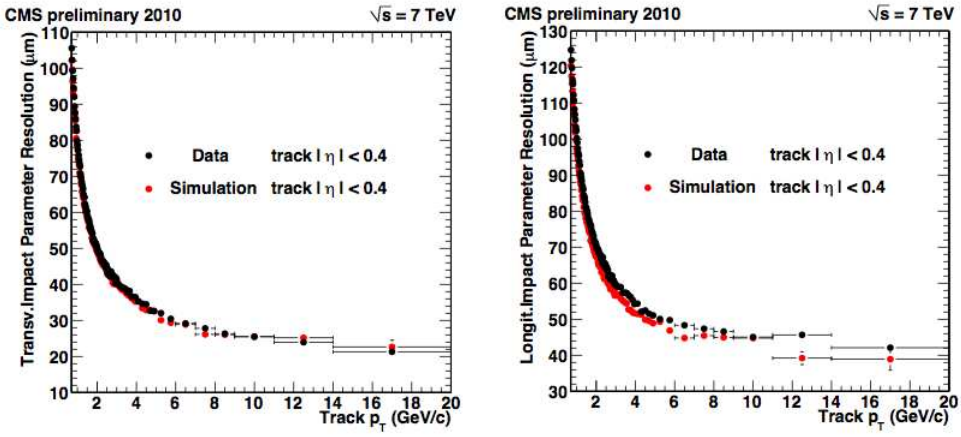

Figure 6: Track transverse (left) and longitudinal (right) impact parameter resolution as a function of the track p_{T} [4].

crystal is tapered, with an area of 22x22 mm^2 at the front face and 26x26 mm^2 at the back face. The crystals are arranged in a semi-projective array, so that the axes make an angle of approximately 3° with respect to the vector from the center of the detector, in order to avoid having the cracks aligned with the particle trajectories. The distance between the centers of the front faces of the crystals and the nominal interaction point is 1.29 m.

Each endcap contains 7,324 crystals. The crystals are grouped into groups of 5x5 crystals to form supercrystals. The endcaps are divided into two "Dees" each, which have 3,662 crystals. Each Dee contains 138 supercrystals and 18 partial supercrystals along the inner and outer edges. The crystal faces are 315.4 cm from the interaction point, and are pointed toward a spot 1300 mm farther than the interaction point. This gives angles between 2-8°.

The preshower detector is a sampling calorimeter, with two layers covering the range $1.653 < |\eta| < 2.6$. The purposes of the preshower detector are to identify neutral pions in the endcaps, help identify electrons from minimum ionizing particles, and improve the position resolution for electrons and photons. It is made of alternating layers of lead radiators and silicon strip sensors. The lead radiators initiate the shower, while the

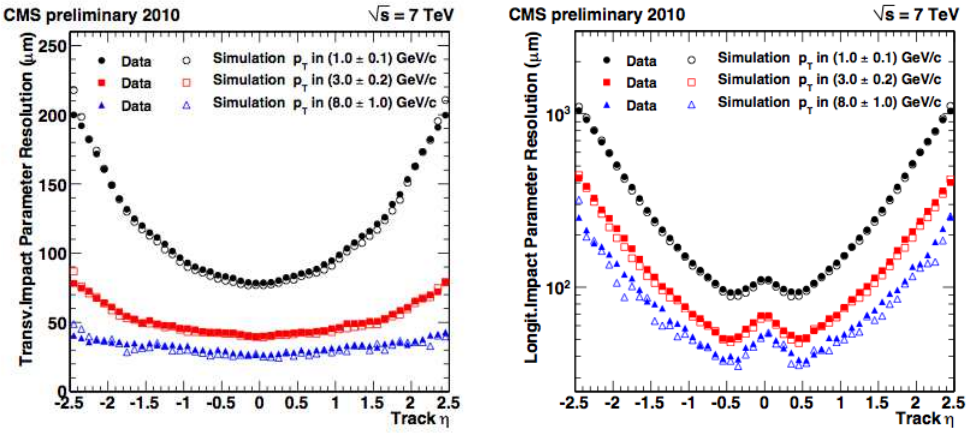

Figure 7: Track transverse (left) and longitudinal (right) impact parameter resolution as a function of η of the track for different values of the track p_{T} [4].

silicon strips measure the deposited energy and the shape of the shower. The strips in the two layers are oriented orthogonal to each other, and have a pitch of 1.9 mm. The preshower detector has a total thickness of 20 cm.

2.2.4 The Hadronic Calorimeter

The hadronic calorimeter (HCAL) is a sampling calorimeter, and compliments the energy measurement of the ECAL. The HCAL is composed of the barrel (HB), endcap (HE), outer (HO), and forward (HF) calorimeters. The HB and HO cover the range $|\eta| < 1.3$, the HE covers $1.3 < |\eta| < 3$ and the HF covers $3 < |\eta| \leq 5.2$. The HB, HE, and HO are made of alternating layers of brass or steel absorbers and plastic scintillators. The HCAL, when combined with the ECAL, measures jets with a resolution $\Delta E/E \approx 100\,\%/\sqrt{E\,[GeVns]} \oplus 5\,\%$. Figure 9 shows the layout of the HCAL.

The HB is made of 36 identical azimuthal wedges which are formed into two half barrels. The wedges are constructed out of plates of absorbers alternated with tiles of plastic scintillator, parallel to the beam axis. The innermost and outermost absorber plates are made of stainless steel for structural strength. The other absorber plates are composed of a 40 mm steel front plate, eight 50.5 mm brass plates, six 56.5 mm brass

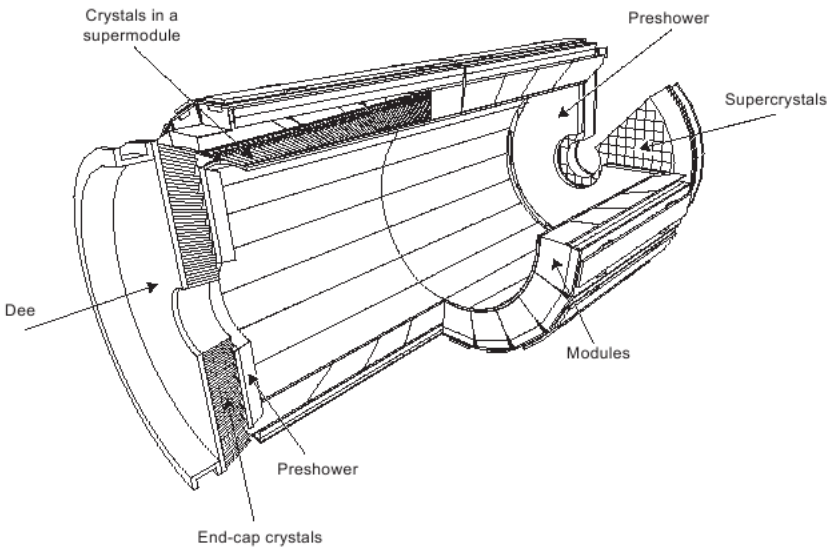

Figure 8: Layout of the ECAL including the barrel, endcaps, and preshower.

plates, and a 75 mm steel back plate. The light from the scintillators is collected with wavelength shifting fibers embedded in the scintillators, which are spliced to clear fibers when they leave the scintillator and are read out by hybrid photodiodes.

The amount of material for the HB is limited by the ECAL and the solenoid, so the HO is located outside of the solenoid to contain the hadronic shower in the central psuedorapidity region. The HO is the first sensitive layer in each of the five iron return yoke rings. In the central ring, there are two layers of scintillator on either side of a 19.5 cm piece of iron. All other rings have a single HO layer.

The HF is located 11.2 m from the interaction point, with the inner radius at 12.5 cm from the beamline. Since the HF is at such high pseudorapidity it is exposed to large particle fluxes. To account for the harsh environment, quartz fibers were chosen as the active material. The detector operates by the Cherenkov effect. The calorimeter is composed of 5 mm steel absorber plates with the fibers inserted into grooves. The fibers run parallel to the beamline. Half of the fibers run the entire length of the HF, while the other half begin at 22 cm from the front of the detector. This is to distinguish

between electrons and photons, which deposit almost all of their energy in the front of the detector, from the hadrons, which deposit approximately equal amounts of energy in the front and back segments.

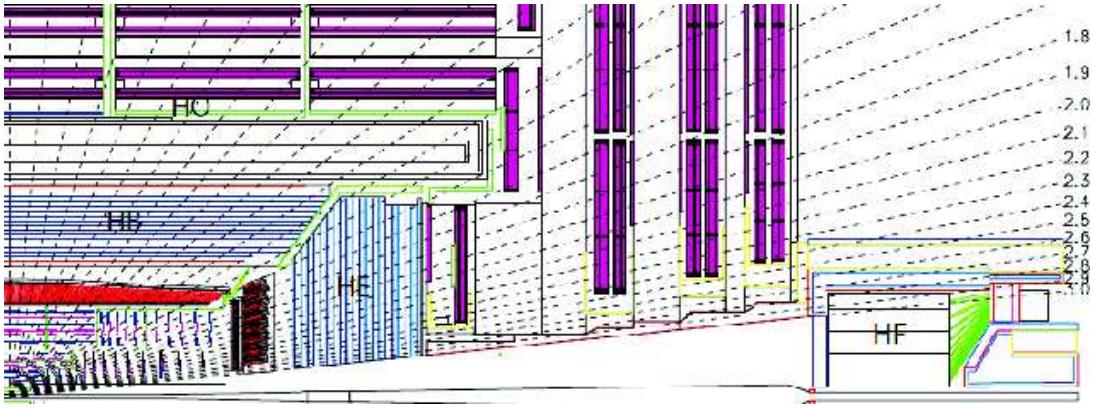

Figure 9: Longitudinal view of the CMS detector showing the positions of the hadron barrel (HB), endcap (HE), outer (HO) and forward (HF) calorimeters.

2.2.5 The Muon System

The detection and measurement of muons has always been one of the central goals of the CMS detector. The muon system covers the pseudorapidity range $|\eta| < 2.4$, and is composed of Drift Tubes (DTs), Cathode Strip Chambers (CSCs), and Resistive Plate Chambers (RPCs). The muon system has three main purposes: muon identification, momentum measurement, and triggering. Matching the muons to the tracks measured in the silicon tracker results in a transverse momentum resolution between 1 and 5 %, for p_{T} values up to 1 TeV/c. The muon detection system has nearly 1 million electronic channels.

The DTs cover the barrel region, $\eta < 1.2$. In this region the magnetic field is uniform and the rate is low, so standard rectangular drift tube cells are used. They are organized into 4 stations and are located between the layers of the iron return yoke. The first three stations each contain 2 groups of 4 chambers that measure the muon position in the $r-\phi$ plane, and another 4 chambers which measure the muon position in the z direction.

The fourth station does not have the 4 z-position chambers.

The CSCs are used in the endcap region ($0.9 < \eta < 2.4$) because of the high rates and background, and non-uniform magnetic field. The CSCs are fast, finely segmented, and radiation resistant. They are multiwire proportional chambers, consisting of 6 layers of anode wire planes interleaved with 7 cathode strip planes. Each endcap has 4 CSC stations, with the chambers perpendicular to the beamline and located between the return yoke plates. The cathode strips run radially outward, and provide the measurement in the $r - \phi$ plane. The anode wires run approximately perpendicular to the cathode strips and are also read out to give a measurement in η.

The DTs and CSCs can both easily trigger on the p_{T} of the muon, but due to the large uncertainty in the background rates and the ability to measure the correct beam-crossing time a complementary trigger system was designed using RPCs. The RPCs are parallel plate gas chambers, operated in avalanche mode. They have a very good time resolution, but a coarser position resolution than the DTs or CSCs. There are 6 layers of RPCs in the barrel region: 2 in each of the first 2 muon stations and 1 in each of the last 2 muon stations. In the endcap region there are 3 layers of RPCs, covering up to $\eta < 1.5$.

2.2.6 The Forward Detectors

The very forward angles are covered by the Centauro And Strange Object Research (CASTOR) detector and the Zero Degree Calorimeter (ZDC). CASTOR covers the range from ($5.3 < |\eta| < 6.6$), while the ZDC covers ($|\eta| > 8.3$). Two extra tracking stations, built by the TOTal Elastic and diffractive cross section Measurement (TOTEM) experiment, are placed at forward rapidities ($3.1 < |\eta| < 4.7$ and $5.5 < |\eta| < 6.6$).

The ZDC and CASTOR calorimeters are Cherenkov sampling calorimeters, each consisting of electromagnetic (EM) and hadronic (HAD) sections. The calorimeters are built from tungsten absorber plates, alternated with fused silica quartz plates in CASTOR and quartz fibers in the ZDC, and read out by photomultiplier tubes. The

plates are placed at a 45° angle with respect to the incoming particles' direction to maximize the light signal. The CASTOR geometry is shown in Figure 10. CASTOR is placed 14.38 m from the interaction point. The ZDC is located approximately 140 m from the interaction point. Figure 11 shows the geometry of the ZDC.

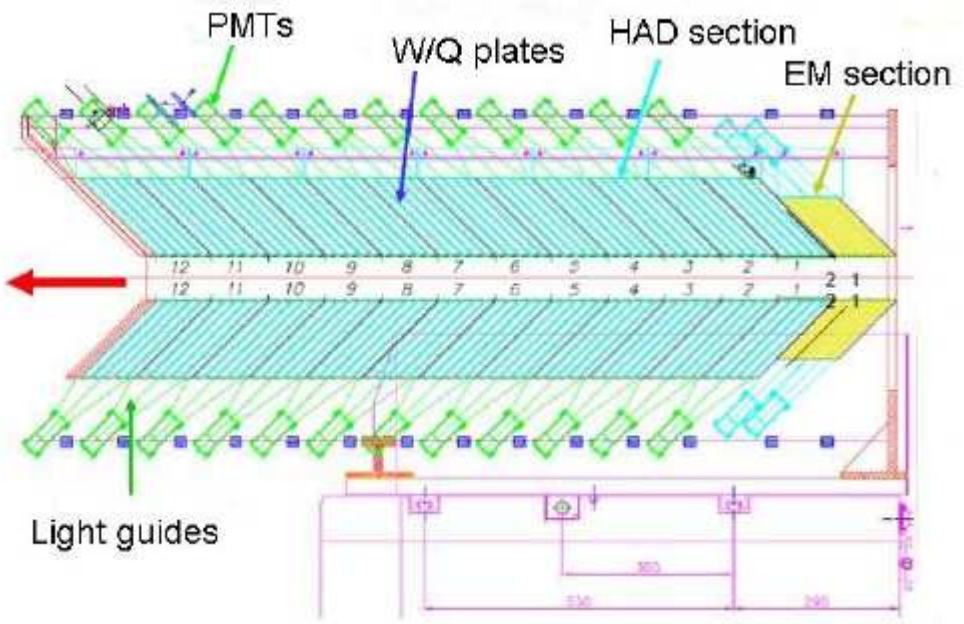

Figure 10: Side cutaway view of CASTOR showing the EM and HAD sections.

2.2.7 The Trigger System

During proton-proton collisions, the LHC is designed to have a beam crossing interval of 25 ns, which corresponds to a crossing rate of 40 MHz. At the design luminosity of $10^{34} cm^{-2} s^{-1}$, there are approximately 20 collisions per bunch crossing. The amount of data associated with this large number of events is impossible to store, and the rate must be reduced. In CMS this is accomplished with a two level trigger system, the Level-1 (L1) trigger and the High-Level Trigger (HLT). The combined L1 and HLT system is designed to be able to reduce the rate by a factor of at least 10^6.

The L1 trigger is mainly hardware based and has a design output rate limit of 100

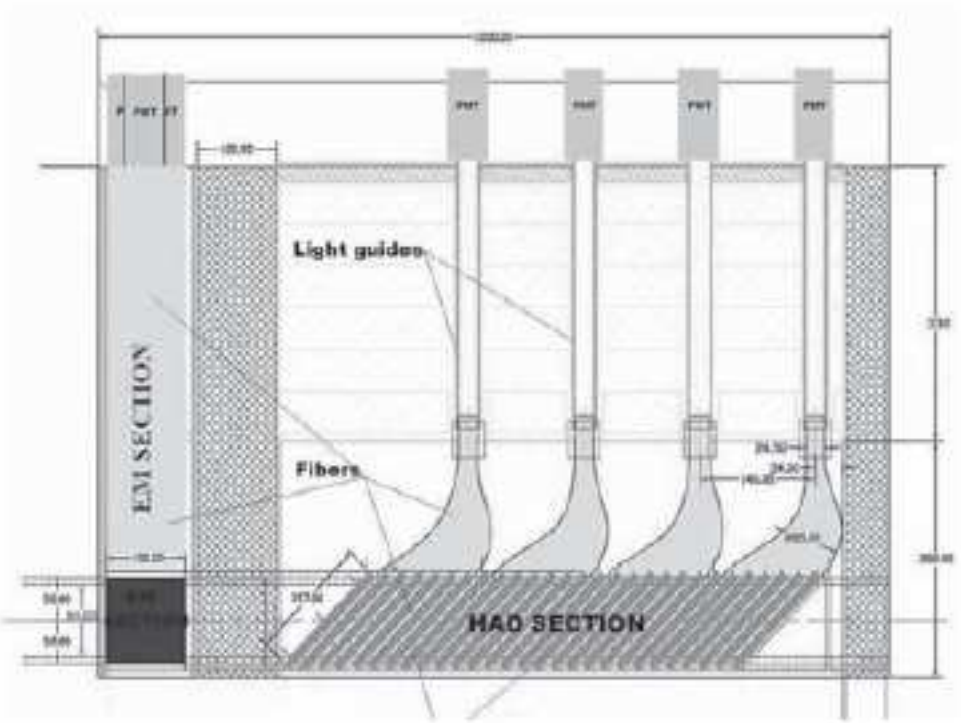

Figure 11: Side cutaway view of the ZDC showing the EM and HAD sections.

kHz. The L1 uses information from the calorimeters and muon detectors to select, in less than 1 μs, the most interesting events. The HLT is software based and has access to the complete read-out data, and can be based on complex calculations. The High Level Trigger (HLT) processor farm further decreases the event rate from around 100 kHz to around 300 Hz before data storage.

3 The CMS Pixel Detector

The silicon pixel detector is the closest subdetector to the interaction point. The main goal of the pixel detector is to provide very good impact parameter resolution and vertexing, as well as three spatial points for track reconstruction. The pixels have a size of 150x100 μm^2, with the 100 μm dimension in the $r-\phi$ direction in the barrel and the r direction in the forward disks. The dimensions were chosen to be nearly square in order to provide similar resolution in both the $r-\phi$ and z directions.

The CMS pixel detector is a "hybrid" pixel detector. A hybrid pixel detector consists of a separate sensor and readout electronics chip, which are designed and manufactured separately and then bump bonded together. The detector layout, sensors, and readout electronics are described briefly in the following sections. More details about the design and construction of the pixel detector can be found elsewhere [38, 3].

3.1 Detector Layout

The pixel detector consists of a barrel section (BPix) with 3 cylindrical layers at radii of 4.4 cm, 7.3 cm, and 10.2 cm, and two forward disks on each end (FPix), at a distance of 34.5 cm and 46.5 cm from the center of the CMS detector. The inner radius of the forward disks is at 6 cm, and the outer radius is at 15 cm. The pixel detector covers the pseudorapidities $-2.5 < \eta < 2.5$, and provides three space tracking points. The layout is shown in Figure 12.

The BPix has a total of 48 million channels and covers an area of 0.78 m^2. There are about 800 modules in the barrel section. There are 672 full modules, and the remaining modules are half modules, located where the two halves of the barrel join. A full module consists of a silicon sensor bump bonded to 16 readout chips (ROCs), while a half module has only 8 ROCs. Each ROC consists of 52x80 pixels of size 150x100 μm^2 [38, 3].

The FPix has a total of 18 million channels and covers an area of 0.28 m^2. The forward disks are divided into plaquettes, which consist of a single sensor bump bonded

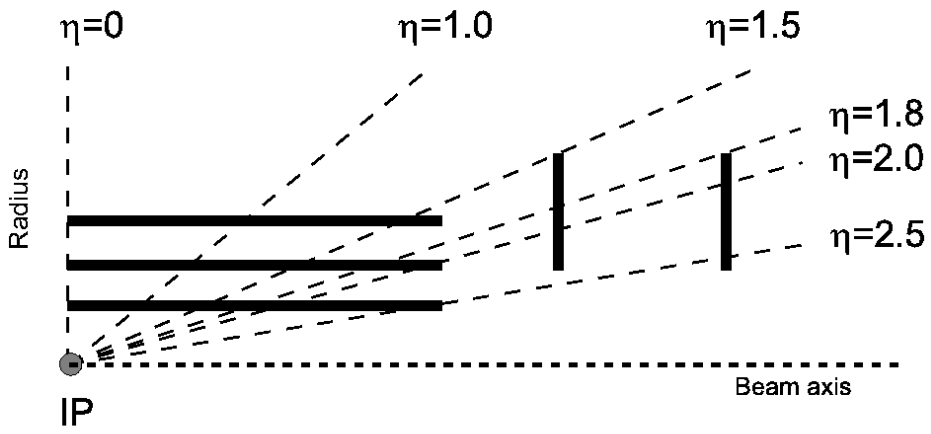

Figure 12: The geometrical layout of one quadrant of the CMS pixel detector, showing the locations of the three barrel layers and two forward disks. [3]

to the ROCs. In order to cover the geometry of the disks with no gaps, there are 5 different types of plaquettes: 1x2, 2x3, 2x4, 1x5, and 2x5, where the numbers refer to the number of ROCs in the plaquette (in the format row x column). The plaquettes are arranged on "blades", which form a turbine-like geometry. There are a total of 672 plaquettes in the FPix [3].

The pixel detector is contained inside the 3.8 T magnetic field. In the barrel region, the drift of the electrons is perpendicular to the magnetic field. The resulting Lorentz-drift leads to a spread of the charge between several pixels. This charge sharing, along with the analog readout of the signal, allows for a spatial resolution of 13 μm in the $r-\phi$ direction and 14 μm in the z direction [39].

In the forward disks, the blades are tilted at a 20° angle so that the particles cross the sensors at a non-normal angle. In addition, the electrons do not drift parallel to the magnetic field. This geometry helps to induce charge sharing. Figure 13 shows the FPix blade geometry. The forward pixels have a spatial resolution of 10 μm in the $r-\phi$ direction and 17 μm in the z direction [5].

Figure 13: One half disk of the supporting structure of the FPix, showing the tilted blades [5].

3.2 Read Out and Control System

The read out and control system of the pixel detector consists of three main parts: the read out of the data from the modules to the pixel front end driver (pxFED), the fast control link between the pixel front end controller (pFEC) and the modules, and the slow control link between a standard front end controller (FEC) and the supply tube. A diagram of the read out and control system is shown in Figure 14.

The read out of the analog data from the ROCs is controlled by the Token Bit Manager (TBM). The data is transferred at 40 MHz to the Analog Optical Hybrid (AOH). The electric signal is then converted to an optical signal and is sent on to the pxFED, where the signals are digitized. The ROC and TBM are discussed in more detail in the following sections. The pFEC sends the 40 MHz clock as well as the fast control signals, such as the trigger and reset signals, to the TBM.

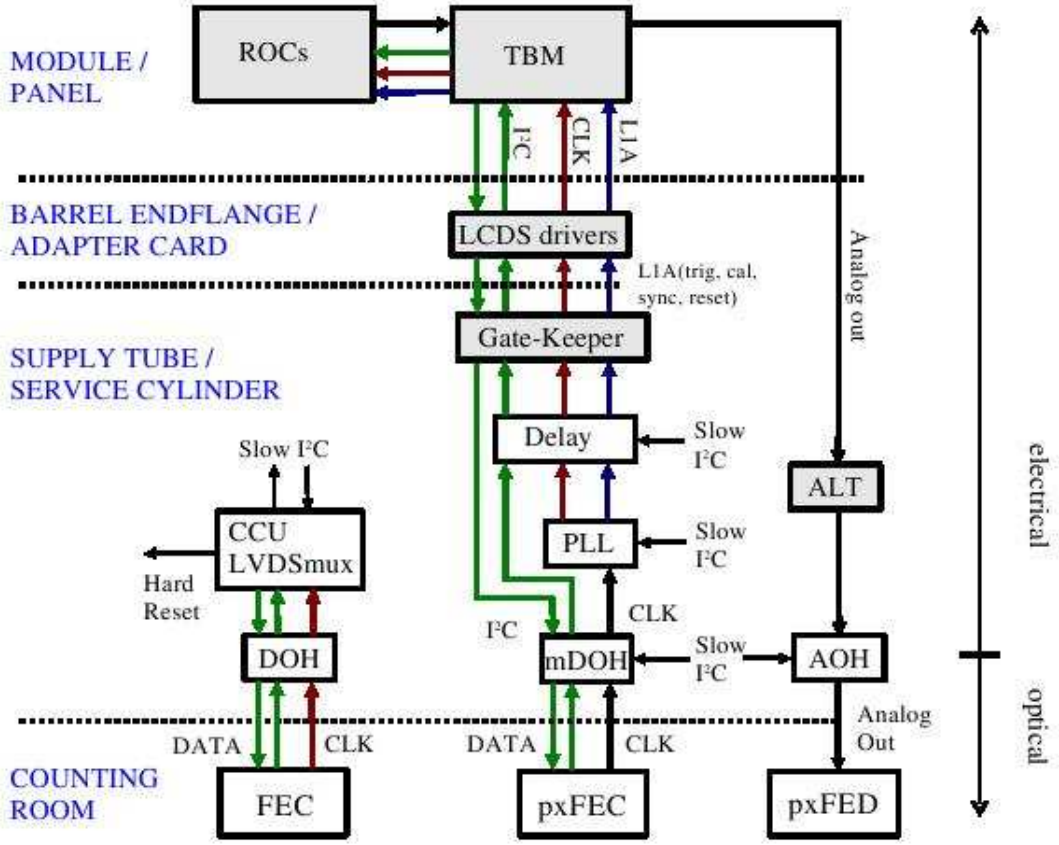

Figure 14: Diagram of the pixel detector read out chain and control system. More details can be found in [3].

3.3 Modules

Figure 15 shows photographs of a barrel pixel full module and a half module, as well as a diagram showing all the main components of a module. The module is composed of the sensor, the ROCs, a high density interconnect (HDI) containing the TBM, a power cable, a Kapton signal cable, and silicon nitride base strips to attach the module to the mechanical structure. The main components are described in the following sections.

3.3.1 The Token Bit Manager

The TBM controls a group of ROCs. In the barrel, the TBM is located on the module and controls either 8 or 16 ROCS, depending on the location and layer. In the forward

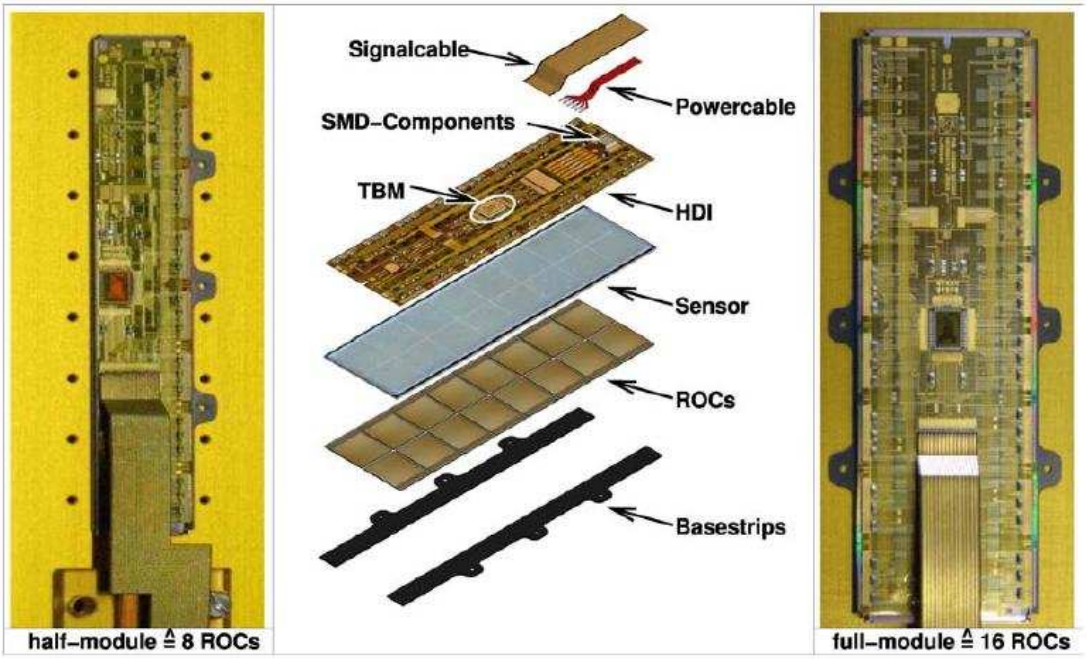

Figure 15: Picture of a BPix half module (left) and full module (right). The center shows an exploded view of a module, with the different components labeled.

disks, the TBM is located on the blade and controls either 21 or 24 ROCS, depending on which side of the blade it is on.

The TBM is responsible for sending the clock to the ROCs and initiating the read out of the module. When the TBM receives a Level 1 trigger, it passes the trigger to the ROCs, to tell the ROC not to delete the data for the triggered event. After some time the TBM passes a token to each ROC in series. When the ROC receives the token, it reports any hits and then passes the token to the next ROC.

The read out of a full module, shown in Figure 16, consists of a TBM header, a header for each ROC, followed by any hits from that ROC, and a TBM trailer. The TBM header begins with a very low signal, called "ultra-black", for 3 clock cycles, followed by a 1, called "black", to signify the beginning of the readout. Following this are four clock cycles containing the 8-bit encoded analog event number [40]. After the TBM header, each ROC adds a header followed by any hits.

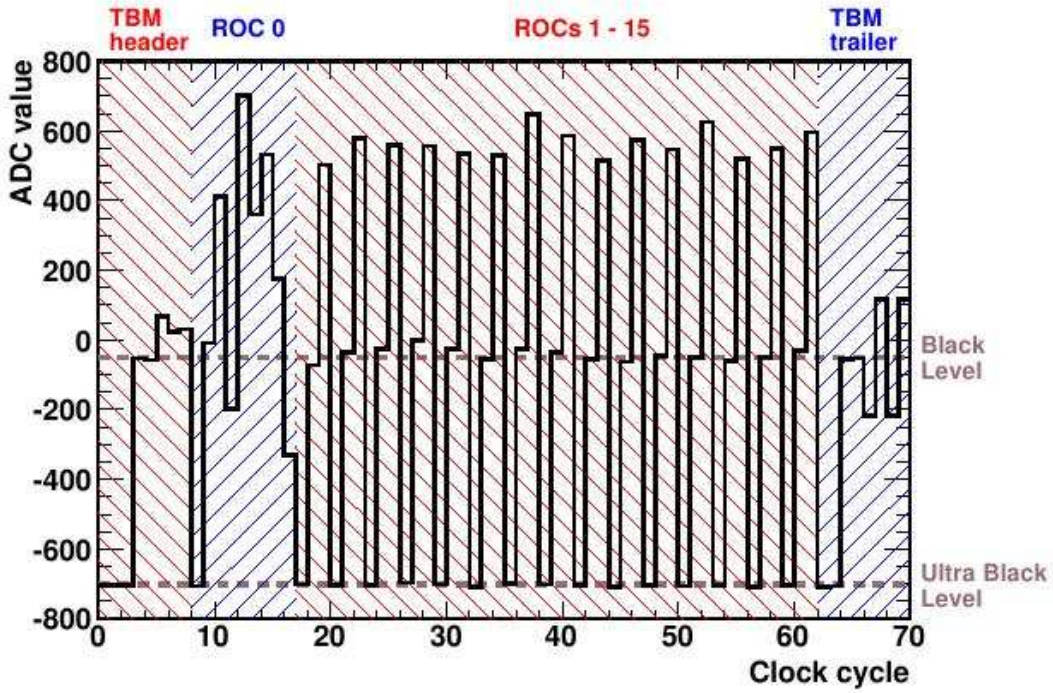

Figure 16: A read out of a full module with a hit in ROC 0, showing the TBM header, hit information from ROC 0, headers from the remaining ROCs, and TBM trailer.

3.3.2 The Readout Chip

The readout chip is a custom designed application-specific integrated circuit (ASIC). It contains 52x80 pixels and is commercially fabricated in a 0.25 μm complementary metal oxide semiconductor (CMOS) process [3]. The ROC has several purposes. It provides zero suppression with an individually adjustable threshold in each pixel unit cell. The ROC also amplifies and buffers the signal from the sensor. It also provides the Level 1 trigger information and discards any hits which do not have a corresponding L1 trigger.

The ROC has three main blocks: the array of pixel unit cells (PUCs), the double column periphery, and the chip periphery. Figure 17 is a picture of the ROC showing these three blocks as well as a double column. The chip periphery contains various control and supply circuits. The double column periphery controls the read out of the double columns, including transfering the hit information from the pixel to the storage

buffers and the trigger verification [41].

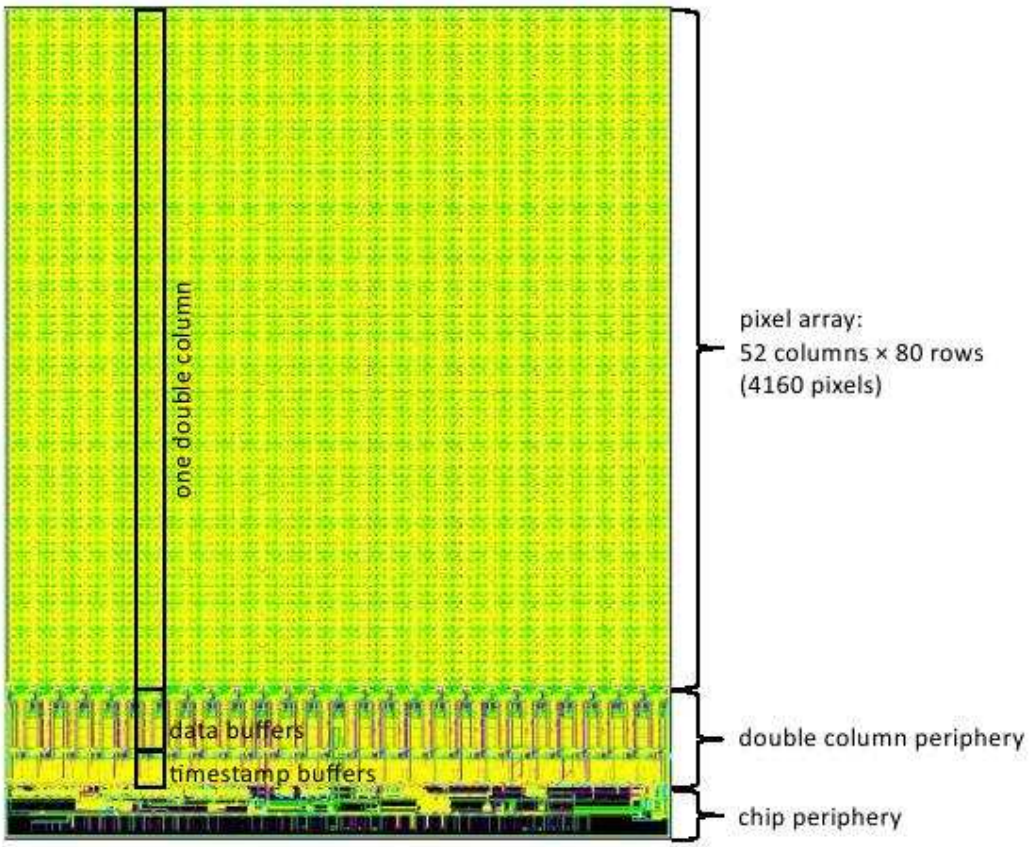

Figure 17: The read out chip.

The schematic of a pixel unit cell is shown in Figure 18. The PUC consists of an analog part (top) and a digital logic part (bottom). The signal enters the PUC from the sensor through the bump bond. A calibrate signal can also be injected, either by a 4.8 fF capacitor connected directly to the amplifier, or via the sensor through the air gap between a top metal pad on the ROC and the sensor. The direct signal injection can be used to adjust the pixel threshold, while the indirect injection can be used to test the bump bonds.

The signal passes through a two-stage preamplifier and shaper system. The signal then passes through a comparator, which provides the zero suppression. There is a 4-bit

digital to analog converter (DAC) to adjust the pixel's individual threshold, as well as a mask bit to disable noisy pixels. Once the signal passes the comparator it is stored in a sample-and-hold circuit. The double column periphery is notified, and the pixel waits for the column readout token. A double column can accept up to three hits before the column readout, and is insensitive to any further hits. When the PUC receives the column readout token, it sends the analog signal and the pixel row address to the double column periphery and passes the token.

The ROC handles the complete pixel address encoding for each hit, and sends this address along with the analog signal pulse height to the TBM. The digital pixel address is encoded in 6 level analog values, which are shown in Figure 19.

An example of a read out of a ROC with one hit is shown in Figure 20. The ROC header is three clock cycles and contains an ultra-black, a black, and a signal inversely proportional to the last addressed DAC value [41]. The pixel address is encoded in the 5 clock cycles following the ROC header. The first two clock cycles are the encoded double column, and the next three contain the encoded row. Finally, the analog pulse height is in the last clock cycle. In the case of multiple hits, the address of the next hit pixel would immediately follow the pulse height of the previous hit.

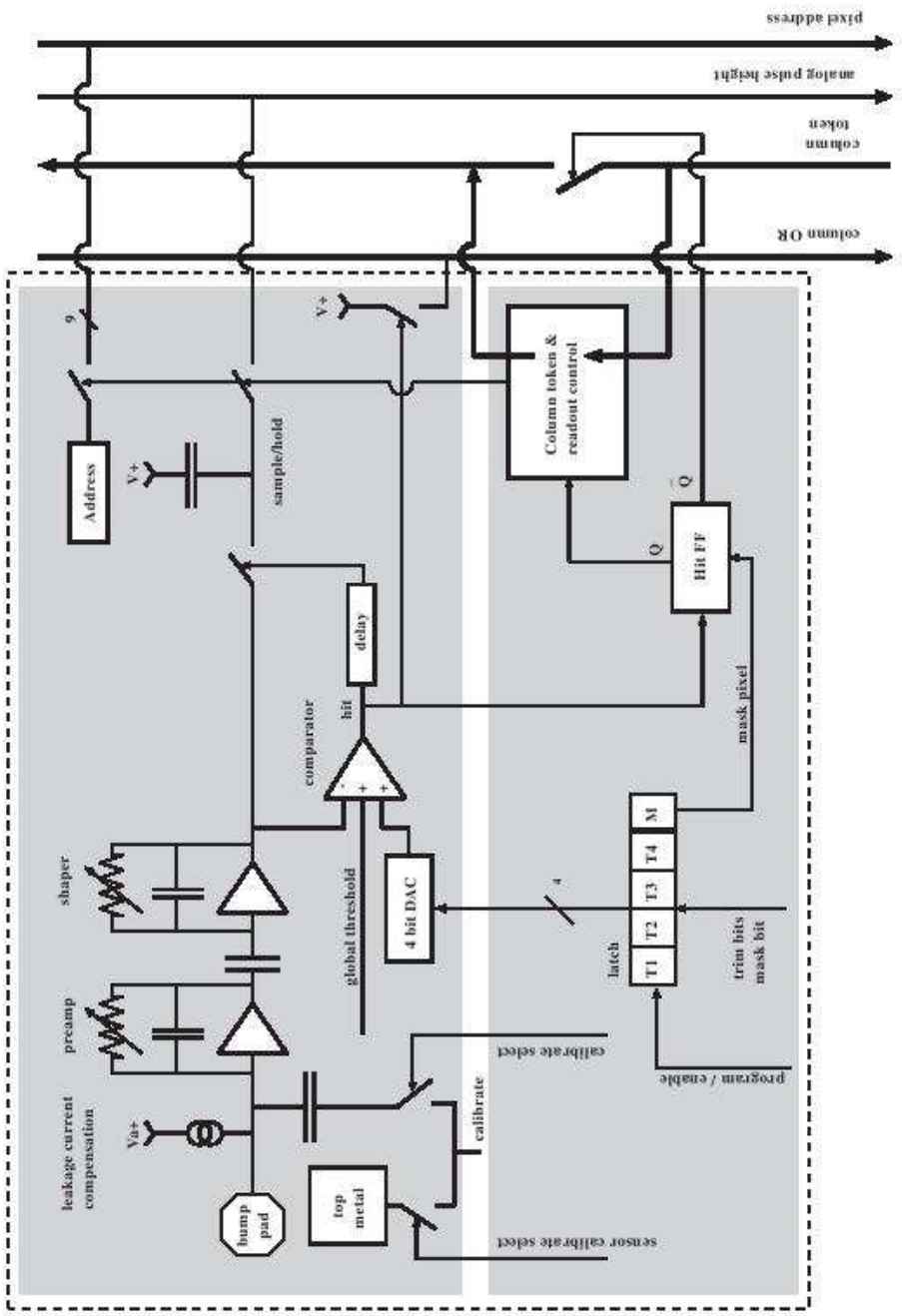

Figure 18: Schematic of the pixel unit cell.

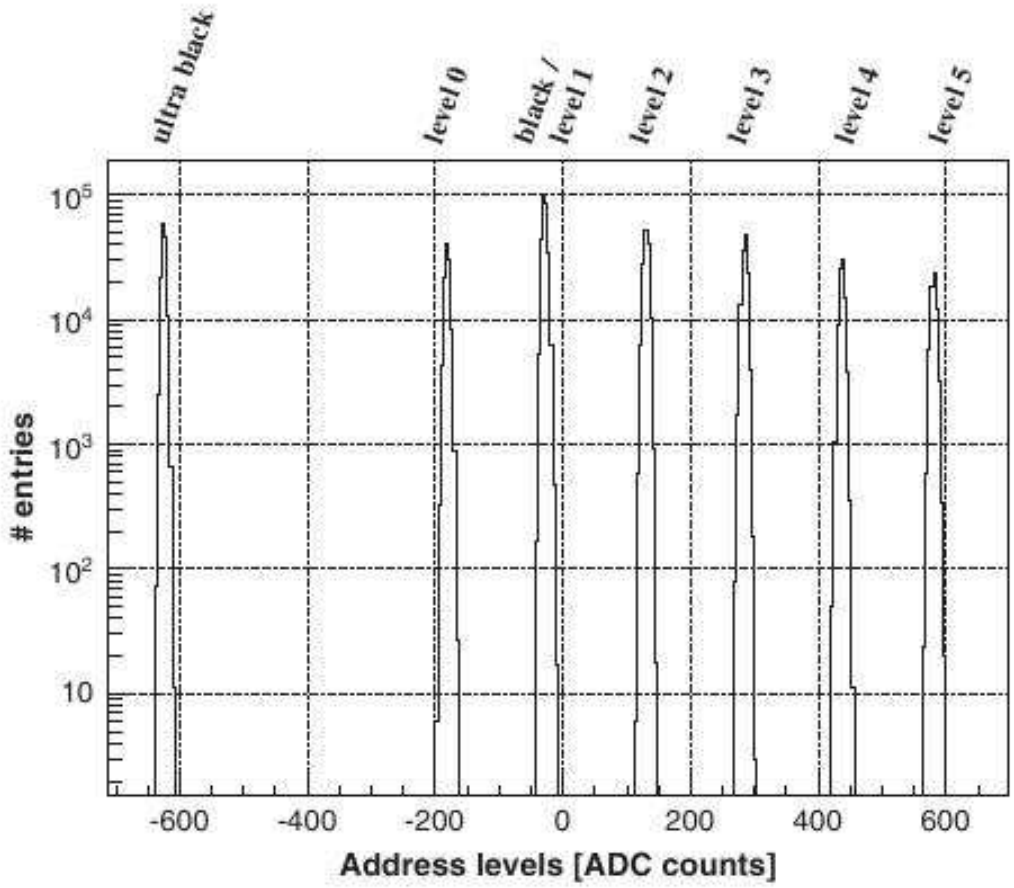

Figure 19: The pixel address encoding levels.

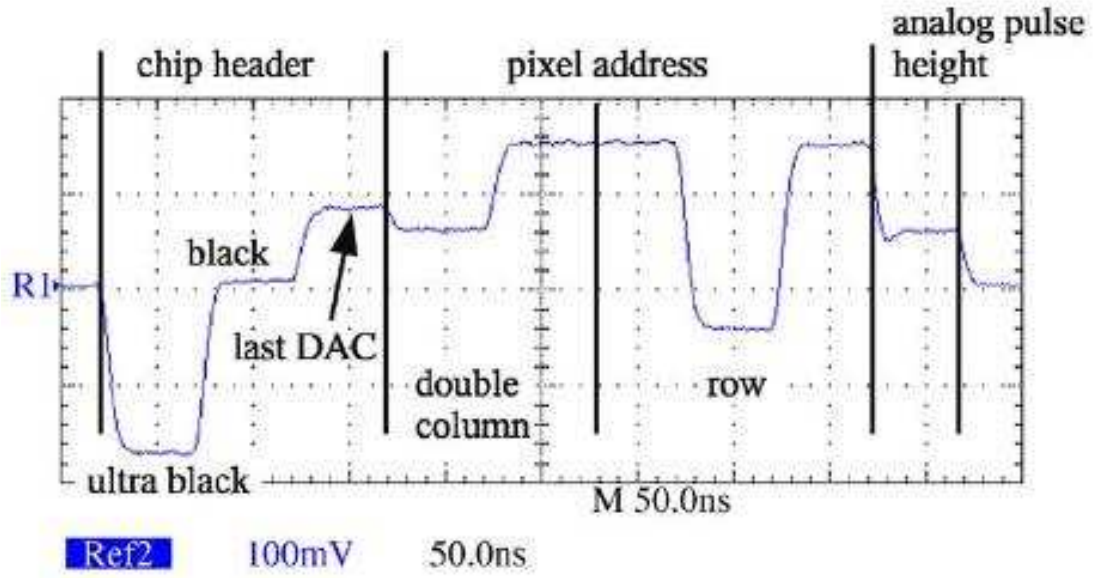

Figure 20: A read out of a hit from a ROC.

3.3.3 The Sensor

The basic operating principle of silicon sensors is discussed in Chapter 4. The sensor is made from 285 μm thick diffused oxygen float zone (DOFZ) silicon, as oxygen-enriched silicon has been shown to have better radiation hardness [1]. The BPix sensors were produced by CiS, using silicon with the $\langle 111 \rangle$ orientation and a resistivity of 3.7 kΩcm [7]. The sensor has a depletion voltage of 50-60 V. The FPix sensors were produced by Sintef, and consist of silicon with the $\langle 100 \rangle$ orientation and a resistivity of approximately 5 kΩcm. The depletion voltage is around 50 V [42].

The n+-in-n sensors consist of highly doped n-implants in an n-type substrate, and the pn-junction on the backside along with a multiple guard ring structure. This design requires double-sided processing, which increases the cost, but allows the edges of the sensor to be at ground potential so that the detector can be operated at high bias voltages (up to 600 V).

When a charged particle crosses the sensor material, it ionizes the silicon and produces electron-hole pairs. The electrons and holes drift in opposite directions, due to the internal electric field. This is shown in Figure 21. A minimum ionizing particle (mip) crossing perpendicularly through the sensor deposits a charge of approximately 22,000 electrons. The n-type pixels were chosen in order to collect electrons, which have a higher mobility. This reduces the effects of charge trapping, and thereby ensures a substantial signal even after high hadron fluences. After irradiation, the depletion region will start from the n+ implants, and will allow operation of the detector with moderate bias voltages.

The entire pixel detector is located within the magnetic field of the CMS solenoid magnet, and the charge carriers are deflected by the Lorentz force. The deflection angle of the charge carriers is called the Lorentz angle. It depends on the mobility of the charge carriers, which in turn depends on the electric field inside the sensor. The Lorentz angle was measured in a test beam [7], and the measured angle as a function of the bias voltage is shown in Figure 22.

In the FPIX open ring p-stops were used for the interpixel isolation. The opening in the p-stop ring provides a high resistance path between pixels after full depletion. The p-stop ring has a width of 8 μm, and the gap between the implants is 12 μm. A picture of four FPix pixels is shown in Figure 23. The seven different sensor designs needed for a blade, to accomodate the different number and arrangements of ROCs, are all produced on one wafer.

In the BPix, a moderated p-spray isolation is used. This technique combines a uniform p-spray implantation with a traditional p-stop, but does not require any additional mask. The technique is described in more detail in [43]. The gap between the implants is 20 μm. The BPix also include a "bias dot", which provides a high resistance punch-through bias structure. This allows IV measurements on the wafer to assess the sensor quality during production. A picture of four BPix pixels with the visible structures labeled is shown in Figure 24.

3.4 Mechanics and Cooling

The pixel barrel system is composed of the modules, their support structure, and the supply tubes to carry services from outside of the tracker volume to the detector. A drawing of one of the supply tubes is shown in Figure 25. The barrel has a length of 570 mm and is centered around the interaction region. The length of the total system, including the supply tubes, is 5.60 m. The barrel is divided vertically into two half cylinders, in order to be installed around the beam pipe and its supports. The two half cylinders are electrically separate and operate almost independently. Each half cylinder can slide into place in CMS on rails around the beam pipe. A schematic of one half barrel is shown in Figure 26.

The main structure is provided by the aluminum cooling tubes. The cooling tubes have a wall thickness of 0.3 mm. The tubes have a trapezoidal cross section. The aluminum cooling tubes are welded to an aluminum container which distributes the cooling fluid through the detector.

The cooling fluid used in the current detector is C_6F_{14}. It is foreseen to cool the detector down to a temperature of -10 °C. So far, the detector has been operated at a temperature of 17 °C in 2010 and 2011, and at 7 °C in 2012.

Carbon fiber blades with a thickness of 0.24 mm are glued to the top and bottom of two adjacent tubes. The individual segments are connected on each end to flanges to provide the half barrel structure. The end flanges are fiberglass frames filled with foam and covered with carbon fiber blades. The end flanges contain connectors for the module cables and for supplying power to the modules.

3.5 Material Budget

Any material in the path of the particles traversing the detector can contribute to multiple scattering, bremsstrahlung, photon conversions, and nuclear interactions. These effects can reduce the accuracy of the reconstruction of the tracks of the incoming particles. Therefore it is necessary to keep the amount of material in the tracker as low as possible.

The amount of material in the path of the particles is called the material budget. It is usually measured in terms of the fraction of radiation lengths, x/X_0. The radiation length, X_0, is defined as the mean distance in which an electron loses all but $1/e$ of its energy by bremsstrahlung.

The material budget for the tracker as a whole, as well as the pixel barrel detector, is shown in Figure 27. The material budget is broken into the different categories of the material. The main contribution of the pixel barrel to the overall tracker material budget is at $|\eta| > 1.2$. This comes from the end flange and the inner part of the supply tube [8].

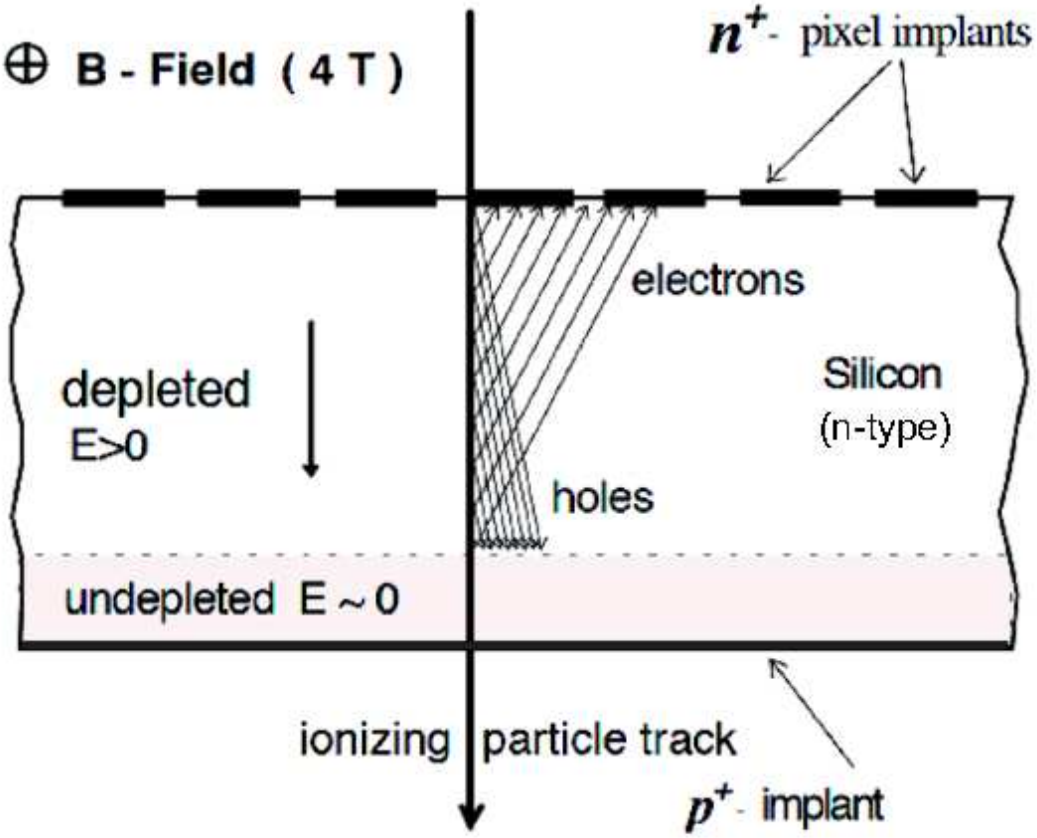

Figure 21: Sketch showing a charged particle crossing the silicon sensor. The n+ pixel implants collect the electrons. [6]

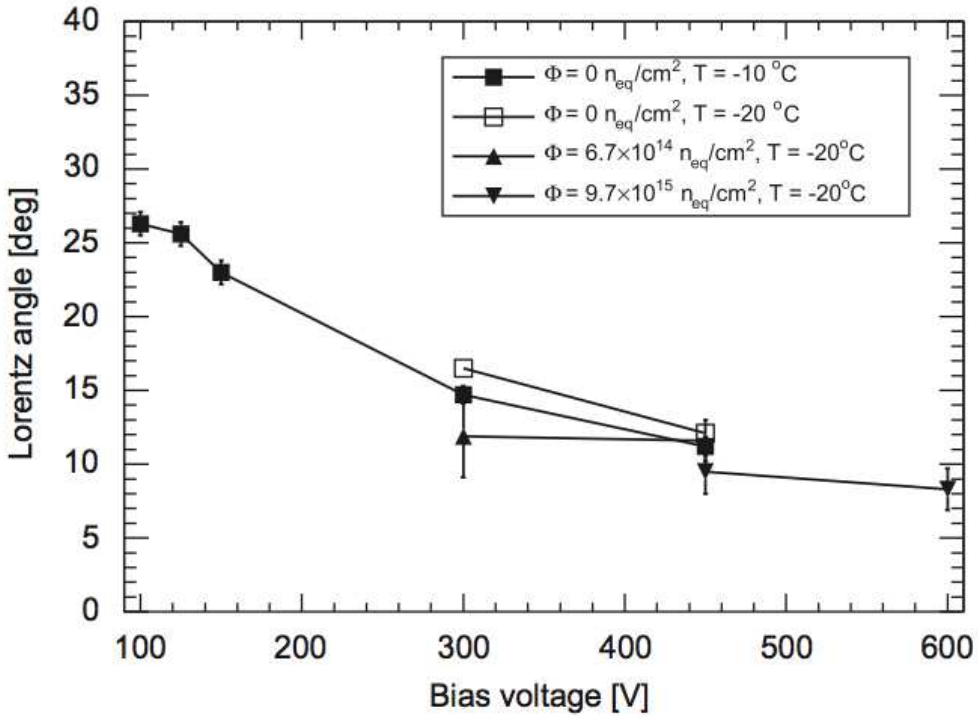

Figure 22: The Lorentz angle for the sensors in a 4 T magnetic field as a function of bias voltage [7].

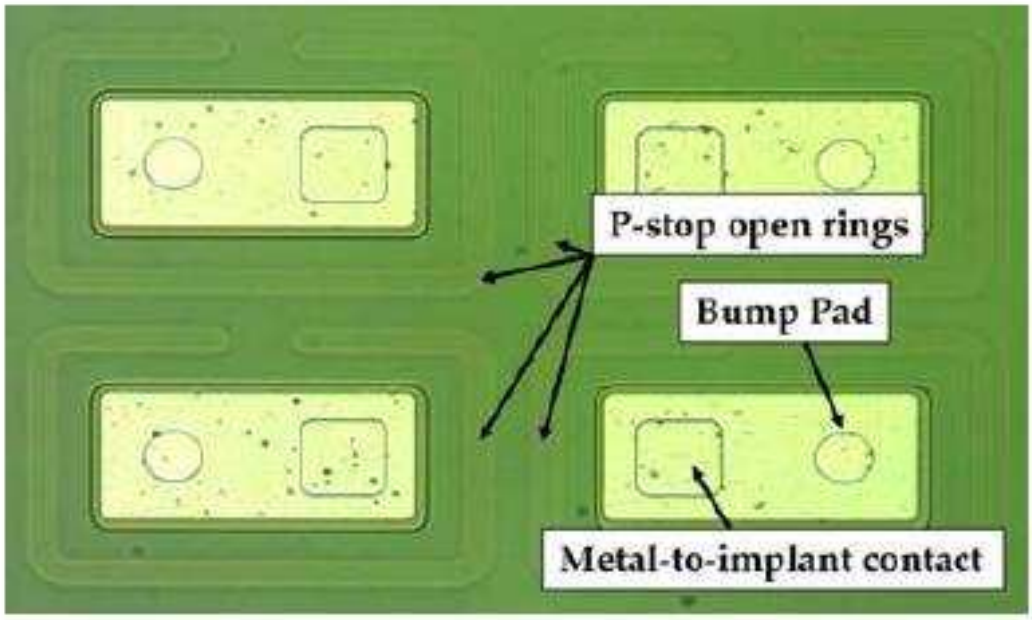

Figure 23: Picture of four pixels in the same double column for the FPix. The pixels have a pitch of 100 x 150 μm. [3]

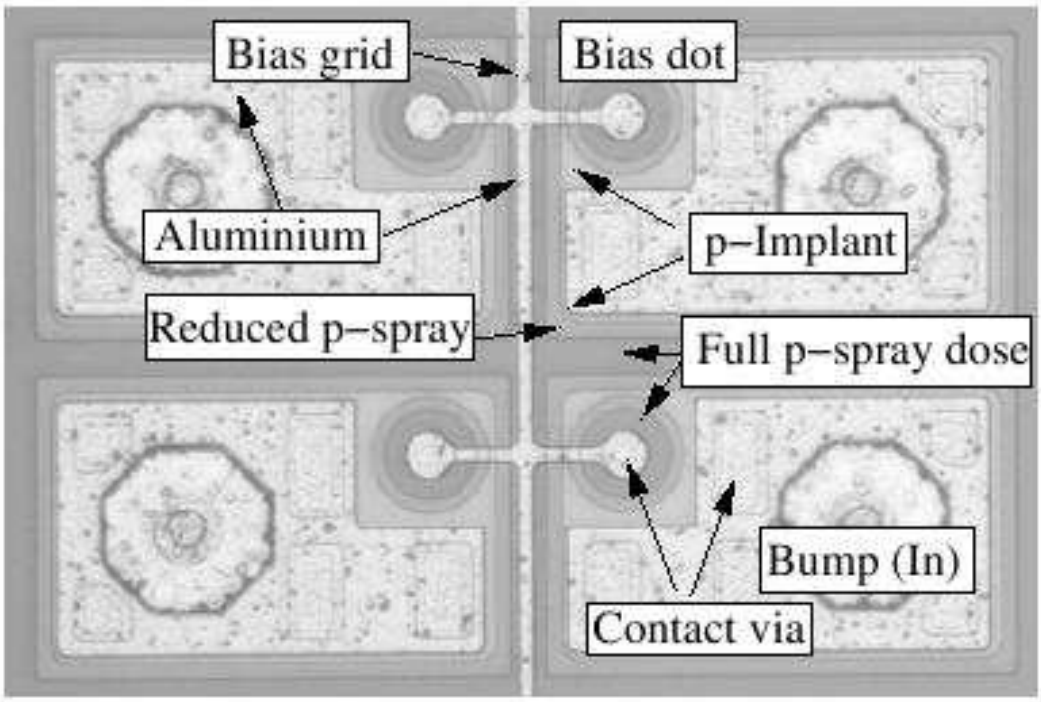

Figure 24: Picture of four pixels in the BPix. The pixels have a pitch of 100 x 150 μm. The indium bumps have been deposited but not reflown, and are visible. [3]

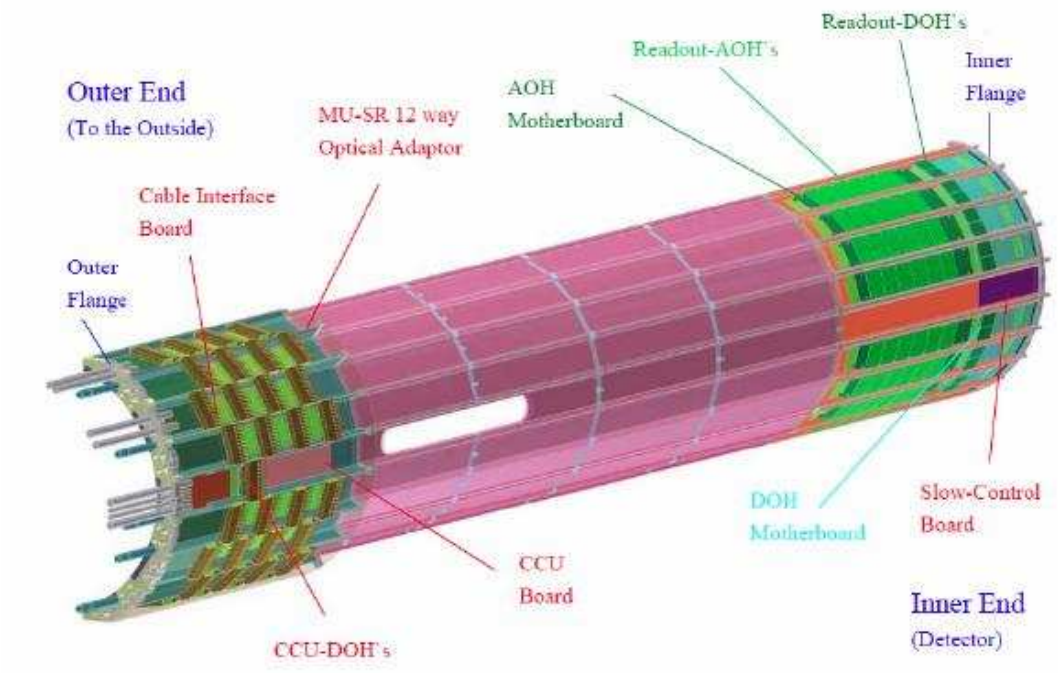

Figure 25: Drawing of one of the supply tubes. [3]

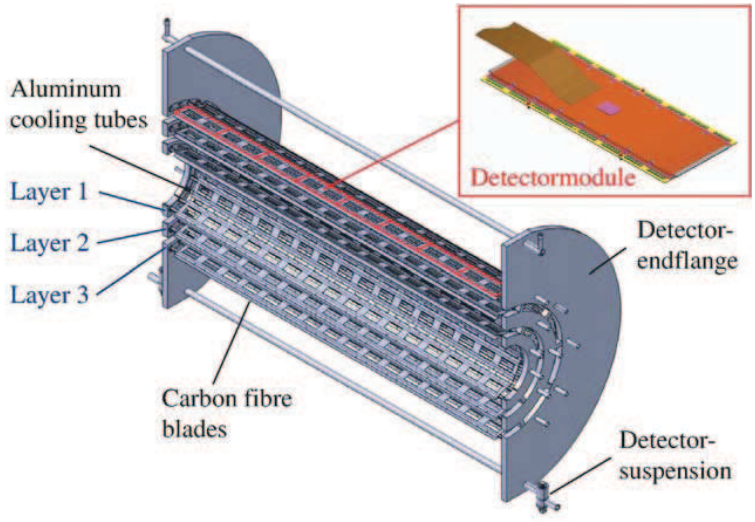

Figure 26: A sketch of one half cylinder of the barrel pixels. [3]

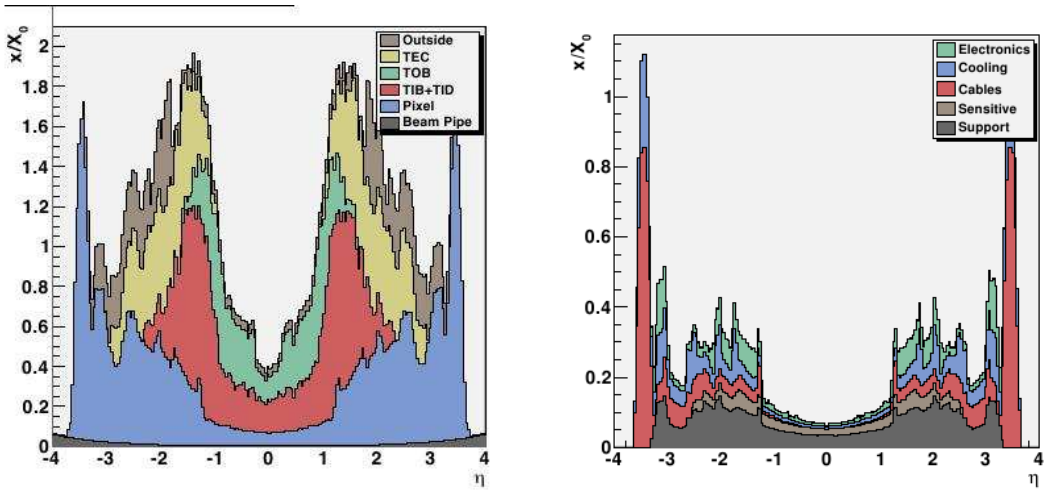

Figure 27: Left: Material budget for the whole CMS tracker, showing the various subdetector contributions. Right: Material budget for the pixel barrel detector, showing the various categories of material. [8]

4 Radiation Damage in Silicon Detectors

One of the challenges of tracking at colliders such as the LHC is designing detectors which can withstand the high radiation environment. Silicon detectors have the capability to be highly segmented, which makes them good choices for the innermost trackers, since a high granularity is important for vertexing and tracking in a dense environment such as the LHC. As commercial vendors are widely available and there is a lot of industrial experience in manufacturing silicon based devices, they are relatively inexpensive to produce. In addition, they have been shown to be sufficiently resistant to radiation damage for all previous applications, but they do degrade during the operation of the LHC. In order to fulfill the LHC specific requirements for long-term operation, it is important to study the degradation of the performance of silicon-based detectors due to the effects of radiation damage and to establish their operational limits [1].

4.1 Basic Properties and Operating Principle of Silicon Sensors

Before discussing the effects of radiation on the silicon sensors, it is necessary to discuss the basic properties of silicon sensors. Silicon atoms have four valence electrons which contribute to the bonding between atoms. It is possible to replace some atoms in the crystal lattice with another element which has either three or five valence electrons. This process is called doping.

In the case of a dopant atom with five valence electrons, four of the electrons are involved in the bonding, while the fifth electron can be excited by its thermal energy into a state shared between many atoms, and can move about the lattice. These atoms are called “donors”. In silicon doped with donor atoms, there is an excess of free electrons. This is called n-type silicon. In the case of a dopant atom with only three valence electrons, one of the four bonding sites is left empty. The dopant atoms are called “acceptors”. This type of material can be described as having an excess of holes which are free to move about the lattice. This type of silicon is called p-type.

When n-type and p-type silicon are joined together, the free electrons (holes) from the n-type (p-type) silicon diffuse across the junction and recombine. The diffusion of electrons from the n-side leaves behind positive ions, while the diffusion of holes from the p-side leaves behind negative ions. An electric field builds up which works against the diffusion, creating a stable region around the junction which is called the space charge region. This is depicted in Figure 28. This region is void of any free charge carriers, and is called the depletion zone. By applying a reverse-bias across the junction, this depletion zone can be increased. In sensors, the junction is abrupt, with one side of the junction several orders of magnitude more heavily doped than the other. The depletion region then extends only into the side with the lower doping concentration. When the size of the depletion zone equals the thickness of the silicon, it is said to be fully depleted.

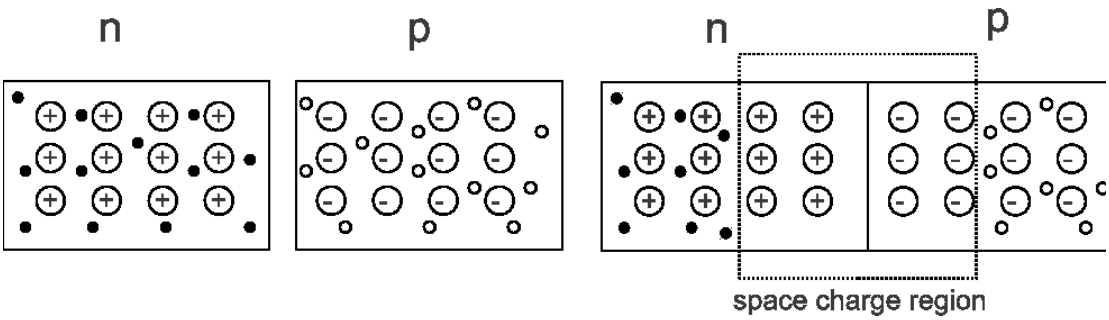

Figure 28: Formation of the space charge region around the pn-junction. The filled circles are free electrons, and the open circles are free holes.

The voltage required for full depletion of the detector depends on the effective doping concentration according to Equation 1, where V_{fd} is the full depletion voltage, q_0 is the charge of an electron, ϵ is the dielectric permitivity of silicon, ϵ_0 is the vacuum permitivity, and d is the thickness of the sensor. The effective doping concentration (N_{eff}) is defined as the number of donors minus the number of acceptors.

$$V_{fd} = \frac{q_0}{\epsilon\epsilon_0}|N_{eff}|d^2 \tag{1}$$

The electric field within the sensor is then given by the Poisson equation (Equa-

tion 2). It is linear and proportional to N_{eff}.

$$\nabla E = \frac{-eN_{eff}}{\epsilon\epsilon_0} \tag{2}$$

When a charged particle crosses through a depleted sensor, it creates many electron-hole pairs along its path. These electrons and holes are separated by the electric field and move towards the n- and p-contacts, respectively. The moving charges induce a signal on the contact, which is then read out by the readout electronics.

Silicon sensors always have leakage current, caused by the creation of electron-hole pairs by thermal excitation. Any defects in the silicon lattice act a centers for electron-hole pairs. The leakage current has an exponential temperature dependence, as shown in Equation 3. In this equation, E_g is the effective energy gap (1.12 eV), and k_b is the Boltzmann constant [44].

$$I \propto T^2 e^{\left(\frac{-E_g}{2k_bT}\right)} \tag{3}$$

4.2 Damage Mechanisms

The effects of radiation on silicon detectors can be separated into two categories: surface damage and bulk damage. Surface damage is the result of ionization in the covering layers of the sensor, and the effects on the overall operation of the CMS pixel detector are counteracted by the design of the sensors. Bulk damage is the result of non-ionizing energy loss, i.e. the displacement of nuclei in the silicon lattice, and leads to the observable degradation in the detector operation and performance.

4.2.1 Surface Damage

Surface damage refers to the defects created in the silicon oxide layer and the interface between the oxide and the bulk silicon. Surface damage comes mainly from ionization and the creation of electron-hole pairs in the oxide. As the interface between the oxide

and the bulk silicon is already irregular, displacement of single atoms does not significantly change the properties of the detector. The main effects of the surface damage are a build up of positive charge along the interface and an increase in the so-called surface current. The holes created near the surface are trapped due to their low mobility, while the electrons are collected. This build up of positive charge is called the "fixed oxide charge." This accumulation layer is a few nanometers thick, and change the electric field distribution in the first few micrometers below the surface. MIPs deposit their energy evenly throughout the bulk of the sensor, and so surface damage has little impact on the operation of the detectors for tracking charged particles. The main impact of the built up surface charge is a change in the electric field close to the surface, which can cause early breakdown. By creating a layout with small gaps between the pixels, this effect can be reduced.

4.2.2 Bulk Damage

Bulk damage is caused by particles which interact with the nucleus of an atom in the silicon lattice. The defects can be described as point and cluster defects, which affect the silicon in different ways. An incoming particle can knock an atom out of its position in the lattice. To knock a silicon atom out of its lattice position requires a recoil energy around 25 eV. For electrons this corresponds to an energy of 260 keV, or an energy of only 190 eV for protons or neutrons. The space left behind is called a vacancy, while the atom, which stops between the regular lattice positions, is called an interstitial. The pair of a vacancy and an interstitial is called a "Frenkel pair" and is a point defect.

This atom can also be called a primary knock on atom (PKA). If the PKA has enough energy, it can in turn knock out other atoms. At the end of the flight path it loses a lot of energy in a small volume and creates many defects. Such regions of high defect density are called cluster defects. A simulation of the path of a PKA through the silicon lattice is shown in Figure 29, with the point defects shown in red and the cluster defects shown in blue.

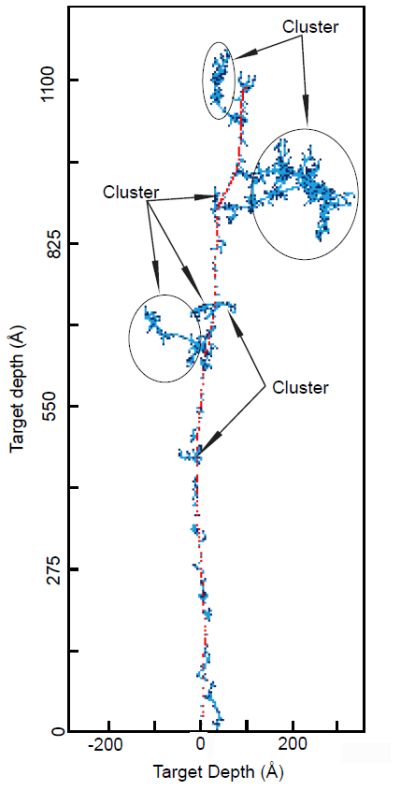

Figure 29: Simulation of the path of a primary knock-on atom through the silicon. Point defects are shown in red and cluster defects are shown in blue [9].

These defects in the silicon can introduce extra levels into the band gap. This leads to three main observable effects in the detector: a change in the space charge, charge trapping, and an increase in the leakage current [1]. These effects are described individually in Section 4.3.

4.3 Macroscopic effects

4.3.1 Effective Doping Concentration

The interstitial and vacancy defects are able to move about the silicon lattice, so it is possible for defects to combine to form compound defects. One possibility is for a vacancy to combine with another defect in the silicon, such as a phosphorus or oxygen

atom. In the case of a phosphorus atom combining with a vacancy, the defect becomes electrically inactive, and the net effect is the reduction of the donor concentration. In the case of an oxygen atom, the compound defect acts as an acceptor. In both cases the result is a shift of the space charge from positive to negative values.

This change in the effective doping concentration causes a change in the voltage required to deplete the silicon, which depends on the space charge ($|N_{eff}|$) as shown in Equation 1. This behavior is shown in Figure 30. Initially the depletion voltage decreases until it reaches very low values, and then begins increasing again. From the point at which the depletion voltage and $|N_{eff}|$ are increasing again, the dominant space charge has changed from positive to negative and therefore the detector is said to be type inverted. This change in the effective doping concentration must be considered when designing a silicon detector which will be in a high radiation environment, to ensure that it will still operate after receiving high fluences.

This explanation of the space charge inversion is limited and does not fully describe the conditions inside the sensor. It has been found in recent years that an uneven occupation of traps in irradiated silicon sensors gives rise to the so-called double peak effect [10, 45]. This is illustrated in Figure 31. The top drawing shows the electric field in an unirradiated detector, which is essentially a constant. Figure 31(b) shows the thermally generated current in the sensor, as well as the individual electron and hole currents. While the overall current is constant, the electron and hole currents are linearly distributed toward the n^+ and p^+ contacts, respectively. In an irradiated sensor, the deep traps are filled unevenly with holes and electrons according to the current distributions. This results in a linearly distributed space charge, as shown in Figure 31(c). The electric field within the sensor is then given by the Poisson equation (Equation 2) and is shown in Figure 31(d). There is a peak in the electric field at each contact, and a minimum in the center of the sensor. The charge collection is therefore not uniform over the sensor, with a slower charge collection from the center of the sensor due to the low electric field.

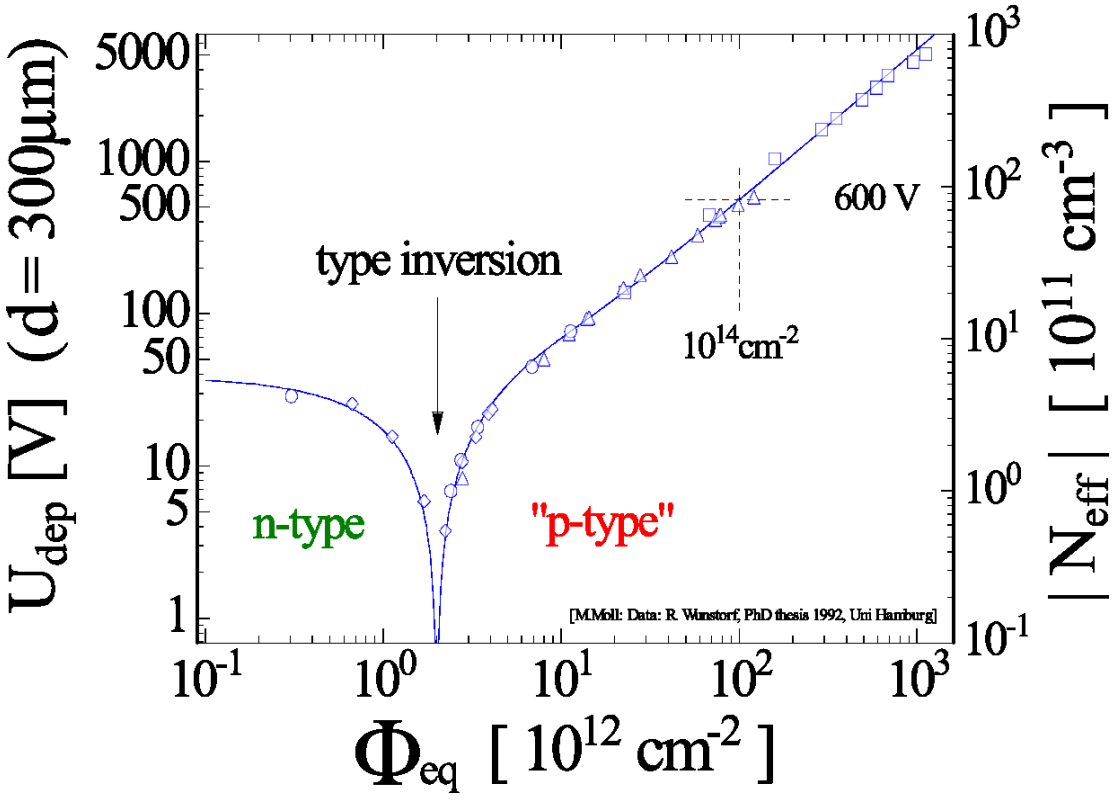

Figure 30: Change in the effective doping concentration as well as the voltage required for full depletion as a function of the fluence [1].

4.3.2 Charge Trapping

The energy levels in the band gap act as traps for charges. Often a charge moving through the lattice will occupy one of these energy levels for a short time. However, this time may be longer than the integration time, and so the collected charge is less than the total deposited charge. This charge-trapping leads to a decreased charge collection efficiency, and for smaller signals, a decreased detection efficiency [1]. It is essential to study these changes to determine at what point the sensors are no longer efficient enough to be used by the experiments.

The different defects induced in the silicon by radiation have been studied on a microscopic level by several groups [1, 9]. However, these methods are only able to see shallow traps and so the amount of signal lost by charge trapping can not be predicted

well. The charge losses must be measured with macroscopic techniques, such as charge collection efficiency (CCE) and Transient Current Technique (TCT) measurements. In this work, the charge losses due to trapping are studied by measuring the charge collection efficiency of sensors which have been irradiated to various fluences. Charge collection efficiency measurements on irradiated CMS barrel pixel sensors are discussed in detail in Chapter 5.

4.3.3 Leakage Current

The energy levels created by the defects in the band gap can act as centers for electron-hole pair generation. This effectively increases the leakage current of the sensor. The amount of current created (ΔI) is proportional to the fluence, according to Equation 4, where Φ_{eq} is the fluence normalized to the damage caused by 1 MeV neutrons (see Section 4.4) and α is a proportionality constant. The changes in the leakage current are independent of the initial resistivity and impurity concentration [44].

$$\Delta I = \alpha \Phi_{eq} V \tag{4}$$

The exponential temperature dependence of the leakage current (Equation 3) still holds in irradiated sensors. In order to keep the current below acceptable limits and to avoid thermal runaway, it is necessary to operate irradiated detectors at low temperature.

4.4 NIEL Scaling

The Non Ionizing Energy Loss (NIEL) hypothesis attempts to allow scaling of the radiation damage produced by different types of particles and particle energies. The NIEL hypothesis is based on the assumption that any changes in the material due to displacement are linearly related to the amount of energy deposited in the collision, independently of how the defects are distributed or of any annealing which occurs after

the initial collision [1]. The non-ionizing energy loss is the amount of energy deposited in the crystal, excluding the energy that went into ionization, which is reversible. 1 MeV neutrons are used as the reference particles, and the fluence of any particle is scaled to the 1 MeV neutron equivalent. Therefore it is common practice to quote fluences in units of neutron equivalent fluence, n_{eq}/cm^2.

The scaling can be done by defining a hardness factor κ in order to compare the amount of damage done by a specific irradiation to the damage which would have occurred from 1 MeV neutrons with the same fluence. The determination of the hardness factor relies on the fact that the changes in leakage curret are independent of the resistivity and impurity concentration. The 1 MeV neutron equivalent fluence can then be calculated according to Equation 5.

$$\Phi_{eq} = \kappa\Phi = \kappa \int \phi(E)dE \tag{5}$$

Here, $\phi(E)$ is the energy spectrum of the radiation. The hardness factor is unique to each radiation source. The hardness factors for the sources used in the measurements presented in Chapter 5 are listed in Appendix A.

This approach is limited, as neutrons and charged hadrons produce different types of defects. The main mechanism by which charged hadrons interact with silicon at low energies is the Coulomb interaction, and they tend to produce mostly point defects. Neutrons can only interact by elastic scattering with the nucleus and by nuclear reactions above 1.8 MeV, and they produce more cluster defects [1].

4.5 Annealing

Defects in the silicon lattice are free to move about the lattice due to thermal energy. The defects can collect at specific locations, such as the surface, or encounter other defects and combine to form complex defects. Complex defects can also break apart if they have enough energy to overcome the binding energy holding them together. These

processes are called annealing.

During the annealing, the space charge changes. The most successful parametrisation is the so-called Hamburg model [1]. It describes the change of the space charge by three components: short term annealing, stable damage, and long term annealing. It can be described as a function of the fluence and time by Equation 6.

$$\Delta N_{eff}(\Phi_{eq}, t(T_a)) = N_A(\Phi_{eq}, t(T_a)) + N_C(\Phi_{eq}, t(T_a)) + N_Y(\Phi_{eq}, t(T_a)) \qquad (6)$$

Here N_A is the short term component, N_C is the stable damage component, and N_Y is the long term component. An example of the change in the effective doping concentration as a function of the annealing time is shown in Figure 32.

The short term annealing is also often called "beneficial annealing" because it is associated with a decrease in the absolute value of the space charge. This takes place over a period of a few days. In long term annealing, the space charge becomes more negative, and is often called "reverse annealing." The long term annealing can be frozen by keeping the detector at low temperatures. Therefore the most important component for the LHC experiments is the stable damage. The stable damage is not influenced by the operating temperature of the detector, but it has been shown that it is different for different types of silicon. In particular, the addition of oxygen to the silicon reduced the stable damage [1].

The annealing rates are highly dependent on temperature. Therefore, in order to be sure that samples are at the same state, the annealing history must be understood. In general, all samples used in this work were subjected to an identical annealing process, and stored at low temperature to halt any further annealing.

4.6 Estimated Requirements for CMS Pixel Detector Sensors

The radiation environment at the LHC is extremely harsh, so there were dedicated studies during the design phase of the detector to determine the amount of radiation

which the different subdetectors needed to be able to withstand. The pixel detector is the closest subdetector to the collision point, and so subjected to the highest amount of radiation. Eventually the pixel detector will need to be replaced, and so was designed so that it can be removed and replaced relatively easily during a shutdown period.

There are several factors which limit the lifetime of the sensors. The increase in charge trapping eventually means that the signal is too low to pass the threshold. Increasing the bias voltage can help recover the signal, but leads to a decrease in the charge sharing between pixels. For high voltages the spatial resolution degrades until it becomes the binary resolution; that is, the resolution given purely by the pixel dimensions, without any charge sharing, which is given by the pitch/$\sqrt{12}$. In addition, the available bias voltage is currently limited by the connectors and power supplies which carry the voltage to the detector to a maximum of 600 V.

At the full LHC design luminosity, it was estimated that the pixel detector would be subjected to a fluence of 3 x 10^{14} n_{eq}/cm^2 per year in the first layer, and 1.2 x 10^{14} and 0.6 x 10^{14} n_{eq}/cm^2 per year in the second and third layers, respectively [7]. The current pixel detector was designed to withstand a fluence of 6 x 10^{14} n_{eq}/cm^2 , corresponding to approximately 250 fb^{-1} of integrated luminosity for the innermost layer. As of the writing of this dissertation, the most recent schedules plan for the pixel detector to be replaced during the extended year-end technical stop in 2016-2017, after an integrated luminosity of approximately 100 fb^{-1}.

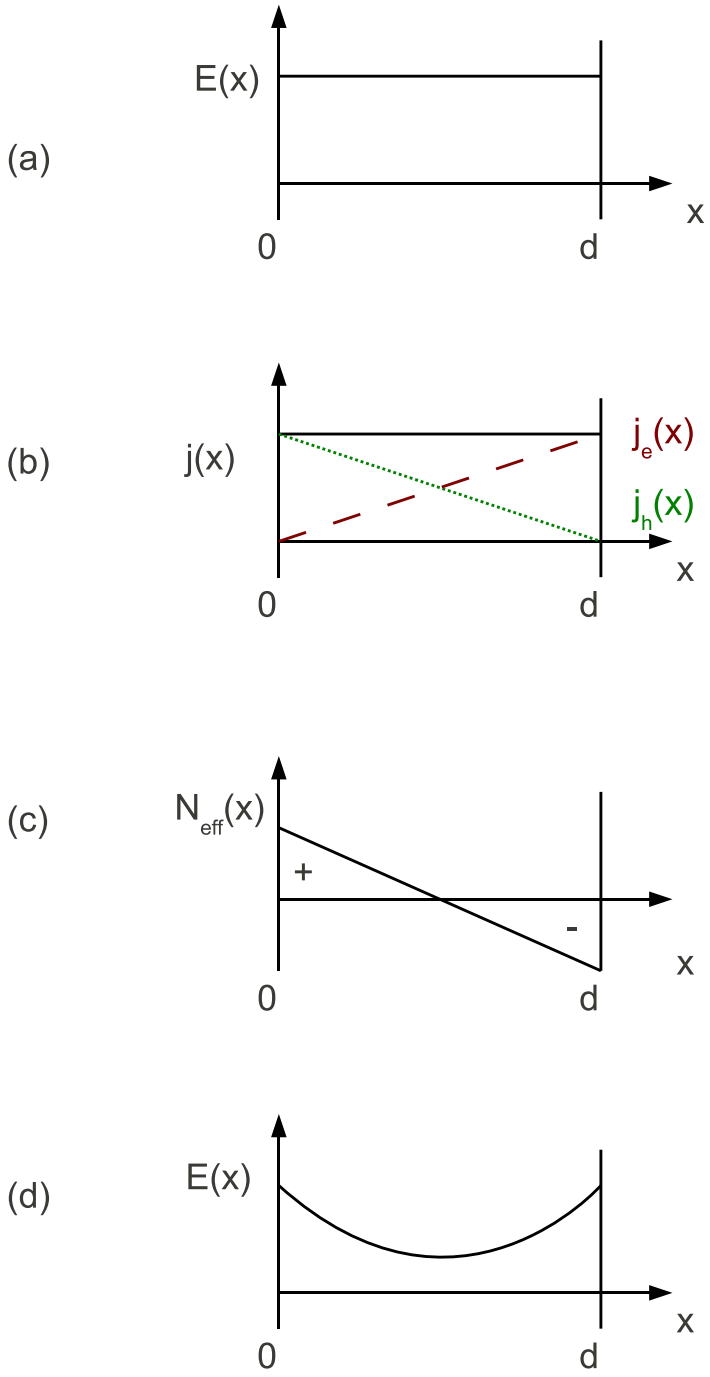

Figure 31: Illustration of the double peak effect. The p^+-contact is at $x = 0$, and the n^+-contact is at $x = d$. (a) Electric field in an unirradiated detector. (b) Thermally generated current, with the electron (red) and hole (green) currents. (c) Space charge distribution in an irradiated detector. (d) Electric field in an irradiated detector. Figure reproduced from [10].

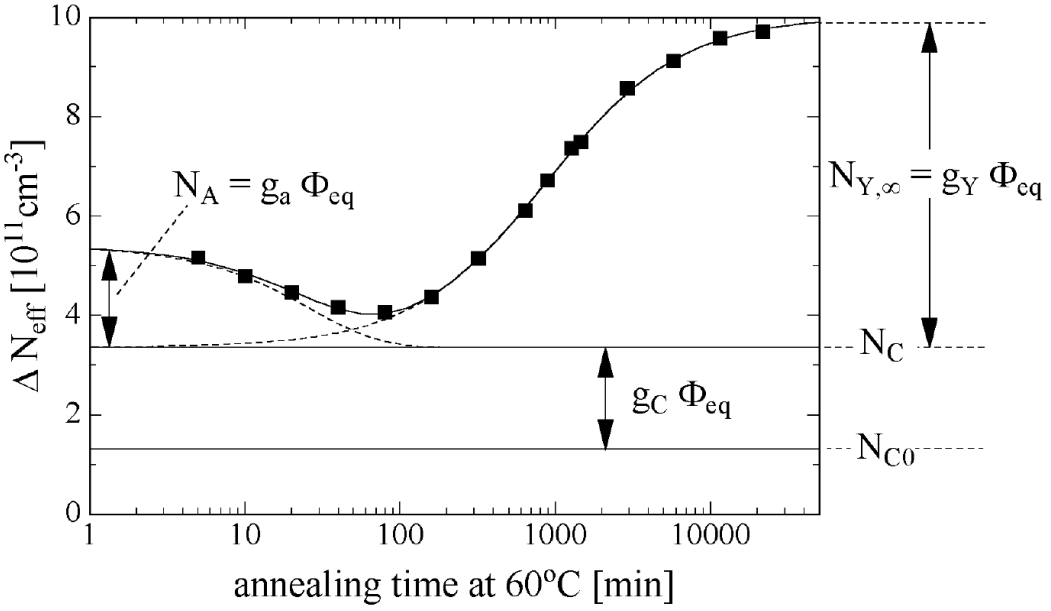

Figure 32: Change in effective doping concentration as a function of annealing time, taken from [1].

5 Sensor Measurements

In order to make measurements of the properties of the CMS barrel pixel sensors and how the operational properties change with radiation damage, a number of samples consisting of a small sensor bump bonded to a single read out chip were prepared. Some of the samples were irradiated to investigate the effect of the radiation damage. Several different fluences were used to see how the properties of the sensor change with increasing fluence. The samples were irradiated after the ROCs were bump-bonded to the sensors. This means that the ROCs as well as the sensors were irradiated. This gives a more realistic picture of the damage that will occur to the pixel detector during LHC operation.

Several different measurements were performed in order to evaluate the effects of the radiation damage on the sensors. Charge collection efficiency measurements were done to measure the amount of signal lost as a function of fluence. An attempt was made to measure the detection efficiency using both a testbeam and a lab setup. The interpixel capacitance was measured as a function of bias voltage for both irradiated and unirradiated samples. Finally, the feasibility of cheaper single-sided sensors was investigated using high voltage tests.

Table 1 lists the different fluences used for the charge collection efficiency and detection efficiency measurements. The different places used for irradiations are the Paul Scherrer Institute (PSI), CERN, and the Karlsruhe Institute for Technology (KIT). A full table listing each individual sample can be found in Appendix B.

The irradiations at PSI were done in 2007 using the piE1 beamline [46]. The irradiations at CERN were also done in 2007, at the PS-IRRAD facility [47]. The irradiations at KIT were done in 2010 at the Karlsruhe Irradiation Facility [48]. After irradiation the sensors were stored in a commercial freezer at $-18°$C to stop any annealing as much as possible. It should be noted that the pion irradiated sensors were accidentally stored at room temperature for a few weeks.

Table 1: Single ROC samples used in the charge collection efficiency and detection efficiency measurements.

Fluence ($10^{14} n_{eq}/cm^2$)	Facility	Particle
0	–	–
3	KIT	p 26 MeV/c
3.2	PSI	π^+ 300 MeV/c
4.2	PSI	π^+ 300 MeV/c
6	KIT	p 26 MeV/c
6.1	CERN	p 24 GeV/c
6.2	PSI	π^+ 300 MeV/c
11	CERN	p 24 GeV/c
12	KIT	p 26 MeV/c
28	CERN	p 24 GeV/c
30	KIT	p 26 MeV/c
51	CERN	p 24 GeV/c
60	KIT	p 26 MeV/c

There are three different sensor designs used in the measurements. They differ only in the size and structure of the gap between pixels. The first type, called "dot1," is the standard design with a gap of 20 μm, which is described in Section 3.3.3. The second type, called "gap30," has a gap of 30 μm, but is otherwise identical to the dot1 design. The third type, called "gap30-2," also has a gap of 30 μm, but with a slightly different geometry for the p-spray isolation between the pixels. The effect of the different gap sizes is discussed more in Section 5.3.

The standard programming and calibration procedure for the pixel detector as a whole is described in detail in [49]. Since only single ROC samples without a TBM are used in these measurements, a simplified version of the calibration procedure is used. The functions of the TBM are handled by a "TBM emulator" on the FPGA testboard. Commonly used values for the DACs are listed in Appendix C.

First the ultra-black level of the ROC is adjusted to match the ultra-black level of the TBM emulator. Then the threshold of the ROC is set by injecting a calibration signal, called "VCal". After the threshold for the ROC as a whole is set, it can be adjusted for each pixel by a 4-bit DAC called the trim bit. After the individual pixel

thresholds have been adjusted, the response of the analog signal is calibrated versus the VCal signal by injecting several different charge values. Finally, the pixel thresholds and noise are measured with an "S-curve scan," where the injected Vcal charge is adjusted from 0 to the maximum value. The threshold is defined as the VCal value where the efficiency is 50%, and the noise is the width of the associated Gaussian.

For the highly irradiated samples, some adjustments need to be made in the DAC values in order for the readout chip to function. For samples irradiated above 10^{15} n_{eq}/cm^2 the preamplifier and shaper feedback circuit had to be adjusted, and the ADC sampling point had to be shifted by a few nanoseconds. Commonly used DAC values for the highly irradiated ROCs are also listed in Appendix C.

5.1 Charge Collection Efficiency

The charge collection efficiency of an irradiated sensor is defined as the ratio of amount of charge collected from a MIP in the irradiated sensor compared to the amount of charge collected from a MIP by an unirradiated detector. As a reference several unirradiated sensors were tested under the same conditions as the irradiated sensors.

5.1.1 Testing Setup and Procedure

The testing setup consists of an insulated cold box, a sensor and ROC sample, a source, and the electronics to read out the signal. The testing setup is shown in Figure 33. The sample is mounted on an aluminum block inside the cold box, which is cooled by a water cooled Peltier element. The box can be flushed with dry nitrogen to keep the humidity as low as possible. Particles are provided by a ^{90}Sr β source which is placed on a clear plastic cap about 10 mm above the sensor. The endpoint energy of the β particles is about 2.3 MeV, which pass through the sample and approximate a MIP. However there are many low energy particles which are stopped in the sample and generate a much larger signal. These low energy signals are reduced in the data analysis.

The ROC is controlled by an FPGA and custom written software. The read out

of the signal was triggered by a random trigger. Since the particles arrive randomly in time, they are not synchronized with the randomly-generated trigger. Therefore the clock cycle where the hits should arrive was stretched in order to increase the chances that a particle passes through the sensor within the correct time window. The FPGA stretches an arbitrary clock cycle to 1000 times the usual length. After a delay, a trigger is sent to the ROC and the data from this stretched clock cycle is read out. The stretch factor of 1000 was chosen such that approximately 80% of the triggers had hit pixels [50].

Later the setup was improved to contain a scintillator and photomultiplier tube beneath the sample. The read out was then triggered by a coincidence of a signal from the scintillator and the clock from the FPGA. The clock cycle stretching was not necessary with the new setup, since the coincidence with the scintillator signal ensured that a particle would pass through the detector during the correct clock cycle.

The sample is placed into the cold box and then cooled down to approximately -20°C. Once the temperature is stable, the standard programming and calibration procedure is performed. After the working parameters have been optimized, a current-voltage (IV) curve is taken for each sample to ensure that it is working properly. The bias voltage is scanned through a range of values, starting from well below the depletion voltage, and ending well into the depletion plateau. At each bias voltage value, data is collected for 15 seconds using the internal trigger.

5.1.2 Analysis

There are several steps in the analysis of the data. First some initial data quality cuts are applied. Pixels can be manually excluded, which is usually done in the case of known noisy pixels and the edge pixels, which are larger. In addition, there are several cuts that can be used to exclude data from a pixel during the analysis of the data:

- The pixel has 10 times fewer hits than its neighbors.
- The pixel charge is very different compared to the charge of its neighbors.

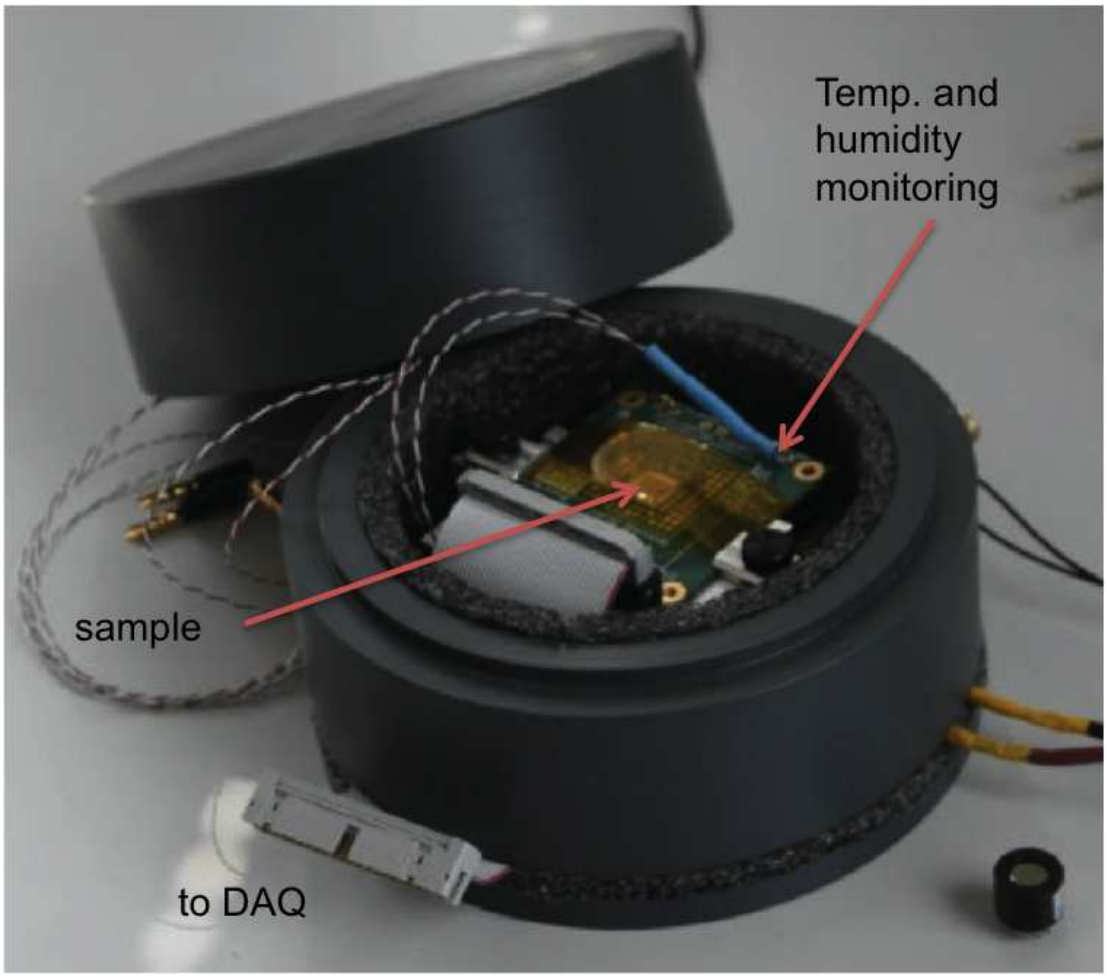

Figure 33: Single sensor testing setup.

- A problem in the pulse height calibration of a pixel results in an invalid charge.
- The occupancy of the pixel is too different from that of its neighbors.
- The pixel is surrounded by masked pixels.

After the initial data quality cuts, the individual pixel hits are combined into "clusters." The cluster finding algorithm combines adjacent hit pixels within a radius of 2 pixels into clusters. The combined charge of all the pixels in the cluster is called the cluster charge, and the cluster position is the center of gravity of the cluster charge.

The ^{90}Sr source used has many low energy particles which produce very large clusters. A histogram of the cluster charge distribution for different cluster sizes is shown in Figure 34. The x-axis shows the cluster charge in arbitrary units. As the cluster size grows, the cluster charge increases, and the shape of the distribution changes. In order to suppress non-MIP-like particles, only the one-pixel clusters are considered in the analysis.

The charge deposited in the silicon is described by a Landau distribution, while the measurement error introduces a Gaussian. Therefore the charge distribution is fit by a LanGau function, which is a Landau convoluted with a Gaussian.

Figure 35 shows an example fitted distribution. The distribution is fit for each value of the applied bias voltage. The peak value, which is the most probable value, is taken as the charge collected in the sample by a MIP at that voltage. The most probable values are plotted as a function of bias voltage for each sample. The increase of the depletion zone and the plateau once the sample is fully depleted are easily seen for unirradiated samples, as shown in Figure 36.

5.1.3 Results

The collected charge versus the bias voltage of all tested samples is shown in Figure 37. In this figure, the lines are obtained in the same way as Figure 36. Instead of the data

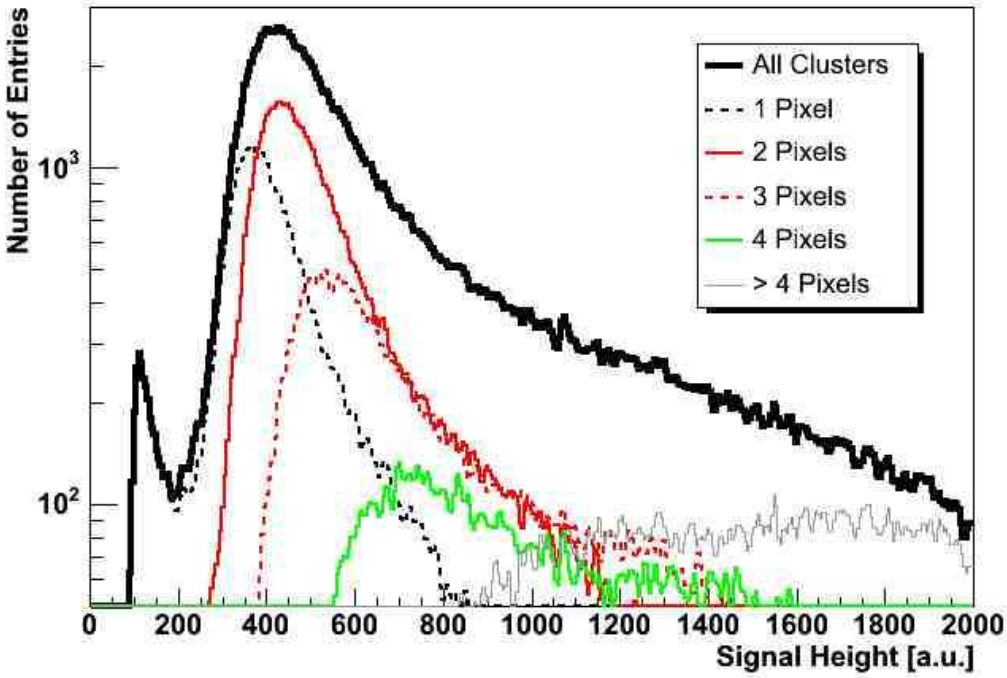

Figure 34: Charge distribution for different cluster sizes.

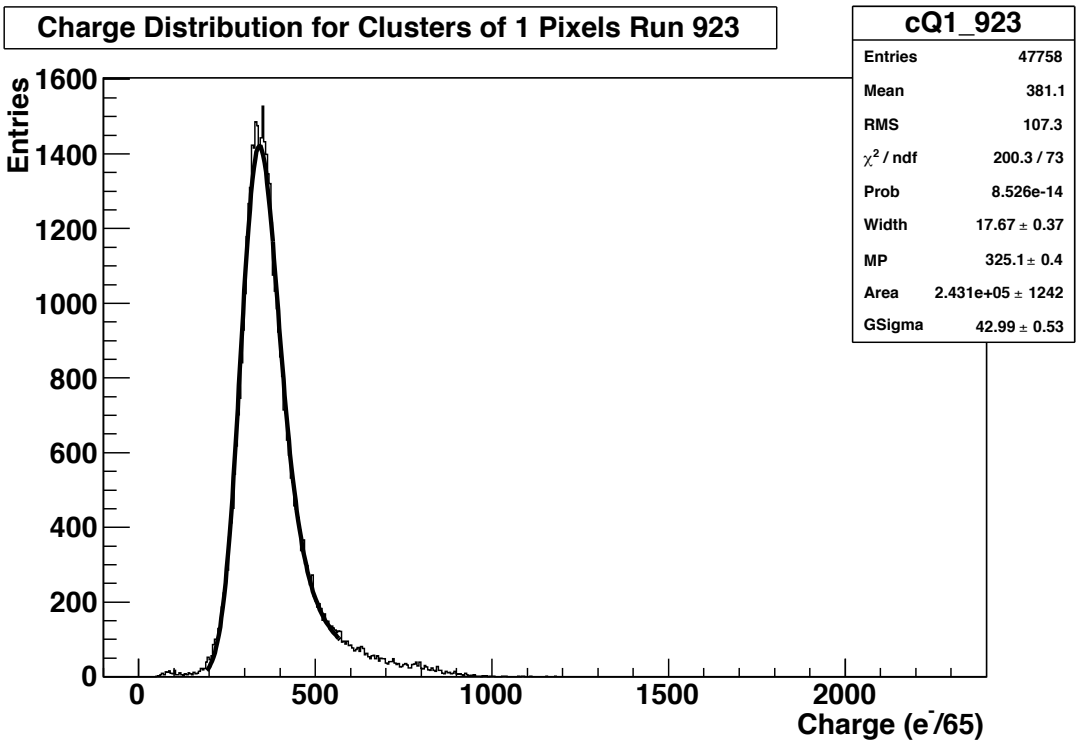

Figure 35: Charge distribution for an unirradiated sample with a bias voltage of -150 V fit by a LanGau function.

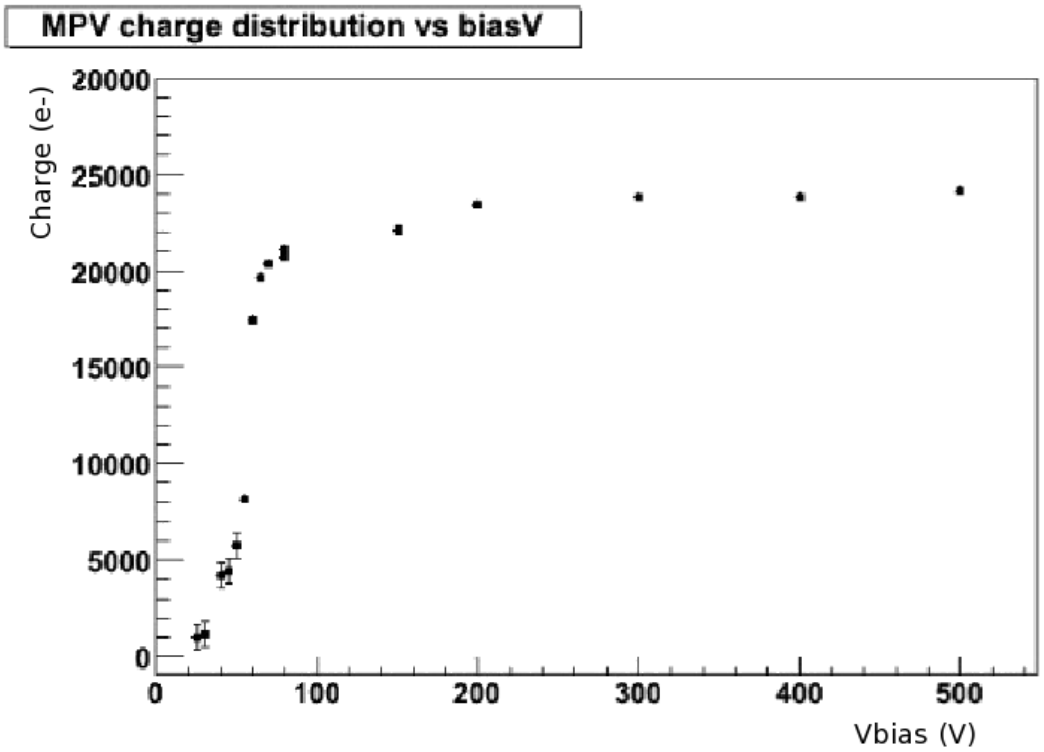

Figure 36: Charge vs bias voltage for an unirradiated sample.

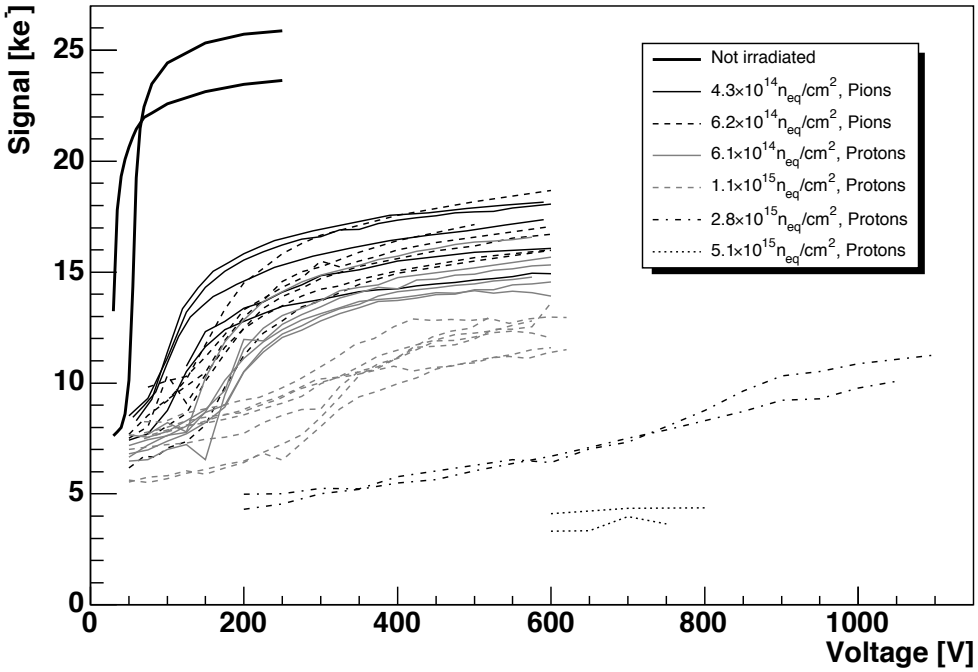

Figure 37: Collected charge vs bias voltage for all tested samples.

points, lines are drawn through the points, so that it is possible to see all the samples on one graph.

In the two unirradiated samples, the collected charge rises sharply and then remains constant. In the irradiated samples, the rise is much slower, showing that in these regions the detector is being operated partially depleted. For the highest fluences ($>$ 10^{15} n_{eq}/cm^2) no saturation of the charge is seen.

The full depletion voltage can be found from the graph of the collected charge vs. the bias voltage. The region where the charge is increasing is fit with a linear function, and the plateau region is fit with a different linear function. The point at which these two lines intersect can be defined as the depletion voltage.

The shift in the depletion voltage is clearly visible in Figure 37. As the fluence increases, the depletion voltage shifts to larger voltages. At the highest fluences the algorithm fails, since there is no plateau reached.

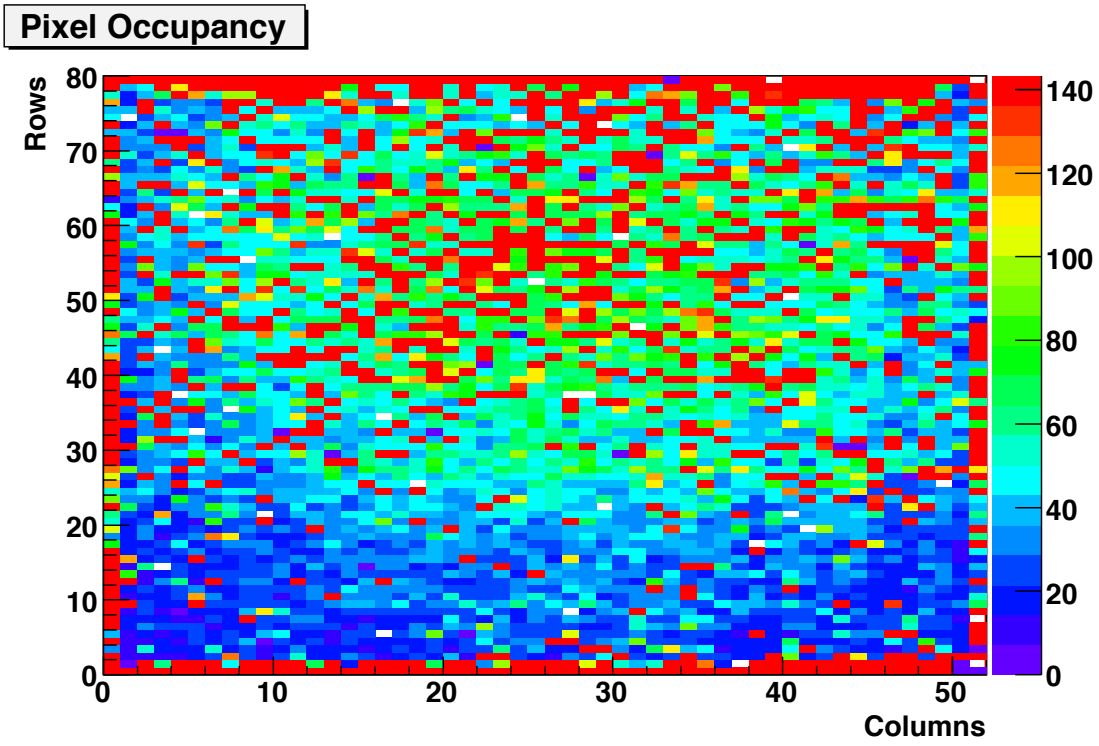

Figure 38: Two dimensional map of hits within the sample irradiated to 5×10^{15} n_{eq}/cm^2. The distinctive "bulls-eye" pattern of a point source is clearly visible, indicating that the signals are produced by actual particles and not noise.

Only two samples irradiated to 5×10^{15} n_{eq}/cm^2 were able to be tested. The amount of charge shown for these samples in Figure 37 is at the nominal threshold level, and does not seem to change with bias voltage. We believe that the threshold is in the tail of the Landau distribution, giving a wrong value for the amount of charge collected. The most probable value of the distribution is then always at the threshold, and does not depend on the bias voltage.

However, by looking at the two dimensional map of the signals versus position in the sensor (Figure 38), it is obvious that the signals are produced by real particles from the ^{90}Sr source crossing the sensor. Particles coming from a point source such as the ^{90}Sr source produce a distinctive "bulls-eye" pattern, while noise produces a uniform distribution.

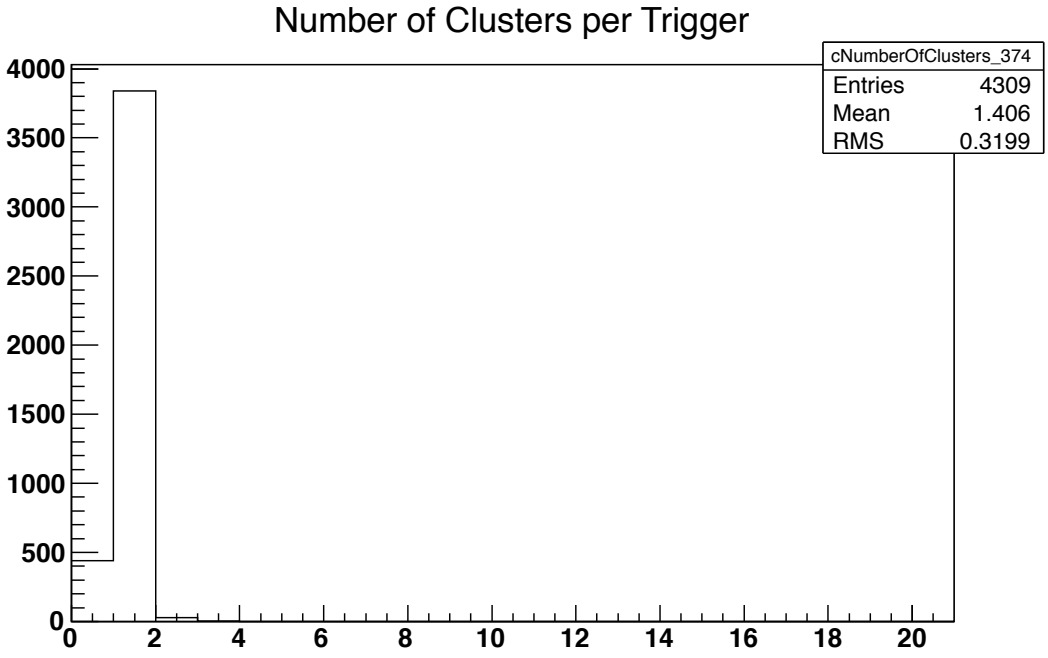

Figure 39: Cluster size for unirradiated sensors.

A rough estimate of the efficiency of the sensor can be made by looking at the fraction of events which have no clusters. Figure 39 shows the distribution of cluster size per trigger for a typical unirradiated sensor. Because the triggers are not synchronized with the source, there are always a fraction of empty readouts, which are the triggers with zero clusters. In a fully efficient sensor, about 10% of the triggers have zero clusters. This fraction of empty events remains the same up to samples with a fluence around 2×10^{15} n_{eq}/cm^2 . Figure 40 shows the same distribution for one of the sensors irradiated to 5×10^{15} n_{eq}/cm^2 . The fraction of zero-cluster events has increased to around 80%. While not an actual efficiency measurement, this comparison of the fraction of zero-pixel clusters gives a strong indication that although the sensor does see particles, the detection efficiency has decreased dramatically, and the sensors can no longer be used.

The most probable value of the signal as a function of fluence for each sample at a bias voltage in the plateau region is shown in Figure 41. The decrease in the total

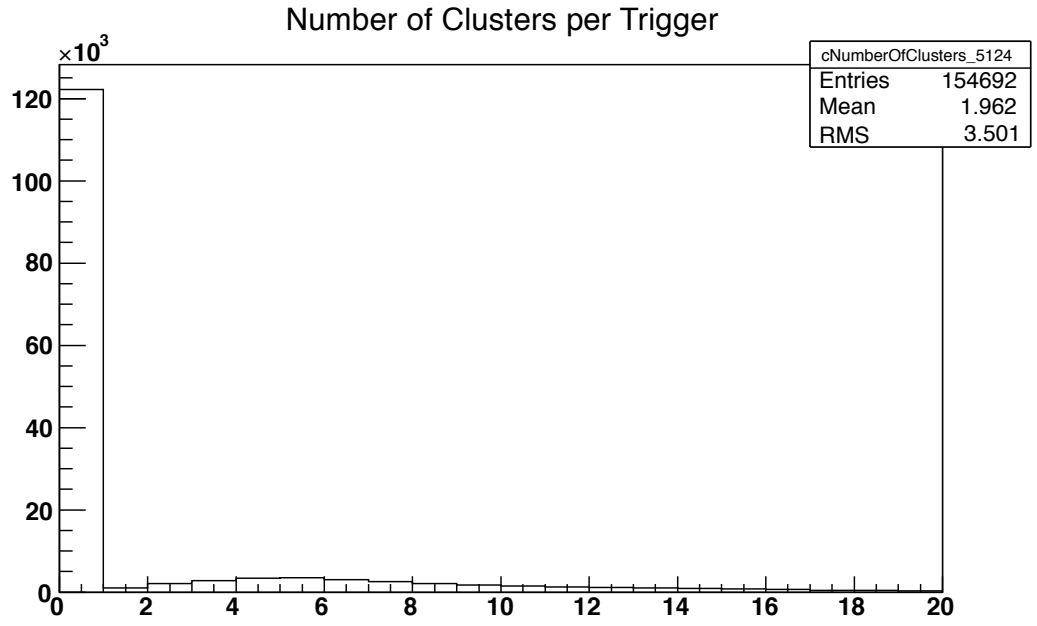

Figure 40: Cluster size for sensors irradiated to a fluence of 5×10^{15} n_{eq}/cm^2 .

collected charge due to charge trapping with increasing fluence is clearly visible.

Other groups have observed a phenomena of charge multiplication in highly irradiated sensors beginning at bias voltages of 1000 V [51, 52]. Charge multiplication occurs where there are very high fields in the sensor, and produces signals larger than those of an unirradiated sensor being collected. No charge multiplication is observed here; the collected charge in the samples irradiated to 3×10^{15} n_{eq}/cm^2 is still far below the amount of charge collected in the unirradiated sensors, even at 1000 V. However, since no saturation of the charge is seen, it would be necessary to go to higher bias voltages in order to see whether any charge multiplication would be present.

It was not possible to test samples at bias voltages above 1000 V due to limits in the experimental setup. The power supply was only able to go to 1100 V. In addition, there were problems with sparking on the printed circuit board (PCB) which holds the samples, and the connectors between the PCB and the FPGA testboard which controls the sample. The sample PCB is connected to the FPGA testboard by a ribbon cable.

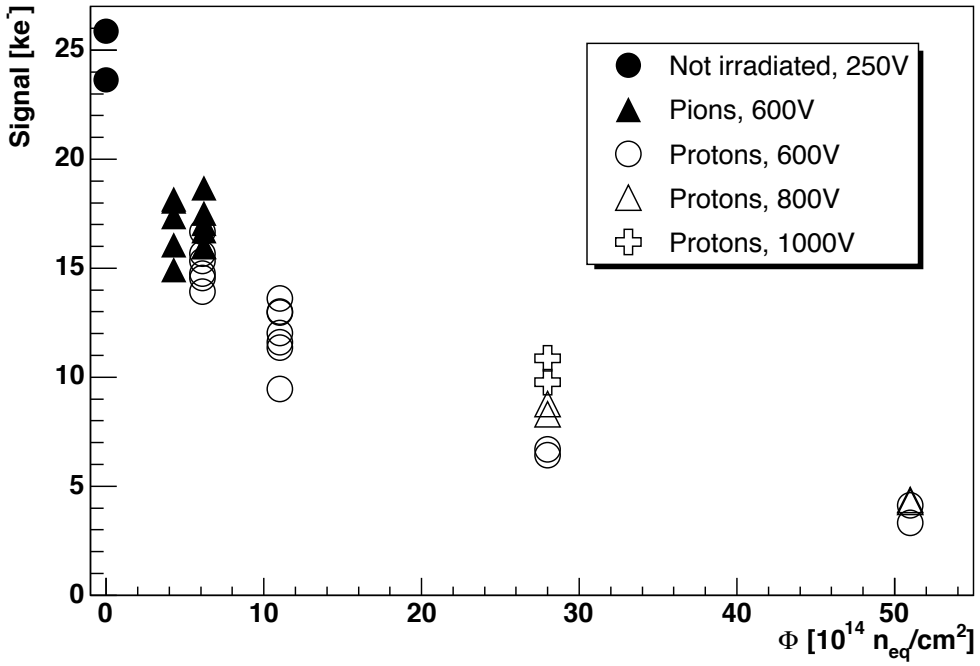

Figure 41: Collected charge vs fluence for all tested samples.

When the testboard was designed, it was not foreseen to use such high bias voltages. Therefore, the relative location of the bias voltage line compared to the others was not carefully considered. This resulted in the bias voltage being sent on a pin directly adjacent to a pin at ground. At such high bias voltages we encountered sparking between the bias voltage pin and the ground pin. Several samples were destroyed before the source of the problem was realized, and only two samples (irradiated to a fluence of 3×10^{15} n_{eq}/cm^2) were able to be tested above 600 V.

The sample PCBs were redesigned to have the bias voltage carried on a separate cable. However, we still encountered issues with sparking. This time, it was between the pins of the LEMO connector and the routing lines on the PCB. The board has been redesigned a second time and preliminary tests have shown it is capable of holding bias voltages of >1000 V for several hours with no problems. It is foreseen to repeat the measurements on the highly irradiated samples at bias voltages up to 2000 V once a power supply is available.

5.2 Detection Efficiency

Radiation damage also decreases the absolute detection efficiency. With the decreased signal due to charge trapping, it is more likely that signals will be lost because they are below the threshold. Two different methods were used to try to measure the detection efficiency of both unirradiated and irradiated detectors: a testbeam using a pixel telescope, and a modified charge collection efficiency setup in the lab. Unfortunately, no conclusive results were obtained. The methods used, and problems encountered, are described in the following sections.

5.2.1 Test Beam

In order to measure the absolute efficiency of the sensors as a function of fluence, a testbeam was performed in the summer of 2010. The setup was at the H2 beamline of the Super Proton Synchrotron (SPS) accelerator at CERN, with a beam of 150 GeV

pions [53]. The setup consisted of a telescope of 4 pixel sensors, an independent trigger consisting of a silicon diode, and the device under test (DUT) in the center. The telescope chips were small CMS pixel sensors bump-bonded to a single ROC. They were identical to the DUT, except that they were not irradiated. A diagram of the telescope is shown in Figure 42. This setup was placed between a pair of Helmholtz coils which produced a 3 T magnetic field, in order to also measure the change in the Lorentz angle as a function of fluence.

The DUT was placed inside an insulated cold box, so that the irradiated sensors could be tested at a temperature of -10°C. The sample was cooled by two Peltier coolers. The heat was removed from the Peltier coolers by cooling fluid, which passed through a chiller placed outside the beam area.

The FPGA testboard which controlled the telescope and DUT was placed inside the magnet below the telescope. All of the other controlling electronics (power supplies, triggering electronics, data acquisition computers) were placed outside of the beam area so that they could be easily accessed during the beam operation.

The readout of the telescope required an external trigger. The trigger consisted of a standard CMS barrel pixel silicon sensor, which was not bump bonded to a ROC. The charge was read out using a fast commercial amplifier and discriminator wirebonded to the back side of the sensor. The threshold and width of the signal pulse could be adjusted by two potentiometers on the trigger board. The trigger was controlled by standard Nuclear Instrumentation Module (NIM) electronics, located in the control room. The trigger board is shown in Figure 43.

The telescope and DUT were controlled by a modified version of the software used in the characterization and testing of modules before they were installed in CMS. The telescope and DUT are considered a "module" consisting of only 5 ROCs. The telescope chips and the DUT were programmed and calibrated using the standard calibration procedure, and data taking followed the same procedure as for the charge collection efficiency measurements.

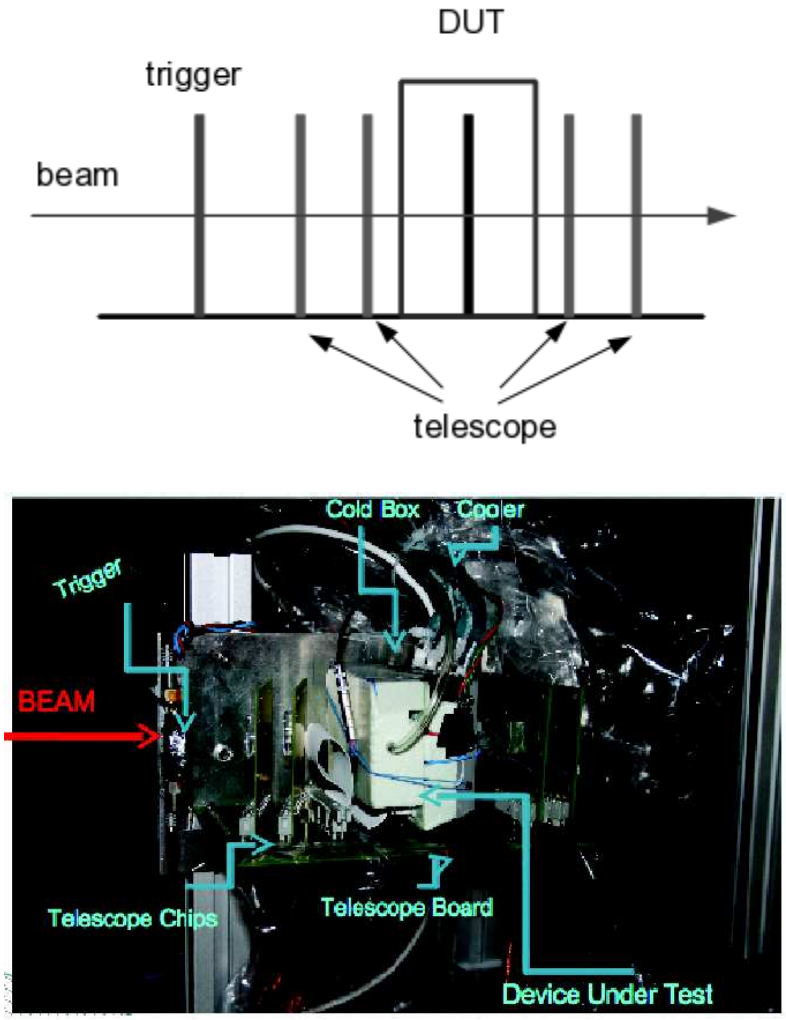

Figure 42: Top: Diagram of the pixel telescope used at the testbeam, showing the location of the device under test. Bottom: Photograph of the pixel telescope.

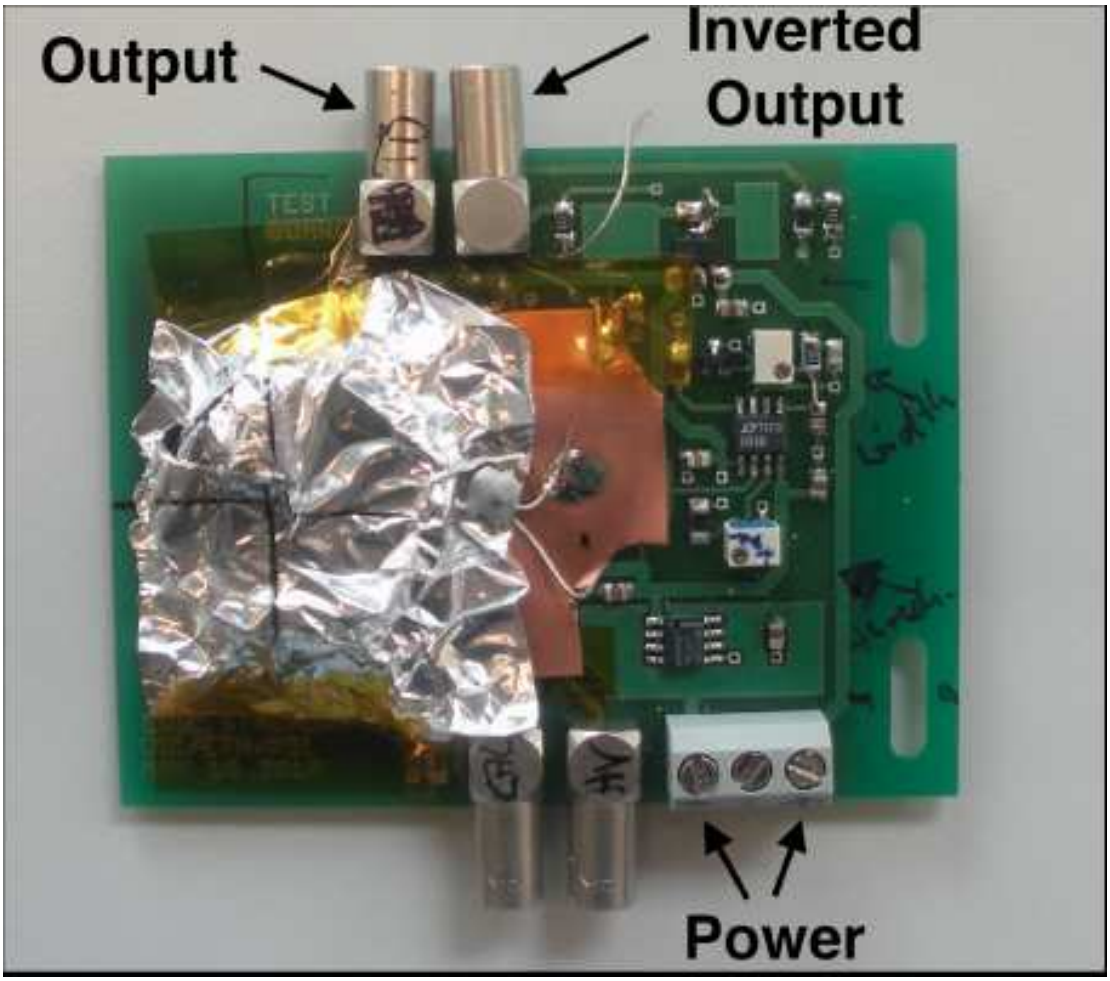

Figure 43: Photograph of the trigger board. The sensor is under the foil cap.

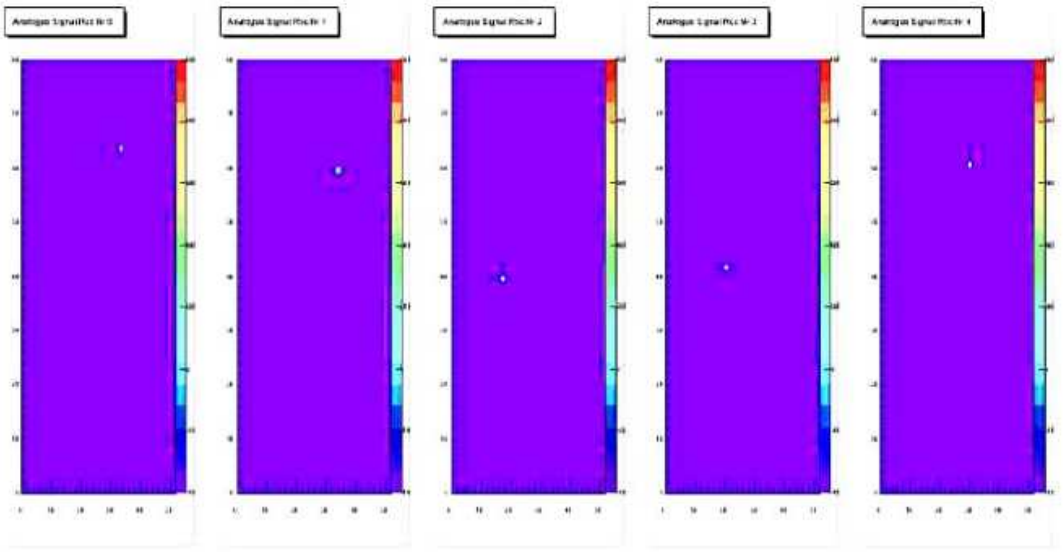

Figure 44: An example beam event. The small white spots correspond to the hit position. The four maps on the left are the telescope sensors, while the map on the right is the device under test.

The telescope sensors are not perfectly aligned in the telescope, so a simple alignment algorithm was developed. As shown in Figure 44, there is almost always only one hit on each sensor per triggered event. A 2 dimensional correlation plot between the hit position on any two chips can be used to distinguish noise or multiple scattering hits from actual beam particles passing through the telescope. An example correlation plot is shown in Figure 45.

To measure the hit efficiency, we look at events in which a particle has been reconstructed as passing through the telescope, and then project the hit onto the DUT. We then search for a corresponding hit in the DUT around the projected position. In order to measure the hit efficiency of the DUT, the efficiency of the telescope sensors must be nearly 100%. The same procedure was used to check the efficiency of the telescope sensors, by treating one of the center telescope sensors as the DUT.

We found that the efficiency of the telescope sensors was only around 85%. With such a low efficiency for each of the telescope chips, a measurement of the hit efficiency

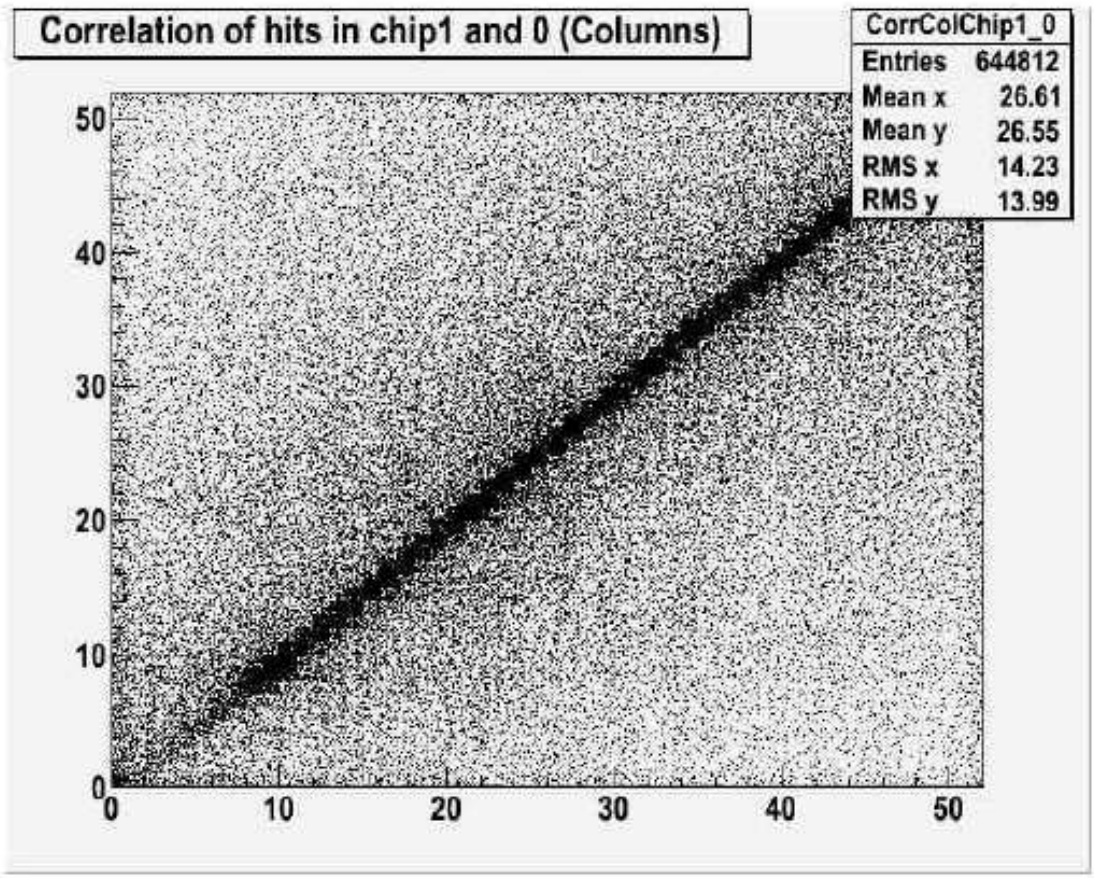

Figure 45: Correlation plot between the hit column in two telescope sensors. The correlated hits, corresponding to particles passing through the telescope, are seen in the dark line along the diagonal. The scattered off-diagonal points correspond to noise hits in one or both of the telescope sensors.

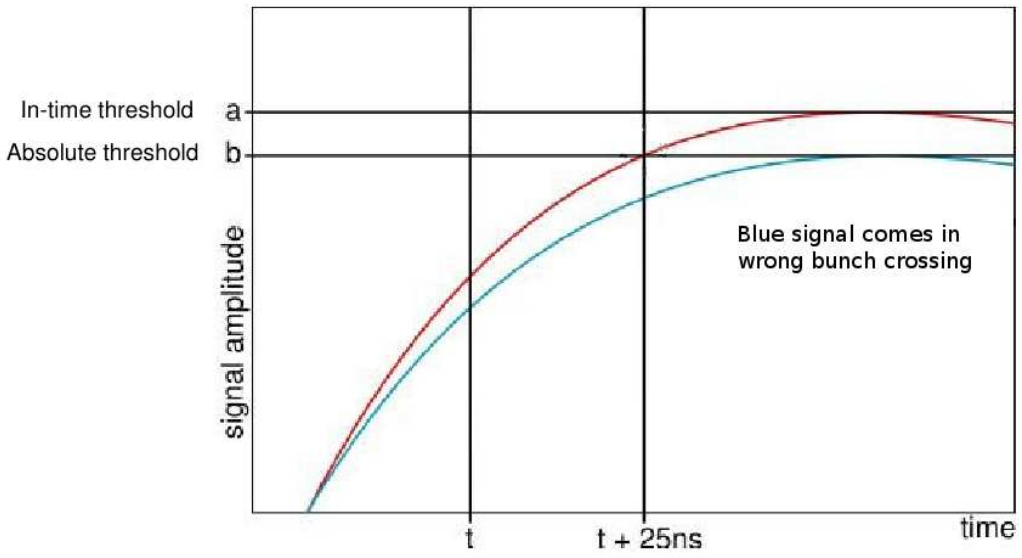

Figure 46: Illustration of timewalk. Low amplitude signals cross threshold late and are assigned to the wrong bunch crossing.

in the DUT is impossible, as the expected effects are on the order of a few percent. The low efficiency appears to be due to a timing problem. In the LHC, the clock of the pixel detector is synchronized to the beam. However, at the testbeam the clock is not synchronized. This leads to two possible timing problems: triggers arriving too late in the bunch crossing, and timewalk.

The timewalk problem is illustrated in Figure 46. Low amplitude signals reach the threshold later than high amplitude signals. This leads to the effect that a low amplitude signal may not cross the threshold in the correct bunch crossing. By using the right delays, this problem is neglible in events where the clock is synchronized to the beam. In the case of an unsynchronized beam, the particles may arrive too late in the time window for low amplitude signals to cross the threshold in time. Then the "in-time threshold" can be defined as the minimum amplitude a signal would need in order to cross the absolute threshold within the bunch crossing.

The other timing problem occurs when triggers arrive too late in the bunch crossing,

so the signal does not cross the threshold until the next bunch crossing. These particles are then "lost". In addition, the timing can be slightly different between the different chips of the telescope and the DUT. This means that it is impossible to tell whether a particle which is seen in the telescope but not in the DUT was lost due to this timing effect or a decrease in the sensor efficiency.

In order to avoid these problems and achieve an acceptable efficiency for the telescope, a very small time window for accepting triggers is necessary. This problem will be solved in future test beams.

5.2.2 Lab Setup

The testing setup used in the charge collection efficiency measurements was modified to have an independent trigger by adding a scintillator and photomultiplier tube beneath the sample. A diagram of the setup is shown in Figure 47. The testboard was triggered by a coincidence of a signal from the scintillator and the rising edge of the testboard clock. A photograph of the setup is shown in Figure 48.

The procedure foreseen for the efficiency measurements is the same as for the charge collection efficiency measurements. The sample is placed into the cold box and cooled to -20°C, the programming and calibration procedure is performed, and an IV curve is taken to assess the quality of the sample. After that data is taken for 15 seconds at a bias voltage slightly above the depletion voltage. The detection efficiency is defined as the number of triggered readouts with hits divided by the total number of triggered readouts.

To verify the procedure, the measurement was first performed with an unirradiated sample. The efficiency of the unirradiated sensors has been previously measured, and found to be greater than 99% [54]. However, when testing the efficiency of the unirradiated sensors in the lab setup, the measured efficiency was much lower than expected. It is thought that this is due to multiple scattering of the β particles inside the box. In order to mitigate this effect, lead shielding was added to narrow the available path

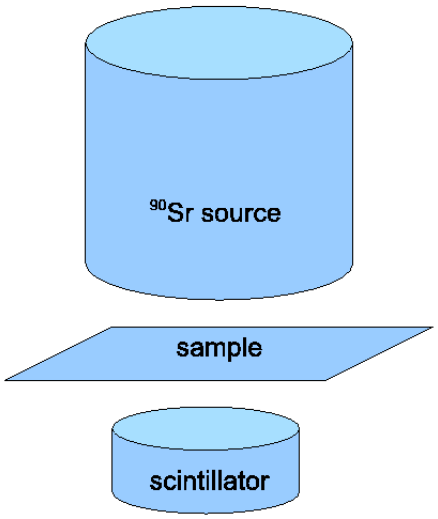

Figure 47: Diagram of modified CCE testing setup. The source is placed above the sample, and the scintillator and photomultiplier tube are placed below the sample.

for the source particles. The efficiency increased with the additional shielding, but was found to vary considerably between measurements.

The ^{90}Sr source was manually positioned above the sensor each time the sample was placed into the cold box. Therefore the position of the source could vary significantly between different samples. This change in source position was found to greatly affect the efficiency measured with this setup (up to 5% variation), due to the different paths available for the particles to scatter around the sample. This is illustrated in Figure 49. As the expected efficiency for fluences of the order of 10^{15} n_{eq}/cm^2 is about 98%, this introduces too much uncertainty to make a reliable efficiency measurement.

5.3 Interpixel Capacitance

The capacitance between individual pixels and their neighbors influences the noise and the cross-talk in the detector, and has an important impact on the analog power of the chip. The capacitance depends on the gap between the pixels. Pixels with a larger gap

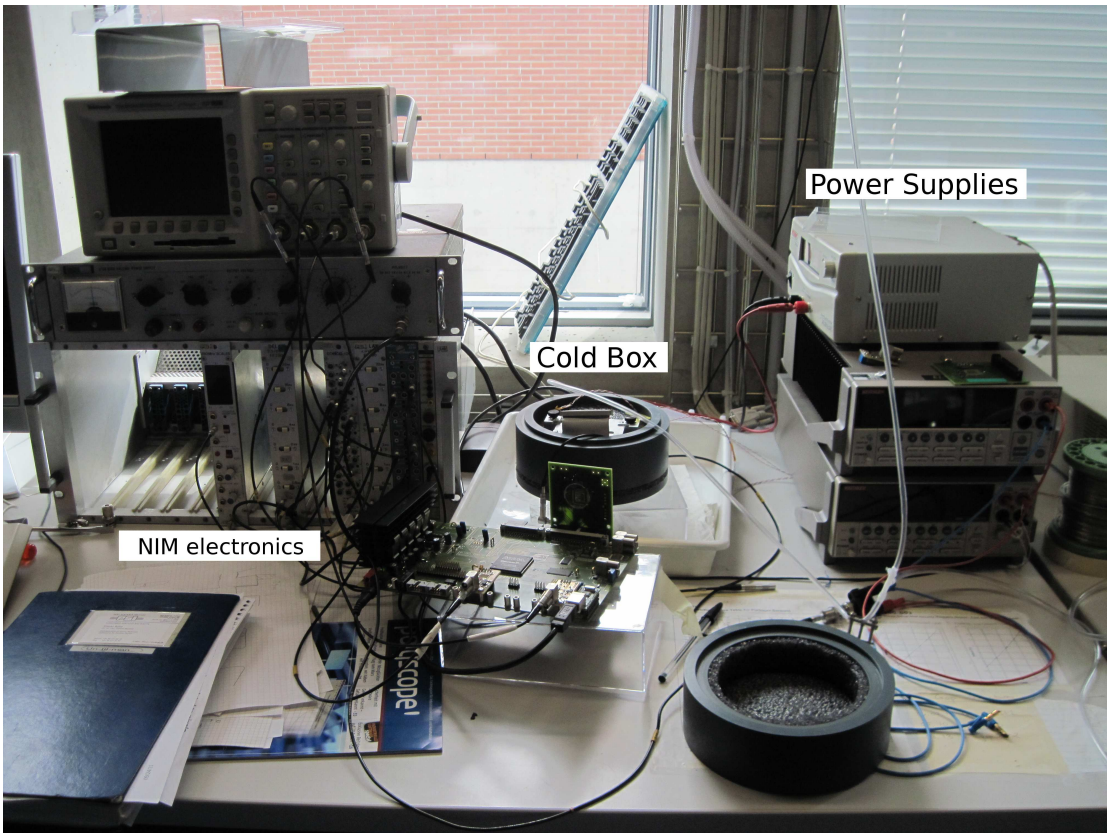

Figure 48: Photograph of the modified CCE testing setup and trigger electronics.

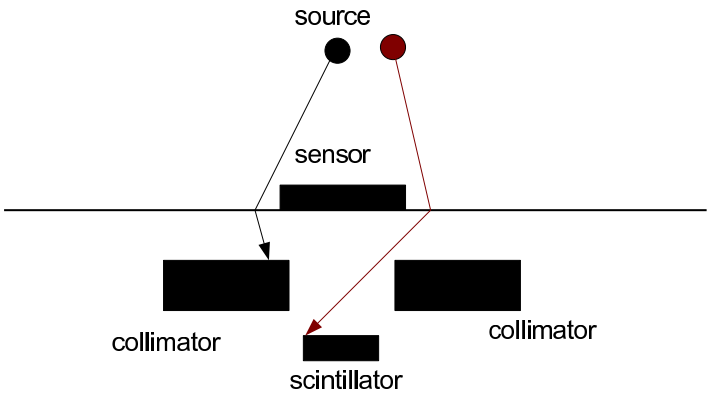

Figure 49: Diagram showing how the source position affects the efficiency. Different source positions provide different paths for the scattered particles.

size have a smaller interpixel capacitance, but the larger gaps produce an inhomogenous drift field inside the sensor. Therefore it is important to find a balance between the capacitance and the gap size.

The current CMS barrel pixel sensors have small gaps (20 μm), and accordingly a relatively high interpixel capacitance. In order to test whether reducing the interpixel capacitance by increasing the gap size would be beneficial, several samples were produced with a gap size of 30 μm, typically referred to as "gap-30". The interpixel capacitance is measured as a function of bias voltage for both the standard and gap-30 samples. The samples are then irradiated with a ^{60}Co source and then measured again. The measurements are described in Section 5.3.1

A first attempt was made at simulating the interpixel capacitance using a Synopsis TCAD simulation [55]. The results can be qualitatively compared with the results of the measurements. The simulation is described in Section 5.3.2.

5.3.1 Measurements

The small value of the capacitance, combined with the small pixel size, makes measuring the interpixel capacitance a challenge. A new method to measure the interpixel capacitance was developed, where a simple chip is bump bonded onto the sensor instead of the ROC. This chip is referred to as the "readout replacement chip."

The concept of the measurement method is to form a basic unit cell of one pixel surrounded by the eight directly neighboring pixels. The eight neighboring pixels are connected together. Then the capacitance can be measured between the central pixel and the eight connected neighbor pixels. A picture of this basic unit cell is shown in Figure 50. This basic unit is repeated over the entire chip. The central pixel of each cell is connected together and routed to a pad on the edge of the chip. The eight neighbor pixels of each cell are also connected together over the whole chip and routed to a second pad on the edge of the chip. These two pads can be contacted with a needle, and the capacitance can be measured. The measurement setup is shown in Figure 51.

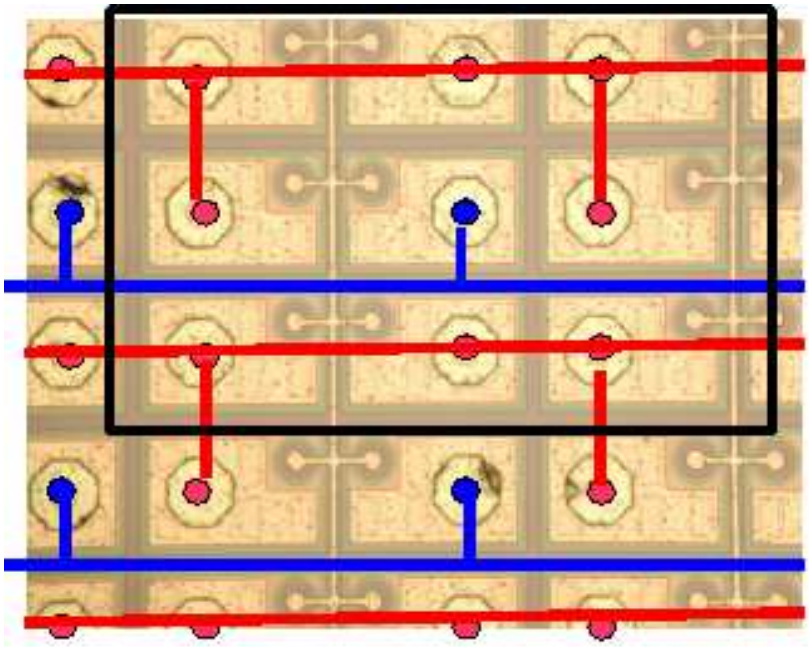

Figure 50: Picture of part of the readout replacement chip. The basic cell of one pixel in the center (blue), surrounded by the eight neighboring pixels (red), is highlighted.

The capacitance between two pixels can be regarded as a combination of two effects. The first is that the p-spray forms a conductive channel with a small resistance between the two pixel implants, with a capacitance at each pixel implant boundary. The second effect is that there is also a capacitance between the pixels through the bulk silicon. This is shown in Figure 52. The total capacitance between the pixels can be described by Equation 7.

$$\begin{aligned} C_{total} &= C_0 + \frac{1}{\frac{1}{C_1} + \frac{1}{C_1}} \\ &= C_0 + \frac{1}{2} C_1 \end{aligned} \tag{7}$$

Here, the notation from Figure 52 is used, where C_0 is the capacitance through the bulk and C_1 is the capacitance at the boundary between the pixel implant and the p-

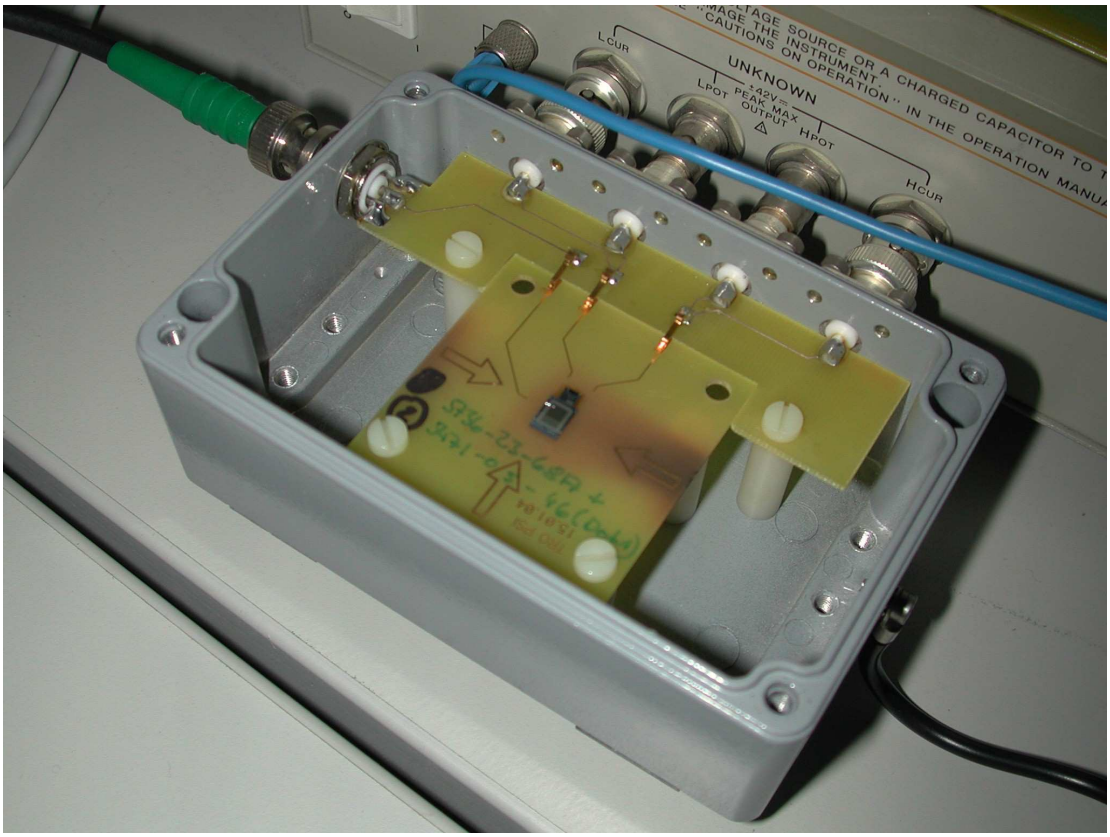

Figure 51: The interpixel capacitance measurement setup.

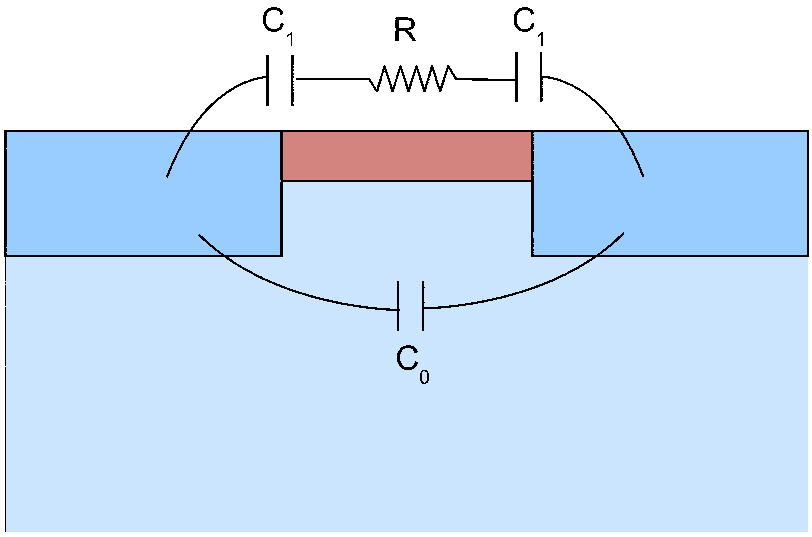

Figure 52: Diagram of interpixel capacitance. C_0 represents the capacitance between pixels through the bulk, C_1 represents the capacitance between the pixel implant and the p-spray, and R represents the resistance of the p-spray.

spray. As the bias voltage increases, the p-spray begins to be depleted of charge carriers, the resistance R increases, and the capacitance between the pixel implant and the p-spray (C_1) decreases. Eventually, the contribution of the C_1 term to the capacitance becomes negligible, and the capacitance approaches the value of C_0.

Because the interpixel capacitance depends mostly on surface effects, the surface damage caused by radiation is important, while the bulk damage has little to no effect. Therefore some of the samples were irradiated at PSI with a ^{60}Co gamma source with a dose of 20 kGy. At this dose the fixed surface charge should be saturated [56].

The samples are listed in Table 2. One sample of each type was measured before and after irradiation.

Table 2: Samples used in the interpixel capacitance measurements and the measured capacitance at a bias voltage of 150 V. Errors are discussed in the text.

Sample Number	Type	Gap Size (μm)	Capacitance (fF)
8609-02-11	Gap20	20	100
8609-02-12	Gap20	20	65
8609-02-10	Gap30	30	20
8609-02-13	Gap30-2	30	50
8609-02-14	Gap30-3	30	85
8609-18-06	Gap20	20	100
8609-18-07	Gap20	20	55
8609-18-05	Gap30	30	65
8609-18-08	Gap30-2	30	30
8609-18-09	Gap30-3	30	45
271947-18-11	Gap20	20	70
271947-18-12	Gap20	20	105
271947-18-10	Gap30	30	45
271947-18-13	Gap30-2	30	45
271947-18-14	Gap30-3	30	45

The main source for errors in these measurements comes from the measurement of the stray capacitance of the readout replacement chip. To measure this capacitance, the sample must be removed from the setup, the readout replacement chip must be forcibly removed from the sensor, and then the readout replacement chip is placed back into the setup to be measured alone. This process can change something on the chip,

for instance smear the bump bonds, or the contact resistances might be changed by putting the readout replacement chip in a slightly different position. The best way to estimate the size of the errors introduced here is to compare the measurements of identical samples.

There are two samples from each wafer of the gap20 type, which are shown in Table 2. For samples 8609-02-11 and 8609-02-12, the measured capacitances are 100 fF and 65 fF, respectively, with a difference of 35 fF between the two measurements. For samples 8609-18-06 and 8609-18-07, the measured capacitances are 100 fF and 55 fF, respectively, with a difference of 45 fF. For samples 271947-18-11 and 271947-18-12 the measured capacitances are 70 fF and 105 fF, respectively, with a difference of 35 fF. The average difference between identical samples is 38 fF, so 40 fF is taken as the uncertainty on the measurements.

The results of the interpixel capacitance measurements before irradiation are shown in Figure 53. Before full depletion, the pixels are not isolated from each other. The relevant part of the curve is the part from the full depletion voltage onwards, which can easily be seen by the sharp spike around 50 V. After the full depletion, the capacitance decreases with increasing voltage until a plateau is reached.

The results of the measurements of the irradiated samples are shown in Figure 54. The solid lines are the measurements of the samples before irradiation, and the dashed lines are the measurements of the samples after irradiation. The capacitance of the gap-30 samples is indeed lower than the capacitance of the standard samples. The interpixel capacitance after irradiation is lower than before irradiation. This is likely due to the build up of positive charges along the surface after irradiation. This layer of positive charges begins the depletion of the p-spray earlier than in the unirradiated samples, so the capacitance decreases faster.

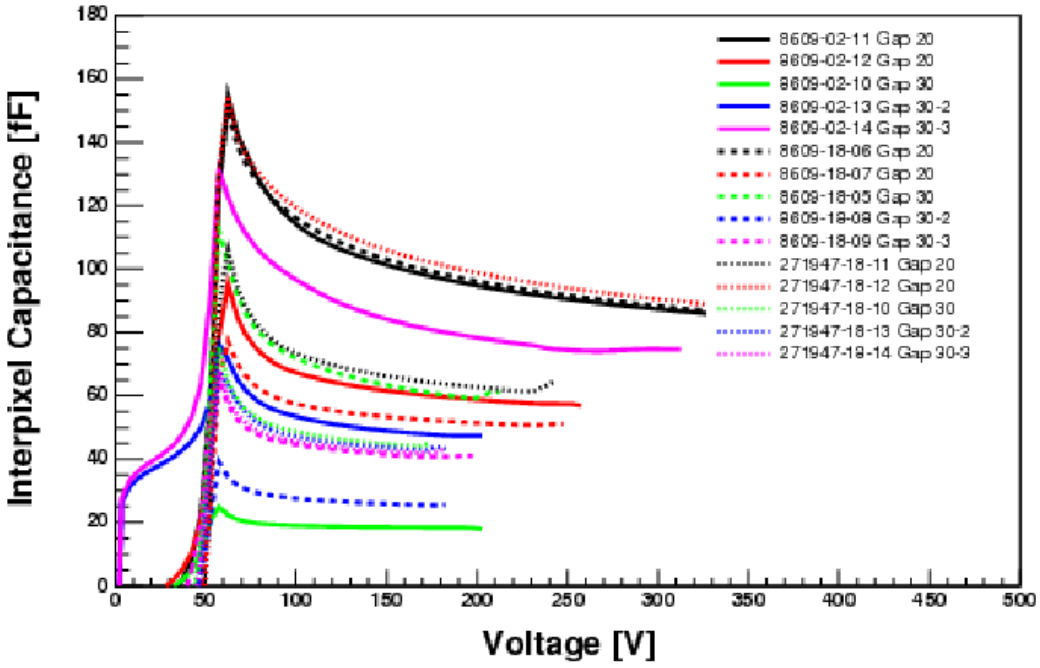

Figure 53: Interpixel capacitance vs. bias voltage before irradiation.

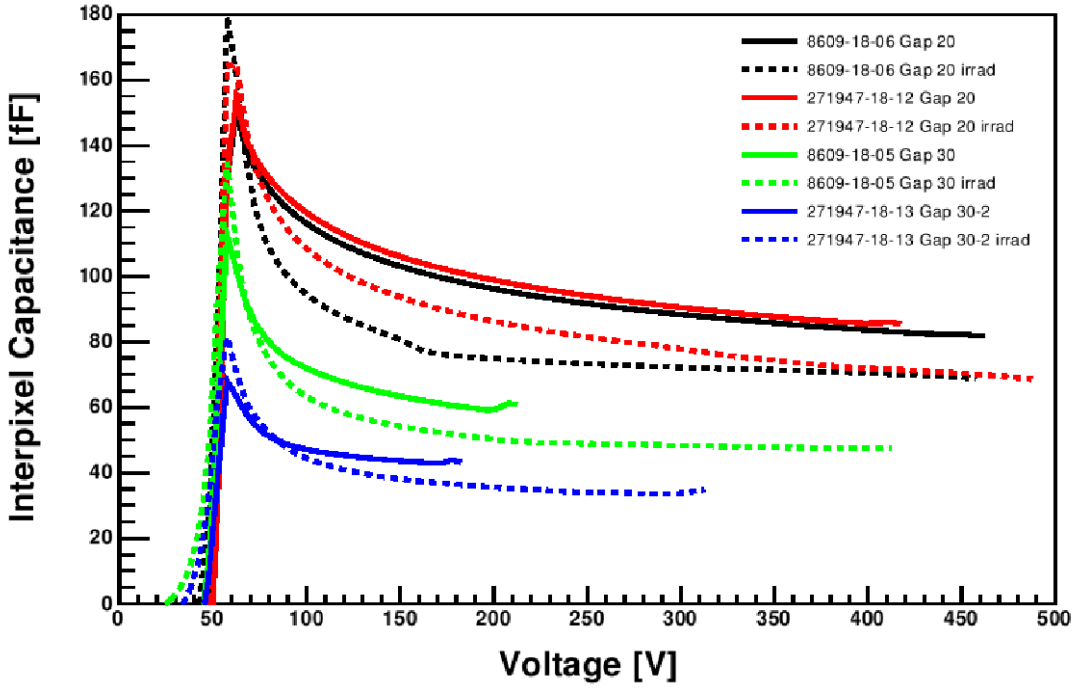

Figure 54: Results of the interpixel capacitance measurements.

5.3.2 Simulations

A simple simulation of the sensor was made to investigate the interpixel capacitance as a function of bias voltage, and how this changes with the gap size between pixels. The simulation was done with Synopsis TCAD [55].

The simulation uses a simple two dimensional geometry, which is shown in Figure 55. On each side is a half pixel, with the p-spray isolation in the center. There is a metalization on top of the oxide layer. Since this is a two dimensional geometry, it only considers the effects of one of the eight neighboring pixels.

There are two commonly used sets of boundary conditions: the von Neumann boundary conditions, which require the normal component of the electric field to be exactly 0 at the boundary, and the gate boundary conditions, which include a simple RC circuit connected to the metalization at the boundary. The RC circuit consists of a resistor and a capacitor in parallel, where the resistor has a very high resistance (10^{18} Ω) and

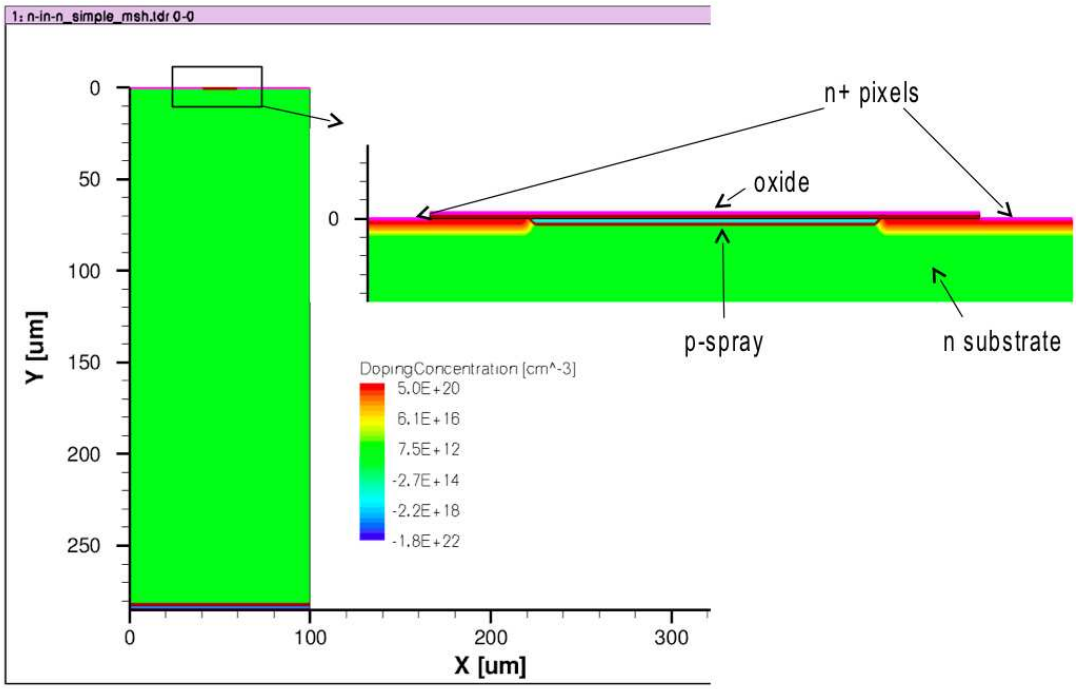

Figure 55: The geometry and doping profile of the simulated sensor area.

the capacitor has a very low capacitance (10^{-18} F). Requiring the potential to be zero at the boundary represents the situation in vacuum, and creates high fields inside the sensor. Our measurements are performed in a normal ambient environment, so the gate boundary conditions represent a more realistic picture of the measurement environment and fields inside the sensor.

The gate boundary conditions are a better reflection of the environment, since our measurements are not performed in vacuum, and so the simulations are done with the gate boundary conditions. The capacitances to be simulated are very small, and a small signal analysis tends to have convergence problems. The best convergence with the gate boundary conditions is given by indirectly simulating the capacitance by injecting a voltage into the pixel and measuring the induced current. The capacitance is proportional to the induced current, as shown in Equation 8, where Q is the charge, C is the capacitance, and V is the potential, and $\frac{dQ}{dt} = I$ is the current.

$$\begin{aligned} Q &\propto CV \\ \frac{dQ}{dt} &\propto C\frac{dV}{dt} \\ C &\propto \frac{I}{\frac{dV}{dt}} \end{aligned} \tag{8}$$

The simulation is run using three different gap sizes: 20 μm, 30 μm, and an extreme case of 50 μm. The current for each of these is shown in Figure 56. As expected, the current decreases with increasing gap size.

This simulation is greatly simplified and can not be compared quantitatively with the measurements. Many other effects are not considered here, such as the effect of the corner pixels. However, a qualitative comparison can be made. The general trend of the measurements is fairly well reproduced, with the current decreasing with increasing bias voltage, although the simulation underestimates the reduction of the capacitance with increasing bias voltage.

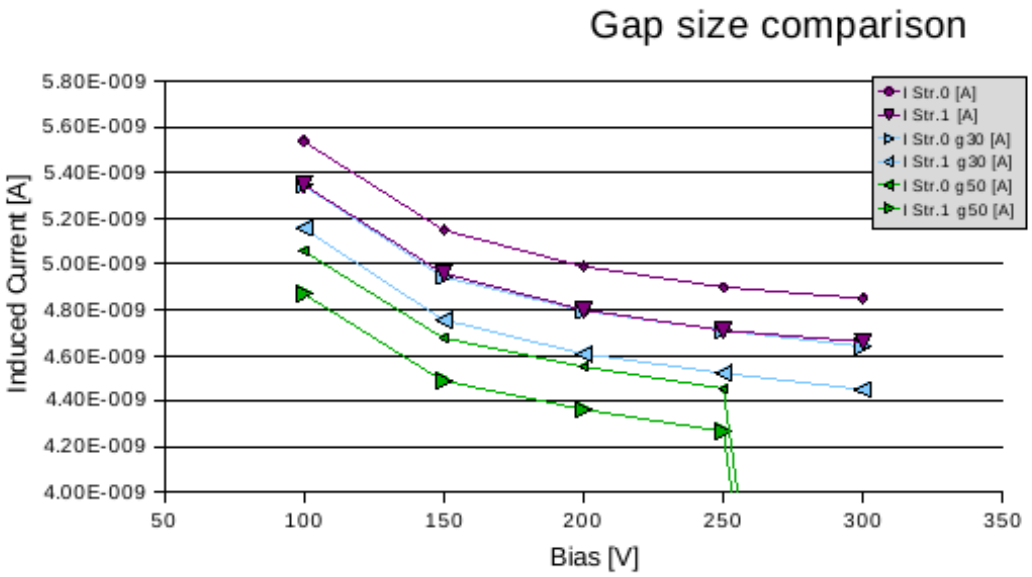

Figure 56: The current induced in the gate as a function of bias voltage in the simulation for different gap sizes.

5.4 High Voltage Tests on Single Sided Sensors

Single-sided sensors offer a cheaper alternative to double-sided processed sensors. Previous tests have shown them to have equivalent radiation hardness to double-sided sensors [57]. However the single side processing does not allow a guard ring structure on the back side of the sensor. This leaves the edges of the sensor at high voltage, while the ROC is at ground, as shown in Figure 57. There is nothing between the sensor and the ROC besides air. Air has a breakdown electric field of $\sim$3 V/μm. The distance between the sensor and the ROC depends on the bump bonding process, but is on the order of 10's of μm. In the case of the CMS pixels, the distance between the sensor and the ROC is 20 μm. When a bias voltage of a few hundred Volts is applied to the sensor there is a non-negligible chance of sparking between the ROC and the sensor. In order for single sided sensors to be a viable alternative to the more expensive double sided sensors, there must be an inexpensive and easily scalable solution to the sparking problem.

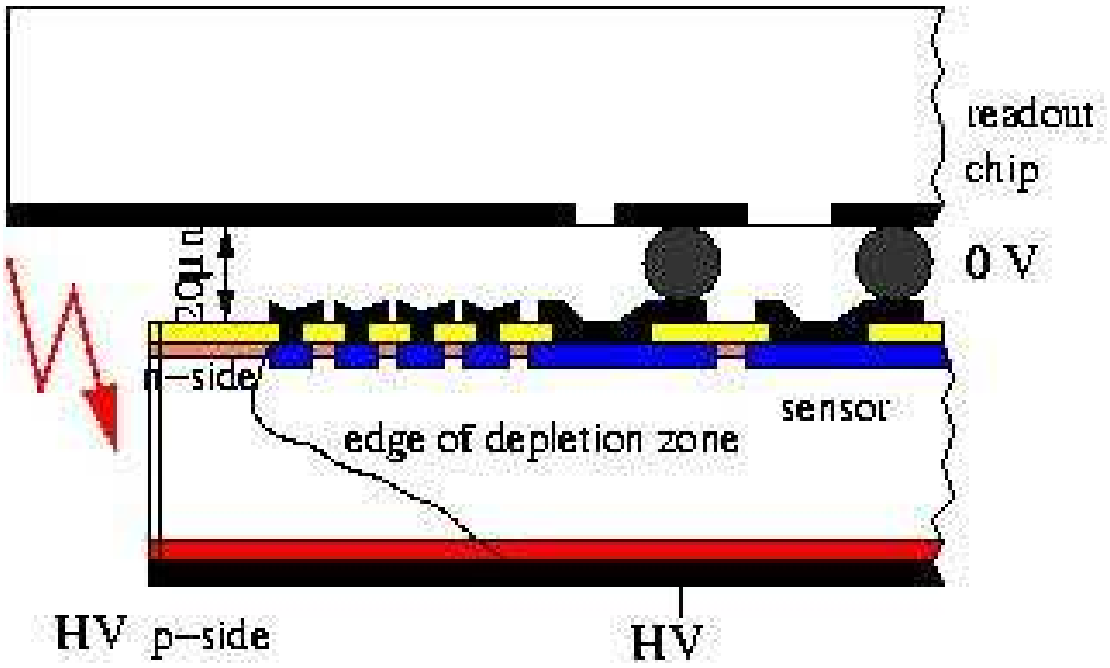

Figure 57: Diagram of single sided sensor showing the potential for sparking between the sensor and ROC.

In order to establish whether or not the problem exists we obtained some defective samples from the PSI Pilatus project [58]. The samples were single sided p-in-n sensors with defective ROCs. We applied a bias voltage to the sensor while keeping the ROC grounded. The bias voltage was slowly ramped up and the current monitored. We observed a breakdown around 500 V. The current increased rapidly and there was an audible "sparking" sound. When we visually inspected the sample we found that the ROC ground pad was completely destroyed, and other nearby pads were damaged as well. The aluminum on the back side of the sensor was also vaporized. Figures 58 and 59 show the damage to the sample.

A breakdown voltage of 500 V is higher than expected using the estimate of 3 V/μm and a distance of 20 μm between the ROC and sensor, and implies a distance of approximately 200 μm. The sensor is 280 μm thick. There is also clear damage to the aluminum on the back side of the sensor near the edge. This leads to the hypothesis that the spark occurs between the back side of the sensor and the ROC, instead of the

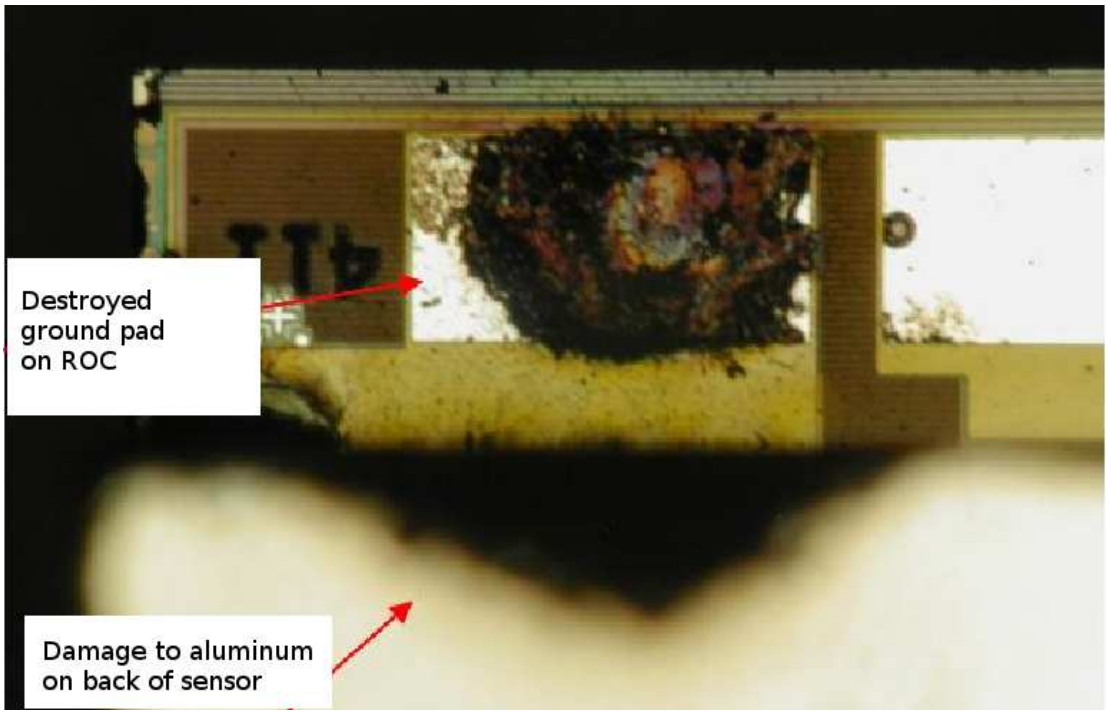

Figure 58: Damage to sensor from high voltage sparking. The ground pad of the ROC is completely destroyed. Damage to the aluminum on the back of the sensor is also visible in the bottom of the picture.

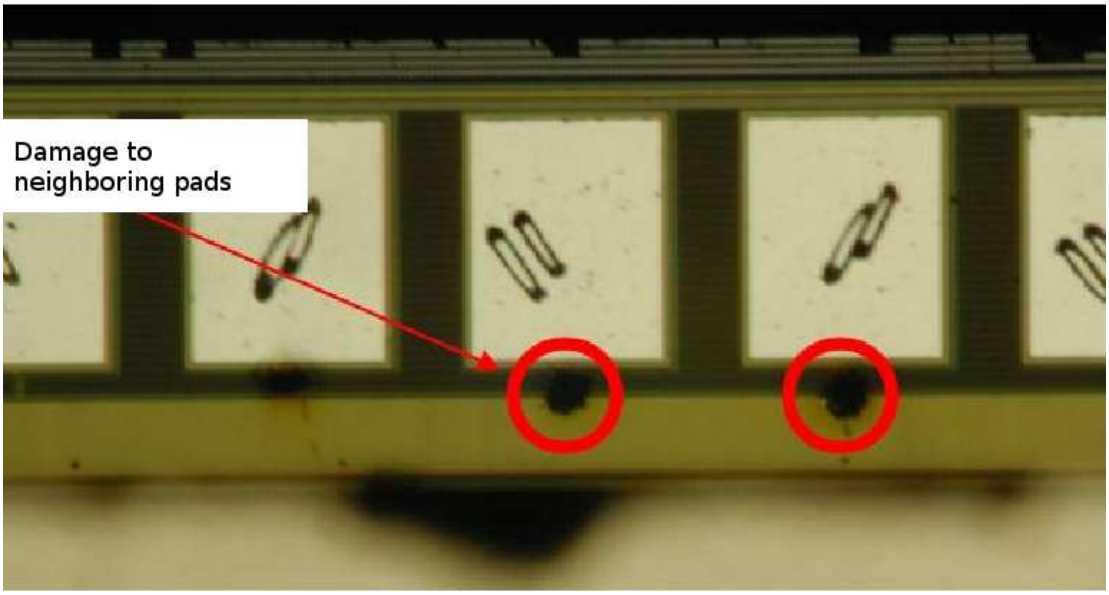

Figure 59: Damage to neighboring pads on the ROC from high voltage sparking.

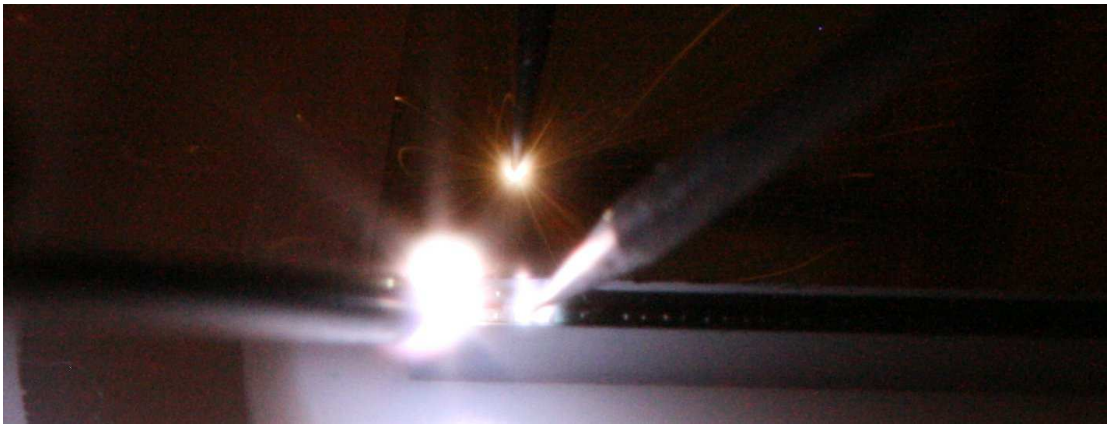

Figure 60: Photograph of sparks between ROC and sensor.

edge closest to the ROC. We set up a digital camera to try to photograph the spark to see where it originates. The photo is shown in Figure 60. It is not obvious from the photograph where the spark comes from.

The next step was to try to determine a technique to prevent the sparks from occurring. The idea is to fill the gap along the edge of the sensor and ROC with a material which has a higher breakdown voltage than air. This material must be easy to apply when the modules are produced. The first attempt was to use a glue to fill the gap. The glue fills in between the sensor and ROC while still liquid, and then is stable once cured. This is shown in Figure 61. We used two different glues, Araldit and EPO-TEK 310 [59, 60]. Araldit is a standard glue used in the construction of the current CMS modules. EPO-TEK 310 is a more liquid glue, which fills more of the gap than the Araldit. With the Araldit we observed no change in the breakdown voltage. The sample coated with the EPO-TEK glue showed a breakdown at approximately 700 V. The photographs are shown in Figure 62.

We also attemped to passivate the edges using a chemical vapor deposition (CVD) process of Parylene C. Parylene is a polymer which is often used to coat printed circuit boards and medical devices. The coating acts as a moisture and dielectric barrier. Parylene C is the most common variety. A sample was successfully tested for several

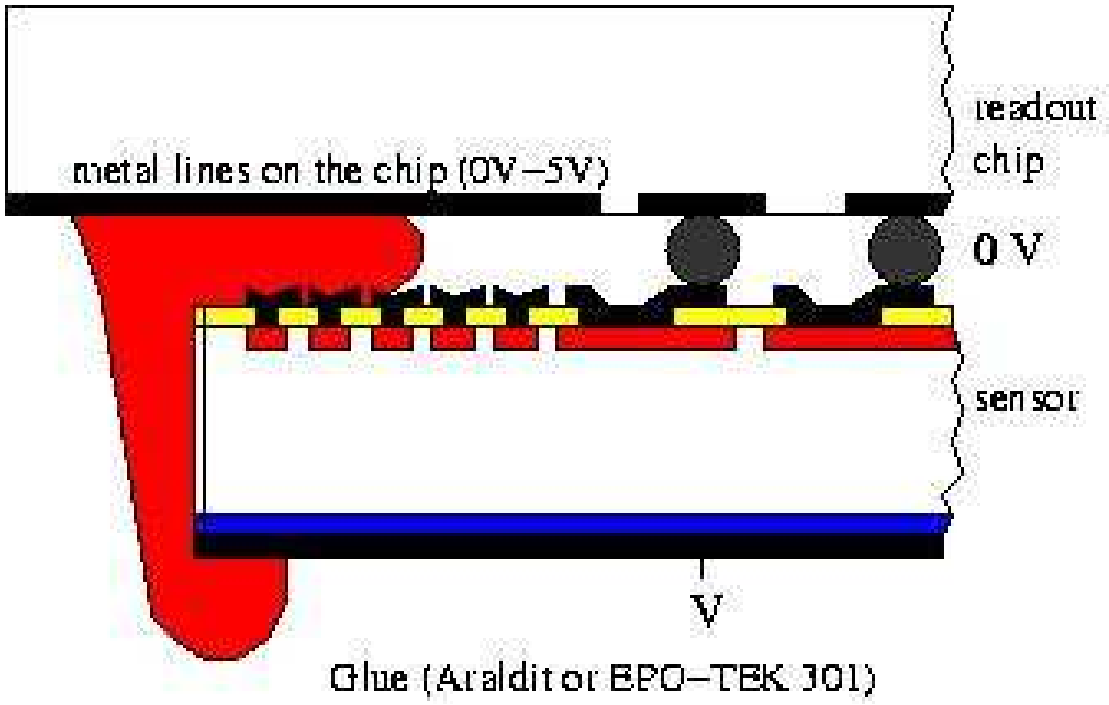

Figure 61: Diagram of single sided sensor using glue to fill the edge gap between the sensor and the ROC.

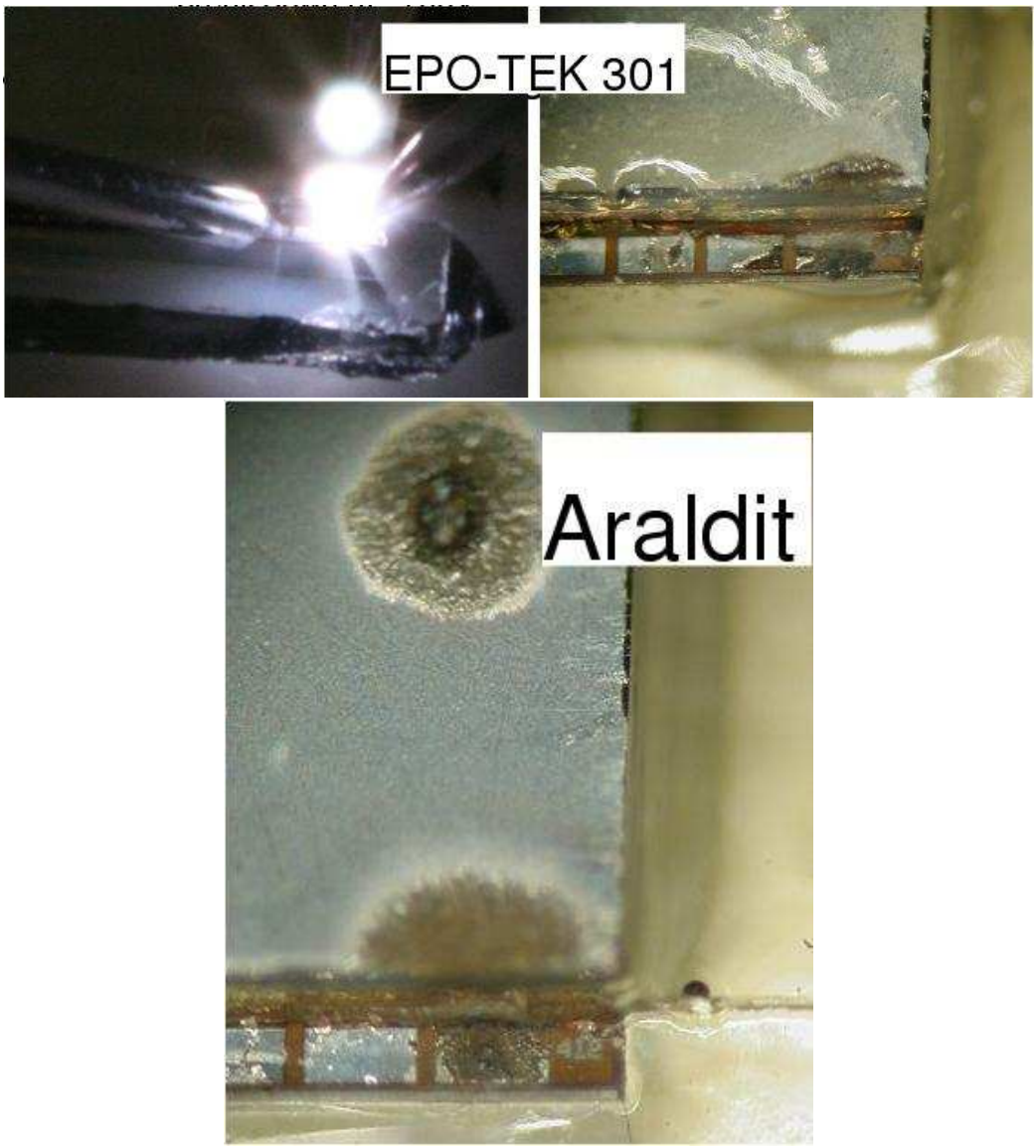

Figure 62: Damage to sensors with glue filled gaps.

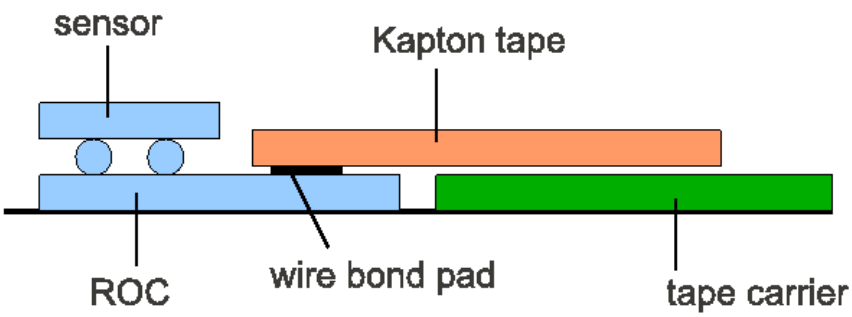

Figure 63: Diagram of the proposed solution to protect wire bond pads during Parylene deposition.

hours at 1000 V.

Discussions with the company are ongoing to determine if a Parylene coating is a feasible solution for mass production of pixel modules. As the parylene coats everything in the CVD process, any bond pads must be masked. This is usually done by covering the area with Kapton tape which is removed after the CVD process. However in the case of the pixel modules the dimensions of the bond pads are on the order of 200 μm, which are very difficult to reliably mask with Kapton tape. One possible solution considered is to coat the module after the wire bonding. This has not been done before, so the effect of the Parylene on the wire bonds must be tested. Coating the modules after wire bonding also has the consequence that if a wire bond is removed it cannot be rebonded, since the rest of the bond pad will be coated with the Parylene.

Another possible solution is to cover the bond pads with a piece of "blue-tape", which is used for dicing wafers, using a piece of aluminum as a carrier for the tape. There would be a small space between the end of the ROC and the carrier, and the tape would bridge the gap and cover the bond pads on the ROC. This idea is illustrated in Figure 63. This solution seems to be the most likely choice at the time of the writing of this dissertation.

6 b Production

6.1 Theory

Measurements of heavy flavor quark production at hadron colliders provide a good test of quantum chromodynamics (QCD) [61]. The leading order (LO) process for b quark production at hadron colliders is flavor creation, where a $b\bar{b}$ pair is produced by quark-antiquark annihilation or gluon-gluon fusion. Since the final state is a two-body state, the b quarks are usually produced back-to-back and with balanced p_{T}.

At the LHC next to leading order (NLO) processes become important. In flavor excitation, a $b\bar{b}$ pair from the quark sea of one proton is excited into the final state, after one of the quarks undergoes a hard scattering off a parton from the other proton. Because only one of the final quarks was involved in the hard scattering process, the b quarks can be produced with asymmetric p_{T} . In gluon splitting, a gluon in either the initial or final state splits into a $b\bar{b}$ pair. Neither quark is involved in the hard scattering, and the $b\bar{b}$ pair can be produced with a small angular separation. Figure 64 shows the Feynmann diagrams for these processes. The small-x effects ($x \simeq m_b/\sqrt{s}$) are relevant in the low-p_T domain [62, 63], while multiple gluon radiation is more imporant at high p_{T} [64]. Measurements which help to discriminate effects in different p_{T} and η regions are needed to test the calculations.

6.2 Monte Carlo Event Generators

The measurements are often compared with theoretical predictions. This is generally done using Monte Carlo event generators, which allow an event-by-event prediction of the QCD processes. The first step in the event generation is to calculate the matrix element with pQCD. Next a parton shower algorithm is run to generate the secondary partons, followed by a hadronization algorithm, which groups the partons into hadrons.

Two common codes for computing these predictions at next-to-leading order are the Monte Carlo for FeMtobarn processes (MCFM) [65] and the Fixed Order plus Next-to-

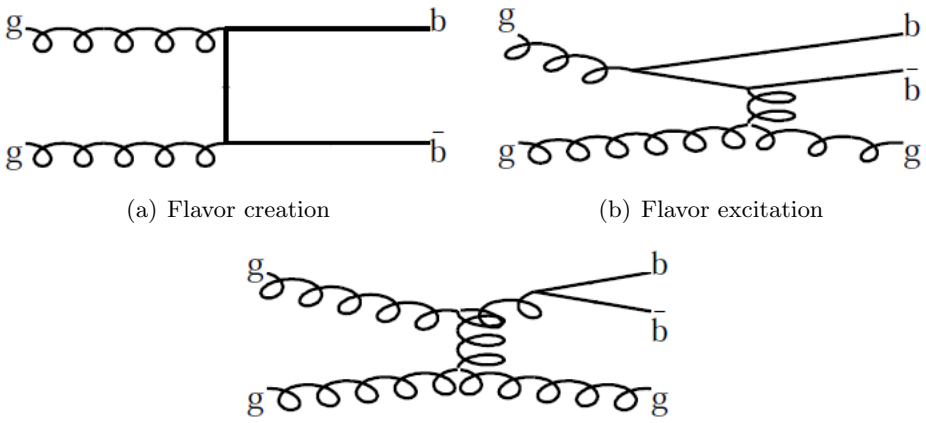

(a) Flavor creation

(b) Flavor excitation

(c) Gluon splitting

Figure 64: Examples of the LO and NLO processes for heavy quark production at hadron colliders. [11]

Leading Logarithm (FONLL) [66]. The MCFM code is a NLO calculation, while the FONLL code is, as the name suggests, a NLO calculation including the resummation of p_{T} logarithms to next-to-leading order. Other common leading order event generators are PYTHIA [67] and Herwig [68]. In PYTHIA and Herwig, the matrix elements are calculated using leading-order pQCD. There are a few ways to extend the LO event generators to include NLO corrections. MC@NLO is a package which combines the LO Herwig event generator with NLO calculations of rates of QCD processes [69, 70]. POWHEG is a method for combining any LO parton-shower generators with NLO QCD calculations [71].

The Monte Carlo sample used in the measurement presented in Chapter 7 was produced using the PYTHIA6 generator. The matrix elements are computed in LO pQCD, and the underlying event is simulated with the D6T tune [72]. The parton shower algorithm uses a leading-logarithmic approximation for QCD radiation and a string fragmentation model, implemented in JET-SET [73, 74]. The Lund symmetric fragmentation function [75] is used for light quarks, and the Peterson fragmentation function [76] for c and b quarks. The hadronic decay chain is also implemented by the

JET-SET algorithm. The mass of the b-quark is set to 4.8 GeV/c^2 [67, 6].

6.3 Other Measurements

There have been many measurements of the b cross section before, using various methods. In the following sections a few such measurements from different experiments are summarized, specifically from the Tevatron and early measurements from the LHC. The full details for each measurement can be found in the corresponding references.

CDF, LHCb, and ATLAS have all published measurements which investigate the same decay chain. The semileptonic decay of B hadrons is used, resulting in a muon and a D^0. The D^0 may be produced directly, or a D^{*+} can be produced, which immediately decays to a D^0 and π^+. This pion usually has a low p_{T}, and is hereafter referred to as the slow pion. The D^0 is reconstructed using the decay $D^0 \to K^-\pi^+$. A schematic of an event is shown in Figure 65. CMS has published similar results, although in slightly different channels. In all measurements, charge conjugate states are also included.

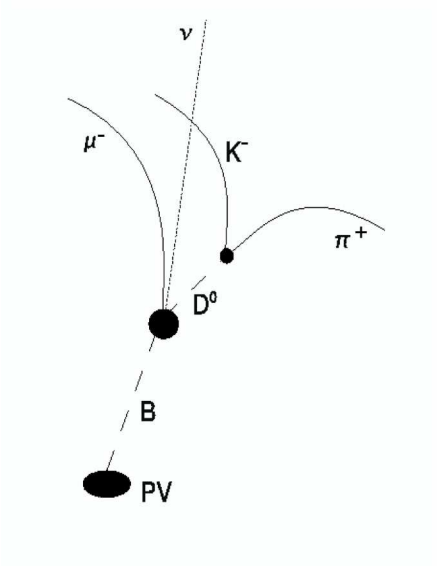

Figure 65: Topology of B hadron event.

As each detector has a different acceptance, it is necessary to "unfold" the results to compare across experiments. Unfolding is a technique to find a quantity which can

not be directly measured, by measuring a similar quantity. Then by comparing the two quantities in Monte Carlo simulations, a matrix can be found to transform the measured quantity into the desired quantity. In the case of these measurements, the desired quantity is the $p_{\mathrm{T}}(H_b)$ distribution, where H_b is the b-hadron, but since the H_b can not be fully reconstructed due to at least the missing neutrino, only the $p_{\mathrm{T}}(\mu D^0)$ distribution can be measured.

6.3.1 CDF measurement of b hadron production cross section

The Collider Detector at Fermilab (CDF) collaboration at the Fermilab Tevatron made a measurement of the b hadron (H_b) production cross section in $p\bar{p}$ collisions at $\sqrt{s} =$ 1.96 TeV [12]. The measurement uses an integrated luminosity of 83 pb^{-1} of data taken with the CDF II detector. The detector consists of a charged particle tracker inside a 1.4 T solenoid magnet, calorimeters, and muon detectors.

In the reconstruction of an event, the kaon and pion candidate tracks are required to originate from a displaced vertex which is consistent with the decay of a D^0. To include the decay $D^* \to D^0\pi, D^0 \to K\pi$, the track of the slow pion is also required. The branching ratios used in the measurement are $\mathcal{B}(H_b \to \mu^- D^0 X) \times \mathcal{B}(D^0 \to K^-\pi^+)$ for the $\mu^- D^0$ mode and $\mathcal{B}(H_b \to \mu^- D^{*+} X) \times \mathcal{B}(D^{*+} \to D^0\pi^+) \times \mathcal{B}(D^0 \to K^-\pi^+)$ for the $\mu^- D^{*+}$ mode. The b hadron cross section is obtained by unfolding the measured $p_{\mathrm{T}}(\mu D^0)$ distribution back to the $p_{\mathrm{T}}(H_b)$ distribution. The differential cross section is shown in Figure 66. The measured total cross section for b hadrons with $p_{\mathrm{T}} >$ 9 GeV/c and $|\eta| < 0.6$ is shown in Equation 9, where $0.07(\mathcal{B})$ is the uncertainty from the branching ratio.

$$\sigma(p\bar{p} \to H_b X) = 1.30 \pm 0.05(stat) \pm 0.14(syst) \pm 0.07(\mathcal{B})\ \mu b \tag{9}$$

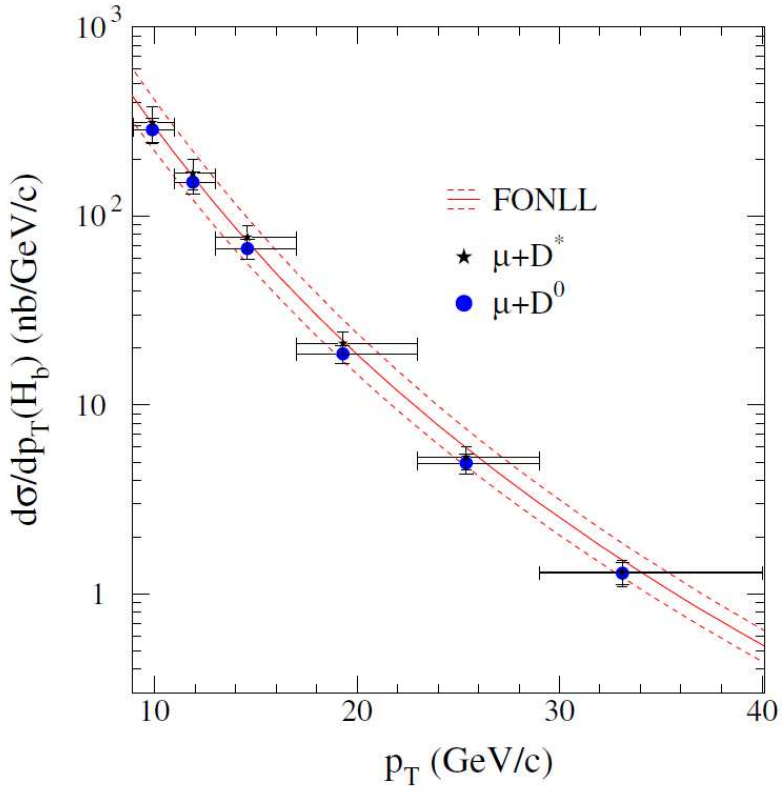

Figure 66: The unfolded b hadron differential cross section in $p\bar{p}$ collisions for the CDF measurements at $\sqrt{s} = 1.96$ TeV of $H_b \to \mu D^0 X$ and $H_b \to \mu D^* X$ for $p_T(H_b) > 9$ GeV/c and $|y(H_b)| < 0.6$ compared with predictions from FONLL theory [12].

6.3.2 LHCb

The LHCb detector was built as a forward spectrometer and is focused on measuring CP violation and rare decays of b and c hadrons. The detector consists of tracking and vertexing systems, calorimeters, and muon identification systems. The LHCb experiment has measured the b-hadron production fractions for $2 < |\eta| < 5$ [77] with 2011 data from a luminosity of 0.3 fb^{-1}. Here the $D^0\mu$ decay is separated into particular b-hadron parents to measure the production fraction, but no cross section results are given.

The LHCb experiment has also measured the $pp \to b\bar{b}X$ cross section at $\sqrt{s} = 7$ TeV in the $2 < |\eta| < 6$ region using the $b \to \mu D^0 X$ decay channel, where X can be

anything [13]. The measurement uses a branching ratio of $\mathcal{B}(b \to D^0 X \mu^- \bar{\nu}) \times \mathcal{B}(D^0 \to K^- \pi^+)$, where $\mathcal{B}(b \to D^0 X \mu^- \bar{\nu}) = (6.84 \pm 0.35)\%$ and $\mathcal{B}(D^0 \to K^- \pi^+) = (3.89 \pm 0.05)\%$. The collaboration used two independent data sets, collected at different times. The first is from the earliest period of data taking, when the rate was low enough to accept all events with at least one reconstructed track. This sample is called "microbias" and has an integrated luminosity $\mathcal{L} = 2.9$ nb^{-1}. The second sample, called "triggered," was collected using a trigger which selects events with at least one muon. The triggered sample has an integrated luminosity $\mathcal{L} = 12.2$ nb^{-1}. The two samples are analyzed separately and then the results are combined.

To select signal events the D^0 is reconstructed by combining a kaon and pion candidate whose tracks are inconsistent with originating at the primary vertex, and are consistent with coming from a common decay vertex. The D^0 candidate is matched with a muon track to select an event likely belonging to the decay chain of interest. The cross section as a function of $\eta(\mu D^0)$ is shown in Figure 67. The comparison with two theoretical calculations is also shown. Averaging the data from both the microbias and triggered data sets and summing over $\eta(\mu D^0)$ in the range $2 < \eta(\mu D^0) < 6$, the measured cross section is shown in Equation 10. The results are consistent with the theoretical calculations within the theoretical uncertainties for both FONLL and MCFM (not shown in the plot) [13].

$$\sigma(pp \to b\bar{b}X) = (75.3 \pm 5.4 \pm 13.0)\ \mu b \tag{10}$$

6.3.3 ATLAS

The ATLAS experiment at the LHC has also published a measurement of the $pp \to b\bar{b}X$ cross section at $\sqrt{s} = 7$ TeV [14]. The ATLAS detector is a general purpose high energy physics collider detector, similar to CMS, with tracking and vertexing detectors, calorimeters, and muon identification systems covering almost the full solid angle around

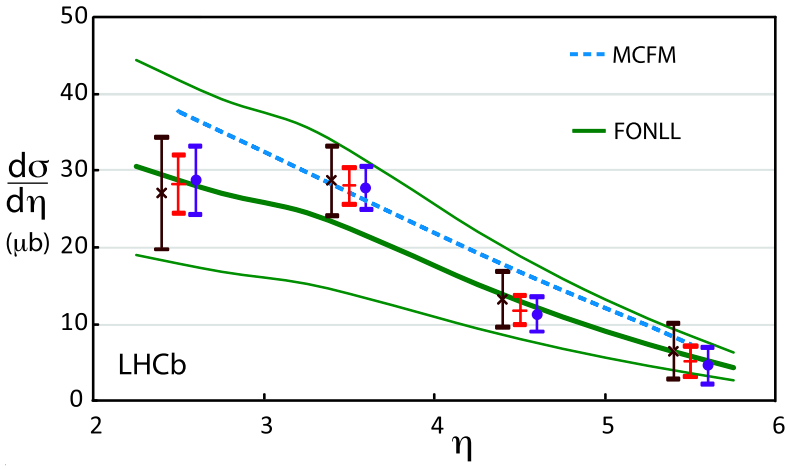

Figure 67: LHCb measurement of $\sigma(pp \to H_b X)$ as a function of $\eta(\mu D^0)$ [13] for the microbias ($\times$) and triggered ($\bullet$) samples, shown displaced from the bin center and the average ($+$). In both data sets, $p_T(K,\pi) > 300$ MeV is required. The muon $p_{\rm T}$ is required to be at least 500 MeV for the microbias dataset and at least 1.3 GeV for the triggered dataset. The data are shown as points with error bars, the MCFM prediction as a dashed line, and the FONLL prediction as a thick solid line. The thin upper and lower lines indicate the theoretical uncertainties on the FONLL prediction. The systematic uncertainties in the data are not included.

the collision point.

The data were taken during 2010 using a single muon trigger with $p_{\rm T} > 6$ GeV. The total integrated luminosity of the data is 3.3 pb^{-1}. The measurement uses the decay $b \to D^{*+}\mu^- X, D^{*+} \to D^0\pi^+, D^0 \to K^-\pi^+$. To reconstruct the events, all pairs of opposite charge tracks are fit together to reconstruct the D^0 , assigning each track the kaon or pion mass. The D^0 is then extrapolated back and fit with another track with charge opposite to the one of the candidate kaon, which is assigned the pion mass, to reconstruct the D^*. The D^* candidate is fit with a muon to form the b-hadron vertex. The number of candidates is found by fitting the distribution of the difference between the mass of the D^* candidate and the D^0 candidate with a modified Gaussian.

The result is unfolded to get the differential cross section as a function of the $p_{\rm T}$ and $|\eta|$ of the b-hadron, shown in Figure 68. An acceptance correction is applied to obtain the integrated b-hadron cross section for $p_{\rm T}$ $(H_b) > 9$ GeV and $|\eta(H_b)| < 2.5$, shown in

Equation 11. Here α denotes the uncertainty due to the acceptance correction, $\mathcal{B}$ is the uncertainty due to the branching ratio, and $\mathcal{L}$ is the uncertainty due to the luminosity measurement.

$$\sigma(pp \to b\bar{b}X) = 32.7 \pm 0.8(stat.) \pm 3.1(syst.)^{+2.1}_{-5.6}(\alpha) \pm 2.3(\mathcal{B}) \pm 1.1(\mathcal{L})\ \mu b \qquad (11)$$

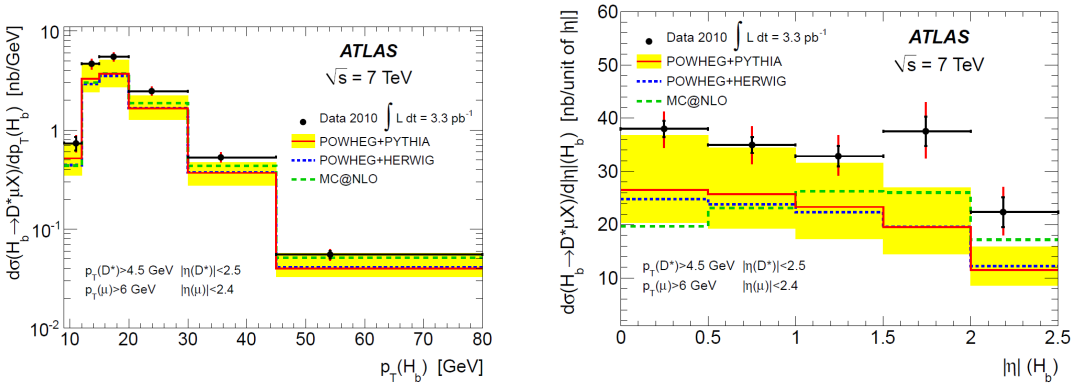

Figure 68: ATLAS measurement of $\sigma(pp \to H_b X)$ unfolded and as a function of $p_T(H_b)$ (left) and $|\eta(H_b)|$ (right) for $p_T(H_b) > 9$ GeV/c and $|\eta(H_b)| < 2.5$, compared with theoretical predictions. The inner error bars are the statistical uncertainties, and the outer error bars are the statistical plus total systematic uncertainties [14].

6.3.4 CMS

There have been previous measurements of the $b\bar{b}$ cross section with the CMS detector. A measurement of the b-fraction for $\sqrt{s} = 7$ TeV of a sample of muon events exploiting the transverse momentum of the muon with respect to the jet axis (p_T^{rel}) [6, 78] for $p_T(\mu) > 6$ GeV/c and $|\eta(\mu)| < 2.1$ showed that this inclusive cross section fell below the predictions of PYTHIA [67], especially for the lower $p_T(\mu)$ region, but above those for MCNLO [69, 70], shown in Figure 69. The error in this analysis was dominated by the systematic error which included a large contribution from the p_T^{rel} template uncertainty. A measurement of the correlated $b\bar{b}$ cross section measured with di-muons [79] also found

that the cross section was between PYTHIA and MCNLO. Here, templates for the transverse impact parameter of the muon with respect to the primary vertex (d_{xy}) were used to determine the flavor composition in the fit and the largest systematic uncertainty ($\simeq 8.3\%$) was from the trigger efficiency. Each of these muon analyses uses the direction of the muon as the estimate for the direction of the $b-$hadron. There have also been measurements of the inclusive b-jet production using jets with $p_T^{\text{jet}} > 18$ GeV/c [80]. Here, MCNLO described the overall fraction of b-jets well, but there were differences found in the p_T^{jet} and y^{jet} distributions with the dominant systematic uncertainty coming from the b-tagging efficiency (20%).

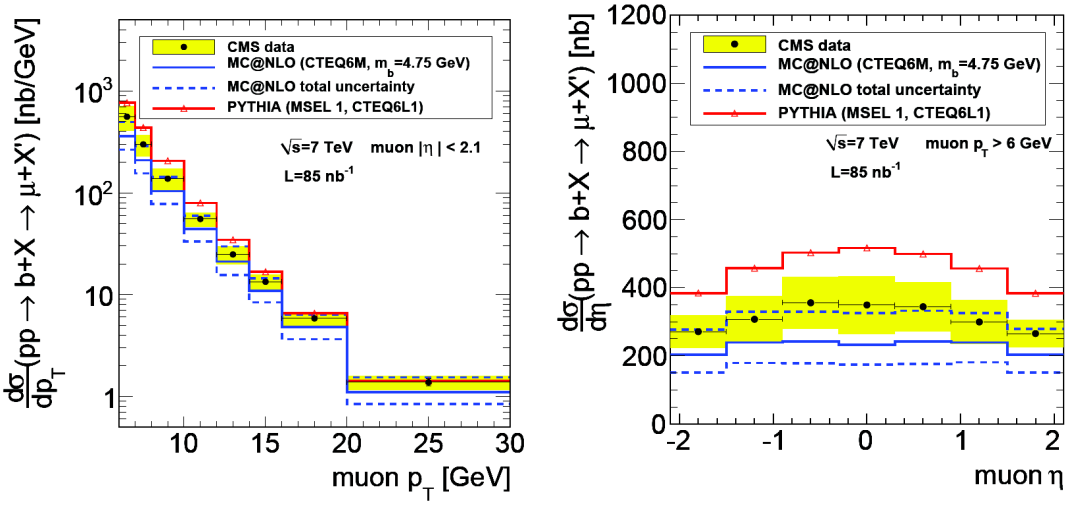

Figure 69: CMS measurement of $\sigma(b\bar{b} \to \mu X)$ for $p_T(\mu) > 6$ GeV/c and $|\eta(\mu)| < 2.1$, as a function of p_{T} (left) and $|\eta|$ (right), compared with theoretical predictions. The PYTHIA predictions, shown in green, overestimate the cross section, while the MC@NLO predictions, shown in red, underestimate the cross section [6].

Figure 70 shows a comparison of different generators for the cross section of $b\bar{b} \to \mu X$ to show the spread between different generators. Both the Herwig and PYTHIA predictions use POWHEG to combine with NLO calculations. PYTHIA tends to predict higher b-production cross sections than FONLL, while Herwig predictions are lower.

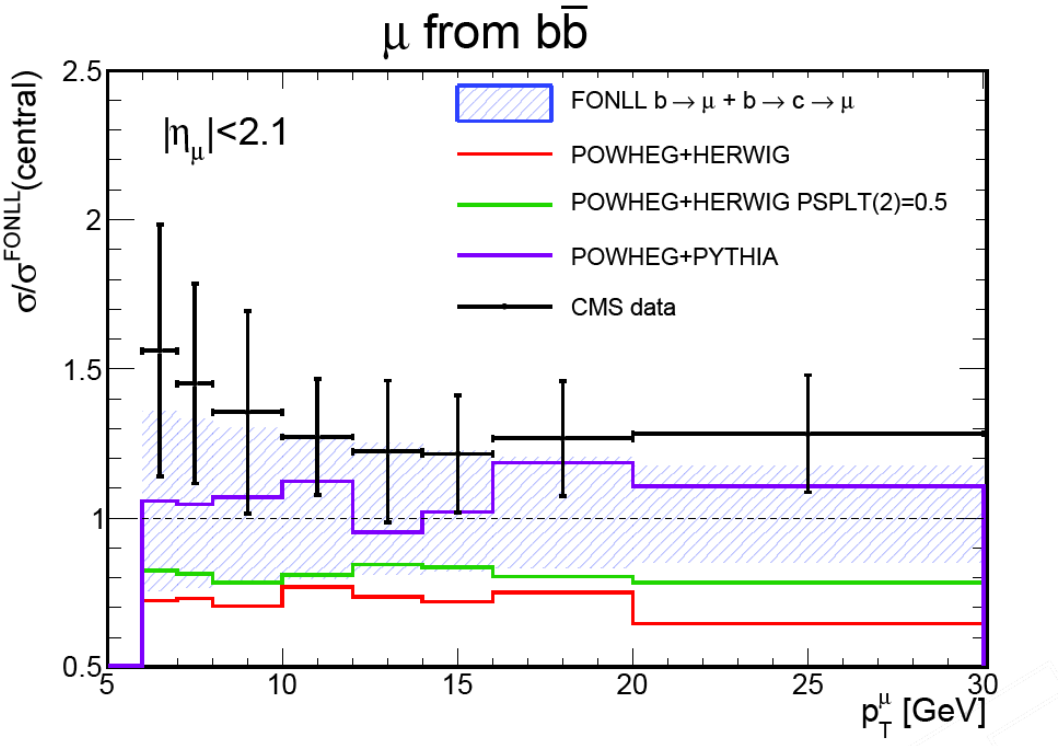

Figure 70: Comparison of the $b\bar{b} \to \mu X$ cross section as a function of muon p_{T} for various Monte Carlo event generators with the expected cross section for FONLL. The CMS data are also superimposed [15].

6.4 Summary

The large b production cross section at the LHC makes it a good opportunity to study how well pQCD describes reality. In addition it is an important background to new physics searches, so it is essential that the cross section is well understood.

Both the ATLAS and LHCb experiments have published similar measurements to the one presented in Chapter 7. CMS has also published $b\bar{b}$ cross section measurements, but so far not in the $B \to \mu D^0 X, D^0 \to K\pi$ channel. The CMS measurements showed that the LO PYTHIA predictions are too high, especially in the lower $p_T(\mu)$ region. Combining PYTHIA with POWHEG to add NLO effects brings the prediction down, in better agreement with the data and with the predictions from other Monte Carlo event generators. The ATLAS results are just in agreement with the POWHEG+PYTHIA

predictions within the errors. The LHCb results are consistent with FONLL predictions.

To compare results between experiments, the cross sections must be unfolded to account for differences in acceptance. It is however difficult to compare between LHCb and the two general-purpose experiments, because the overlapping region in η is small, and ATLAS and CMS suffer from low efficiencies. The goals of this analysis are to provide a cross section measurement at the LHC at relatively low muon p_{T} , to provide a complimentary measurement to the LHCb measurement for $\eta < 2$, and to provide a potential direct comparison between CMS and LHCb.

7 $b\bar{b}$ Cross Section Measurement

7.1 Introduction

This chapter presents a measurement of the $b\bar{b}$ cross section at $\sqrt{s} = 7$ TeV using the decay channel $b \to \mu^- D^0 X$. Charge conjugate states are included. The differential cross section is measured for $p_T^{\mu D^0} > 6$ GeV/c and $|\eta_{\mu D^0}| < 2.4$. Cross section measurements from this decay channel provide a complimentary measurement to both the inclusive muon and b-jet results. The direction of the b-hadron is better measured with the addition of a D^0 compared to those using only the muon direction, although we present the differential cross section as a function of $p_T(D^0\mu)$ and $\eta(D^0\mu)$ and not the b-hadron direction. The low p_{T} region helps to constrain predictions at small-x compared to the CMS inclusive b-jet production results. Results from $|\eta| > 2$ are presented in order to compare to those measured by LHCb.

The data were recorded with the CMS experiment at the Large Hadron Collider (CERN) in 2010 using unprescaled single muon triggers corresponding to a total luminosity of 24 pb^{-1}. One goal of this analysis is to provide information on the differential cross section for low p_{T} values (> 6 GeV/c) and η values greater than 2.1.

7.2 Data and Monte Carlo Samples

The data used in this analysis were obtained during the 2010 data taking period using two single muon triggers, HLT_Mu5 (p_{T} (μ) > 5 GeV/c) and HLT_Mu15_v1 (p_{T} (μ) > 15 GeV/c). The single muon trigger HLT_Mu5 ($p_{\mathrm{T}} > 5$ GeV/c) was prescaled early into the 2010 data taking, so in addition the HLT_Mu15 ($p_{\mathrm{T}} > 15$ GeV/c) trigger is used to obtain more statistics for the higher p_{T} b-hadron region. Only runs where the trigger was unprescaled were used. The valid runs were specified using a JSON (JavaScript Object Notation) file, which is a standard file format used to represent data structures in a human-readable form. A run is considered good and valid for analysis when all detector components are working fine and correctly calibrated and used in the reconstruction.

Table 3: 2010 Data samples used for the analysis.

Trigger	Data set	Runs	$\mathcal{L}$ $[pb^{-1}]$
HLT_Mu5	`Mu/Run2010A-Dec22ReReco_v1`	136035-141952	0.203
HLT_Mu15_v1	`Mu/Run2010B-Dec22ReReco_v1`	147196-149294	23.9

The JSON file used is

`Cert_136033-149442_7TeV_Dec22ReReco_Collisions10_JSON_v3`.

The muon secondary datasets were used, and a summary of the datasets, runs, and integrated luminosity can be found in Table 3. The luminosity was calculated with the LumiCalc.py script by summing the luminosity for each run where the relevant single-muon trigger was used and not prescaled, as measured by the HF detector. The data have been analyzed within the CMSSW_3_9_7 version of the CMS software and the analysis code is available at `CMSSW/UserCode/JSibille`.

The Monte Carlo sample used is a muon enriched sample with multijet final states produced using Pythia6 [67],

`/QCD_MuPt5EtaFilter_7TeV-pythia6/Fall10-START38_V12-v1`.

A generator level filter requires a muon with $p_{\mathrm{T}} > 5$ GeV/c and $|\eta| < 2.5$. Multiple proton collisions per event, commonly called pileup, were not included in the simulation. A total of 10^7 events is contained in this sample, with a luminosity of 1.23 pb^{-1}. The samples have been produced with the full CMSSW simulation.

7.3 Event Selection

We look for events where a b-hadron decays to a muon, a D^0 , and anything else. One example of an event is shown in Figure 71.

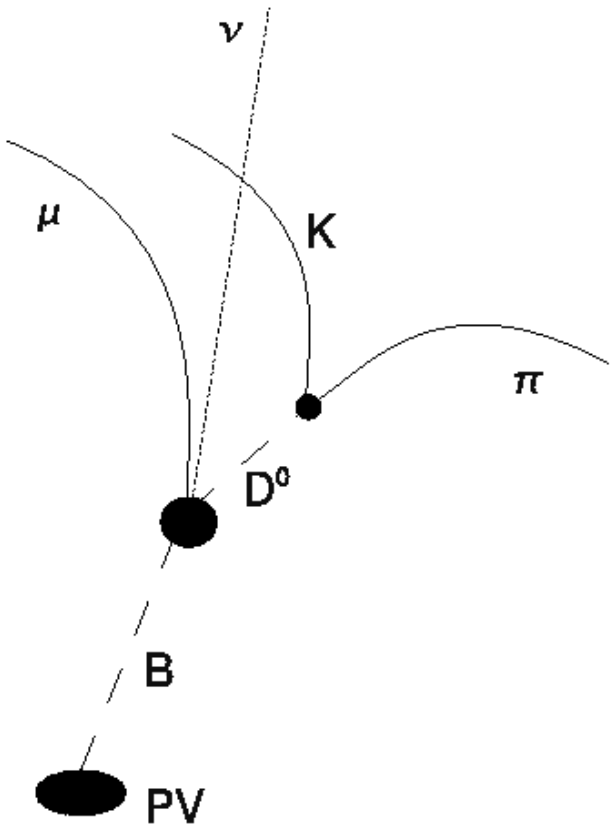

Figure 71: Example of a $B \to \mu D^0 X$ decay. The B travels from the primary vertex (PV) shown by the dotted line then decays at the black circle shown.

In the Monte Carlo sample, events can be tagged as either signal or background by looking at the generator level information. An event is tagged as signal if it contains a muon, kaon, and a pion, where the kaon and pion are the only decay products of a D^0 , which shares a b-hadron mother with the muon. Events where the muon does not come directly from the b-hadron are considered background. The D^0 may first go through a D^*. Any event which does not satisfy these criteria is considered a background event.

Backgrounds can come from the following sources:

1. Fake muons

2. Misassignment of the kaon and pion tracks

3. Real kaons and real pions that are not from a D^0 decay

4. Real muons and real D^0 decays that do not originate from a b-hadron decay

5. Real muons and real D^0 decays that originate from different b's

The different sources of backgrounds are shown in Figure 72.

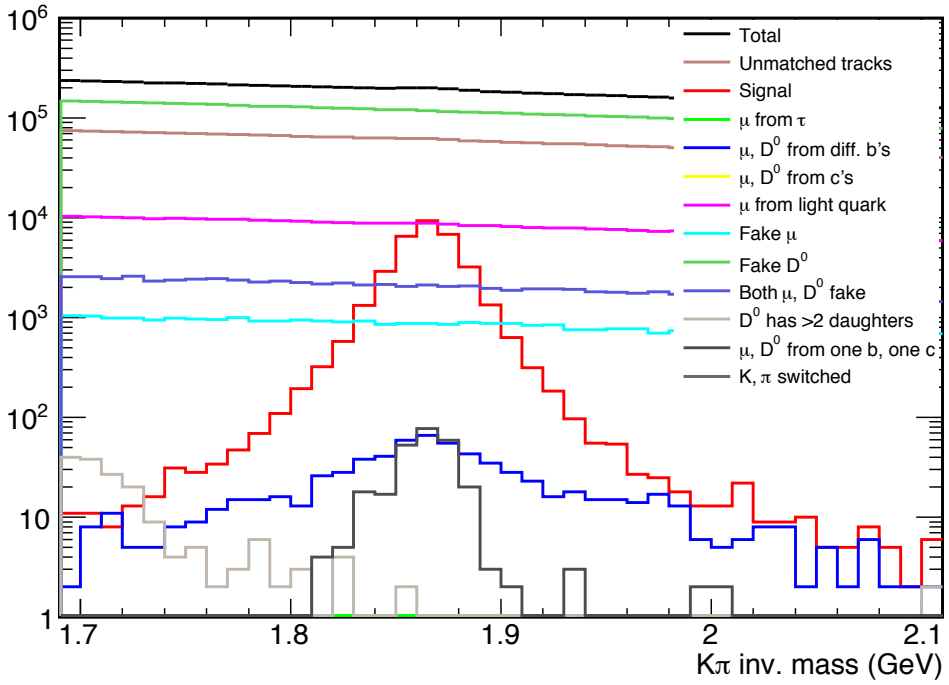

Figure 72: D^0 candidate invariant mass distribution before cuts showing different sources of background in Monte Carlo.

We require tight tracking and muon selection to reduce the amount of background from the first three sources. To select candidate events we fit the kaon and pion tracks to a common displaced vertex to form a D^0 candidate, which further reduces background from the second and third sources. The D^0 candidate and the muon track are fit to another common displaced vertex to form a B candidate, thus cutting down background

from the fourth source. The KinematicParticleVertexFitter [81] is used to create a kinematic particle from the daughter particles. A skim is run to extract interesting events before the full analysis (selection) cuts are applied to enhance the b-hadron signature sensitivity. We separate the events into the correct sign combinations (whhere the muons and kaons have the same charge) and wrong sign combinations. After the selection cuts with the correct charge assignments, we find only D^0 candidates from the signal should be present as a resonance in the invariant $K^-\pi^+$ mass spectrum (charge conjugate states are included), which is fit to extract the signal.

7.3.1 Acceptance and Quality Cuts

A first set of cuts is made in order to assure the quality of the selected events. Events with no more than 1000 tracks are chosen. For the muon, kaon, and pion tracks we require hits in at least 2 pixel layers to ensure that only good quality tracks are used. Additionally, we require at least 10 tracker hits (pixels plus strips) for the muon track, and at least 5 tracker hits for the kaon and the pion tracks. Muons satisfy the `GlobalMuonPromptTight` criteria [82]. The muon, kaon, and pion tracks must have $|\eta| < 2.4$. The muon is required to have $p_{\mathrm{T}} > 5$ GeV/c, while the kaon and pion are required to have $p_{\mathrm{T}} > 0.5$ GeV/c. Figure 73 shows the p_{T} and η distributions for the muon candidates in Monte Carlo events and the 2010A data, while Figure 74 shows these distributions for the kaon/pion track candidates. The kaon candidate and the pion candidate must have opposite charges, but there are no explicit particle identification cuts placed on either of them.

Cuts of $\Delta R(\mu K) \leq 1.5$ and $\Delta R(\mu\pi) \leq 1.5$ are made to increase the probability that the muon, kaon, and pion come from a b-hadron. Here, $\Delta R = \sqrt{\Delta\phi^2 + \Delta\eta^2}$. The distributions for ΔR are shown for signal and background Monte Carlo events in Figure 75. The kaon candidate track and the pion candidate track form a D^0 candidate which is required to have an invariant mass (using the particle data group (PDG) masses for each of the kaon and pion) within 0.3 GeV/c^2 of the mass of the D^0 (1.8646

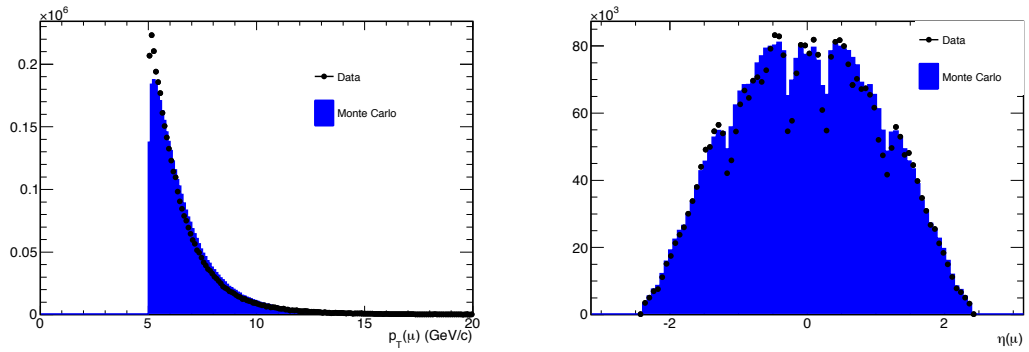

Figure 73: Distributions of p_{T} (left) and η (right) for tracks identified as tight muons shown after the track quality cuts for Monte Carlo events (filled histogram) and 2010A data events (points). The Monte Carlo is normalized to the Run A luminosity.

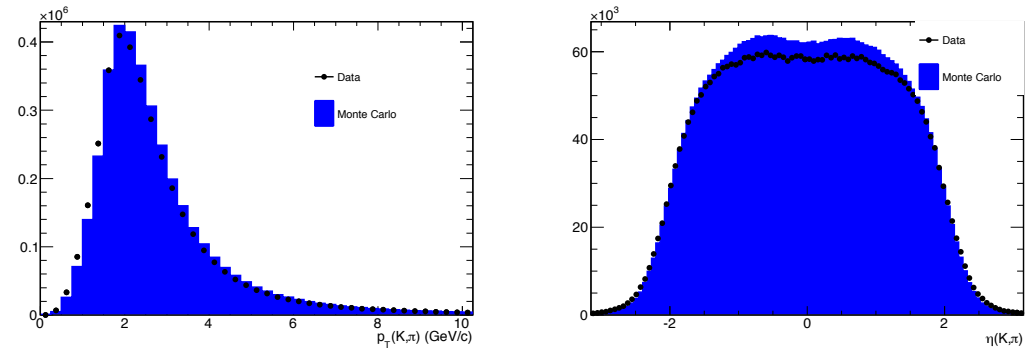

Figure 74: Distributions of p_{T} (left) and η (right) for kaon/pion tracks shown after the track quality cuts for Monte Carlo events (filled histogram) and 2010A data events (points). The Monte Carlo is normalized to the run A luminosity.

GeV/c^2) [83]. This "D^0 " mass distribution after the skim cuts for both the 2010A and 2010B datasets is shown in Figure 76, and for Monte Carlo events in Figure 77. We also require that the vertex probability for both the D^0 and B candidates is greater than 0.01, to eliminate cases where the vertex fit fails.

The masses of the $B^{\pm}$ and B^0 mesons are 5.28 GeV/c^2 [83], so we require that the invariant mass of the μD^0 candidate is less than 5 GeV/c^2. Since we do not reconstruct any other possible daughters of the B meson there is no minimum requirement on the μD^0 invariant mass. The μD^0 candidate invariant mass distribution is shown in

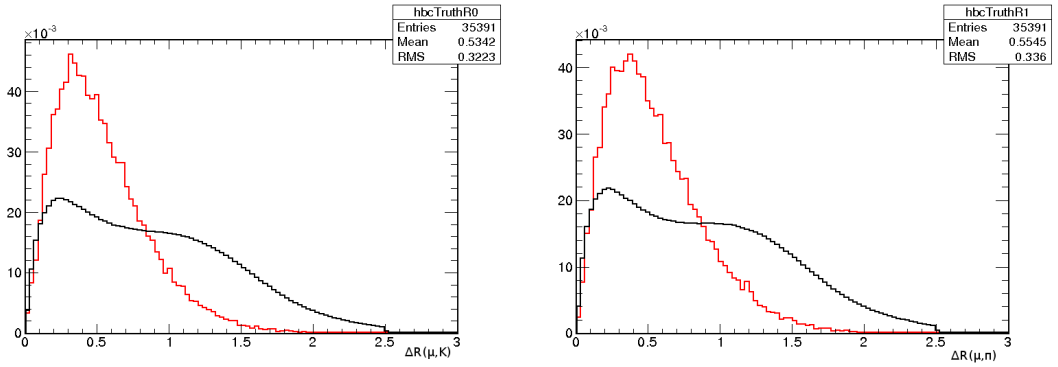

Figure 75: Distributions of $\Delta R(\mu, K)$ (left) and $\Delta R(\mu, \pi)$ (right) after skim cuts for tagged signal (red) and background (black) Monte Carlo events. The distributions are normalized to unit area.

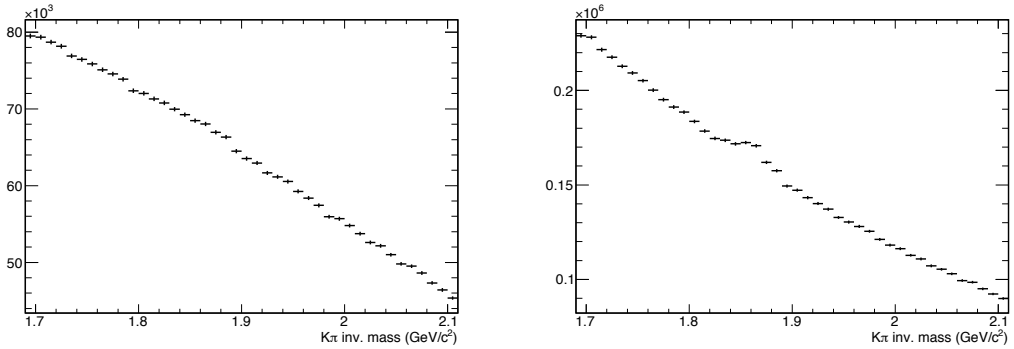

Figure 76: The $K^-\pi^+$ invariant mass distribution for the 2010A dataset (left) and 2010B dataset (right) after the acceptance and quality cuts.

Figure 78 for signal and background Monte Carlo events.

In summary, the following cuts are made for acceptance and track quality.

1. The primary vertex must have a longitudinal impact parameter less than 24 cm.

2. All tracks must have $|\eta| < 2.4$.

3. The muon and kaon are required to have $\Delta R(\mu, K) \leq 1.5$.

4. The muon and pion are required to have $\Delta R(\mu, \pi) \leq 1.5$.

5. The muon track must have $p_{\mathrm{T}} > 5$ GeV/c.

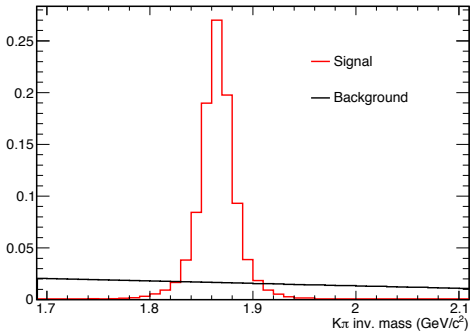

Figure 77: The $K^-\pi^+$ invariant mass distribution for tagged signal (red) and background (black) Monte Carlo events after the acceptance and quality cuts. The distributions are normalized to unit area.

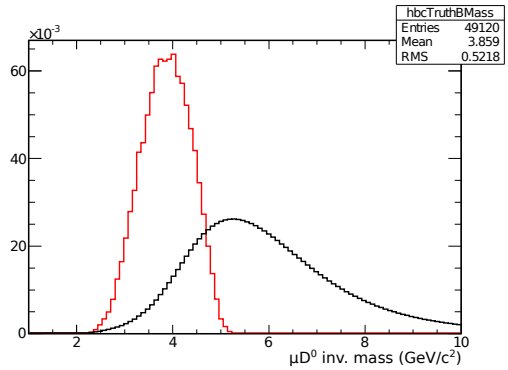

Figure 78: The μD^0 invariant mass distribution for tagged signal (red) and background (black) Monte Carlo events after the acceptance cuts. The distributions are normalized to unit area.

6. The kaon and pion candidate tracks are required to have $p_T > 0.5$ GeV/c.

7. The mass of the $D^0\mu$ must be less than 5 GeV/c^2.

8. The D^0 vertex probability must be greater than 0.01.

9. The B vertex probability must be greater than 0.01.

Table 4 shows the cuts which are made for acceptance and track quality cuts. There are 49K signal candidates and 515M background candidates in the Monte Carlo before the acceptance cuts.

Table 4: Variables used for acceptance and quality cuts and their cut values. The Signal Eff and BG MC Eff columns show the efficiencies of the truth matched signal and background events, respectively, after each cut.

Variable	Cut Value	Signal Eff	BG MC Eff
PV long. IP	< 24 cm	1	$\simeq 1$
Track quality	see text	0.88	0.65
p_{T} (μ)	≥ 5 GeV/c	1	1
$\lvert\eta(\mu)\rvert$	< 2.4	1	1
p_{T} (K,π)	≥ 0.7 GeV/c	0.83	0.32
$\lvert\eta(K,\pi)\rvert$	< 2.4	0.97	0.97
$\Delta R(\mu K, \mu\pi)$	< 1.5	0.98	0.46
μD^0 mass	< 5 GeV/c^2	0.99	0.29
Vertex prob.	> 0.01		
ALL quality cuts		0.70	0.04

7.3.2 Selection Cut Variables

In order to avoid the trigger turn-on region, the cut on the muon p_{T} is raised 1 GeV/c above the trigger p_{T} value (6 GeV/c for the HLT_Mu5-triggered data, and 16 GeV/c for the HLT_Mu15_v1-triggered data). Additional cuts are added at the analysis level including event cuts, D^0 candidate cuts, and b-hadron candidate cuts. We consider using the following variables, which are described in the following sections, for the event selection after the quality cuts have been made:

1. D^0 doca
2. B doca
3. D^0 3D flight distance
4. B 3D flight distance
5. muon signed transverse impact parameter
6. x_b
7. D^0 pointing angle

8. B pointing angle

D^0 and B doca From the KinematicVertexParticleFitter, the distance of closest approach (doca) for each of the D^0 and b-hadron candidates can be found. The doca is defined to be the distance between two tracks at their point of closest approach. Figure 79 shows how the doca is defined for the D^0 vertex. Figure 80 shows the signal and data distributions of the doca for the D^0 and b-hadron candidates.

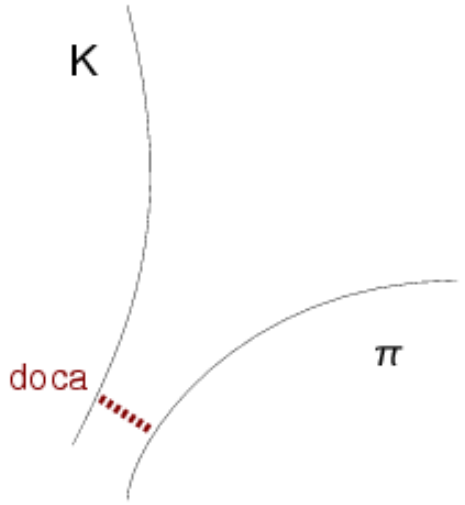

Figure 79: Definition of the distance of closest approach (doca).

D^0 and B 3D Flight Distance Significance The 3D flight distance significance can also be found for each of the D^0 and b-hadron candidates from the KinematicVertexParticleFitter. Figure 81 shows the distribution of the 3D flight distance for the D^0 and b-hadron candidates.

Muon Signed Transverse Impact Parameter The muon signed transverse impact parameter can be determined as the distance of closest approach of the muon track to the primary vertex, with the sign determined by the angle between a line connecting

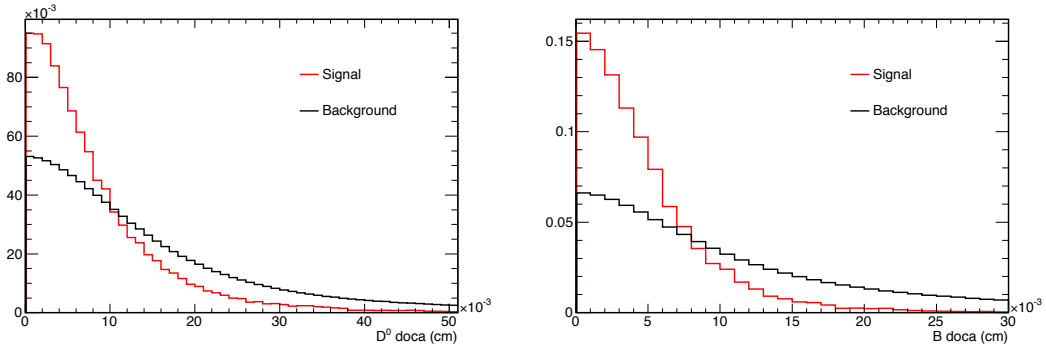

Figure 80: Distributions of the D^0 (left) and b-hadron (right) candidate doca (right) after all other selection cuts for tagged signal (red) and background (black) Monte Carlo events. The distributions are normalized to unit area.

the primary vertex with the point of closest approach and a reference direction, which is the direction of the D^0 candidate. This is shown in Figure 82. The signed muon transverse impact distributions found for signal and data are shown in Figure 83. As one can see, the distribution is symmetric for the background case, and is asymmetric in the case of the signal. This indicates that the muon came from a long-lived particle, which is more likely to have a positive signed impact parameter.

x_b **Variable** We make a requirement on the isolation of the μD^0 candidate using the variable x_b, which is the p_{T} of the b-hadron candidate divided by the sum of the p_{T} of all other tracks (with $p_{\mathrm{T}} > 0.5$ GeV/c) within a cone of ΔR less than 1 around the b-hadron candidate. Mathematically this is defined as

$$x_b = \frac{p_{\mathrm{T}}(\mu D^0)}{\sum_{\Delta R(\mu D^0, X)<1} p_{\mathrm{T}}(X)} \tag{12}$$

Signal candidates will tend to have larger values in this variable as can be seen by the distributions shown in Figure 84.

Since the x_b variable is a measure of the isolation of the B candidate, it depends on the fragmentation and on the underlying event. In addition, since the B is not fully reconstructed, this variable is blurred. The distributions of the x_b variable in data and

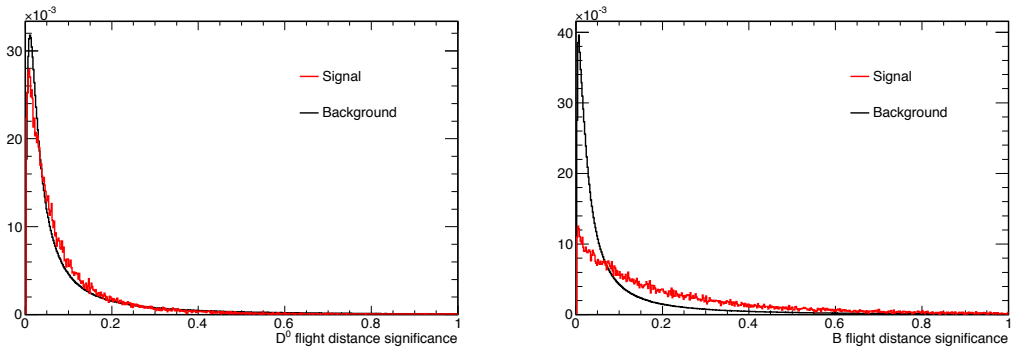

Figure 81: Distribution of 3D flight distance significance for the D^0 (left) and b-hadron (right) candidates after the acceptance cuts for tagged signal Monte Carlo events (red) and tagged background MC events (black). The distributions are normalized to unit area.

Monte Carlo events are shown in Figure 85. The distributions are similar but do not agree.

D^0 and B Pointing Angle We define the pointing angle as the angle between the flight direction and the momentum of the particle, as shown in Figure 86. If the decay could be completely reconstructed, this angle should be zero. The distributions of the pointing angle for both the D^0 and b-hadron candidates are shown in Figure 87. The signal distribution has a peak at zero, while in the background distribution there is a peak at zero and also at $\simeq \pi$.

7.3.3 Cut Optimization

The pointing angle must be considered together with the flight distance of the particle concerned: as the flight distance goes to zero, the pointing angle becomes a random number. Since the pointing angle and flight distance must be considered together, we first make the cuts on these variables. The 3D flight distances of the B and D^0 candidates are required to be greater than 0.01 cm to eliminate the cases where the pointing angle is meaningless.

To choose which of the remaining variables are useful and what the best cut value

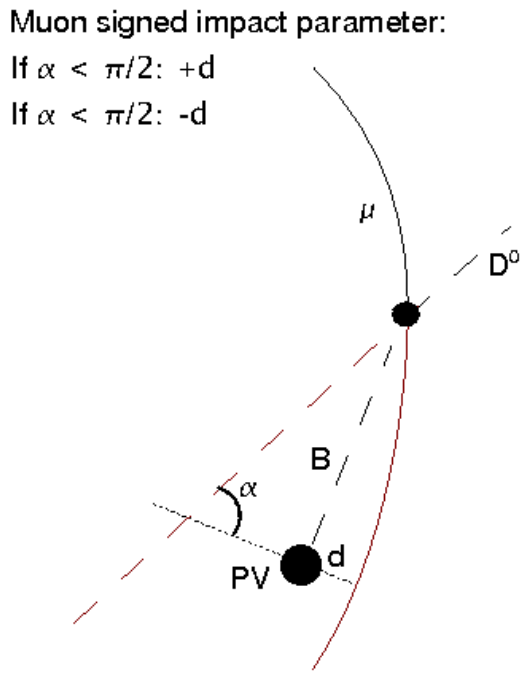

Figure 82: Definition of the muon signed transverse impact parameter.

is we optimize the significance of each variable. The significance is defined as $S/\sqrt{B}$, where S is the number of tagged signal Monte Carlo events passing the cut, and B is the number of background Monte Carlo events passing the cut. The direction of the cut is based on looking at the distributions of the signal and background Monte Carlo events for each variable, and choosing it such that more signal than background events pass the cut. Specifically, for the μ signed transverse impact parameter, D^0 and B flight distance significance, and x_b, the event is defined as passing the cut if the value is greater than the cut value. For the D^0 and B doca and pointing angle, the event is defined as passing the cut if the value is less than the cut value.

A subset of the Monte Carlo events is used for the cut tuning. We start with a subset of 1M candidates after the quality cuts, with 1439 of those being true signal. After the cuts on the distance and pointing angle variables, there were 324028 total candidates (1105 signal candidates and 322923 background candidates).

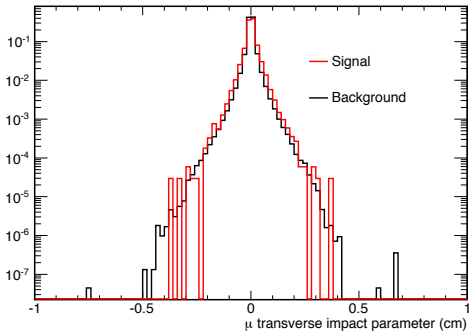

Figure 83: Distribution of muon signed impact parameter shown after the acceptance cuts for tagged signal Monte Carlo events (red) and tagged background MC events (black). The distributions are normalized to unit area.

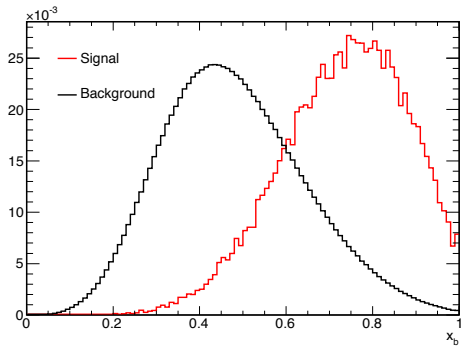

Figure 84: Distributions of x_b after all acceptance cuts for tagged signal Monte Carlo events (red) and background MC events (black). The distributions are normalized to unit area.

We use a sequential procedure to tune the cuts. For the first pass, we look at the significance distribution for each of the variables under consideration. We choose the variable with the highest significance as the first variable to use as a selection cut. The value is determined by finding the maximum of the significance distribution. The distributions for the first pass are shown in Figure 88.

From these distributions we determine that the x_b variable has the best significance after the acceptance cuts, and the significance is maximum at a cut value of 0.7. For the second pass, we require $x_b > 0.7$ and repeat the procedure for all other variables.

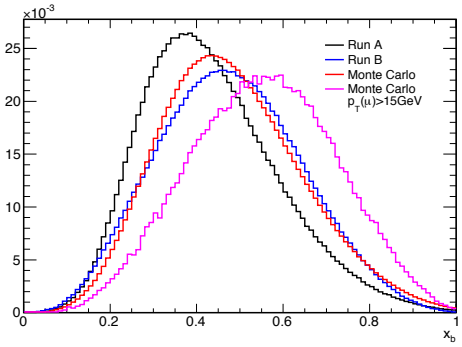

Figure 85: Distributions of x_b for Monte Carlo events (red), Monte Carlo events with $p_{\mathrm{T}}(\mu) > 15$ GeV/c (purple), Run A data events (black), and Run B data events (blue). The distributions are normalized to unit area.

The distributions for the second pass are shown in Figure 89.

After the second pass we determine that the B doca shows the best significance. The maximum is at a cut value of 0.007. For the third pass, we repeat the procedure, requiring that both $x_b > 0.7$ and the B doca < 0.007. The distributions for the remaining variables after the third pass are shown in Figure 90.

The D^0 doca shows the best discrimination between signal and background after the third pass. The significance is at its maximum at a cut value of 0.015. For the fourth pass, we require $x_b > 0.7$, the B doca < 0.007, and the D^0 doca < 0.015. The distribution for the muon transverse impact parameter after the fourth is shown in Figure 91.

The muon transverse impact parameter does not give any significant discrimination between signal and background except in the right tail of the distribution. This would severely reduce the statistics, and so it does not make sense to use a cut on this variable. Finally, for the event selection we require:

1. x_b greater than 0.7
2. B doca less than 0.007
3. D^0 doca less than 0.015

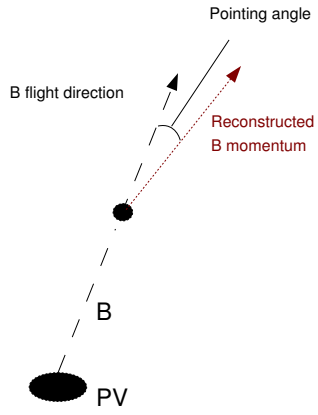

Figure 86: Diagram of the pointing angle.

The cut optimization procedure was repeated, choosing a different variable for the first cut, to show that the order of variables does not bias the final results. The results of this are shown in Appendix E.

Due to the difference in the x_b variable distributions between Monte Carlo simulations and data, a less stringent cut on this variable is used in the final analysis. Since the order of choosing the cut values does not matter, the adjustment of this cut value does not affect the cuts on the other variables. The final cut value on the x_b variable is 0.6.

The cut flow and efficiency are shown in Table 5 for the HLT_Mu5-triggered data, and in Table 6 for the HLT_Mu15_v1-triggered data.

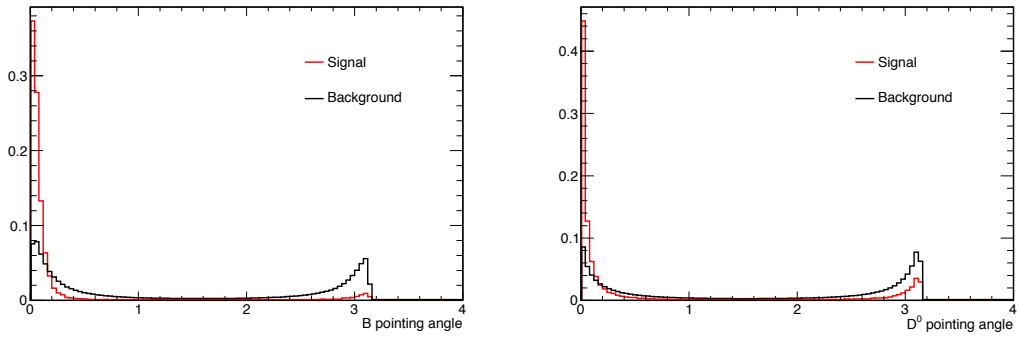

Figure 87: Distributions of the b-hadron (left) and D^0 (right) candidate pointing angle after the acceptance cuts for tagged signal (red) and background (black) Monte Carlo events. The distributions are normalized to unit area.

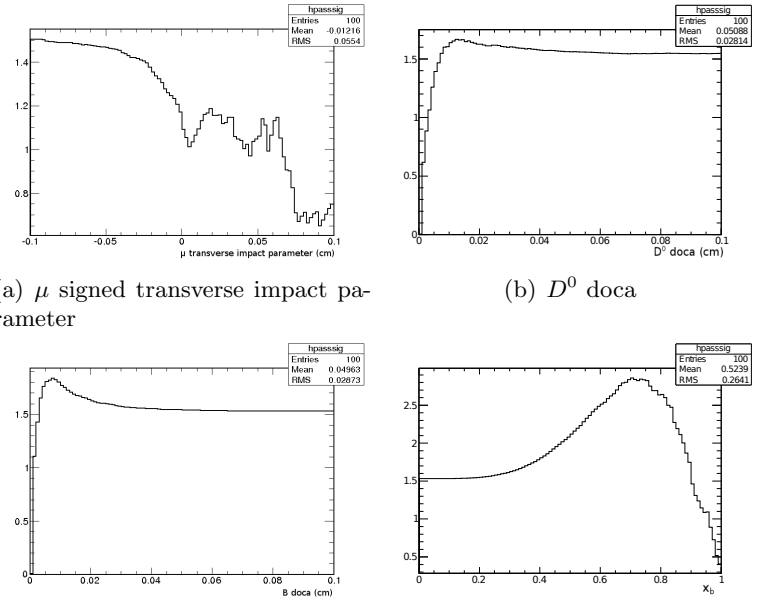

(a) μ signed transverse impact parameter

(b) D^0 doca

(c) B doca

(d) x_b

Figure 88: Distributions of $S/\sqrt{B}$ after the quality cuts.

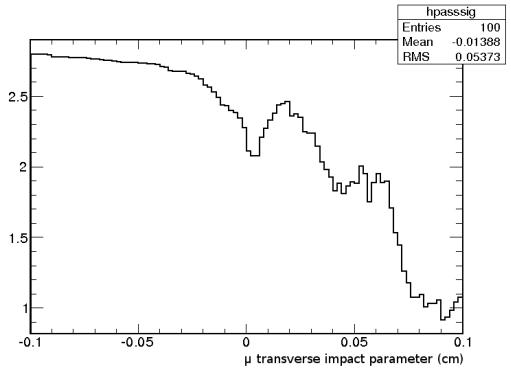

(a) μ signed transverse impact parameter

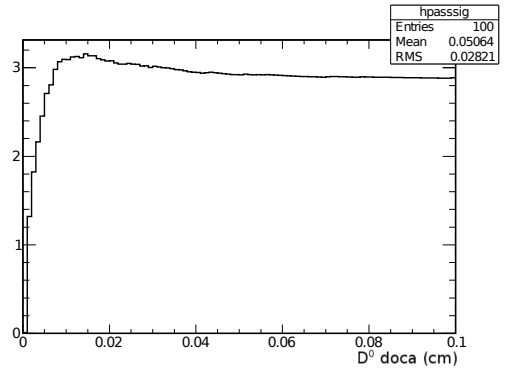

(b) D^0 doca

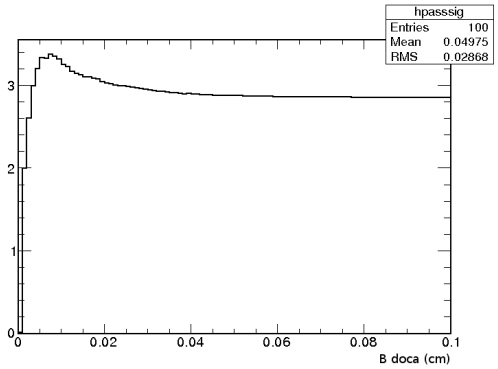

(c) B doca

Figure 89: Distributions of $S/\sqrt{B}$ after the quality cuts, and $x_b > 0.7$.

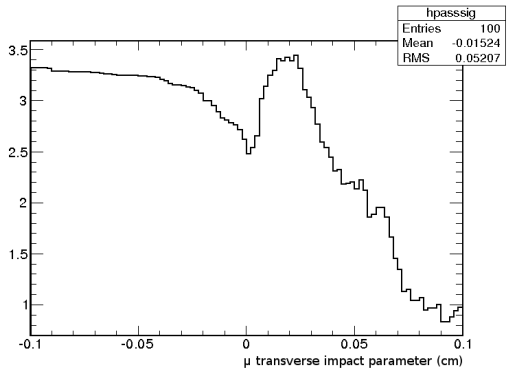

(a) μ signed transverse impact parameter

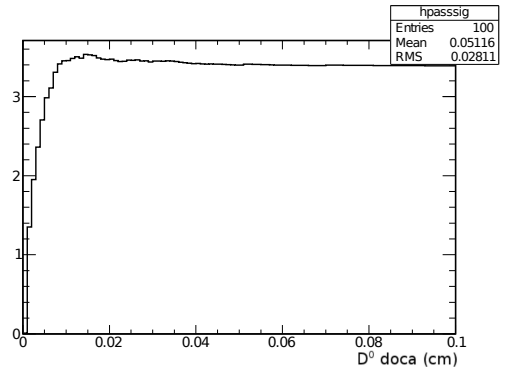

(b) D^0 doca

Figure 90: Distributions of $S/\sqrt{B}$ after the acceptance cuts, $x_b > 0.7$, and B doca < 0.007.

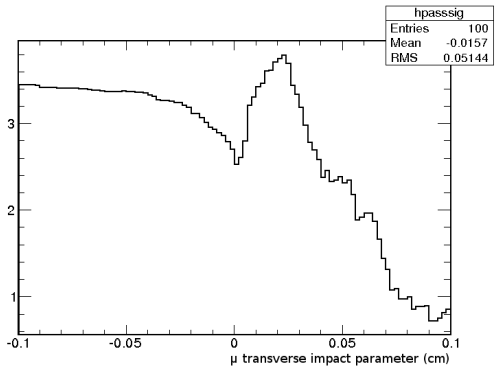

(a) μ signed transverse impact parameter

Figure 91: Distribution of $S/\sqrt{B}$ for the muon transverse impact parameter after the acceptance cuts, $x_b > 0.7$, B doca < 0.007, and D^0 doca < 0.015.

Table 5: Selection cut efficiencies in bins of $p_{\rm T}(\mu D^0)$ using Monte Carlo events with $p_{\rm T}(\mu) > 5$ GeV and $|\eta(\mu)| < 2.4$.

Bin	Total	Passing	Eff
$6 \le p_{\rm T} < 11$	13413	1269	0.095 ± 0.003
$11 \le p_{\rm T} < 16$	12851	4008	0.312 ± 0.005
$16 \le p_{\rm T} < 20$	4227	1994	0.47 ± 0.01
$20 \le p_{\rm T} < 30$	3145	1771	0.56 ± 0.01
$30 \le p_{\rm T} < 50$	768	511	0.67 ± 0.03
$50 \le p_{\rm T} < 80$	79	57	0.72 ± 0.10
$0 \le \|\eta\| < 0.9$	17333	4684	0.270 ± 0.004
$0.9 \le \|\eta\| < 1.5$	9569	2673	0.279 ± 0.005
$1.5 \le \|\eta\| < 2.1$	6701	1982	0.296 ± 0.007
$2.1 \le \|\eta\| < 2.4$	894	279	0.31 ± 0.02

Table 6: Selection cut efficiencies in bins of $p_{\mathrm{T}}(\mu D^0)$ using Monte Carlo events with $p_{\mathrm{T}}(\mu) > 15$ GeV and $|\eta(\mu)| < 2.4$.

Bin	Total	Passing	Eff
$16 \leq p_{\mathrm{T}} < 20$	35	0	0
$20 \leq p_{\mathrm{T}} < 30$	646	231	0.36 ± 0.02
$30 \leq p_{\mathrm{T}} < 50$	442	262	0.59 ± 0.04
$50 \leq p_{\mathrm{T}} < 80$	58	39	0.67 ± 0.11
$0 \leq \|\eta\| < 0.9$	637	275	0.43 ± 0.03
$0.9 \leq \|\eta\| < 1.5$	281	129	0.46 ± 0.04
$1.5 \leq \|\eta\| < 2.1$	229	113	0.49 ± 0.05
$2.1 \leq \|\eta\| < 2.4$	42	23	0.55 ± 0.11

7.4 Efficiencies

The efficiency can be broken into three parts: the tracking and reconstruction efficiency (ϵ_{rec}), the trigger efficiency (ϵ_{trig}), and the cut efficiency (ϵ_{cut}). The formula is given in Equation 13. Each of these parts is described separately in the following sections. The efficiency is calculated in bins of the p_{T} and η of the μD^0.

$$\epsilon = \epsilon_{rec} \cdot \epsilon_{cut} \cdot \epsilon_{trig} \tag{13}$$

The tracking and reconstruction efficiency and the cut efficiency can be found using Monte Carlo. One method is to apply the full analysis procedure to the Monte Carlo and fit the Kπ invariant mass distributions to find the number of μD^0 candidates. The fits are shown in Figures 92 and 93, and Figures 94 and 95 for bins of p_{T} (μ) and $|\eta(\mu)|$, respectively.

The distributions are fit with a double Gaussian function plus a linear background, shown in Equation 14. The Gaussians are required to have the same center, described by parameter p_2. Parameters p_0 and p_1 describe the linear background, parameters p_3 and p_4 describe the amplitudes of the Gaussians, and parameters p_5 and p_6 describe the widths of the Gaussians. The fits are done using binned likelihood fits, in order to sensibly model the background in low statistics bins. The minimization is done with the MINUIT package [84] in ROOT [85]. For variables with a Gaussian distribution, the likelihood is related to the χ^2, as shown in Equation 15. The likelihood fits provide a χ^2 value which can be used as an approximate goodness-of-fit estimate.

$$y = p_0 + p_1 \cdot x + p_3 e^{\frac{-1}{2}\left(\frac{x-p_2}{p_5}\right)^2} + p_4 e^{\frac{-1}{2}\left(\frac{x-p_2}{p_6}\right)^2} \tag{14}$$

$$\chi^2 \propto -2 \ln L \tag{15}$$

The number of D^0 candidates can be calculated from the fit parameters according

to Equation 16, where p_3 and p_4 are the amplitudes of the double Gaussian, p_5 and p_6 are the standard deviations of the double Gaussian, and Δm is the bin size of the $K\pi$ invariant mass distribution.

$$N(D^0) = \frac{\sqrt{2\pi}}{\Delta m}\left(p_3 p_5 + p_4 p_6\right) \tag{16}$$

The efficiency is defined as the number of D^0 candidates from the fit divided by the number of signal events generated in the acceptance. The efficiency for the tracking, reconstruction, and event selection is shown in Figures 96 and 97.

Due to the low statistics, the efficiencies have very large errors in some bins. This contributes a large systematic uncertainty to the final result. Another method to find the efficiencies is to use the tagged Monte Carlo. A potential problem with this method would be if there was a significant fraction of signal events which are not in the mass peak, or if there is a peak in the background in the peak region. In addition, the tagging in Monte Carlo is not 100% efficient. Sometimes the reconstructed tracks can not be matched to the generator level particles. In the event that these effects would be significant, it would be necessary to use the fit method. These are not expected to be significant effects, so the tagged Monte Carlo efficiencies are used in this analysis. For more details, and plots of the different backgrounds at each step of the selection procedure, separated into categories, see Appendix D.

The efficiency found from the tagged Monte Carlo compared with the efficiency found from the Monte Carlo fits is shown in Figure 98 as a function of p_{T} , and in Figure 99 as a function of $|\eta|$. The efficiencies are completely consistent with each other. Therefore the efficiencies from the tagged Monte Carlo are used, since they contribute much less to the systematic uncertainty. The total reconstruction and selection efficiencies are shown in Table 7.

Table 7: The reconstruction and selection efficiency ($\epsilon_{rec} \cdot \epsilon_{cut}$) in each p_{T} (μD^0) and $|\eta(\mu D^0)|$ bin. The Eff5 column is using Monte Carlo events with p_{T} (μ) > 5 GeV, and the Eff15 column is using Monte Carlo events with p_{T} (μ) > 15 GeV. In both cases $|\eta(\mu)| < 2.4$ is required.

Bin	Eff5	Eff15
$6 \leq p_{\mathrm{T}} < 11$	0.042 ± 0.001	–
$11 \leq p_{\mathrm{T}} < 16$	0.21 ± 0.003	–
$16 \leq p_{\mathrm{T}} < 20$	0.35 ± 0.008	–
$20 \leq p_{\mathrm{T}} < 30$	0.43 ± 0.01	0.27 ± 0.02
$30 \leq p_{\mathrm{T}} < 50$	0.51 ± 0.02	0.47 ± 0.03
$50 \leq p_{\mathrm{T}} < 80$	0.48 ± 0.06	0.44 ± 0.07
$0 \leq \|\eta\| < 0.9$	0.17 ± 0.002	0.33 ± 0.02
$0.9 \leq \|\eta\| < 1.5$	0.16 ± 0.003	0.30 ± 0.03
$1.5 \leq \|\eta\| < 2.1$	0.14 ± 0.003	0.32 ± 0.03
$2.1 \leq \|\eta\| < 2.4$	0.07 ± 0.004	0.21 ± 0.04

7.4.1 Trigger Efficiency

The muon trigger which is used to select the data is not 100% efficient, so in order to determine how many events were produced, the observed events must be corrected for the trigger efficiency. Since it is a muon trigger, the trigger efficiency depends on the p_{T} and η of the muon. The Monte Carlo does not require a trigger to select the events, so no correction for the trigger efficiency is required.

The trigger efficiencies are calculated using independently triggered data sets: an electron-triggered data set for the HLT_Mu5 trigger, and a jet-triggered data set for the HLT_Mu15_v1 trigger. The data sets used are listed in Table 8. The method is described in detail in [86]. The efficiency is calculated by looking at muons which are reconstructed offline, and then matching them to the HLT muons. The muons are matched to the HLT muons by searching within a cone of $\Delta R < 0.5$. The muons are required to satisfy the `GlobalMuonPromptTight` criteria. In order to reduce the possibility of mismatching, the events are required to have only one reconstructed muon.

In order to further reduce background from pion and kaon decays, as well as from punch-through hadrons, the muons are chosen to come from semileptonic heavy flavor

Table 8: 2010 Data samples used for the trigger efficiency calculation.

Trigger	Data set
HLT_Mu5	`EG/Run2010A-Nov4ReReco_v1/AOD`
HLT_Mu15_v1	`/Jet/Run2010B-Dec22ReReco_v1/AOD`

decays by selecting muons in b-tagged jets. The trigger efficiencies for muons in b-tagged jets are generally lower than for isolated muons due to the density of tracks. As this analysis uses muons coming from semileptonic b decays, this method is particularly appropriate.

The efficiencies, in bins of p_{T} (μ) and $|\eta(\mu)|$, are shown in Figures 100 and 101 for the HLT_Mu5 trigger, and in Figures 102 and 103 for the HLT_Mu15_v1 trigger.

Since we ultimately want to measure the cross section as a function of the p_{T} and η of the μD^0 candidate, the trigger efficiency can not be simply multiplied with the other efficiencies. In addition, the two data sets use different triggers, so we must correct for the trigger efficiencies in order to compare results between the two data sets. We therefore apply a weighting of $\frac{1}{\epsilon_{trig}}$ to the data in the Kπ invariant mass distribution before fitting. The Monte Carlo does not need to be corrected for trigger efficiency. The effect of the trigger efficiency weighting can be seen in Figure 104.

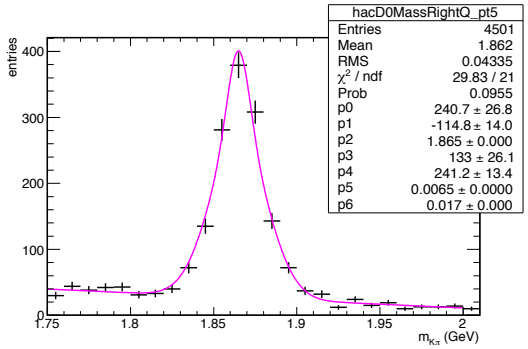

(a) $6 \leq p_{\mathrm{T}} < 11$

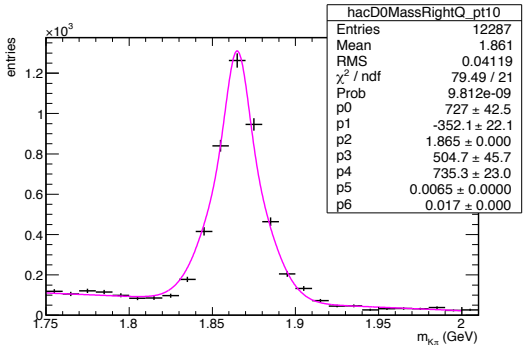

(b) $11 \leq p_{\mathrm{T}} < 16$

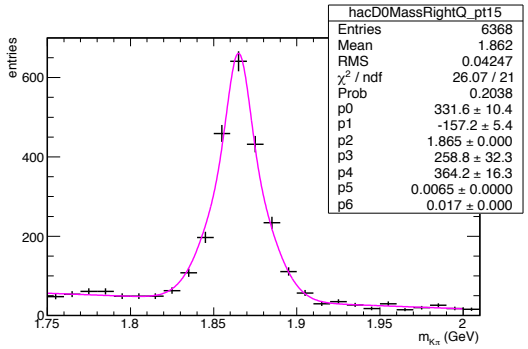

(c) $16 \leq p_{\mathrm{T}} < 20$

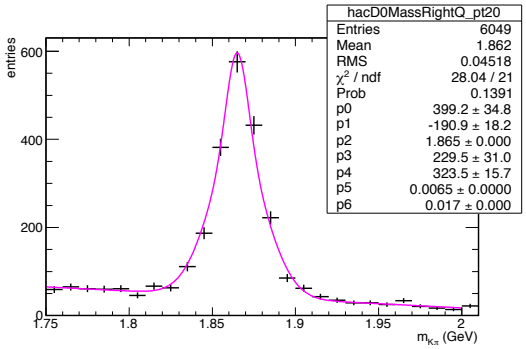

(d) $20 \leq p_{\mathrm{T}} < 30$

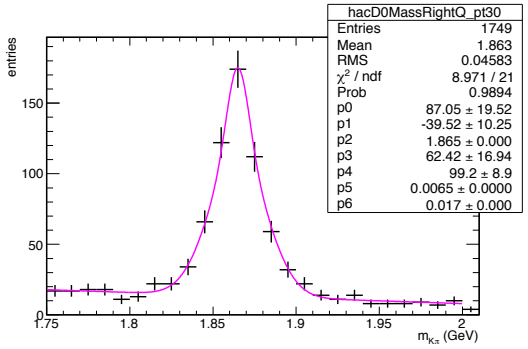

(e) $30 \leq p_{\mathrm{T}} < 50$

Figure 92: D^0 mass distributions in bins of p_{T} (μD^0) (GeV/c) for Monte Carlo events with $|\eta(\mu, K, \pi)| < 2.4$, $p_{\mathrm{T}}(\mu) > 6$ GeV/c, and $p_{\mathrm{T}}(K, \pi) > 0.5$ GeV/c. The distributions are fit with a linear background plus a double Gaussian signal.

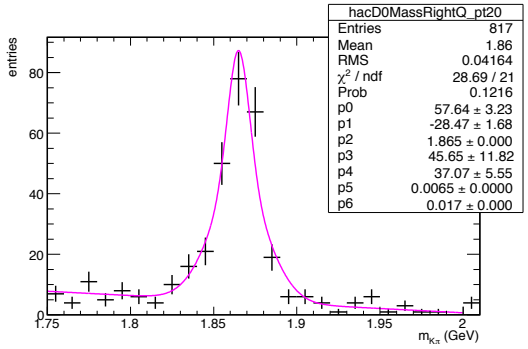

(a) $20 \leq p_{\mathrm{T}} < 30$

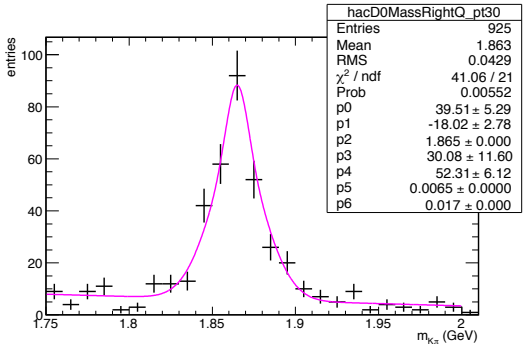

(b) $30 \leq p_{\mathrm{T}} < 50$

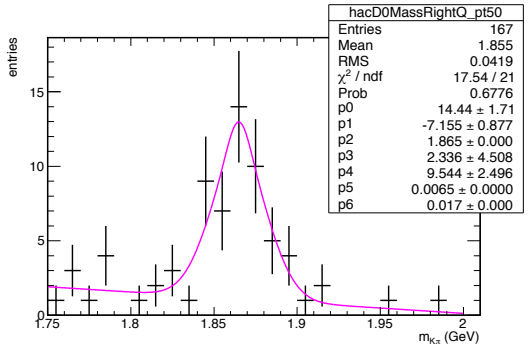

(c) $35 \leq p_{\mathrm{T}} < 80$

Figure 93: D^0 mass distributions in bins of p_{T} (μD^0) (GeV/c) for Monte Carlo events with p_{T} (μ) > 16 GeV/c, $p_{\mathrm{T}}(K, \pi) > 0.5$ GeV/c, and $|\eta(\mu, K, \pi)| < 2.4$. The distributions are fit with a linear background plus a double Gaussian signal.

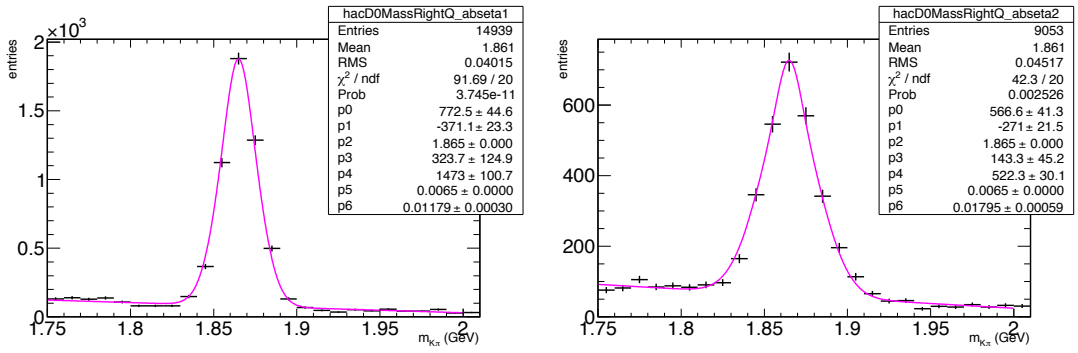

(a) $0 \leq |\eta| < 0.9$

(b) $0.9 \leq |\eta| < 1.5$

(c) $1.5 \leq |\eta| < 2.1$

(d) $2.1 \leq |\eta| < 2.4$

Figure 94: D^0 mass distributions in bins of $|\eta(\mu D^0)|$ for Monte Carlo events with $p_{\rm T}$ $(\mu) > 6$ GeV/c and $p_{\rm T}(K, \pi) > 0.5$ GeV/c. The distributions are fit with a linear background plus a double Gaussian signal.

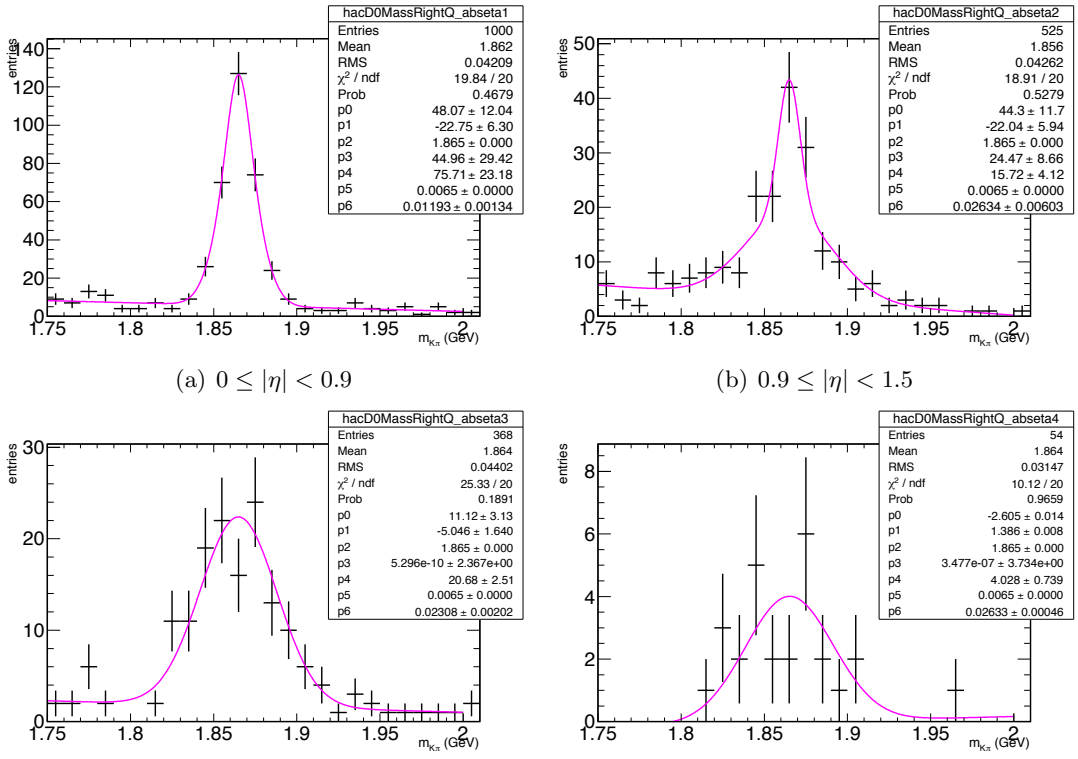

(a) $0 \leq |\eta| < 0.9$

(b) $0.9 \leq |\eta| < 1.5$

(c) $1.5 \leq |\eta| < 2.1$

(d) $2.1 \leq |\eta| < 2.4$

Figure 95: D^0 mass distributions in bins of $|\eta(\mu D^0)|$ for Monte Carlo events with p_{T} $(\mu) > 16$ GeV/c and $p_{\mathrm{T}}(K, \pi) > 0.5$ GeV/c. The distributions are fit with a linear background plus a double Gaussian signal.

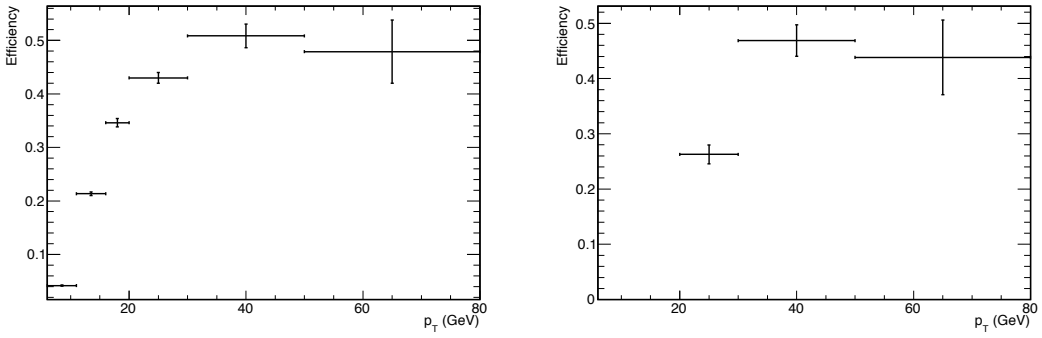

Figure 96: The tracking, reconstruction, and event selection efficiency ($\epsilon_{rec} \cdot \epsilon_{cut}$) for Run A (left) and Run B (right) as a function of p_{T} (μD^0) with $|\eta(\mu)| < 2.4$.

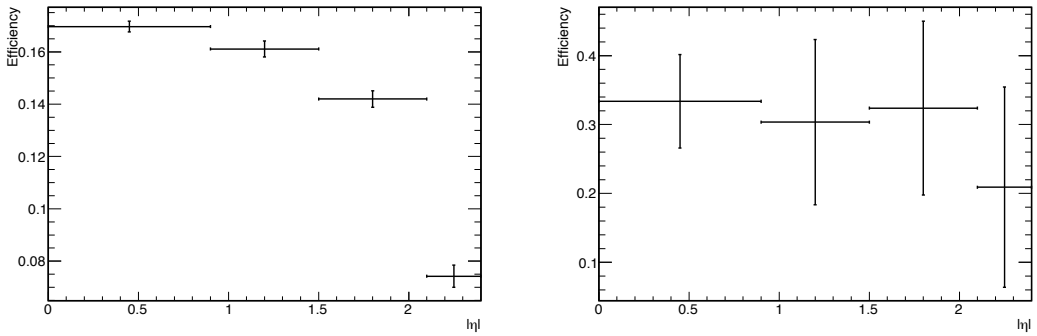

Figure 97: The tracking, reconstruction, and event selection efficiency ($\epsilon_{rec} \cdot \epsilon_{cut}$) for Run A (left) and Run B (right) as a function of $|\eta(\mu D^0)|$ with p_{T} $(\mu D^0) > 6$ GeV/c for Run A and p_{T} $(\mu D^0) > 16$ GeV/c for Run B.

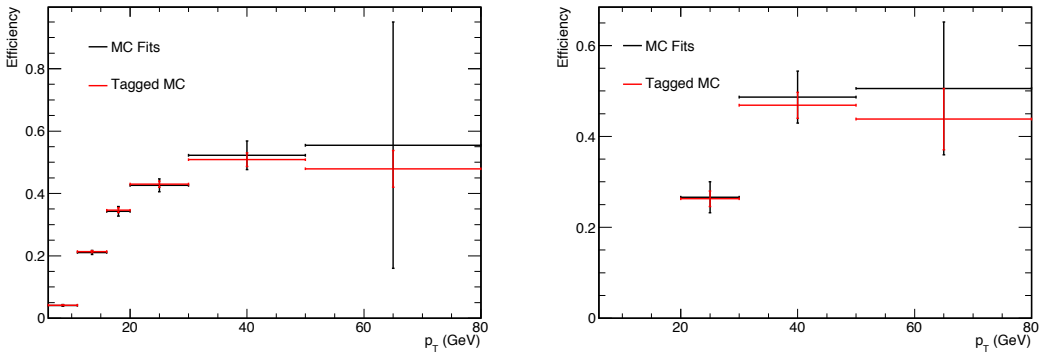

Figure 98: The tracking, reconstruction, and event selection efficiency ($\epsilon_{rec} \cdot \epsilon_{cut}$) for Run A (left) and Run B (right) as a function of p_{T} (μD^0) with $|\eta(\mu)| < 2.4$.

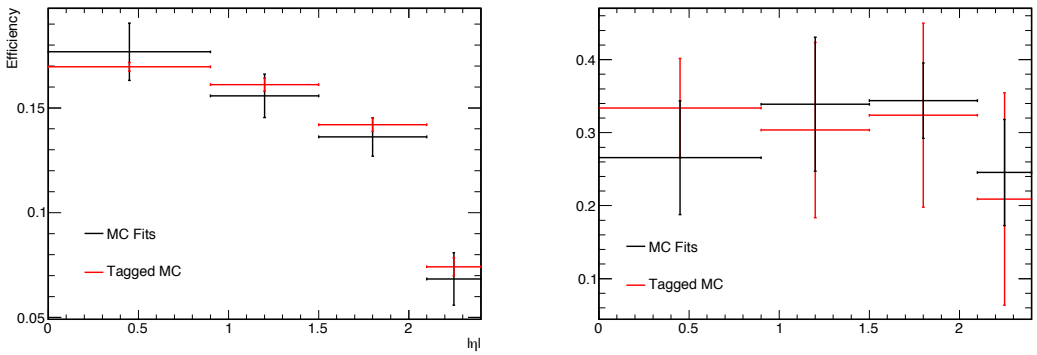

Figure 99: The tracking, reconstruction, and event selection efficiency ($\epsilon_{rec} \cdot \epsilon_{cut}$) for Run A (left) and Run B (right) as a function of $|\eta(\mu D^0)|$ with $p_{\rm T}$ (μ) > 6 GeV/c.

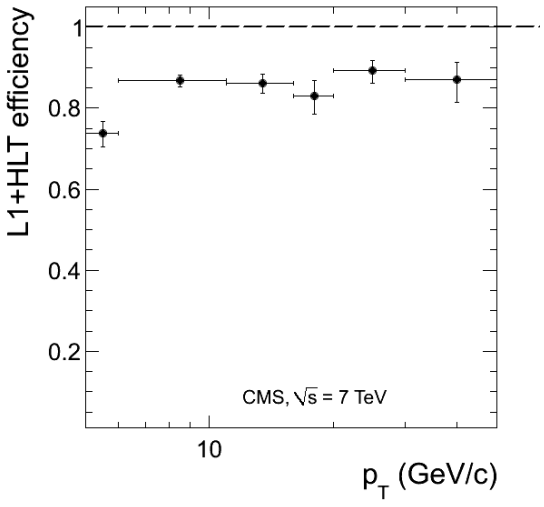

(a) $|\eta(\mu)| < 2.4$

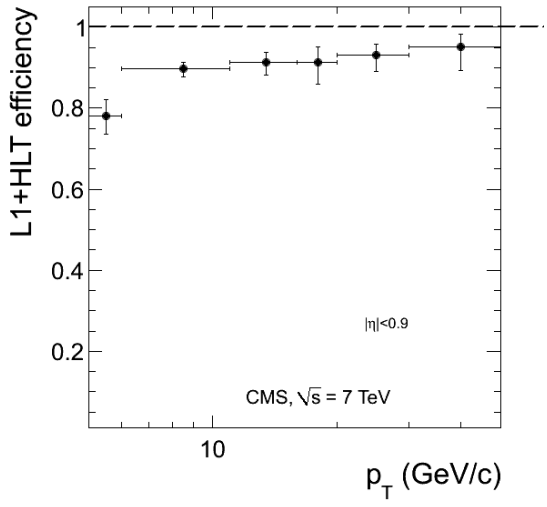

(b) $|\eta(\mu)| < 0.9$

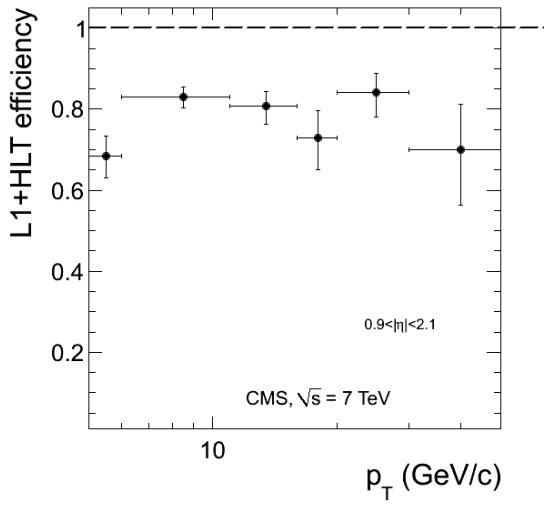

(c) $0.9 < |\eta(\mu)| < 2.1$

Figure 100: HLT_Mu5 trigger efficiency in bins of p_{T} (μ) (GeV/c)

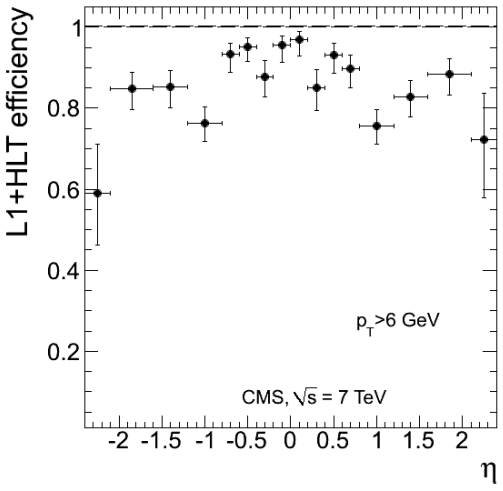

Figure 101: HLT_Mu5 trigger efficiency in bins of $|\eta(\mu)|$

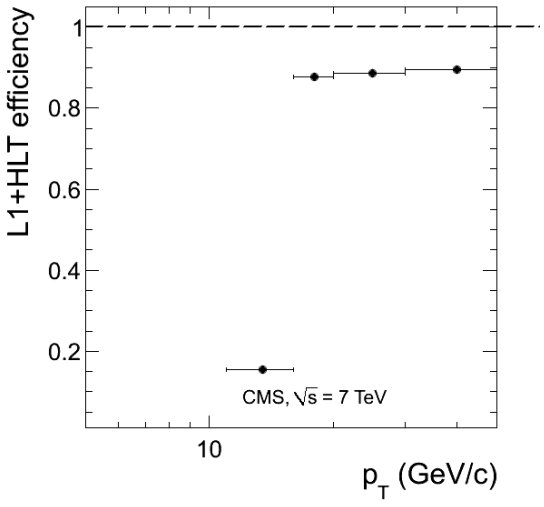

(a) $|\eta(\mu)| < 2.4$

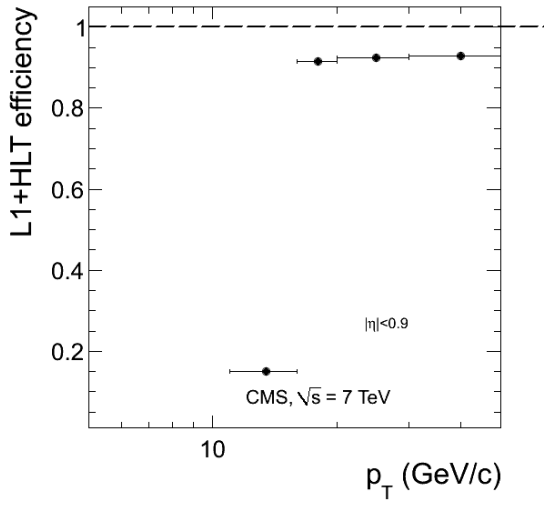

(b) $|\eta(\mu)| < 0.9$

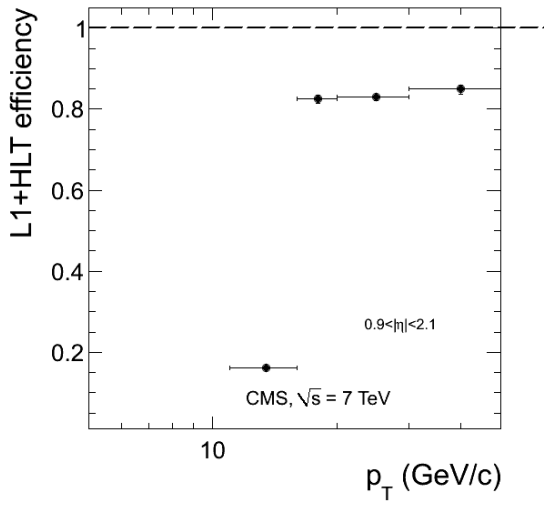

(c) $0.9 < |\eta(\mu)| < 2.1$

Figure 102: HLT_Mu15_v1 trigger efficiency in bins of p_{T} (μ) (GeV/c)

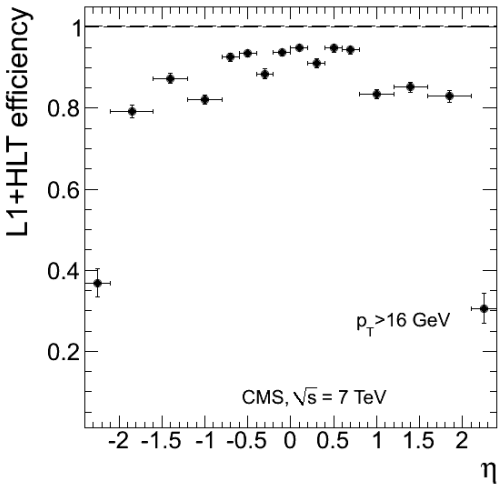

Figure 103: HLT_Mu15_v1 trigger efficiency in bins of $|\eta(\mu)|$

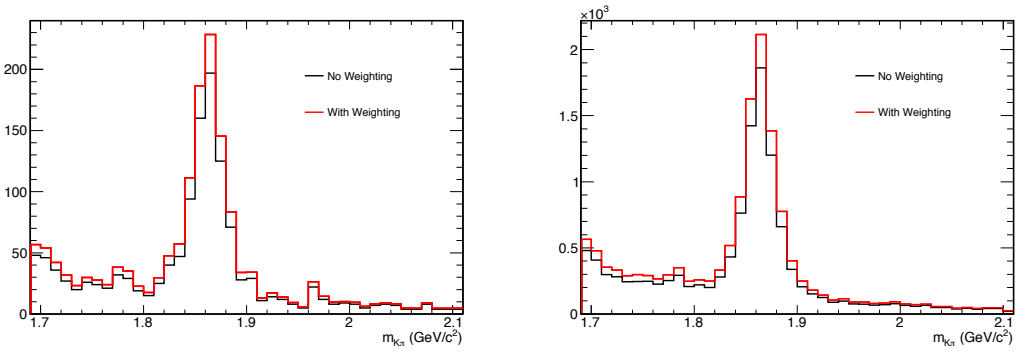

Figure 104: The Kπ invariant mass distribution before and after the trigger efficiency weighting for Run A (left) and Run B (right).

7.5 D^0 Mass Fits

Similarly to what was already described for the Monte Carlo, the number of μD^0 candidates in data is found by fitting the $K\pi$ invariant mass distribution. The distribution is fit with the double Gaussian function plus a linear background, shown in Equation 14, and the number of D^0 candidates is found from Equation 16. As before, binned likelihood fits are used, and the related χ^2 value is shown to have an idea of the goodness-of-fit. In the Run A dataset, the higher p_{T} bins, which overlap with the Run B dataset, have low statistics. In these bins the widths, peak position, and ratio of amplitudes are fixed to those from the equivalent bin in the Run B dataset.

Figure 105 shows the $D\pi$ invariant mass distribution in the data compared to the Monte Carlo, and shows that the means and the widths of the distributions agree between data and Monte Carlo. The fits are tuned on the Monte Carlo mass distributions in order to fix the Gaussian widths. The mass distributions for the data are fit, with the widths fixed to the values from the Monte Carlo fits. The distribution for p_{T} $(\mu) > 6$ GeV/c and $|\eta(\mu)| < 2.4$ with the correct charge correlation is shown in Figure 106 before applying the trigger efficiency weighting to the data, and in Figure 107 after the trigger efficiency weighting of the data.

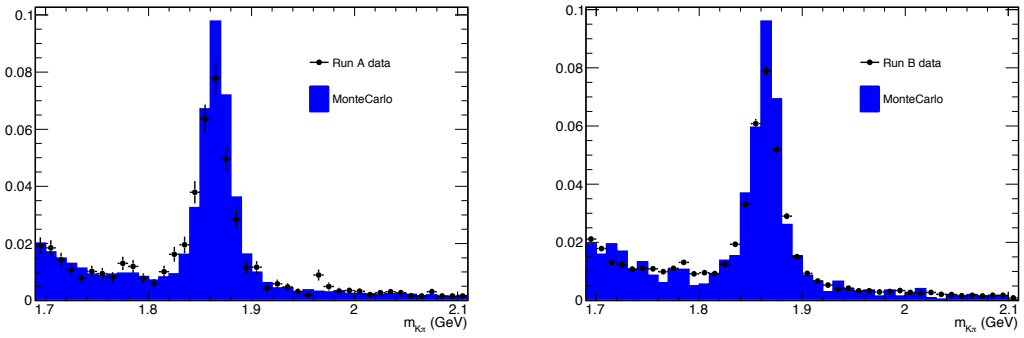

Figure 105: $K\pi$ invariant mass distribution for $p_{\mathrm{T}}(K,\pi) > 0.5$ GeV/c, and $|\eta(\mu,K,\pi)| < 2.4$, p_{T} $(\mu) > 6$ GeV/c for Run A and Monte Carlo (left), and with p_{T} $(\mu) > 16$ GeV/c for Run B and Monte Carlo (right). The data events are weighted by the trigger efficiency. The Monte Carlo is scaled to the luminosity of the data.

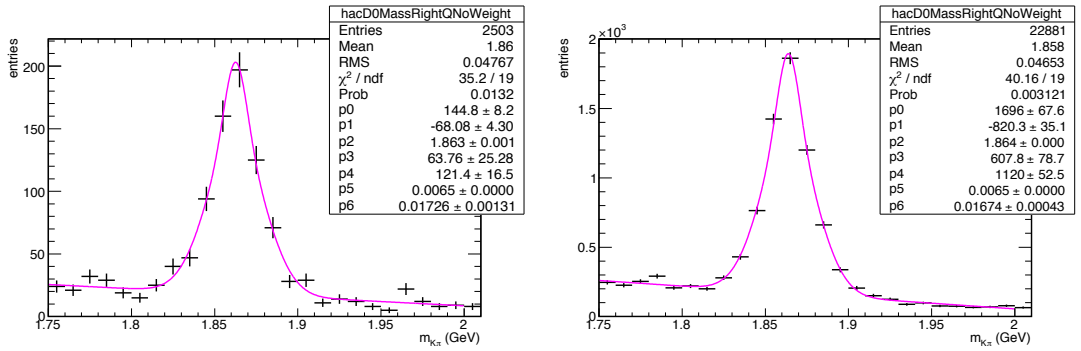

Figure 106: D^0 mass distribution for p_{T} $(\mu) > 6$ GeV/c for Run A (left), p_{T} $(\mu) > 16$ GeV/c for Run B (right), $p_{\mathrm{T}}(K, \pi) > 0.5$ GeV/c, and $|\eta(\mu, K, \pi)| < 2.4$, before weighting the data events by the trigger efficiency.

The trigger efficiency weighting corrects the data upward to find the number of D^0 candidates that were produced. Table 9 compares the number of D^0 candidates found by fitting the invariant mass distributions before and after the trigger efficiency weighting, as well as the ratio of the unweighted to weighted data. The ratio is used as a cross check that the trigger efficiency weighting is working correctly. The ratios are 0.85 ± 0.18 for Run A and 0.87 ± 0.07 for Run B, which are in agreement with the measured trigger efficiencies (see Figures 100 and 102). The Monte Carlo was produced with a trigger efficiency of 100%, so does not need to be weighted to correct for the trigger efficiency.

Table 9: The number of D^0 candidates in each dataset before and after the trigger efficiency weighting, as well as the ratio of unweighted to weighted data. All datasets have at least p_{T} $(\mu) > 6$ GeV/c, $p_{\mathrm{T}}(K, \pi) > 0.5$ GeV/c, and $|\eta(\mu, K, \pi)| < 2.4$. The uncertainty is the uncertainty from the fit.

Dataset	Before Weighting	After Weighting	Ratio
Run A	629 ± 77	738 ± 98	0.852 ± 0.009
Run B	5692 ± 280	6556 ± 288	0.868 ± 0.005

The distributions and fits for each p_{T} (μD^0) bin are shown in Figures 108 and 109, and for each $|\eta(\mu)|$ bin in Figures 110 and 111.

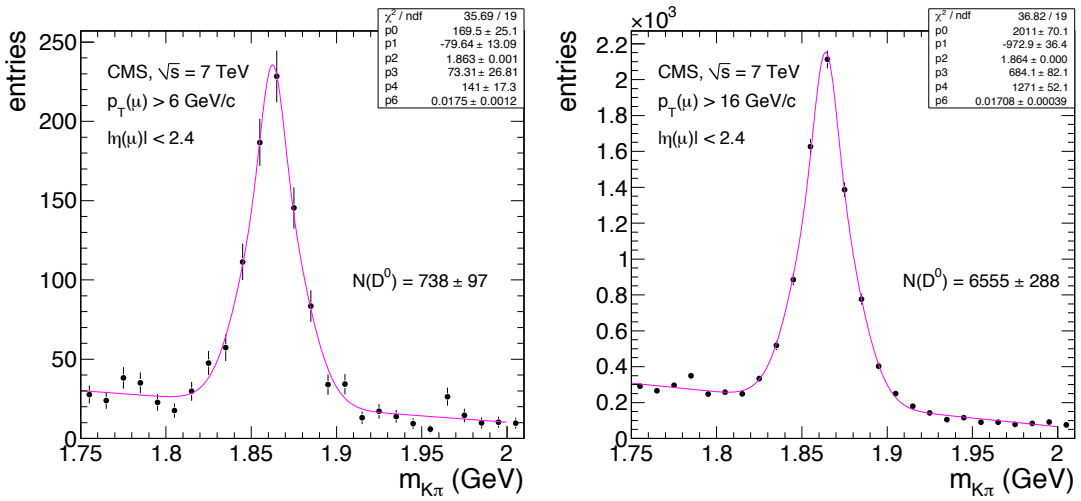

Figure 107: D^0 mass distribution for p_{T} $(\mu) > 6$ GeV/c for Run A (left), p_{T} $(\mu) > 16$ GeV/c for Run B (right), $p_{\mathrm{T}}(K, \pi) > 0.5$ GeV/c, and $|\eta(\mu, K, \pi)| < 2.4$, after weighting the data events by the trigger efficiency.

The number of D^0 candidates for data and Monte Carlo in each bin are listed in Table 10.

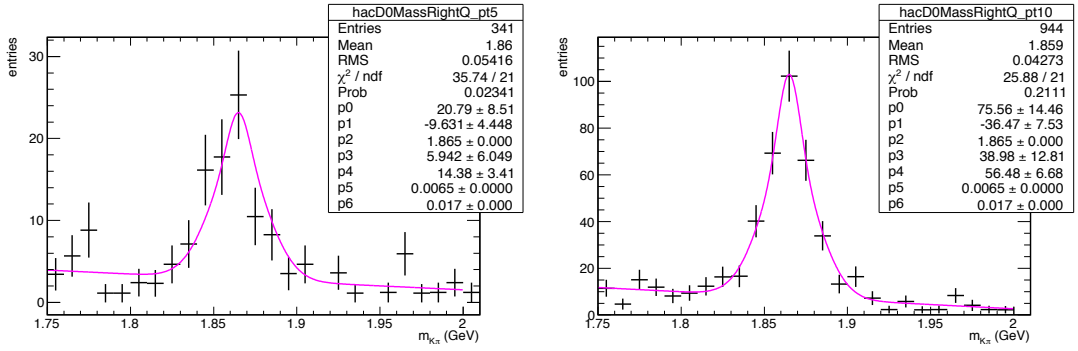

(a) $6 \leq p_{\mathrm{T}} < 11$

(b) $11 \leq p_{\mathrm{T}} < 16$

(c) $16 \leq p_{\mathrm{T}} < 20$

(d) $20 \leq p_{\mathrm{T}} < 30$

Figure 108: D^0 mass distributions in bins of p_{T} (GeV/c) for the 2010A dataset with p_{T} $(\mu) > 6$ GeV/c, $p_{\mathrm{T}}(K, \pi) > 0.5$ GeV/c and $|\eta(\mu, K, \pi)| < 2.4$, weighted by the trigger efficiency.

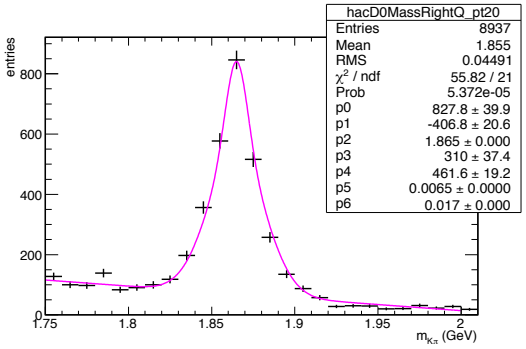

(a) $20 \leq p_{\mathrm{T}} < 30$

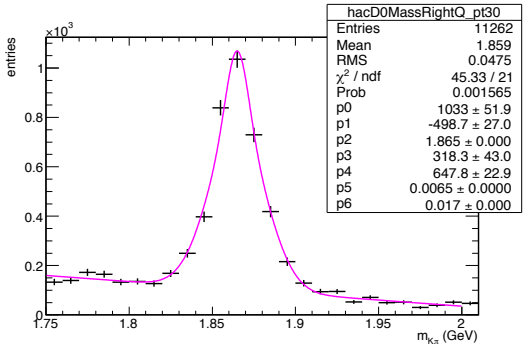

(b) $30 \leq p_{\mathrm{T}} < 50$

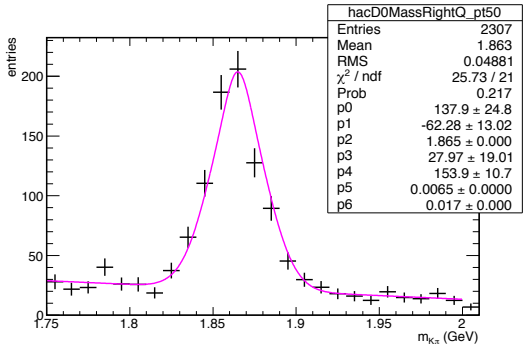

(c) $50 \leq p_{\mathrm{T}} < 80$

Figure 109: D^0 mass distributions in bins of p_{T} (GeV/c) for the 2010B dataset with p_{T} $(\mu) > 16$ GeV/c, $p_{\mathrm{T}}(K, \pi) > 0.5$ GeV/c and $|\eta(\mu, K, \pi)| < 2.4$, weighted by the trigger efficiency.

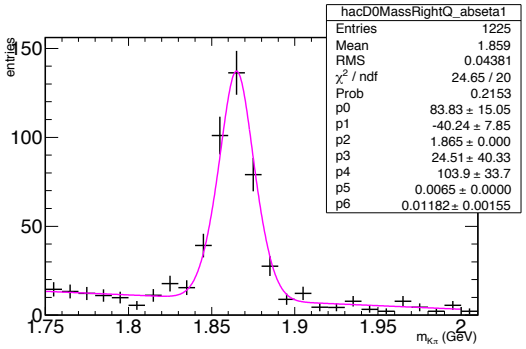

(a) $0 \leq |\eta| < 0.9$

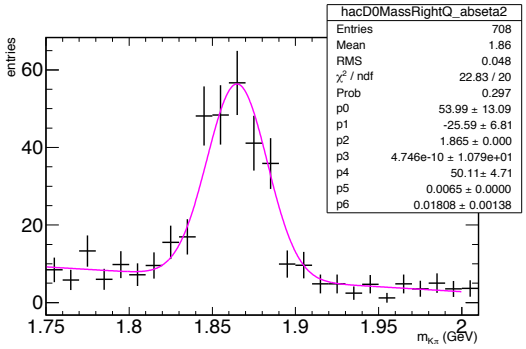

(b) $0.9 \leq |\eta| < 1.5$

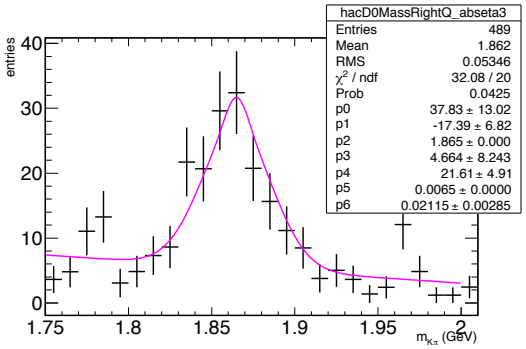

(c) $1.5 \leq |\eta| < 2.1$

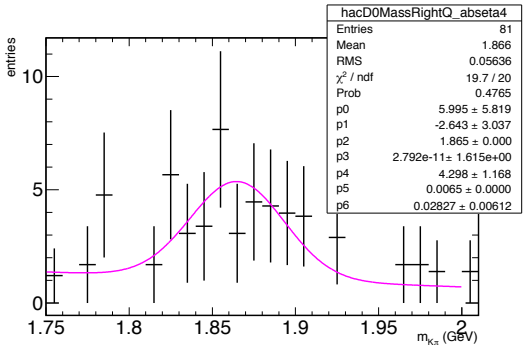

(d) $2.1 \leq |\eta| < 2.4$

Figure 110: D^0 mass distributions in bins of $|\eta|$ for the 2010A dataset with p_{T} $(\mu) > 6$ GeV/c and $p_{\mathrm{T}}(K, \pi) > 0.5$ GeV/c, weighted by the trigger efficiency.

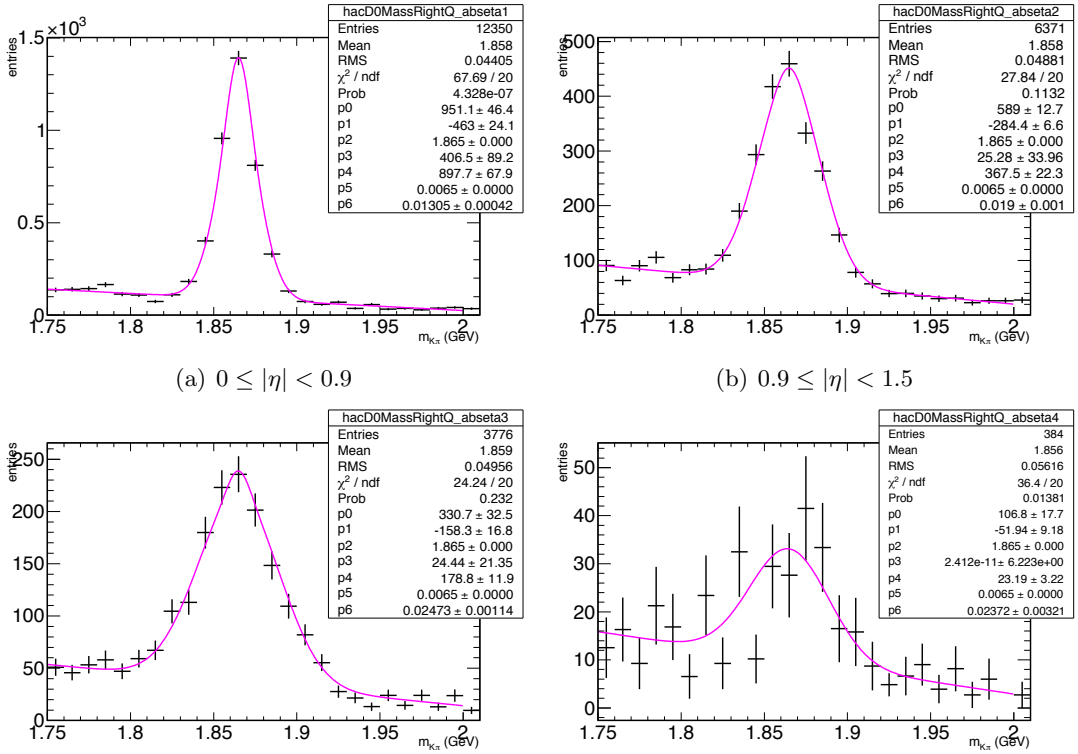

(a) $0 \leq |\eta| < 0.9$

(b) $0.9 \leq |\eta| < 1.5$

(c) $1.5 \leq |\eta| < 2.1$

(d) $2.1 \leq |\eta| < 2.4$

Figure 111: D^0 mass distributions in bins of $|\eta|$ for the 2010B dataset with p_{T} (μ) > 16 GeV/c and $p_{\mathrm{T}}(K, \pi) > 0.5$ GeV/c, weighted by the trigger efficiency.

Table 10: The number of D^0 candidates in each bin. For the 2010A and 2010B columns, the numbers are the results from the invariant mass fits in Run A and Run B data, respectively. For the MC columns they are the number of tagged signal events in the Monte Carlo. All columns have at least p_{T} $(\mu) > 6$ GeV and $|\eta(\mu)| < 2.4$. The uncertainty is the uncertainty from the fit.

Bin	2010A	2010B	MC $p_T(\mu) > 6$ GeV	MC $p_T(\mu) > 16$ GeV
$6 \leq p_{\mathrm{T}} < 11$	71 ± 17	–	1245 ± 71	–
$11 \leq p_{\mathrm{T}} < 16$	305 ± 35	–	3955 ± 122	–
$16 \leq p_{\mathrm{T}} < 20$	164 ± 37	0 ± 0	1974 ± 87	0 ± 0
$20 \leq p_{\mathrm{T}} < 30$	127 ± 24	2480 ± 101	1755 ± 84	234 ± 30
$30 \leq p_{\mathrm{T}} < 50$	8 ± 0	3281 ± 120	525 ± 46	272 ± 32
$50 \leq p_{\mathrm{T}} < 80$	–	702 ± 55	66 ± 47	45 ± 13
$0 \leq \|\eta\| < 0.9$	348 ± 126	3599 ± 282	4880 ± 377	300 ± 88
$0.9 \leq \|\eta\| < 1.5$	227 ± 33	1792 ± 135	2584 ± 172	144 ± 39
$1.5 \leq \|\eta\| < 2.1$	122 ± 33	1148 ± 96	1901 ± 128	120 ± 18
$2.1 \leq \|\eta\| < 2.4$	30 ± 11	138 ± 29	257 ± 47	27 ± 8

7.5.1 Wrong Charge Correlation Distributions

Requiring the muon and the kaon to have the same charge ensures that the muon and D^0 come from the same b-hadron. Events with the wrong charge correlation can come from a variety of sources, including events with a real muon and a real D^0 coming from different b-hadrons. In order to check whether signal is missed by making the charge correlation, the distributions for candidates with the wrong charge correlation, which is when the muon and the kaon have opposite charges, are fit one time assuming there is signal present, and one time assuming there is only background. For the fits including signal, a single Gaussian is used, and the mean and width of the signal peak are fixed to the values from the fits of the right charge correlation distributions. The fits with signal present are shown in Figure 112 for the whole p_{T} and η range, and the fits with only background are shown in Figure 113. The background-only fits have a good χ^2 value, and are consistent with having no signal in the wrong charge correlation candidates.

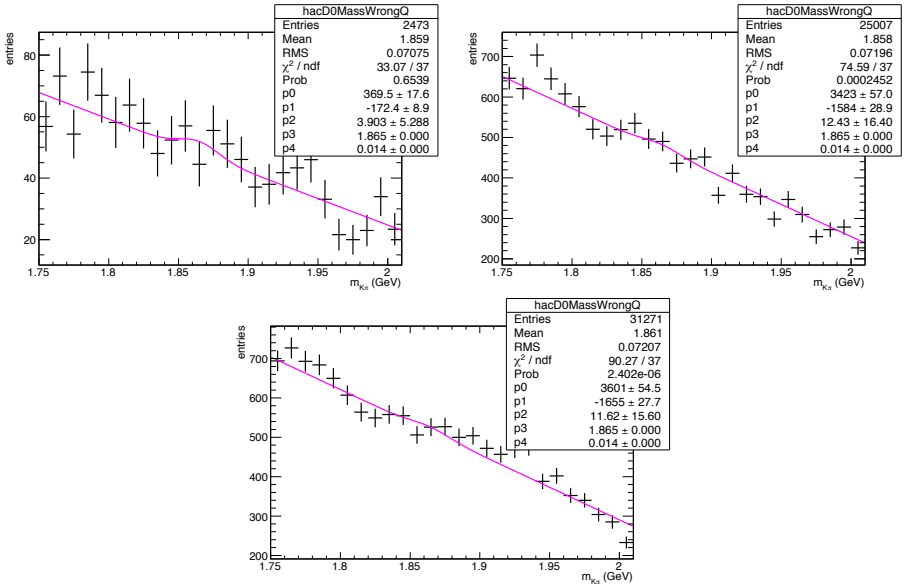

Figure 112: D^0 mass distribution of the wrong charge correlation candidates for p_{T} (μ) > 6 GeV/c, $p_{\mathrm{T}}(K,\pi) > 0.5$ GeV/c, and $|\eta(\mu,K,\pi)| < 2.4$ for the 2010A data (top left), 2010B data (top right), and Monte Carlo events (bottom). Fits assume a Gaussian signal plus a linear background.

Table 11 shows the number of D^0 candidates for each dataset from fits assuming a signal in the wrong charge correlation. They are all consistent with having zero D^0 candidates.

Table 11: The number of D^0 candidates found by the fit assuming a signal for the wrong charge correlation for p_{T} $(\mu) > 6$ GeV/c and $|\eta(\mu)| < 2.4$.

Dataset	Number of D^0 candidates
Run A	14 ± 19
Run B	44 ± 58
MC	41 ± 55

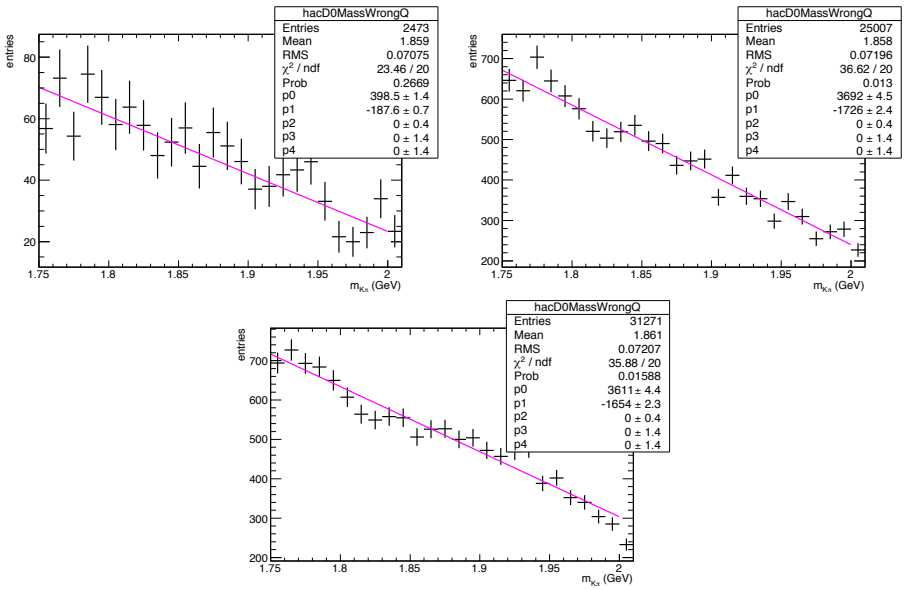

Figure 113: D^0 mass distribution of the wrong charge correlation candidates for p_{T} $(\mu) > 6$ GeV/c, $p_{\mathrm{T}}(K, \pi) > 0.5$ GeV/c, and $|\eta(\mu, K, \pi)| < 2.4$ for the 2010A data (top left), 2010B data (top right), and Monte Carlo events (bottom). Fits assume background only.

7.6 Systematic Uncertainties

There are several sources of systematic uncertainty in the analysis. They are due to the uncertainties on other quantities which go into the final result, such as efficiencies. Some of these uncertainties are bin-dependent, while others are overall uncertainties. The muon reconstruction and tracking efficiency, hadron tracking efficiency, luminosity, cut efficiency and trigger efficiency all contribute systematic uncertainties to the cross section.

There are bin-dependent systematic uncertainties due to the trigger efficiencies and the statistical error on the selection efficiency. Since the trigger efficiency is applied by weighting the data events in the invariant mass distribution, the systematic uncertainty due to the trigger efficiency is found by varying the trigger efficiency up and down by the statistical errors, and checking the effect on the final cross section in each bin. The uncertainty for each bin resulting from the error on the trigger efficiency is shown in Tables 12 and 13.

There is a systematic uncertainty due to the statistical error on the selection efficiency. The uncertainties are symmetric. This is the dominant uncertainty in this analysis, due to the low statistics in the Monte Carlo. The uncertainty for each bin resulting from the error on the selection efficiency is shown in Tables 14 and 15.

There are also systematic uncertainties which are bin-independent, which are due to the muon reconstruction efficiency, the hadron tracking efficiency, and the luminosity measurement. The muon and hadron reconstruction and tracking efficiencies are found from Monte Carlo, which may incorrectly model the efficiencies. The agreement between the efficiency in Monte Carlo versus data has been studied by other groups in CMS.

The systematic uncertainty due to the muon reconstruction efficiency is 3% [87]. It is evaluated using the tag-and-probe method. The tag-and-probe method exploits dimuon resonances, such as the J/Ψ. The resonance is reconstructed by putting very strict requirements on one muon, called the *tag*, and loose requirements on the second, called the *probe*. The usual reconstruction requirements are then placed on the probe

muon, and the relative efficiency between the two sets of requirements is defined as the efficiency.

There is a systematic uncertainty on the hadron tracking efficiency for each of the pion and kaon tracks. The relative efficiency of tracking hadrons in data and Monte Carlo simulation is evaluated using the ratio between the decays $D^0 \to \mathrm{K}\pi\pi\pi$ and $D^0 \to \mathrm{K}\pi$. The total uncetainty on the hadron tracking efficiency is 3.9% [88]. The uncertainties for the two tracks are treated as uncorrelated.

There is a dedicated group within CMS to measure the collected luminosity. The absolute luminosity determination is done using Van Der Meer scans. The size and shape of the interaction area are measured by scanning the beams across each other and measuring the interaction rate as a function of the beam separation. More details can be found in [89]. The luminosity calculation for 2010 contributes a systematic uncertainty of 4%.

Combining the systematic uncertainties due to the muon reconstruction efficiency, the hadron tracking efficiency, and the luminosity, the total bin-independent systematic uncertainty is found to be 7.4%.

To see whether there is any significant systematic uncertainty introduced by the selection cuts, a cross check is done by varying the cut on the x_b variable up and down by 0.05, as this variable has the largest significance. In order to avoid effects from any other efficiencies or systematics, the cross check is done on the Monte Carlo at the generator level.

Tables 16 and 17 show the change in the number of events passing the x_b cut. The change in the number of events is of the same order of magnitude as the statistical fluctuations, and it is unclear how to tell whether the efficiency due to the cut on the x_b variable is modeled correctly in the Monte Carlo, so we can not conclude that there is any systematic effect of changing the value of the x_b cut, although it is probable that changing this cut does change the efficiency.

The different contributions to the systematic uncertainty are summarized in Ta-

ble 18. The uncertainties are combined by adding them in quadrature.

Table 12: Systematic uncertainty due to the error on the trigger efficiency in each p_{T} (μD^0) bin. The Run A data uses the HLT_Mu5 trigger, and the Run B data uses the HLT_Mu15_v1 trigger.

Dataset	p_{T} (μD^0)	Cross Section (nb)	Cross Section (nb) Trig. eff. up	Cross Section (nb) Trig. eff. down	Uncertainty Trig. eff. up	Uncertainty Trig. eff. down
Run A	6 - 11 GeV/c	315 ± 75	306 ± 76	329 ± 80	2.8%	4.2%
	11 - 16 GeV/c	265 ± 30	256 ± 30	275 ± 30	3.3%	3.9%
	16 - 20 GeV/c	110 ± 25	106 ± 25	114 ± 84	3.7%	3.7%
	20 - 30 GeV/c	27.4 ± 5.2	26.3 ± 5.2	28.4 ± 5.4	4.0%	3.7%
	30 - 50 GeV/c	5.4 ± 1.8	5.1 ± 1.5	5.8 ± 1.3	5.6%	7.4%
Run B	20 - 30 GeV/c	34.8 ± 1.4	34.4 ± 1.4	35.0 ± 1.4	1.2%	0.6%
	30 - 50 GeV/c	4.95 ± 0.18	4.90 ± 0.18	5.01 ± 0.18	1.0%	1.2%
	50 - 80 GeV/c	0.562 ± 0.044	0.557 ± 0.044	0.567 ± 0.046	0.9%	0.9%

Table 13: Systematic uncertainty due to the error on the trigger efficiency in each $|\eta(\mu D^0)|$ bin. The Run A data uses the HLT_Mu5 trigger, and the Run B data uses the HLT_Mu15_v1 trigger.

Dataset	$\|\eta(\mu D^0)\|$	Cross Section (nb)	Cross Section (nb) Trig. eff. up	Cross Section (nb) Trig. eff. down	Uncertainty Trig. eff. up	Uncertainty Trig. eff. down
Run A	0.0 - 0.9	2111 ± 764	2062 ± 758	2171 ± 782	2.3%	2.9%
	0.9 - 1.5	2175 ± 316	2098 ± 307	2271 ± 316	3.5%	4.4%
	1.5 - 2.1	1326 ± 359	1261 ± 359	1414 ± 370	4.9%	6.6%
	2.1 - 2.4	1248 ±458	1123 ± 416	1081 ± 291	10%	13%
Run B	0.0 - 0.9	94.3 ± 7.4	93.7 ± 7.4	95.0 ± 7.4	0.6%	0.7%
	0.9 - 1.5	77.5 ± 5.8	76.6 ± 5.8	78.4 ± 6.3	1.1%	1.2%
	1.5 - 2.1	46.5 ± 3.9	46.0 ± 3.9	47.2 ± 3.9	1.2%	1.4%
	2.1 - 2.4	17.3 ± 3.6	15.8 ± 3.4	15.4 ± 2.0	8.7%	11%

Table 14: Systematic uncertainty due to the statistical error on the selection efficiency for Run A with p_{T} (μ) > 6 GeV/c and $|\eta(\mu)| < 2.4$.

	Bin	Generated	Tagged	Efficiency	Syst. Uncertainty
p_{T} (μD^0)	6 - 11 GeV/c	30422	1269	(4.2 ± 0.1)%	2.5%
	11 - 16 GeV/c	18775	4008	(21 ± 0.3)%	1.4%
	16 - 20 GeV/c	5760	1994	(35 ± 0.8)%	2.3%
	20 - 30 GeV/c	4119	1771	(43 ± 1)%	2.3%
	30 - 50 GeV/c	1005	511	(51 ± 2)%	3.9%
	30 - 50 GeV/c	119	57	(48 ± 6)%	12.5%
$\|\eta(\mu D^0)\|$	0.0 - 0.9	27610	4684	(17 ± 0.2)%	1.2%
	0.9 - 1.5	16592	2673	(16 ± 0.3)%	1.9%
	1.5 - 2.1	13961	1982	(14 ± 0.3)%	2.1%
	2.1 - 2.4	3759	279	(7 ± 0.4)%	5.7%

Table 15: Systematic uncertainty due to the statistical error on the selection efficiency for Run B with p_{T} (μ) > 16 GeV/c and $|\eta(\mu)| < 2.4$.

	Bin	Generated	Fit	Efficiency	Syst. Uncertainty
p_{T} (μD^0)	16 - 20 GeV/c	879	231	(27 ± 2)%	7.4%
	20 - 30 GeV/c	559	262	(47 ± 3)%	6.4%
	30 - 50 GeV/c	89	39	(44 ± 7)%	15.9%
$\|\eta(\mu D^0)\|$	0.0 - 0.9	824	275	(33 ± 2)%	6.7%
	0.9 - 1.5	425	129	(30 ± 3)%	9.4%
	1.5 - 2.1	349	113	(32 ± 3)%	14.3%
	2.1 - 2.4	110	23	(21 ± 4)%	19.0%

Table 16: The number of D^0 candidates found when varying the cut on x_b by 0.05 for Monte Carlo with p_{T} (μ) > 6 GeV/c. The last column, labeled "Stat. Uncert.", shows the statistical uncertainty as a comparison.

Bin	xb = 0.6	xb = 0.55	% Change	xb = 0.65	% Change	Stat. Uncert.
6 GeV/c $\leq p_{\mathrm{T}}$ (μD^0) < 11 GeV/c	16324	14239	12.8%	18153	11.2%	0.8%
11 GeV/c $\leq p_{\mathrm{T}}$ (μD^0) < 16 GeV/c	12204	10779	11.7%	13299	9.0%	0.9%
16 GeV/c $\leq p_{\mathrm{T}}$ (μD^0) < 20 GeV/c	4086	3668	10.2%	4323	5.8%	1.6%
20 GeV/c $\leq p_{\mathrm{T}}$ (μD^0) < 30 GeV/c	2964	2722	8.2%	3111	5.0%	1.8%
30 GeV/c $\leq p_{\mathrm{T}}$ (μD^0) < 50 GeV/c	732	692	5.5%	763	4.2%	3.7%
$0 \leq \lvert\eta(\mu D^0)\rvert < 0.9$	17457	15338	12.1%	19184	9.9%	0.7%
$0.9 \leq \lvert\eta(\mu D^0)\rvert < 1.5$	10077	8890	11.8%	11040	9.6%	1.0%
$1.5 \leq \lvert\eta(\mu D^0)\rvert < 2.1$	8059	7142	11.4%	8761	8.7%	1.1%
$2.1 \leq \lvert\eta(\mu D^0)\rvert < 2.4$	1794	1636	8.8%	1903	6.1%	2.4%
Total	37982	33529	11.7%	41543	9.4%	0.5%

Table 17: The number of D^0 candidates found when varying the cut on x_b by 0.05 for Monte Carlo with p_{T} (μ) > 16 GeV/c. The last column, labeled "Stat. Uncert.", shows the statistical uncertainty as a comparison.

Bin	xb = 0.6	xb = 0.55	% Change	xb = 0.65	% Change	Stat. Uncert.
20 GeV/c $\leq p_{\mathrm{T}}$ (μD^0) < 30 GeV/c	625	584	6.56%	657	5.12%	4.0%
30 GeV/c $\leq p_{\mathrm{T}}$ (μD^0) < 50 GeV/c	413	393	4.84%	430	4.12%	4.9%
50 GeV/c $\leq p_{\mathrm{T}}$ (μD^0) < 80 GeV/c	57	54	5.26%	59	3.51%	13.3%
$0 \leq \lvert\eta(\mu D^0)\rvert < 0.9$	606	569	6.1%	633	4.5%	4.0%
$0.9 \leq \lvert\eta(\mu D^0)\rvert < 1.5$	294	280	4.76%	311	5.78%	5.8%
$1.5 \leq \lvert\eta(\mu D^0)\rvert < 2.1$	248	230	7.26%	261	5.24%	6.3%
$2.1 \leq \lvert\eta(\mu D^0)\rvert < 2.4$	63	60	4.76%	66	4.76%	12.6%
Total	1225	1152	5.96%	1286	4.98%	2.9%

Table 18: Systematic uncertainties on the cross section.

Source	Cross section uncertainty
Trigger efficiency	1% - 13%
Selection efficiency	1% - 19%
Muon reconstruction efficiency	3%
Hadron tracking efficiency (x2)	3.9%
All Efficiencies	6.8% - 24.4%
Luminosity	4%
Branching Ratio	5.3%

7.7 Results

Equations 17 and 18 show the formulas to calculate the differential cross section in bins of p_{T} and $|\eta|$ of the μD^0 .

$$\frac{d\sigma(pp \to b + X \to \mu D^0 X' \to K\pi, p_{\mathrm{T}}(\mu) > 6\mathrm{GeV}/c, p_{\mathrm{T}}(K,\pi) > 0.5\mathrm{GeV}/c, |\eta(\mu,K,\pi)| < 2.4)}{dp_{\mathrm{T}}}$$
$$= \frac{N(\mu^- D^0 \text{ and } \mu^+ \bar{D^0})}{2 \cdot \mathcal{L} \cdot \epsilon_{rec} \cdot \epsilon_{sel} \cdot \mathcal{B} \cdot \Delta p_{\mathrm{T}}} \tag{17}$$

$$\frac{d\sigma(pp \to b + X \to \mu D^0 X' \to K\pi, p_{\mathrm{T}}(\mu) > 6\mathrm{GeV}/c, p_{\mathrm{T}}(K,\pi) > 0.5\mathrm{GeV}/c, |\eta(\mu,K,\pi)| < 2.4)}{d|\eta|}$$
$$= \frac{N(\mu^- D^0 \text{ and } \mu^- \bar{D^0})}{2 \cdot \mathcal{L} \cdot \epsilon_{rec} \cdot \epsilon_{sel} \cdot \mathcal{B} \cdot \Delta|\eta|} \tag{18}$$

$N(\mu D^0)$ is the number of observed μD^0 candidates in each bin, weighted by the trigger efficiency, which is found by fitting the Kπ invariant mass distribution in the bin, and are listed in Table 10. $\mathcal{L}$ is the luminosity of the dataset. ϵ_{rec} is the reconstruction efficiency and ϵ_{sel} is the selection efficiency. The combined efficiencies $\epsilon_{rec} \cdot \epsilon_{sel}$ are found in Table 7. $\mathcal{B}$ is the branching ratio $\mathcal{B}(b \to \mu^- D^0 X) \times \mathcal{B}(D^0 \to K^-\pi^+)$, where $\mathcal{B}(b \to \mu^- D^0 X) = (6.84 \pm 0.35)\%$ and $\mathcal{B}(D^0 \to K^-\pi^+) = (3.89 \pm 0.05)\%$ [83], making the total branching ratio $0.266 \pm 0.014)\%$ in the data. The branching ratio used in the Monte Carlo is 0.332% [67]. The branching ratio used in the Monte Carlo was determined by counting the number of b-hadrons, and the number of those which are signal events, as defined in Section 7.3. Δp_{T} ($\Delta|\eta|$) is the bin size. The cross section is defined as being in the acceptance, and no correction is made for it. The factor of 2 in the denominator is to account for the fact that no distinction is made between measuring a $\mu^- D^0$ and a $\mu^+ \bar{D^0}$.

Ideally the differential cross section should be presented as a function of the p_{T} and $|\eta|$ of the b-hadron, but the b-hadron can not be fully reconstructed, due to at least the missing neutrino. This would also allow a more direct comparison to measurements from other experiments. Since the Monte Carlo sample has the requirement for a muon with at least $p_{\mathrm{T}} > 5$ GeV/c, it is not possible to do the unfolding. A Monte Carlo sample without any cuts on the p_{T} and $|\eta|$ of the particles would be required to unfold to the full region. New Monte Carlo samples could not be generated since the data was processed in an old CMSSW version, which is no longer available.

As an example and cross check, here I follow one bin through the entire analysis sequence in the Monte Carlo. For this purpose I use the bin with p_{T} (μ) from 16-20 GeV/c. First, using the generator information, I follow the number of true signal events through each step in the analysis. At the end I compare the true number of tagged signal events remaining with the number found from fitting the Kπ invariant mass distribution.

Before any event selection, there are 6531 generated signal events. 5760 of these events are in the acceptance (see Table 14), which means that the μ, K and π have $|\eta| < 2.4$. After all of the selection cuts, there are 1994 tagged Monte Carlo signal events remaining. From the fit of the Kπ invariant mass distribution, there are 1974 $\pm$ 87 D^0 candidates, which is consistent with the true value of 1994 tagged Monte Carlo signal events.

To calculate the differential cross section for the Monte Carlo, $N(\mu D^0)$ is the number of generated signal events in the acceptance of $p_{\mathrm{T}}(\mu) > 6\mathrm{GeV/c}, \mathrm{p_T(K,\pi)} > 0.5\mathrm{GeV/c}, \mathrm{and} |\eta(\mu, \mathrm{K}, \pi)| < 2.4$ and in the particular bin. In Equation 17, the efficiency ϵ is equal to 1 by definition. The luminosity of the Monte Carlo sample is 1.23 pb^{-1}. The cross section in Monte Carlo for the bin 16 GeV/c $\leq p_{\mathrm{T}}(\mu D^0) <$ 20 GeV/c is shown below, and is also shown in Table 19. The branching ratio of $b \to \mu D^0 X \to K\pi$ in the Monte Carlo is 0.00332, as described above, and the p_{T} bin width Δp_{T} is 4 GeV/c.

$$\sigma(pp \to b + X \to \mu D^0 X' \to K\pi, 16\text{GeV/c} \leq p_{\text{T}}(\mu) < 20\text{GeV/c}, |\eta(\mu, K, \pi)| < 2.4)$$
$$= \frac{5760}{2 \cdot 1.23\text{pb}^{-1} \cdot 0.00332 \cdot 4\text{GeV}}$$
$$= 176.3nb/GeV \tag{19}$$

The differential cross section for the region p_{T} $(\mu D^0) > 6$ GeV/c and $|\eta(\mu)| < 2.4$ is shown in Figure 114 as a function of p_{T} (μD^0), and in Figures 115 and 116 as a function of $|\eta(\mu D^0)|$. The Monte Carlo cross section is calculated using the number of generated signal events and an efficiency of 1.

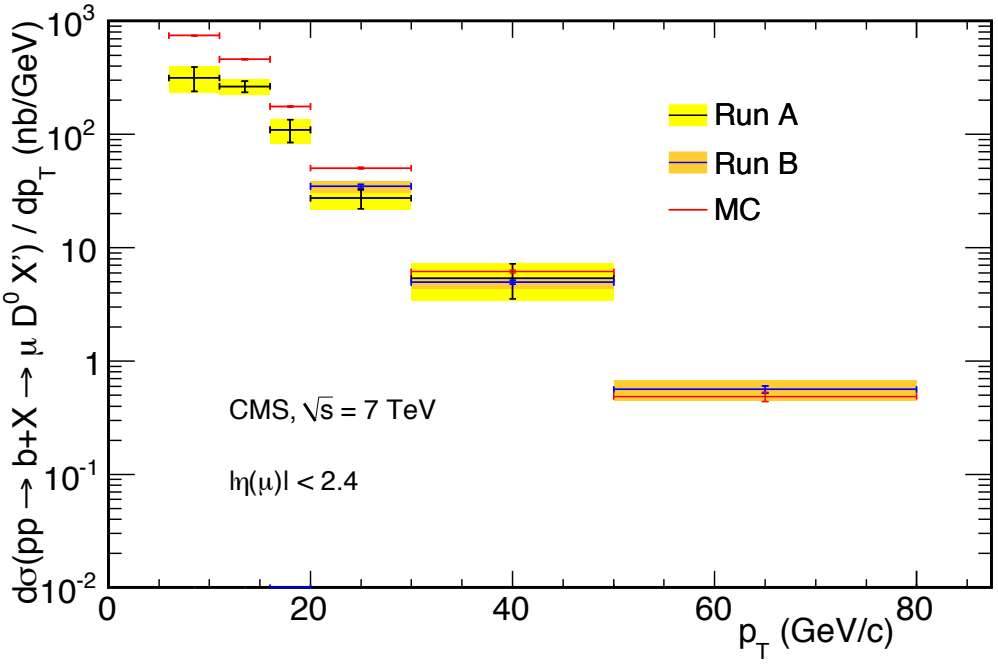

Figure 114: Cross section as a function of $p_{\text{T}}(\mu D^0)$ for Run A (black), Run B (blue), and Monte Carlo (red) events with $|\eta(\mu)| < 2.4$. Error bars show the statistical uncertainty, and the colored bands show the combined statistical and systematic uncertainty.

The cross section in each bin is listed in Table 19 as a function of p_{T} (μD^0), and in

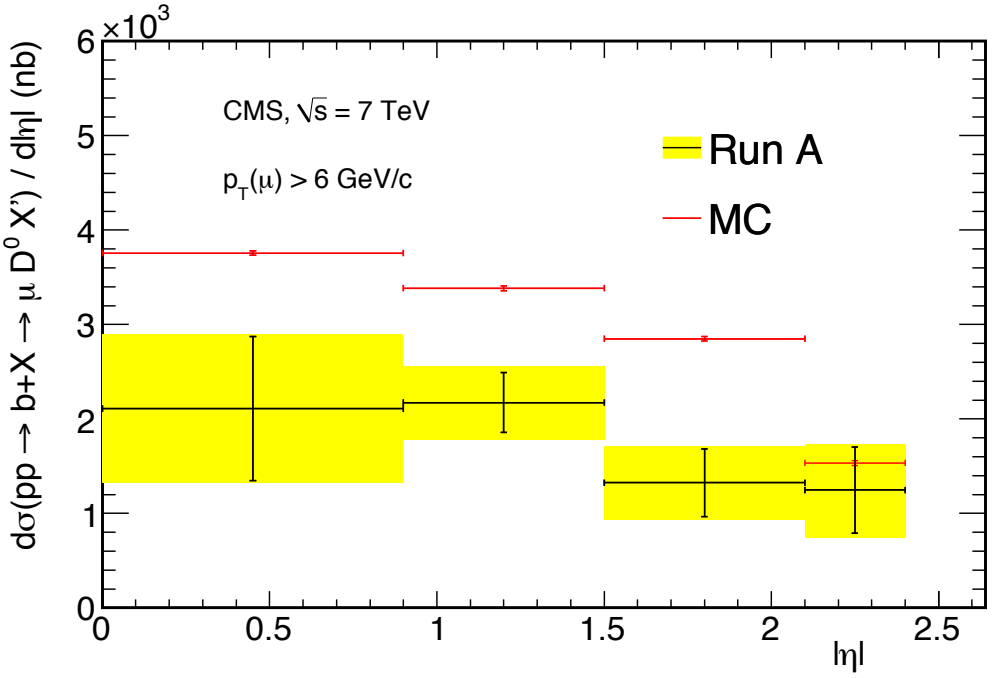

Figure 115: Cross section as a function of $|\eta|(\mu D^0)$ for Run A (black) and Monte Carlo (red) events with p_{T} $(\mu) > 6$ GeV/c. Error bars show the statistical uncertainty, and the colored bands show the combined statistical and systematic uncertainty.

Table 20 as a function of $|\eta(\mu D^0)|$.

The total cross section for $pp \to bX \to \mu D^0 X' \to K\pi, p_T(\mu) > 6\mathrm{GeV/c}, |\eta(\mu)| < 2.4$ is found by combining the two datasets. The Run A dataset is used for 6 GeV/c $< p_{\mathrm{T}}(\mu D^0) <$ 20 GeV/c, and the Run B dataset is used for p_{T} $(\mu D^0) > 20$ GeV/c. There are two approaches to combine the datasets. The first approach is to integrate the differential cross section which was already presented in Figure 114. The second approach is to fit the Kπ invariant mass distributions for the full datasets and calculate the cross section for each dataset according to Equation 17 and add them. The former is used as a cross check, while the final result uses the latter.

The total cross section found by integrating the differential cross section is 3802 $\pm$ 419 (stat.) nb. As this number is presented only as a cross check, the systematic uncertainties are not addressed. The total cross section found by fitting the full datasets

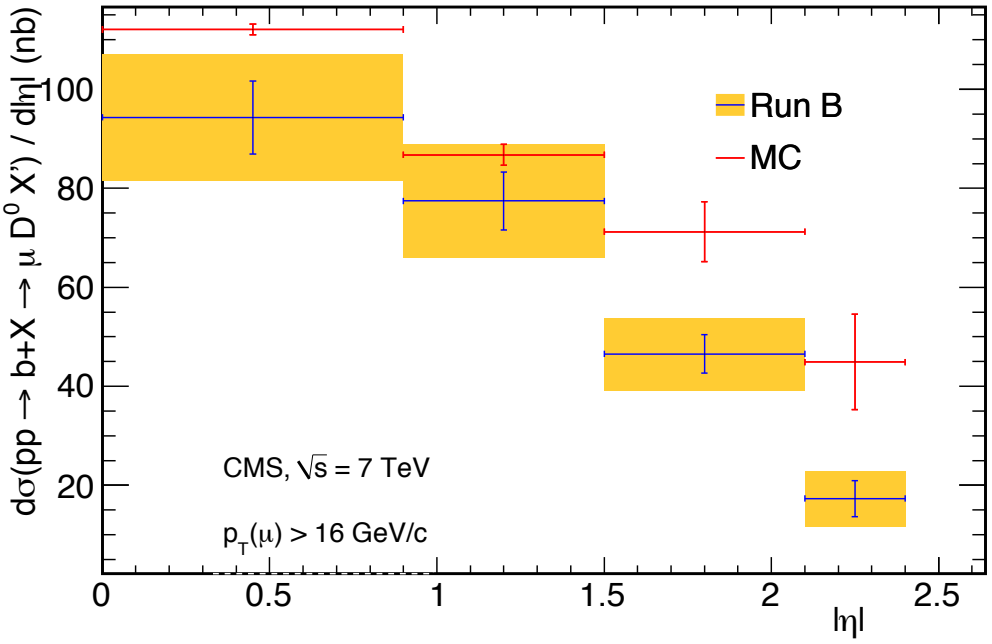

Figure 116: Cross section as a function of $|\eta|(\mu D^0)$ for Run B (blue) and Monte Carlo (red) events with p_{T} $(\mu) > 16$ GeV/c. Error bars show the statistical uncertainty, and the colored bands show the combined statistical and systematic uncertainty.

is shown in Equation 20.

$$\begin{aligned}&\sigma(pp \to b + X \to \mu D^0 X' \to K\pi, p_{\mathrm{T}}(\mu) > 6\mathrm{GeV/c}, |\eta(\mu)| < 2.4) \\ &= 4.36 \pm 0.54(stat.)^{+0.28}_{-0.25}(sys.) \pm 0.17(\mathcal{B}) \pm 0.23(\mathcal{L})\mu\mathrm{b}\end{aligned} \tag{20}$$

Table 19: The cross section in each p_{T} (μD^0) bin.

Bin	2010A	2010B	Monte Carlo	MC15
$6 \leq p_{\mathrm{T}} < 11$	315.3 ± 75.5 (stat.) ± 31.4 (sys.)	–	745.0 ± 4.3 (stat.)	–
$11 \leq p_{\mathrm{T}} < 16$	264.6 ± 30.4 (stat.) ± 26.0 (sys.)	–	460.0 ± 3.4 (stat.)	–
$16 \leq p_{\mathrm{T}} < 20$	109.7 ± 24.7 (stat.) ± 10.8 (sys.)	–	176.3 ± 2.3 (stat.)	176.3 ± 17.0 (stat.)
$20 \leq p_{\mathrm{T}} < 30$	27.4 ± 5.2 (stat.) ± 2.8 (sys.)	34.8 ± 1.4 (stat.) ± 3.9 (sys.)	50.4 ± 0.8 (stat.)	50.4 ± 1.7 (stat.)
$30 \leq p_{\mathrm{T}} < 50$	5.4 ± 1.8 (stat.) ± 0.6 (sys.)	5.0 ± 0.2 (stat.) ± 0.6 (sys.)	6.2 ± 0.2 (stat.)	6.2 ± 0.3 (stat.)
$50 \leq p_{\mathrm{T}} < 80$	–	0.56 ± 0.04 (stat.) ± 0.11 (sys.)	0.49 ± 0.04 (stat.)	0.49 ± 0.05 (stat.)

Table 20: The cross section in each $|\eta(\mu D^0)|$ bin.

Bin	2010A	2010B	Monte Carlo	MC15
$0 \leq \|\eta\| < 0.9$	2111 ± 764 (stat.) ± 201 (sys.)	94.3 ± 7.4 (stat.) ± 10.3 (sys.)	3756 ± 23 (stat.)	112.1 ± 1.1 (stat.)
$0.9 \leq \|\eta\| < 1.5$	2175 ± 316 (stat.) ± 217 (sys.)	77.5 ± 5.8 (stat.) ± 9.9 (sys.)	3386 ± 26 (stat.)	86.7 ± 2.1 (stat.)
$1.5 \leq \|\eta\| < 2.1$	1326 ± 359 (stat.) ± 141 (sys.)	46.5 ± 3.9 (stat.) ± 6.1 (sys.)	2849 ± 24 (stat.)	71.2 ± 6.1 (stat.)
$2.1 \leq \|\eta\| < 2.4$	1248 ± 458 (stat.) ± 185 (sys.)	17.3 ± 3.6 (stat.) ± 4.2 (sys.)	1534 ± 25 (stat.)	44.9 ± 9.6 (stat.)

8 Conclusion

Measuring the b production cross section provides a good test of pQCD. Since b-quarks constitute a significant source of background for many future studies it is important to have a good understanding of their production. Because of the reliance of this analysis on the reconstruction of secondary vertices, it is essential to have a reliable tracking detector with good resolution. The detector is exposed to considerable amounts of radiation, and the effects of the radiation must be understood.

Several measurements of the current CMS barrel pixel sensors were performed in order to evaluate their performance in the harsh radiation environment of the LHC. These measurements were charge collection efficiency measurements to measure the amount of signal lost, detection efficiency measurements, and interpixel capacitance measurements. The goals of the measurements were to determine the operational limits of the sensors, and their suitability for use in the CMS Phase 1 Upgrade pixel detector. In addition, high voltage tests were performed on single-sided sensors, which are cheaper to produce, to investigate their feasibility for future upgrades.

The different measurements performed on the current CMS barrel pixel sensors show that they work remarkably well even at high fluences. In particular, the charge collection efficiency measurements show that a significant amount of charge can be collected even after fluences of more than 10^{15} $\mathrm{n_{eq}/cm^2}$, provided that a high bias voltage can be applied. This confirms that the sensors will survive past the design requirement of 250 fb^{-1} of integrated luminosity. The measurements in this dissertation led in part to the decision to maintain the same sensor material and design for the CMS Phase I Upgrade pixel detector.

The main concern prompting the Phase I Upgrade pixel detector is the performance the readout chip with increased luminosity, where the main problems will be filling the buffers on the chip. The amount of signal collected will gradually decline with the radiation damage, with the limiting factors in the bias voltage being the cables and

connectors to supply the voltage to the sensors. The measurements also show that the lifetime of the sensors is not limited by the amount of charge collected, but by the reduction in the spatial resolution due to the increasing bias voltage needed.

In addition to the measurements on the silicon pixel sensors, a measurement of the $b\bar{b}$ cross section at a center-of-mass energy of $\sqrt{s} = 7$ TeV using the decay chain $b \to \mu D^0 X$, $D^0 \to \mathrm{K}\pi$ has been presented. The measurement is based on an integrated luminosity of $\sim$25 pb^{-1} taken during 2010. The total cross section in the acceptance is $\sigma(pp \to b + X \to \mu D^0 X', p_{\mathrm{T}}(\mu) > 6\mathrm{GeV/c}, p_{\mathrm{T}}(\mathrm{K}, \pi) > 0.5\mathrm{GeV/c}, |\eta(\mu, \mathrm{K}, \pi)| < 2.4) = 4.36 \pm 0.54(stat.)^{+0.28}_{-0.25}(sys.) \pm 0.17(\mathcal{B}) \pm 0.23(\mathcal{L})\mu$b.

Comparison with the LO PYTHIA Monte Carlo QCD sample shows that it overestimates the cross section by approximately a factor of 2. This is consistent with observations from other analyses [6]. The measurement is limited by the systematic uncertainty from the selection efficiencies, which is very large due to the limited statistics in the Monte Carlo sample. A similar analysis in CMS showed that the difference between the data and theoretical predictions are much smaller once NLO effects are included [15]. This reflects the fact that NLO processes such as flavor excitation and gluon splittings are important at the LHC.

ATLAS and LHCb have also made measurements of the inclusive $b\bar{b}$ cross section. The ATLAS measurement uses the final state $\mu D^* X$, with the D^* reconstructed with the decay chain $D^* \to \pi D^0, D^0 \to \mathrm{K}\pi$. The ATLAS results are compared to theoretical predictions from POWHEG+PYTHIA, POWHEG+Herwig, and MC@NLO. In all cases the data is higher than the theoretical predictions, although barely consistent within the errors. In LHCb, the same final states as in this dissertation, namely, B $\to \mu D^0 X$, $D^0 \to \mathrm{K}\pi$, are used. The LHCb measurements are presented only as a function of η, but are consistent with the theoretical predictions from FONLL. Until now there has been no equivalent measurement published by CMS.

The measurement presented in this dissertation can not be directly compared to those of the other LHC experiments without first unfolding to the b-hadron and extrap-

olating to the full phase space. This would require a significant effort to produce new Monte Carlo samples, which was not possible in the time frame for this dissertation.

A very general comparison can be made between this measurement and the ones from ATLAS and LHCb by looking at the relative agreement between each measurement and the Monte Carlo predictions, and the differences between the Monte Carlo generators. As seen in Figure 68, ATLAS finds the POWHEG+PYTHIA underestimates the cross section by approximately a factor of 2. The CMS measurement using the p_{T}^{rel} also finds that the POWHEG+PYTHIA underestimates the cross section by about a factor of 1.5 (see Figure 70), and that PYTHIA overestimates the cross section by approximately a factor of 2 (see Figure 69). LHCb compares their measurement with the FONLL predictions and finds the predictions to be consistent with the data, as shown in Figure 67. The CMS p_{T}^{rel} measurement also finds the FONLL predictions to be consistent with the data. In conclusion, it appears that the measurement presented in this dissertation is consistent with the measurements from ATLAS and LHCb, although it should be stressed that this is a very indirect comparison.

An interesting continuation of this analysis would be to compare with the cross section measured by the LHCb experiment, using the same final states. LHCb measures in the forward region ($|\eta| > 2$), where CMS suffers from low efficiencies, making this a challenging task which was not possible to cover in the scope of this dissertation.

References

[1] Michael Moll. *Radiation damage in silicon particle detectors – microscopic defects and macroscopic properties*. PhD thesis, Universität Hamburg, 1999.

[2] CERN. http://home.web.cern.ch/.

[3] The CMS Collaboration. The CMS experiment at the CERN LHC. *Journal of Instrumentation*, 3(8):S08004, 2008.

[4] The CMS Collaboration. Tracking and primary vertex results in first 7 tev collisions. CMS PAS TRK-10-005, 2010.

[5] O. Koybasi, K. Arndt, G. Bolla, D. Bortoletto, P. Merkel, and I. Shipsey. Assembly and qualification procedures of cms forward pixel detector modules. *Nucl. Instrum. Meth. A*, 638:55–62, 2011.

[6] Lea Caminada. *Study of the Inclusive Beauty Production at CMS and Construction and Commissioning of the CMS Pixel Barrel Detector*. PhD thesis, Eidgenössische Technische Hochschule Zürich, 2010.

[7] Y. Allkofer, C. Amsler, D. Bortoletto, V. Chiochia, L. Cremaldi, S. Cucciarelli, A. Dorokhov, C. Hörmann, R. Horisberger, D. Kim, M. Konecki, D. Kotlinski, K. Prokofiev, C. Regenfus, T. Rohe, D.A. Sanders, S. Son, M. Swartz, and T. Speer. Design and performance of the silicon sensors for the CMS barrel pixel detector. *Nuclear Instruments and Methods in Physics Research Section A: Accelerators, Spectrometers, Detectors and Associated Equipment*, 584(1):25 – 41, 2008.

[8] C Amsler, K Bösiger, V Chiochia, W Erdmann, K Gabathuler, R Horisberger, S König, D Kotlinski, R Maier, B Meier, Hp Meyer, A Rizzi, P Robmann, S Scherr, A Schmidt, S Steiner, and S Streuli. Mechanical design and material budget of the cms barrel pixel detector. *Journal of Instrumentation*, 4(05):P05003, 2009.

[9] Alexandra Junkes. *Influence of radiation induced defect clusters on silicon particle detectors*. PhD thesis, Universität Hamburg, 2011.

[10] V Eremin, E Verbitskaya, and Z Li. The origin of double peak electric field distribution in heavily irradiated silicon detectors. *Nuclear Instruments and Methods in Physics Research Section A: Accelerators, Spectrometers, Detectors and Associated Equipment*, 476(3):556 – 564, 2002.

[11] CDF Collaboration. Measurements of bottom anti-bottom azimuthal production correlations in proton-antiproton collisions at $\sqrt{s} = 1.8$ TeV. *Phys. Rev. D*, 71(9):092001, May 2005.

[12] CDF Collaboration. Measurement of the b-hadron production cross section using decays to $\mu^- D^0 x$ final states in $p\bar{p}$ collisions at $\sqrt{s} = 1.96$ TeV. *Phys. Rev. D*, 79(9):092003, 2009.

[13] The LHCb Collaboration. Measurement of $\sigma(pp \to b\bar{b}X)$ at $\sqrt{s} = 7$ TeV in the forward region. *Physics Letters B*, 694:209–216, 2010.

[14] The ATLAS Collaboration. Measurement of the b-hadron production cross section using decays to final states in pp collisions at with the atlas detector. *Nuclear Physics B*, 864(3):341 – 381, 2012.

[15] L. Caminada, W. Erdmann, U. Langenegger, V. Zhukov, D. Troendle, S. Wayand, A. Bean, and G. Tinti. Inclusive $b \to \mu X$ cross section measurement at 7 TeV. CMS AN-10-346, 2010.

[16] S. Glashow. Partial-symmetries of weak interactions. *Nuclear Physics*, 22(4):579 – 588, 1961.

[17] S. Weinberg. A model of leptons. *Phys. Rev. Lett.*, 19:1264–1266, Nov 1967.

[18] Abdus Salam. Weak and electromagnetic interactions. Originally printed in *Svartholm: Elementary Particle Theory, Proceedings Of The Nobel Symposium Held 1968 At Lerum, Sweden*, Stockholm 1968, 367-377.

[19] S. L. Glashow, J. Iliopoulos, and L. Maiani. Weak interactions with lepton-hadron symmetry. *Phys. Rev. D*, 2:1285–1292, Oct 1970.

[20] J. J. Aubert, U. Becker, P. J. Biggs, J. Burger, M. Chen, G. Everhart, P. Goldhagen, J. Leong, T. McCorriston, T. G. Rhoades, M. Rohde, Samuel C. C. Ting, Sau Lan Wu, and Y. Y. Lee. Experimental observation of a heavy particle j. *Phys. Rev. Lett.*, 33:1404–1406, Dec 1974.

[21] J. E. Augustin, A. M. Boyarski, M. Breidenbach, F. Bulos, J. T. Dakin, G. J. Feldman, G. E. Fischer, D. Fryberger, G. Hanson, B. Jean-Marie, R. R. Larsen, V. Lüth, H. L. Lynch, D. Lyon, C. C. Morehouse, J. M. Paterson, M. L. Perl, B. Richter, P. Rapidis, R. F. Schwitters, W. M. Tanenbaum, F. Vannucci, G. S. Abrams, D. Briggs, W. Chinowsky, C. E. Friedberg, G. Goldhaber, R. J. Hollebeek, J. A. Kadyk, B. Lulu, F. Pierre, G. H. Trilling, J. S. Whitaker, J. Wiss, and J. E. Zipse. Discovery of a narrow resonance in e^+e^- annihilation. *Phys. Rev. Lett.*, 33:1406–1408, Dec 1974.

[22] Makoto Kobayashi and Toshihide Maskawa. *cp*-violation in the renormalizable theory of weak interaction. *Progress of Theoretical Physics*, 49(2):652–657, 1973.

[23] S. W. Herb, D. C. Hom, L. M. Lederman, J. C. Sens, H. D. Snyder, J. K. Yoh, J. A. Appel, B. C. Brown, C. N. Brown, W. R. Innes, K. Ueno, T. Yamanouchi, A. S. Ito, H. Jöstlein, D. M. Kaplan, and R. D. Kephart. Observation of a dimuon resonance at 9.5 gev in 400-gev proton-nucleus collisions. *Phys. Rev. Lett.*, 39:252–255, Aug 1977.

[24] Makoto Kobayashi and Toshihide Maskawa. *cp*-violation in the renormalizable theory of weak interaction. *Progress of Theoretical Physics*, 49(2):652–657, 1973.

[25] CDF Collaboration. Observation of top quark production in $\overline{p}p$ collisions with the collider detector at fermilab. *Phys. Rev. Lett.*, 74:2626–2631, Apr 1995.

[26] D0 Collaboration. Search for high mass top quark production in $p\overline{p}$ collisions at $\sqrt{s} =$ 1.8 tev. *Phys. Rev. Lett.*, 74:2422–2426, Mar 1995.

[27] M. L. Perl, G. S. Abrams, A. M. Boyarski, M. Breidenbach, D. D. Briggs, F. Bulos, W. Chinowsky, J. T. Dakin, G. J. Feldman, C. E. Friedberg, D. Fryberger, G. Goldhaber, G. Hanson, F. B. Heile, B. Jean-Marie, J. A. Kadyk, R. R. Larsen, A. M. Litke, D. Lüke, B. A. Lulu, V. Lüth, D. Lyon, C. C. Morehouse, J. M. Paterson, F. M. Pierre, T. P. Pun, P. A. Rapidis, B. Richter, B. Sadoulet, R. F. Schwitters, W. Tanenbaum, G. H. Trilling, F. Vannucci, J. S. Whitaker, F. C. Winkelmann, and J. E. Wiss. Evidence for anomalous lepton production in $e^+ - e^-$ annihilation. *Phys. Rev. Lett.*, 35:1489–1492, Dec 1975.

[28] K. Kodama, N. Ushida, C. Andreopoulos, N. Saoulidou, G. Tzanakos, P. Yager, B. Baller, D. Boehnlein, W. Freeman, B. Lundberg, J. Morfin, R. Rameika, J.C. Yun, J.S. Song, C.S. Yoon, S.H. Chung, P. Berghaus, M. Kubantsev, N.W. Reay, R. Sidwell, N. Stanton, S. Yoshida, S. Aoki, T. Hara, J.T. Rhee, D. Ciampa, C. Erickson, M. Graham, K. Heller, R. Rusack, R. Schwienhorst, J. Sielaff, J. Trammell, J. Wilcox, K. Hoshino, H. Jiko, M. Miyanishi, M. Komatsu, M. Nakamura, T. Nakano, K. Niwa, N. Nonaka, K. Okada, O. Sato, T. Akdogan, V. Paolone, C. Rosenfeld, A. Kulik, T. Kafka, W. Oliver, T. Patzak, and J. Schneps. Observation of tau neutrino interactions. *Physics Letters B*, 504(3):218 – 224, 2001.

[29] Ch. Berger, W. Lackas, F. Raupach, W. Wagner, G. Alexander, L. Criegee, H.C. Dehne, K. Derikum, R. Devenish, G. Flgge, G. Franke, Ch. Gerke, E. Hackmack, P. Harms, G. Horlitz, Th. Kahl, G. Knies, E. Lehmann, B. Neumann, R.L. Thompson, U. Timm, P. Waloschek, G.G. Winter, S. Wolff, W. Zimmermann, O. Achterberg, V. Blobel, L. Boesten, H. Daumann, A.F. Garfinkel, H. Kapitza, B. Koppitz, W. Lhrsen, R. Maschuw, H. Spitzer, R. Van Staa, G. Wetjen, A. Bcker,

S. Brandt, J. Brger, C. Grupen, H.J. Meyer, G. Zech, H.J. Daum, H. Meyer, O. Meyer, M. Rssler, and K. Wacker. Jet analysis of the (9.46) decay into charged hadrons. *Physics Letters B*, 82(34):449 – 455, 1979.

[30] The ATLAS Collaboration. Observation of a new particle in the search for the standard model higgs boson with the atlas detector at the lhc. *Physics Letters B*, 716(1):1 – 29, 2012.

[31] The CMS Collaboration. Observation of a new boson at a mass of 125 gev with the cms experiment at the lhc. *Physics Letters B*, 716(1):30 – 61, 2012.

[32] *ALICE: Technical proposal for a Large Ion collider Experiment at the CERN LHC*. LHC Tech. Proposal. CERN, Geneva, 1995.

[33] *ATLAS detector and physics performance: Technical Design Report*. Technical Design Report ATLAS. CERN, Geneva, 1999. Electronic version not available.

[34] *Technical proposal*. LHC Tech. Proposal. CERN, Geneva, 1994. Cover title : CMS, the Compact Muon Solenoid : technical proposal.

[35] S. Amato et al. LHCb technical proposal. 1998. CERN-LHCC-98-04.

[36] The CMS Collaboration. Dependence on pseudorapidity and on centrality of charged hadron production in PbPb collisions at $\sqrt{s_{\mathrm{NN}}} = 2.76$ TeV. *Journal of High Energy Physics*, 2011:1–34, 2011. 10.1007/JHEP08(2011)141.

[37] Summary of the analysis of the 19 September 2008 incident at the LHC. Technical report, CERN, Geneva, Oct 2008.

[38] S. König *et al.* Building CMS pixel barrel detector modules. *Nucl. Instrum. Meth. A*, 582:776–780, 2007.

[39] Urs Langenegger. Offline calibrations and performance of the cms pixel detector. *Nuclear Instruments and Methods in Physics Research Section A: Accelerators, Spectrometers, Detectors and Associated Equipment*, 650(1):25 – 29, 2011.

[40] E. Bartz. The token bit manager chip for the CMS pixel readout. In *Proceedings of the 11th Workshop on Electronics for LHC and Future Experiments*, Heidelberg, Germany, 2005.

[41] H. C. Kästli, W. Bertl, W. Erdmann, K. Gabathuler, C. Hörmann, R. Horisberger, S. König, D. Kotlinski, B. Meier, P. Robmann, T. Rohe, and S. Streuli. CMS barrel pixel detector overview. *Nuclear Instruments and Methods in Physics Research A*, 582:724–727, 2007, arXiv:physics/0702182.

[42] G.B. Cerati, M.E. Dinardo, A. Florez, S. Kwan, A. Lopez, S. Magni, S. Malvezzi, D. Menasce, L. Moroni, C.R. Newsom, D. Pedrini, M. Rovere, S. Sala, P. Tan, S. Taroni, M. Turqueti, and L. Uplegger. Radiation tolerance of the cms forward pixel detector. *Nuclear Instruments and Methods in Physics Research Section A: Accelerators, Spectrometers, Detectors and Associated Equipment*, 600(2):408 – 416, 2009.

[43] G. Pellegrini, C. Fleta, F. Campabadal, M. Miñano, M. Lozano, J.M. Rafí, and M. Ullán. Technology of p-type microstrip detectors with radiation hard p-spray, p-stop and moderated p-spray insulations. *Nuclear Instruments and Methods in Physics Research Section A: Accelerators, Spectrometers, Detectors and Associated Equipment*, 579(2):599 – 603, 2007.

[44] M. Moll, E. Fretwurst, and G. Lindström. Leakage current of hadron irradiated silicon detectors material dependence. *Nucl. Instrum. Meth. A*, 426(1):87 – 93, 1999.

[45] V. Eremin, Z. Li, S. Roe, G. Ruggiero, and E. Verbitskaya. Double peak electric field distortion in heavily irradiated silicon strip detectors. *Nuclear Instruments and Methods in Physics Research Section A: Accelerators, Spectrometers, Detectors and Associated Equipment*, 535(3):622 – 631, 2004.

[46] PSI piE1 beamline. `http://aea.web.psi.ch/beam2lines/beam_pie1.html`.

[47] CERN Irradiation Facilities. https://irradiation.web.cern.ch/irradiation.

[48] Karlsruhe Irradiation Facility. http://www-ekp.physik.uni-karlsruhe.de/index.php?option=com_content&view=article&id=93&Itemid=12&lang=de.

[49] D. Kotlinski. Status of the cms pixel detector. *Journal of Instrumentation*, 4(4):P03019, 2009.

[50] T. Rohe, J. Acosta, A. Bean, S. Dambach, W. Erdmann, et al. Signal height in silicon pixel detectors irradiated with pions and protons. *Nucl.Instrum.Meth.*, A612:493–496, 2010, 0901.3422.

[51] Gianluigi Casse, A. Affolder, P.P. Allport, H. Brown, and M. Wormald. Enhanced efficiency of segmented silicon detectors of different thicknesses after proton irradiations up to 1x10^{16} n_{eq}/cm^2. *Nuclear Instruments and Methods in Physics Research Section A: Accelerators, Spectrometers, Detectors and Associated Equipment*, 624(2):401 – 404, 2010.

[52] Igor Mandi, Vladimir Cindro, Andrej Goriek, Gregor Kramberger, Marko Miku, and Marko Zavrtanik. Observation of full charge collection efficiency in heavily irradiated n+p strip detectors irradiated up to 3x10^{15} n_{eq}/cm^2. *Nuclear Instruments and Methods in Physics Research Section A: Accelerators, Spectrometers, Detectors and Associated Equipment*, 612(3):474 – 477, 2010.

[53] CERN H2 Beamline. http://sba.web.cern.ch/sba/BeamsAndAreas/resultbeam.asp?beamline=H2.

[54] T. Rohe, D. Bortoletto, V. Chiochia, L.M. Cremaldi, S. Cucciarelli, A. Dorokhov, C. Hörmann, D. Kim, M. Konecki, D. Kotlinski, K. Prokofiev, C. Regenfus, D.A. Sanders, S. Son, T. Speer, and M. Swartz. Fluence dependence of charge collection of irradiated pixel sensors. *Nuclear Instruments and Methods in Physics Research Section A: Accelerators, Spectrometers, Detectors and Associated Equipment*, 552(12):232 – 238, 2005.

[55] Synopsis TCAD. http://www.synopsys.com/tools/tcad/Pages/default.aspx.

[56] Jens Wüstenfeld. *Characterisation of ionisation induced surface effects for the optimisation of silicon detectors for particle physics applications.* PhD thesis, Technische Universität Dortmund, 2001.

[57] L Andricek, T Gebhart, D Hauff, E Koffeman, G Lutz, R.H Richter, and T Rohe. Single-sided p+n and double-sided silicon strip detectors exposed to fluences up to $2x10^{14}/cm^2$ 24 gev protons. *Nuclear Instruments and Methods in Physics Research Section A: Accelerators, Spectrometers, Detectors and Associated Equipment*, 409(13):184 – 193, 1998.

[58] Ch. Broennimann, E. F. Eikenberry, B. Henrich, R. Horisberger, G. Huelsen, E. Pohl, B. Schmitt, C. Schulze-Briese, M. Suzuki, T. Tomizaki, H. Toyokawa, and A. Wagner. The pilatus 1m detector. *Journal of Synchrotron Radiation*, 13(2):120–130, Mar 2006.

[59] Huntsman Advanced Materials. http://www.huntsman.com/advanced_materials/index.cfm?PageID=5865.

[60] Epoxy Technology. http://epotek.com/.

[61] S. Frixione, M.L. Mangano, P. Nason, and G. Ridolfi. Heavy-quark production. *Adv. Ser. Direct. High Energy Phys.*, pages 609–706, 1998.

[62] J.C. Collins and R. Ellis. Heavy quark production in very high-energy hadron collisions. *Nuclear Physics*, B360:3, 1991.

[63] S. Catani, M. Ciafaloni, and F. Hautmann. High-energy factorization and small-x heavy flavor production. *Nuclear Physics*, B366:135, 1991.

[64] M. Cacciari and M. Greco. Large p_t hadroproduction of heavy quarks. *Nuclear Physics*, B421:530, 1994.

[65] John Campbell, Keith Ellis, and Ciaran Williams. MCFM - Monte Carlo for FeMtobarn processes. `http://aea.web.psi.ch/beam2lines/beam_pie1.html`.

[66] Matteo Cacciari, Stefano Frixione, and Paolo Nason. The p_T spectrum in heavy-flavour photoproduction. *Journal of High Energy Physics*, 03:006, 2001.

[67] T. Sjöstrand, S. Mrenna, and P.Z. Skands. PYTHIA 6.4 Physics and Manual. *Journal of High Energy Physics*, 05:026, 2006.

[68] G. Gorcella *et al.* Herwig 6.5: an event generator for hadron emmission reactions with interfering gluons (including supersymmetric processes). *Journal of High Energy Physics*, 1:10, 2001.

[69] S. Frixione and B.R. Webber. Matching nlo wcd computations and parton shower simulations. *Journal of High Energy Physics*, 6:29, 2002.

[70] S. Frixione, P. Nason, and B.R. Webber. Matching nlo qcd and parton showers in heavy flavour production. *Journal of High Energy Physics*, 8:007, 2003.

[71] Stefano Frixione, Paolo Nason, and Giovanni Ridolfi. The powheg-hvq manual version 1.0. 2007.

[72] P. Bartalini and L. Fano. Multiple parton interactions at the lhc. DESY-PROC-2009-06, 2009.

[73] Torbjörn Sjöstrand. The lund monte carlo for jet fragmentation and e+e- physics - jetset version 6.2. *Computer Physics Communications*, 39(3):347 – 407, 1986.

[74] Torbjörn Sjöstrand and Mats Bengtsson. The lund monte carlo for jet fragmentation and e+ e- physics - jetset version 6.3 - an update. *Computer Physics Communications*, 43(3):367 – 379, 1987.

[75] B. Andersson, G. Gustafson, and B. Söderberg. A general model for jet fragmentation. *Zeitschrift für Physik C Particles and Fields*, 20(4):317–329, 1983.

[76] C. Peterson, D. Schlatter, I. Schmitt, and P. M. Zerwas. Scaling violations in inclusive e^+e^- annihilation spectra. *Phys. Rev. D*, 27:105–111, Jan 1983.

[77] The LHCb Collaboration. Measurement of b-hadron production fractions in $\sqrt{s} =$ 7 TeV centre-of-mass energy pp collisions. *LHCb-CONF-2011-028*, 2011.

[78] The CMS Collaboration. Inclusive b-hadron production cross section with muons in pp collisions at $\sqrt{s} = 7$ TeV. *Journal of High Energy Physics*, 03:90, 2011.

[79] The CMS Collaboration. Correlated $b\bar{b}$ cross section with dimuons. CMS PAS BPH-10-015, 2010.

[80] The CMS Collaboration. Inclusive b-jet production in pp collisions at sqrt(s)=7 TeV. CMS PAS BPH-10-009, 2010.

[81] Th. Speer K.Prokoev. A kinematic t and a decay chain reconstruction library. CMS IN-2004/020, 2004.

[82] M. Mulders, I. Bloch, E. James, A. Everett, D. Barge, C. Campagnari, P. Kalavase, V. Krutelyov, D. Kovalskyi, J. Ribnik, and N. Amapane. Muon Identification in CMS. CMS AN-2008/098, 2008.

[83] K. Nakamura *et al.* (Particle Data Group). *J. Phys. G*, 37:075021, 2010.

[84] F. James and M. Roos. Minuit: A system for function minimization and analysis of the parameter errors and correlations. *Comput.Phys.Commun.*, 10:343–367, 1975.

[85] Rene Brun and Fons Rademakers. Root - an object oriented data analysis framework. In *Proceedings AIHENP'96 Workshop*, pages 81–86, Lausanne, Sep. 1996. Nucl. Inst. & Meth. in Phys. Res. A. See also http://root.cern.ch/.

[86] The CMS Collaboration. Performance of cms muon reconstruction in pp collisions at $\sqrt{s} = 7$ TeV. CMS PAS MUO-10-004, 2010.

[87] The CMS Collaboration. Performance of muon identification in pp collisions at $\sqrt{s} = 7$ TeV. CMS PAS MUO-10-002, 2010.

[88] The CMS Collaboration. Measurement of tracking efficiency. CMS PAS TRK-10-002, 2010.

[89] The CMS Collaboration. Measurement of cms luminosity. CMS PAS EWK-10-004, 2010.

[90] L. Rossi, P. Fischer, T. Rohe, and N. Wermes. *Pixel Detectors: From Fundamentals to Applications*. Springer, 2006.

[91] S. Frixione, G. Ridolfi, and P. Nason. A positive-weight next-to-leading-order monte carlo for heavy flavour hadroproduction. *Journal of High Energy Physics*, page 126, 2007.

[92] Lukas Bäni. Measurement of the $B \to \mu D^0 X$ production cross section at the CMS experiment at $\sqrt{s} = 7$ TeV. Master's thesis, Eidgenössische Technische Hochschule Zürich, 2010.

[93] V. Radicci. CMS pixel detector upgrade. *Journal of Instrumentation*, 4:03022, 2009.

[94] The CMS Collaboration. Inclusive open-beauty production cross section with muons and jets in pp collisions at sqrt(s) = 7 TeV. CMS PAS BPH-10-008, 2011.

[95] The CMS Collaboration. Measurements of inclusive w and z cross sections in pp collisions at sqrt(s) = 7 TeV. CMS PAS EWK-10-002, 2010.

[96] ATLAS, CMS, and TOTEM Collaboration. Multiple parton interactions, underlying event and forward physics at LHC. *Proceedings of Multiple Parton Interactions at the LHC*, 2008.

[97] N. Adam, J. Berryhill, V. Halyo, A. Hunt, and K. Mishra. Generic Tag and Probe Tool for Measuring Efficiency at CMS with Early Data. CMS AN-2009/111, 2009.

[98] T. Rohe, A. Bean, W. Erdmann, H.-C. Kastli, S. Khalatyan, et al. Radiation hardness of CMS pixel barrel modules. *Nucl.Instrum.Meth.*, A624:414–418, 2010, 1001.0666.

[99] The CMS Collaboration. The tracker project technical design report. 1998.

[100] M Atac, E Bartz, G Bolla, D Bortoletto, C.Y Chien, L Cremaldi, J Doroshenko, K Giolo, B Gobbi, P Gomez, G Grim, T Koeth, Y Kozhevnikov, R Lander, S Malik, D Pellett, L Perera, M Pernicka, C Rott, A Roy, D Sanders, S Schnetzer, H Steininger, R Stone, M Swartz, R Tilden, and X Xie. Beam test results of the us-cms forward pixel detector. *Nuclear Instruments and Methods in Physics Research Section A: Accelerators, Spectrometers, Detectors and Associated Equipment*, 488:271 – 281, 2002.

A Hardness Factors

Table 21: Hardness factors of irradiation facilities used in this work [1].

Facility	Particles	κ
CERN	p 24 GeV/c	0.51 ± 0.01
KIT	p 26 MeV/c	~ 2
PSI	π^+ 300 MeV/c	~ 0.8

B Single Chip Samples

Table 22: Complete table of single ROC samples used in the charge collection efficiency and detection efficiency measurements.

Φ ($10^{14} n_{eq}/cm^2$)	Sample	Gap Type	Facility	Particle
0	8085-19-7B	dot1	–	–
0	8244-17-06	dot1	–	–
0	271947-10-08	gap30-2	–	–
3	8246-15-10	gap30	KIT	p 26 MeV
3	8246-15-12	dot1	KIT	p 26 MeV
3.2	8613-16-10	gap30	PSI	π^+ 300 MeV
4.2	260962-11-06	dot1	PSI	π^+ 300 MeV
4.2	260962-11-07	dot1	PSI	π^+ 300 MeV
4.2	8613-06-10	gap30	PSI	π^+ 300 MeV
4.2	8613-24-11	dot1	PSI	π^+ 300 MeV
4.2	8613-24-12	dot1	PSI	π^+ 300 MeV
6	8246-06-10	gap30	KIT	p 26 MeV
6	8246-06-11	dot1	KIT	p 26 MeV
6	8613-21-05	gap30	KIT	p 26 MeV

6	8613-21-07	dot1	KIT	p 26 MeV
6.1	260962-02-05	gap30	CERN	p 21 GeV
6.1	260962-16-06	dot1	CERN	p 21 GeV
6.1	8613-07-06	dot1	CERN	p 21 GeV
6.1	8613-10-05	gap30	CERN	p 21 GeV
6.1	8613-17-06	dot1	CERN	p 21 GeV
6.1	8613-17-08	gap30-2	CERN	p 21 GeV
6.2	260962-06-06	dot1	PSI	π^+ 300 MeV
6.2	260962-06-07	dot1	PSI	π^+ 300 MeV
6.2	8613-06-11	dot1	PSI	π^+ 300 MeV
6.2	8613-06-12	dot1	PSI	π^+ 300 MeV
6.2	8613-24-10	gap30	PSI	π^+ 300 MeV
11	260962-16-08	gap30-2	CERN	p 21 GeV
11	260962-20-05	gap30	CERN	p 21 GeV
11	260962-20-06	dot1	CERN	p 21 GeV
11	260962-20-08	gap30-2	CERN	p 21 GeV
11	260962-23-06	dot1	CERN	p 21 GeV
11	8613-02-10	gap30	CERN	p 21 GeV
11	8613-13-06	dot1	CERN	p 21 GeV
12	260961-15-10	gap30	KIT	p 26 MeV
12	260961-15-11	dot1	KIT	p 26 MeV
12	8613-08-05	gap30	KIT	p 26 MeV
12	8613-08-06	dot1	KIT	p 26 MeV
12	8613-08-07	dot1	KIT	p 26 MeV
28	260962-21-08	gap30-2	CERN	p 21 GeV
28	8613-13-08	gap30-2	CERN	p 21 GeV
28	8613-18-06	dot1	CERN	p 21 GeV
28	8613-18-08	gap30-2	CERN	p 21 GeV

30	8210-22-05	gap30	KIT	p 26 MeV
30	8210-22-07	dot1	KIT	p 26 MeV
30	8608-02-05	gap30	KIT	p 26 MeV
30	8608-02-06	dot1	KIT	p 26 MeV
30	8608-02-07	dot1	KIT	p 26 MeV
51	260962-14-06	dot1	CERN	p 21 GeV
51	8613-13-05	gap30	CERN	p 21 GeV

C Single ROC DAC values

Table 23: Commonly used DAC values used for testing CMS barrel pixel sensors.

DAC	Value	High Fluence Value
Vdig	6	6
Vana	145	125
Vsf	150	180
Vcomp	10	10
Vleak_comp	0	0
VrgPr	0	0
VwllPr	35	0
VrgSh	0	0
VwllSh	35	0
VhldDel	160	160
Vtrim	7	7
VthrComp	79	91
VIBias_Bus	30	30
Vbias_sf	10	10
VoffsetOp	22	57
VIbiasOp	50	50
VOffsetR0	120	60
VIon	130	130
VIbias_PH	120	220
Ibias_DAC	111	82
VIbias_roc	150	220
VIColOr	99	99
Vnpix	0	0
VSumCol	0	0
Vcal	199	199
CalDel	64	108
RangeTemp	0	0
CtrlReg	0	0
WBC	100	100

D Backgrounds

D^0 invariant mass distribution after each selection cut, showing the signals and the backgrounds. Classification of backgrounds is shown in Table 24.

Table 24: Background classifications.

Sig Number	BG Source
-1	Tagging failed
1	True signal
2	$B \to \tau(\tau \to \mu)D^0X$
3	μ, D^0 from different b's
4	μ, D^0 from c's
5	μ from light quark
6	fake μ
7	fake D^0
8	both μ, D^0 fake
9	D^0 has more than 2 daughters
10	μ, D^0 from one b, one c
11	K, π switched

D.1 Right Sign Charge Correlation

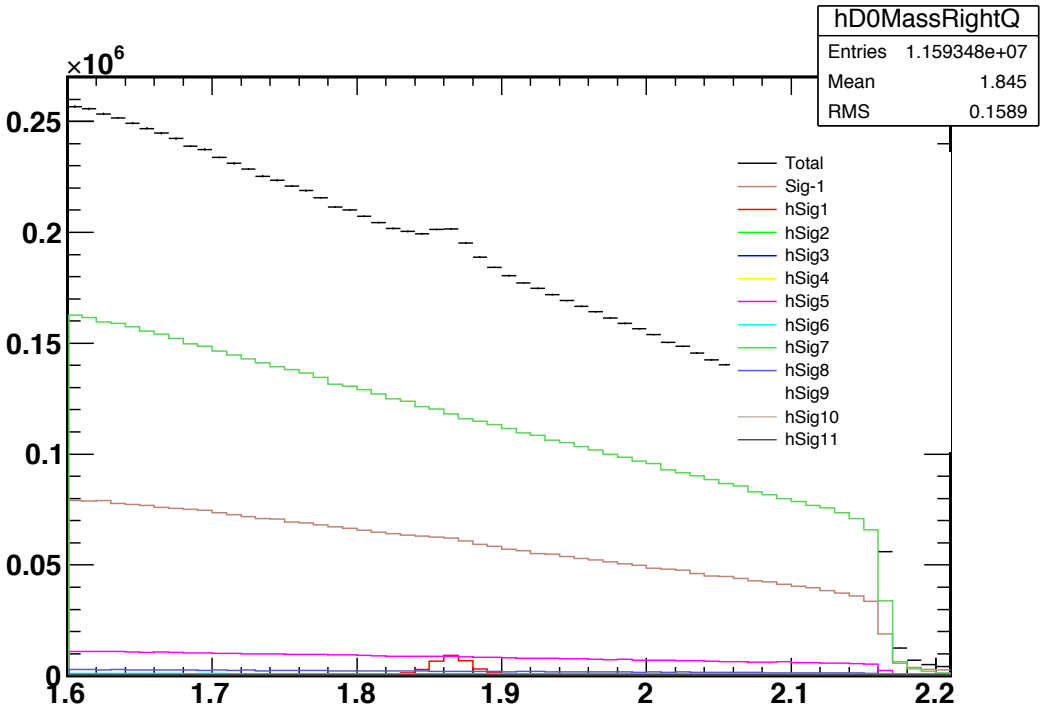

Figure 117: After acceptance cuts only.

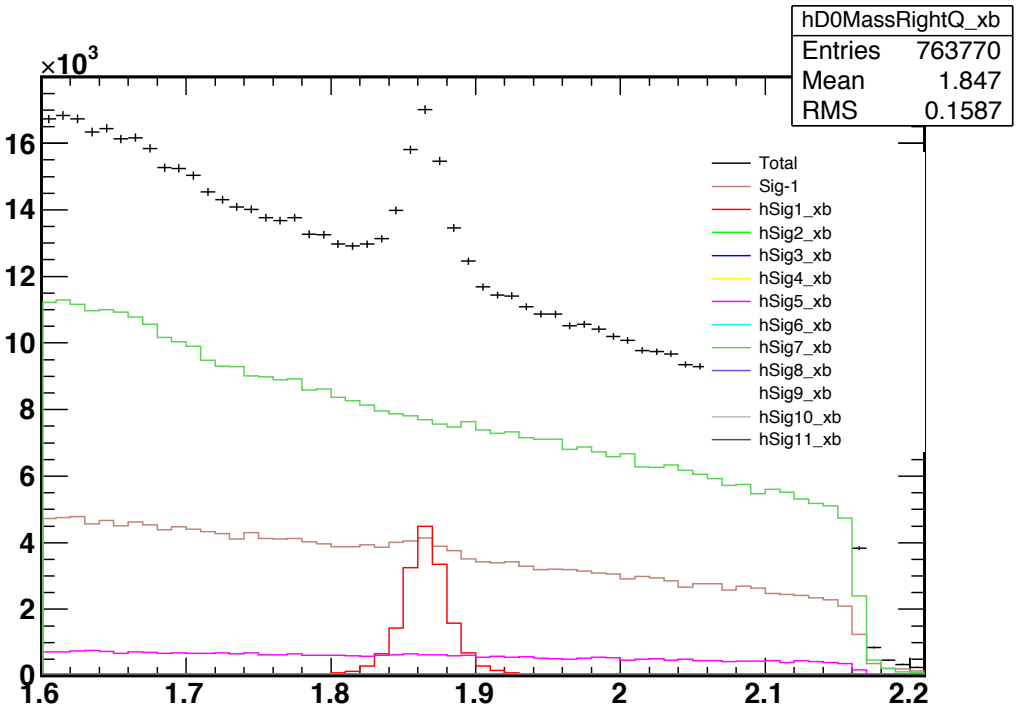

Figure 118: After xb cut.

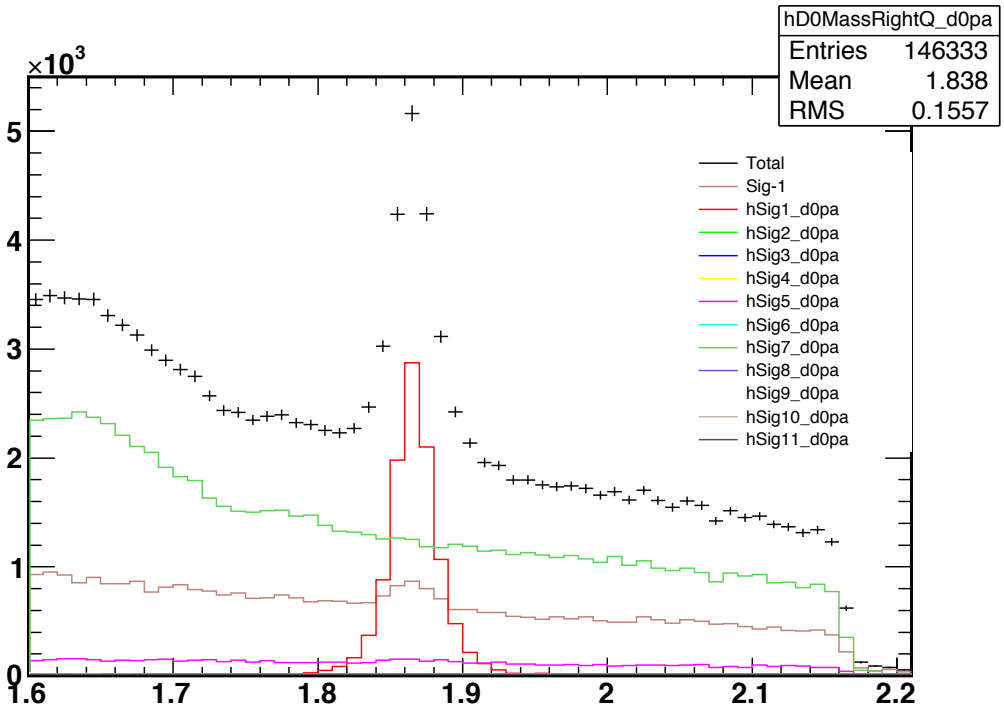

Figure 119: After D^0 pointing angle cut.

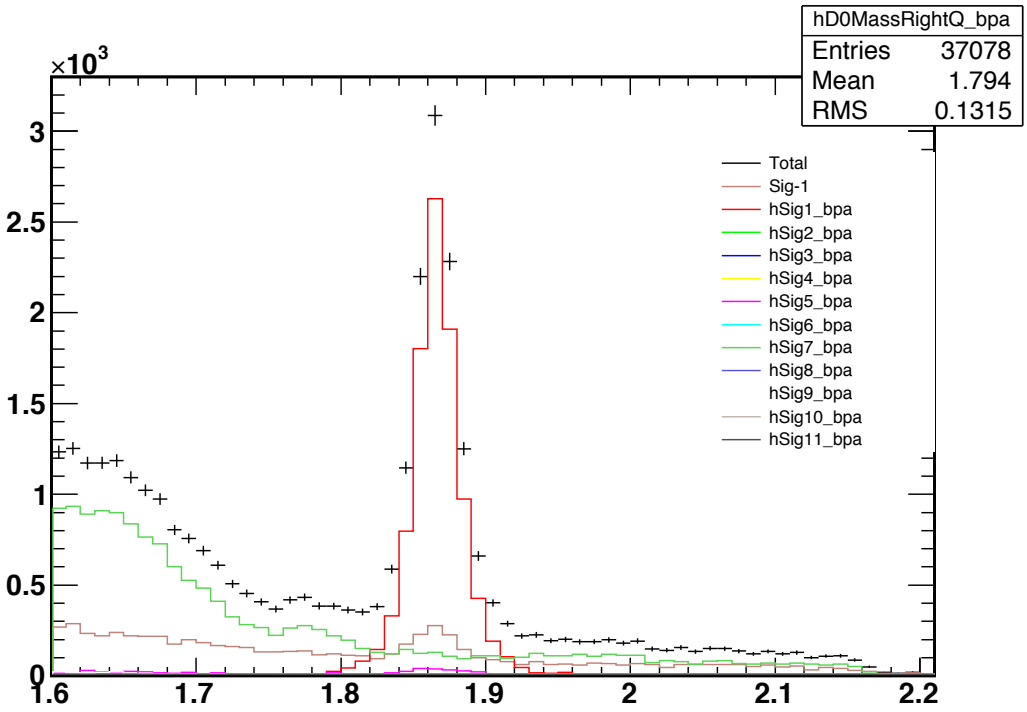

Figure 120: After B pointing angle cut.

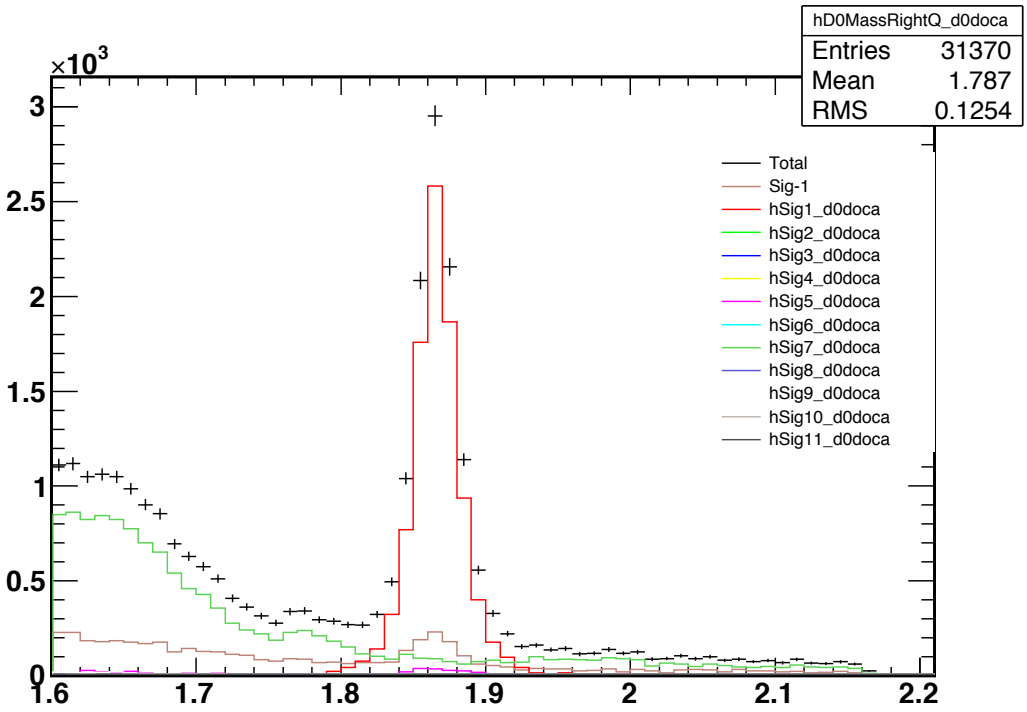

Figure 121: After D^0 doca cut.

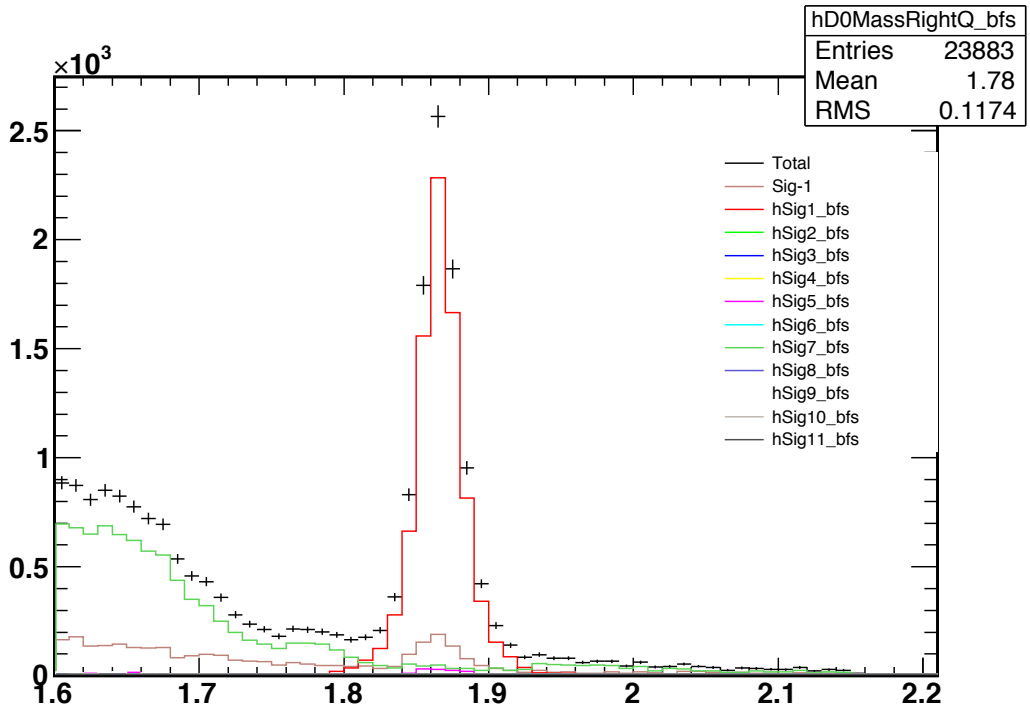

Figure 122: After B 3D flight sig cut.

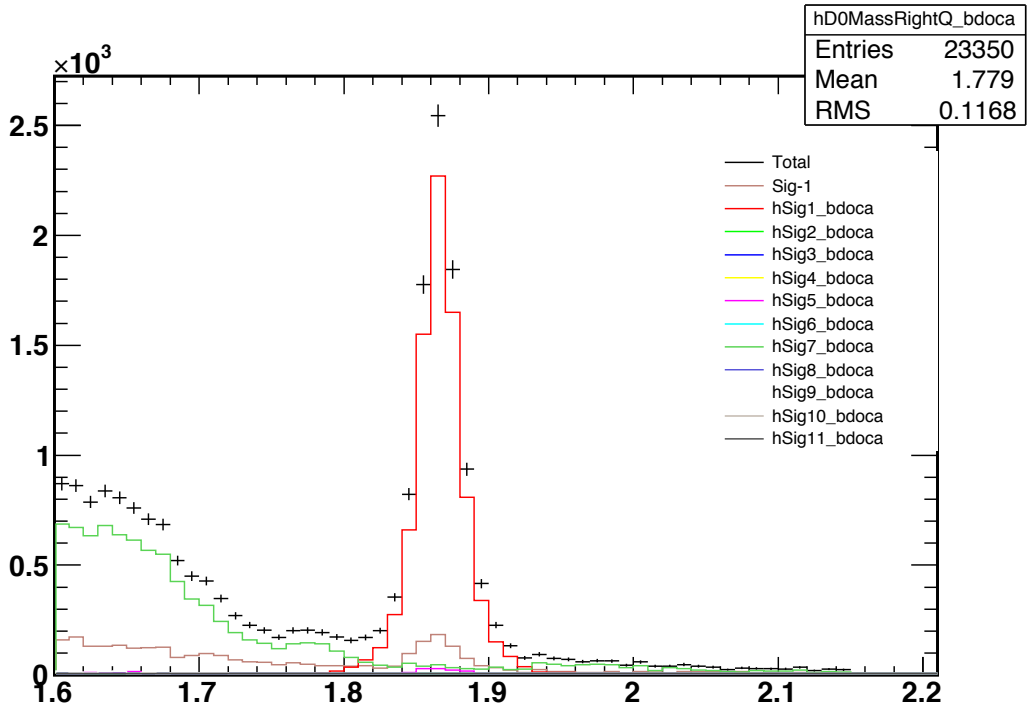

Figure 123: After B doca cut. (all selection cuts)

D.2 Wrong Sign Charge Correlation

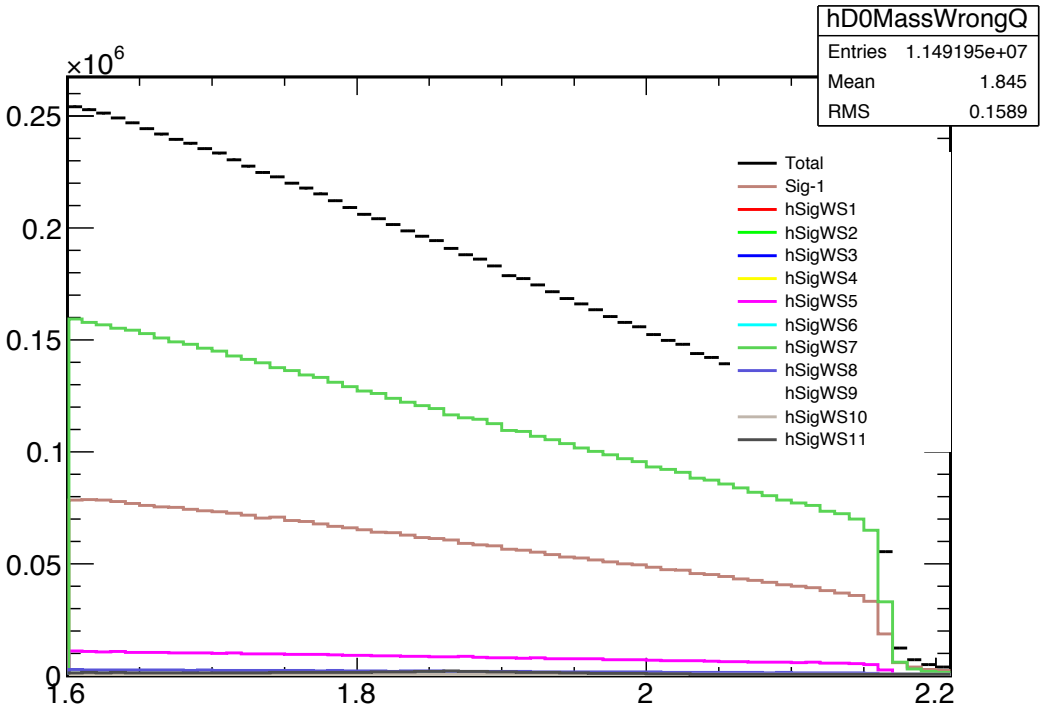

Figure 124: After acceptance cuts only.

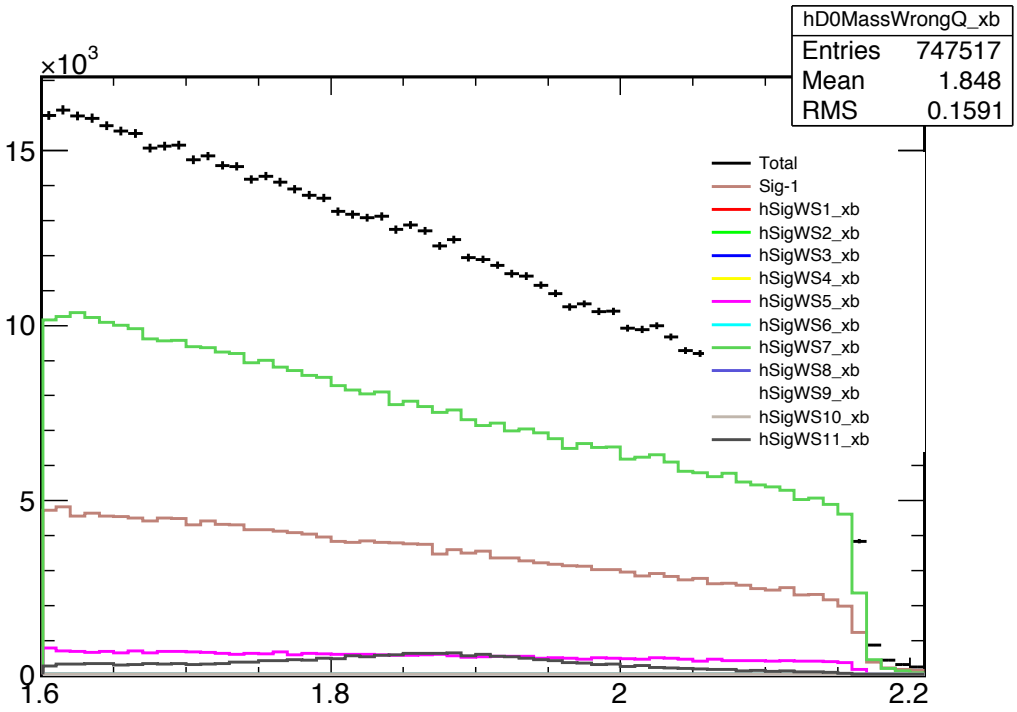

Figure 125: After xb cut.

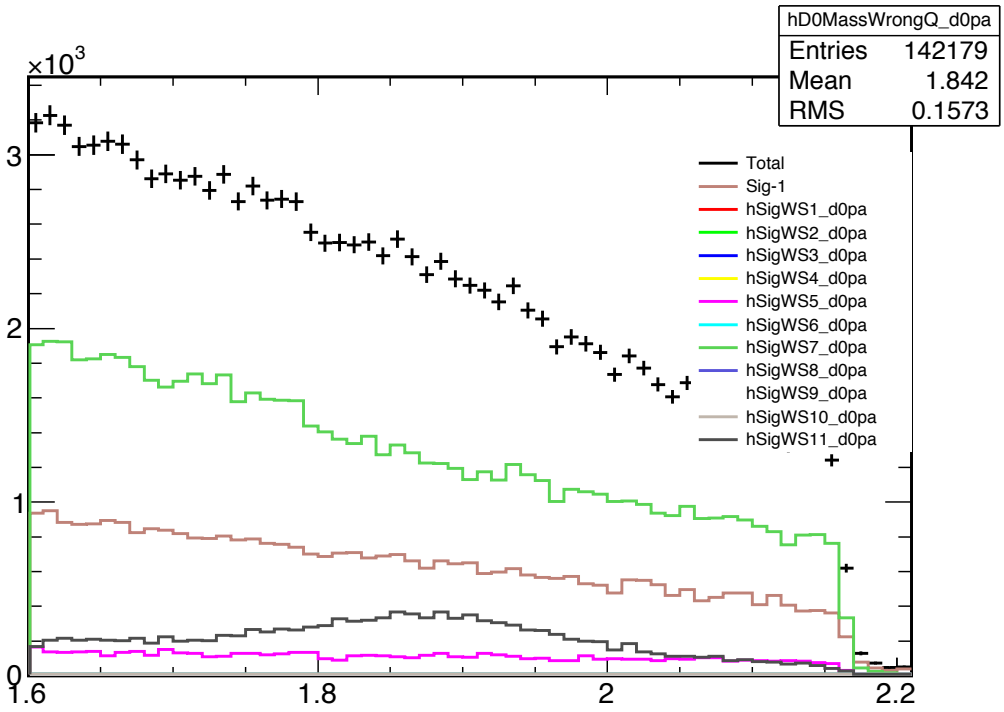

Figure 126: After D^0 pointing angle cut.

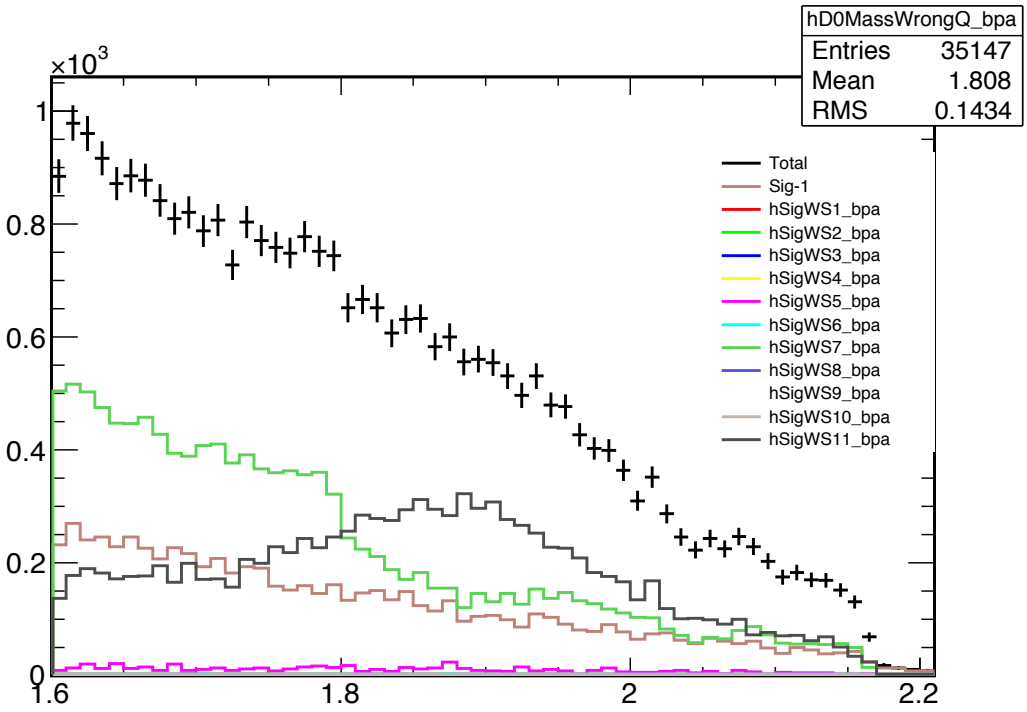

Figure 127: After B pointing angle cut.

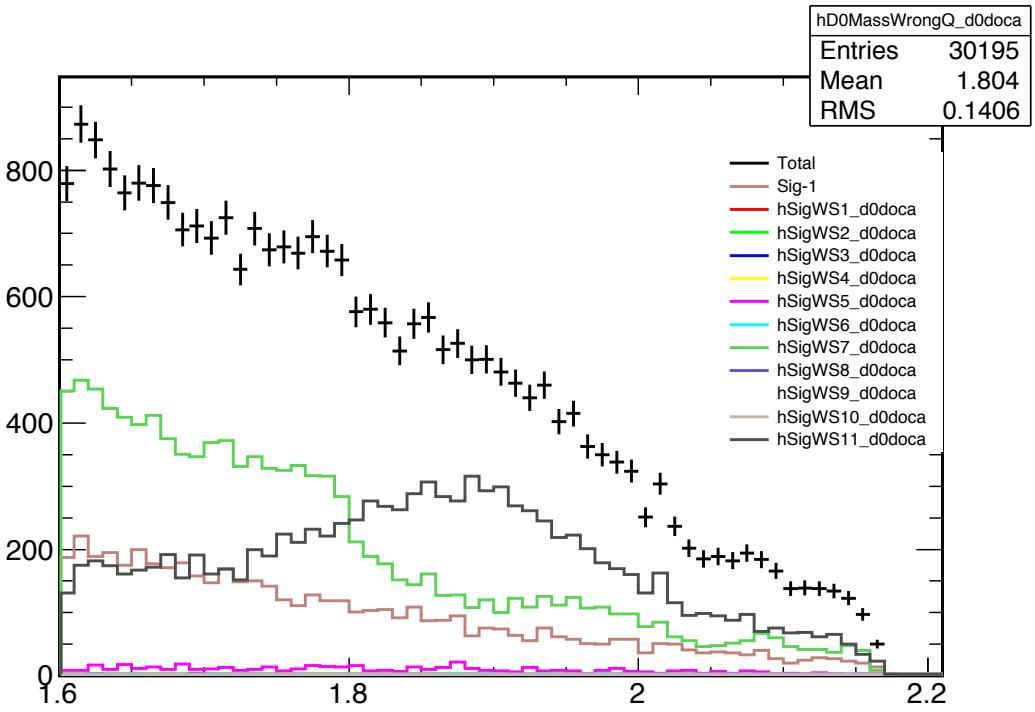

Figure 128: After D^0 doca cut.

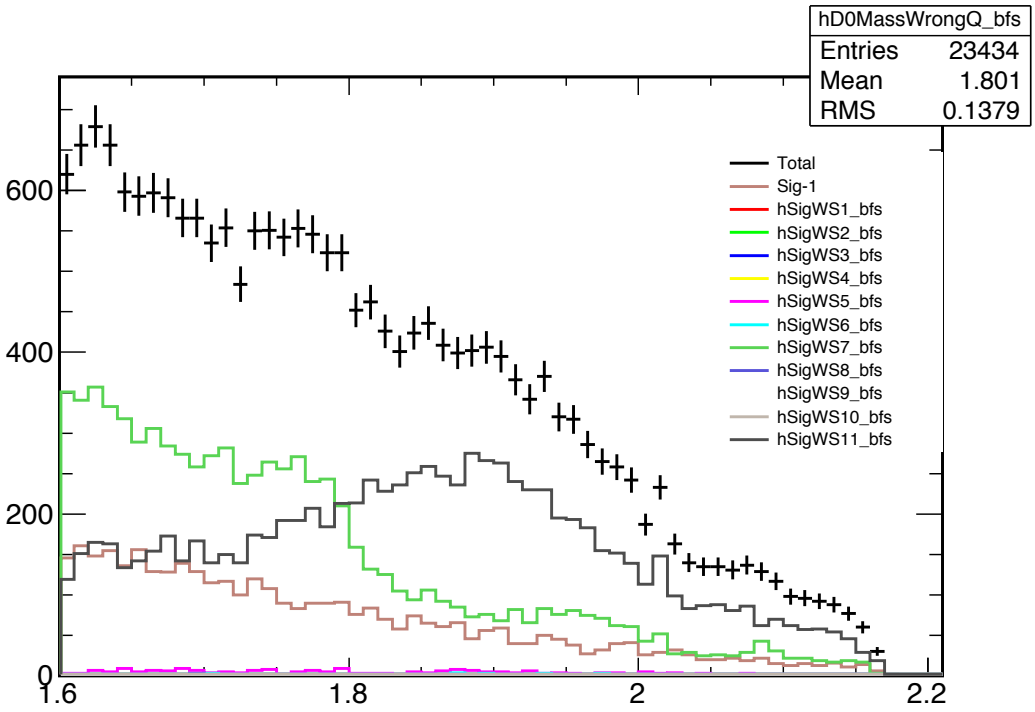

Figure 129: After B 3D flight sig cut.

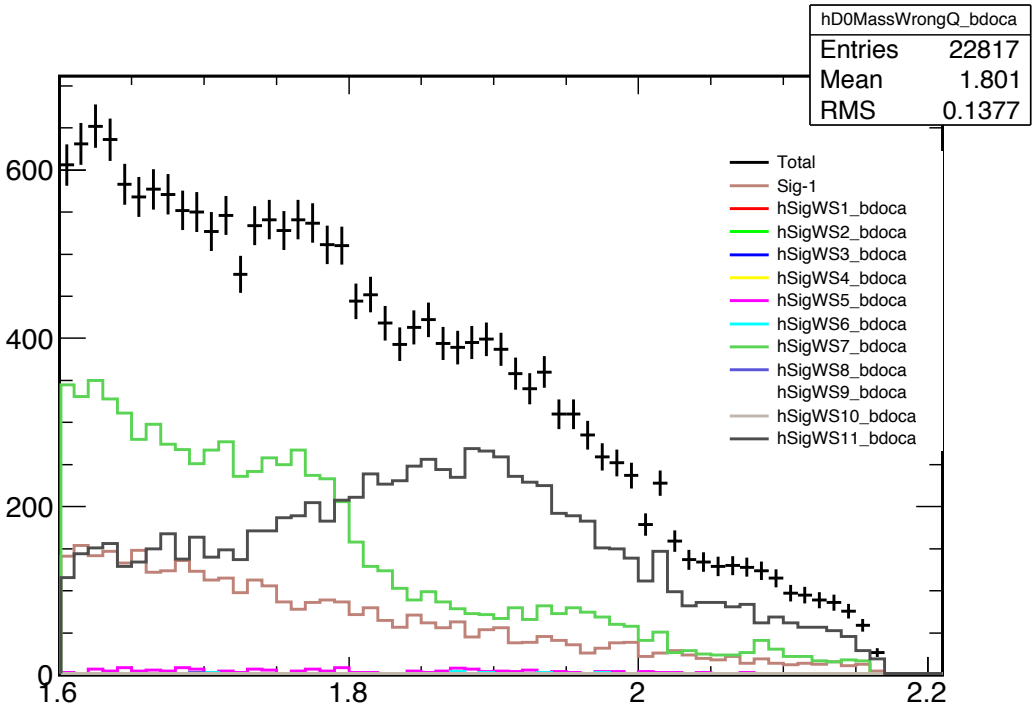

Figure 130: After B doca cut. (all selection cuts)

E Alternate Cut Optimization

In order to show that the order chosen for the cut variables does not change the end result, the cut optimization was redone. The variable with the second highest significance was chosen as the first variable in the procedure. The x_b variable is deliberately chosen last to ensure that it does not influence the choice of cut value on the other variables. The distributions for the first pass are shown again in Figure 131.

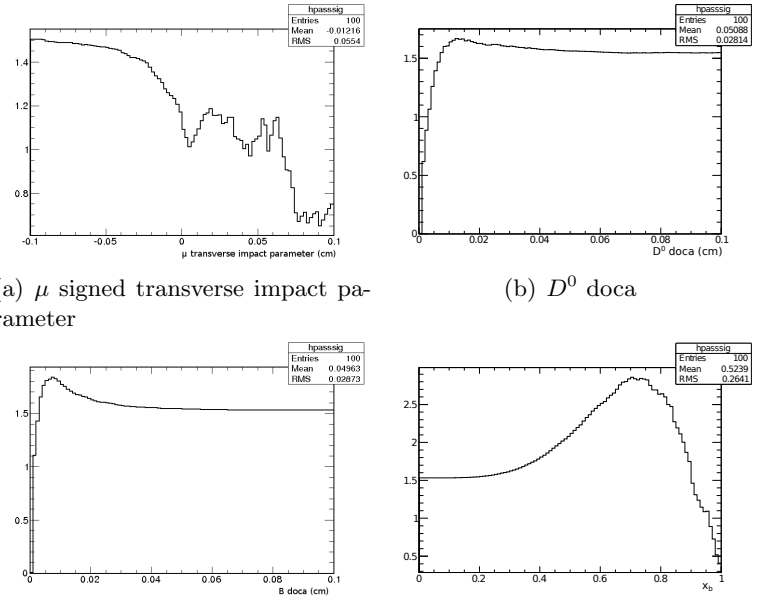

(a) μ signed transverse impact parameter

(b) D^0 doca

(c) B doca

(d) x_b

Figure 131: Distributions of $S/\sqrt{B}$ after the quality cuts.

From these distributions we see that the B doca variable has the second best significance after the acceptance and quality cuts, and the significance is maximum at a cut value of 0.007. For the second pass, we require B doca < 0.007 and repeat the procedure for all other variables. The distributions for the second pass are shown in Figure 132.

After the second pass we determine that the D^0 doca shows the best significance aside from the x_b variable. The maximum is at a cut value of 0.015. For the third pass, we repeat the procedure, requiring that both B doca > 0.007 and the D^0 doca

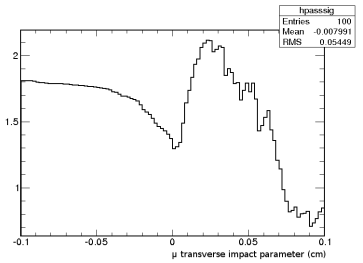

(a) μ signed transverse impact parameter

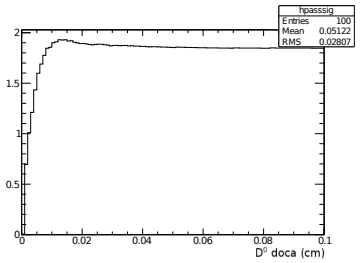

(b) D^0 doca

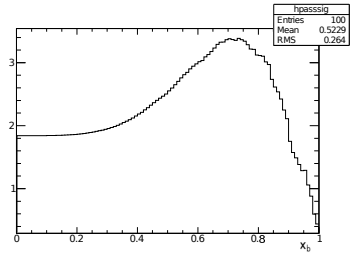

(c) s_b

Figure 132: Distributions of $S/\sqrt{B}$ after the quality cuts, and B doca > 0.007.

< 0.015. The distributions for the remaining variables after the third pass are shown in Figure 133.

Because the muon transverse impact parameter does not show any significant discrimination between signal and background except in the right tail of the distribution, this variable is not used. The maximum value of the significance of the x_b variable is at 0.7. Finally, for the event selection we require:

1. The B doca is less than 0.007.

2. The D^0 doca is less than 0.015.

3. x_b is greater than 0.7.

Changing the order of the variable selection resulted in the same final cut selection. Therefore the cuts are considered to be stable and unbiased.

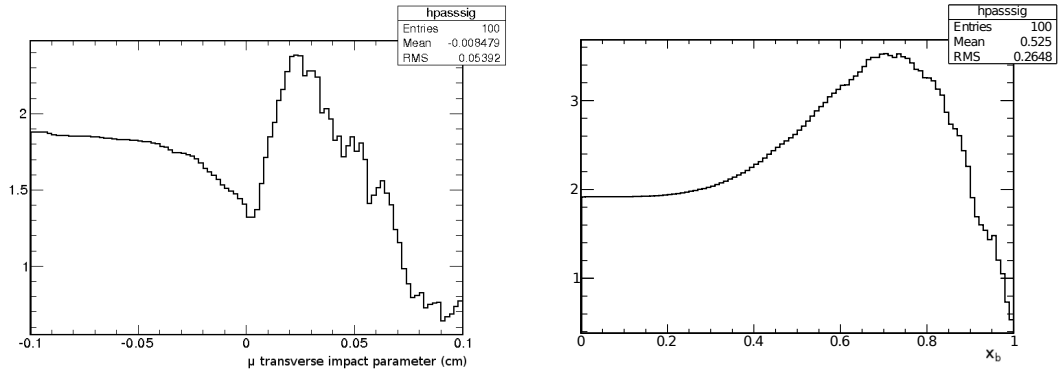

(a) μ signed transverse impact parameter (b) x_b

Figure 133: Distributions of $S/\sqrt{B}$ after the acceptance cuts, $B > 0.007$, and D^0 doca < 0.015.

F μ Bins

The analysis was also performed using bins of p_{T} (μ) and $|\eta(\mu)|$ as a cross check. Using bins of the μ instead of the μD^0 is simpler, as the trigger efficiency has the same binning as the results. The same cut values are used as in the case of the μD^0 bins.

F.1 Reconstruction and Selection Efficiency

Table 25: Selection cut efficiencies in bins of $p_{\mathrm{T}}(\mu)$ using the HLT_Mu5 trigger.

Bin	Total	Passing	Eff
$5 \leq p_{\mathrm{T}} < 10$	19670	7736	0.39
$10 \leq p_{\mathrm{T}} < 15$	2706	1343	0.5
$15 \leq p_{\mathrm{T}} < 20$	570	303	0.53
$20 \leq p_{\mathrm{T}} < 30$	308	200	0.65
$30 \leq p_{\mathrm{T}} < 50$	53	33	0.62
$50 \leq p_{\mathrm{T}} < 80$	5	4	0.8
$0 \leq \|\eta\| < 0.9$	17912	4808	0.27
$0.9 \leq \|\eta\| < 1.5$	9552	2678	0.28
$1.5 \leq \|\eta\| < 2.1$	6106	1835	0.3
$2.1 \leq \|\eta\| < 2.4$	934	298	0.32

Table 26: Selection cut efficiencies in bins of $p_{\mathrm{T}}(\mu)$ using the HLT_Mu15_v1 trigger.

Bin	Total	Passing	Eff
$15 \leq p_{\mathrm{T}} < 20$	570	303	0.53
$20 \leq p_{\mathrm{T}} < 30$	308	200	0.65
$30 \leq p_{\mathrm{T}} < 50$	53	33	0.62
$50 \leq p_{\mathrm{T}} < 80$	5	4	0.8
$0 \leq \|\eta\| < 0.9$	638	278	0.44
$0.9 \leq \|\eta\| < 1.5$	283	130	0.46
$1.5 \leq \|\eta\| < 2.1$	230	112	0.49
$2.1 \leq \|\eta\| < 2.4$	38	20	0.53

F.2 D^0 Candidate Invariant Mass Fits

Table 27: The reconstruction and selection efficiency in each p_{T} (μ) and $|\eta(\mu)|$ bin.

Bin	Eff5	Eff15
$6 \leq p_{\mathrm{T}} < 11$	0.22 ± 0.003	–
$11 \leq p_{\mathrm{T}} < 16$	0.33 ± 0.009	–
$16 \leq p_{\mathrm{T}} < 20$	0.37 ± 0.02	0.37 ± 0.02
$20 \leq p_{\mathrm{T}} < 30$	0.45 ± 0.03	0.45 ± 0.03
$30 \leq p_{\mathrm{T}} < 50$	0.42 ± 0.06	0.42 ± 0.06
$50 \leq p_{\mathrm{T}} < 80$	0.57 ± 0.29	0.57 ± 0.29
$0 \leq \|\eta\| < 0.9$	0.16 ± 0.002	0.33 ± 0.02
$0.9 \leq \|\eta\| < 1.5$	0.16 ± 0.003	0.30 ± 0.03
$1.5 \leq \|\eta\| < 2.1$	0.14 ± 0.003	0.32 ± 0.03
$2.1 \leq \|\eta\| < 2.4$	0.09 ± 0.005	0.2 ± 0.04

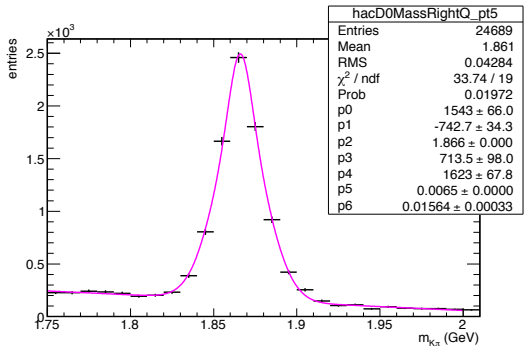

(a) $5 \leq p_{\mathrm{T}} < 10$

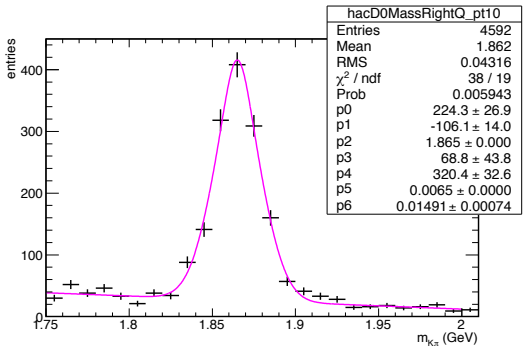

(b) $10 \leq p_{\mathrm{T}} < 15$

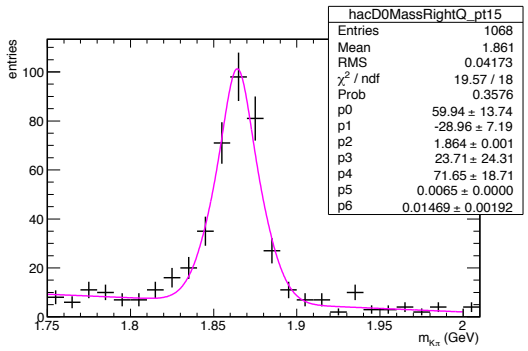

(c) $15 \leq p_{\mathrm{T}} < 20$

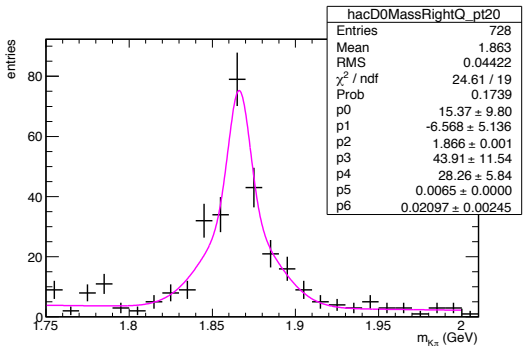

(d) $20 \leq p_{\mathrm{T}} < 30$

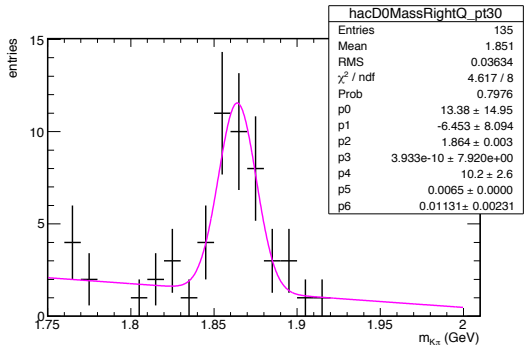

(e) $30 \leq p_{\mathrm{T}} < 50$

Figure 134: D^0 mass distributions in bins of p_{T} (GeV/c) for Monte Carlo events.

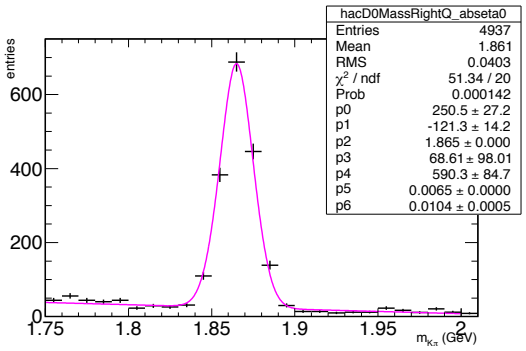

(a) $0.0 \leq |\eta| < 0.3$

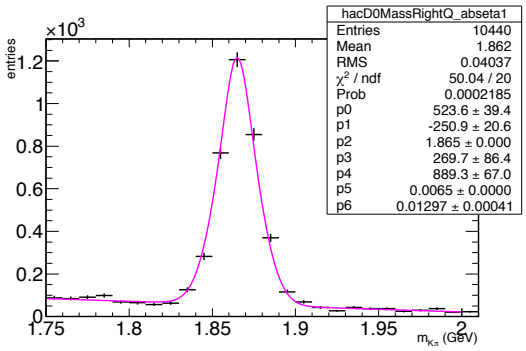

(b) $0.3 \leq |\eta| < 0.9$

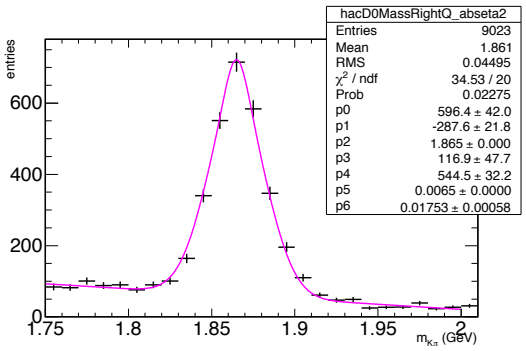

(c) $0.9 \leq |\eta| < 1.5$

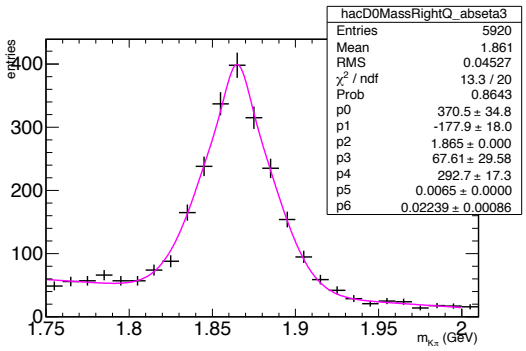

(d) $1.5 \leq |\eta| < 2.1$

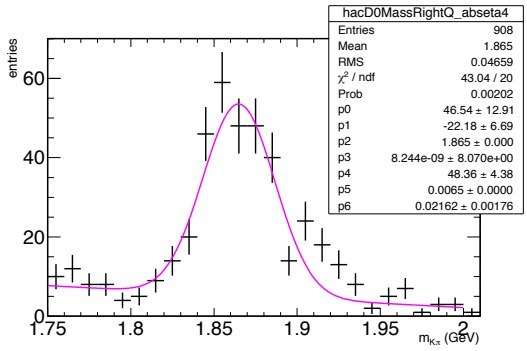

(e) $2.1 \leq |\eta| < 2.4$

Figure 135: D^0 mass distributions in bins of $|\eta|$ for Monte Carlo events.

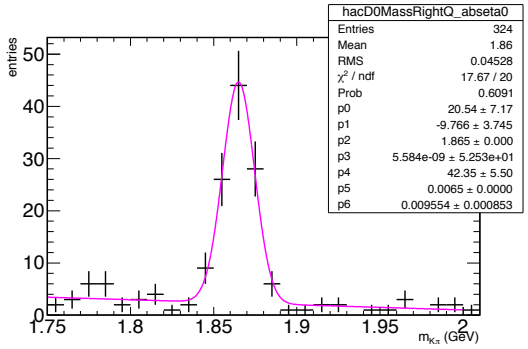

(a) $0.0 \leq |\eta| < 0.3$

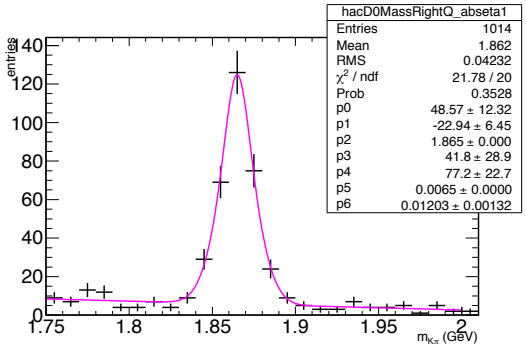

(b) $0.3 \leq |\eta| < 0.9$

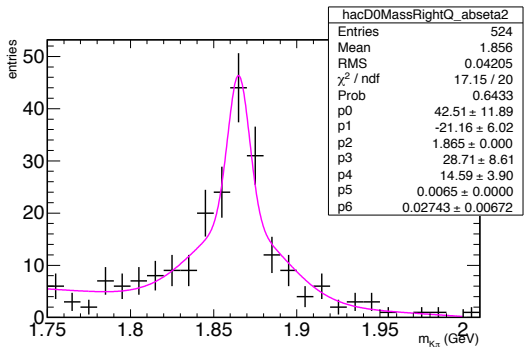

(c) $0.9 \leq |\eta| < 1.5$

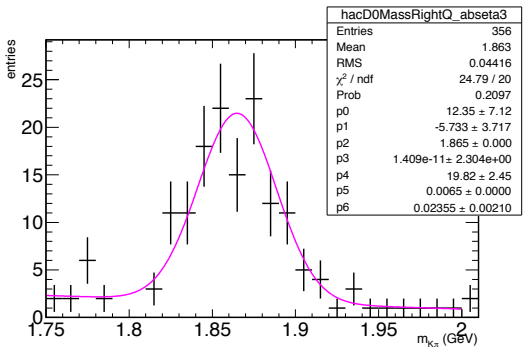

(d) $1.5 \leq |\eta| < 2.1$

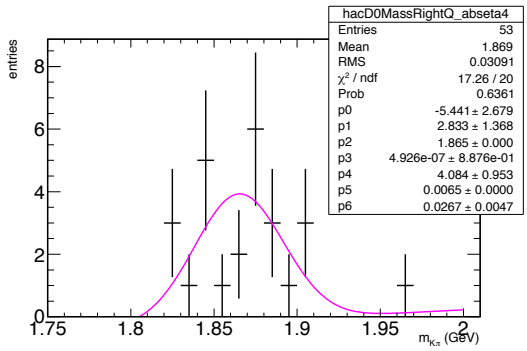

(e) $2.1 \leq |\eta| < 2.4$

Figure 136: D^0 mass distributions in bins of $|\eta|$ for Monte Carlo events with p_{T} $(\mu) >$ 15GeV.

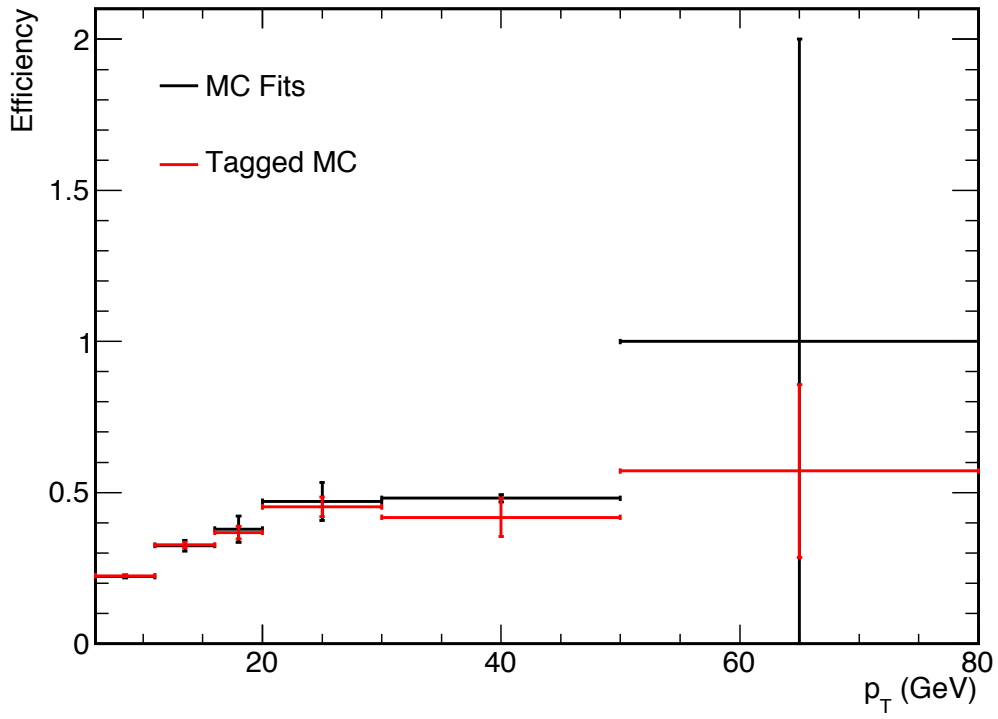

Figure 137: The tracking, reconstruction and event selection efficiency as a function of p_{T} (μ).

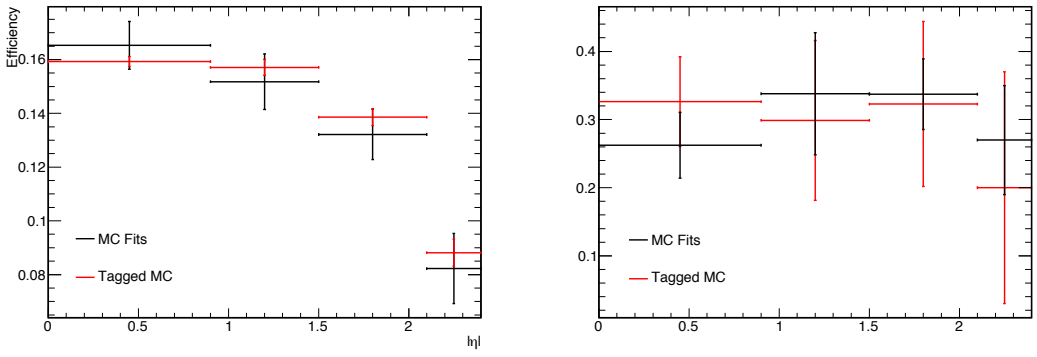

Figure 138: The tracking, reconstruction, and event selection efficiency for Run A (left) and Run B (right) as a function of $|\eta(\mu)|$.

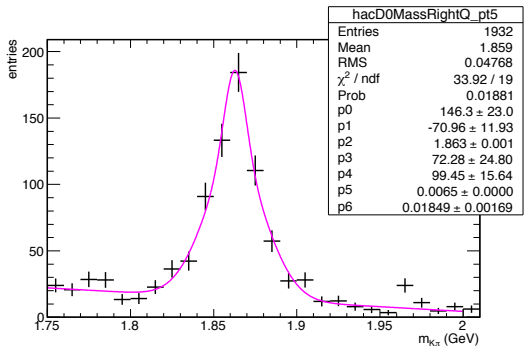

(a) $5 \leq p_{\mathrm{T}} < 10$

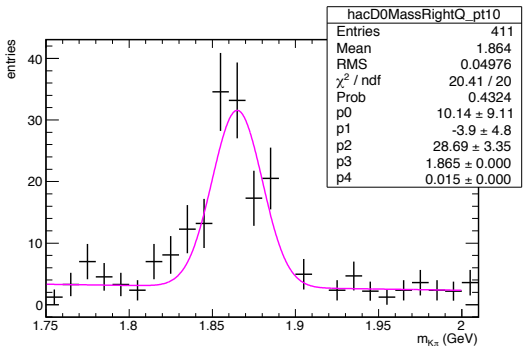

(b) $10 \leq p_{\mathrm{T}} < 15$

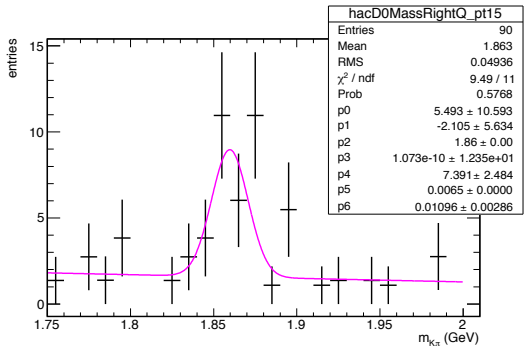

(c) $15 \leq p_{\mathrm{T}} < 20$

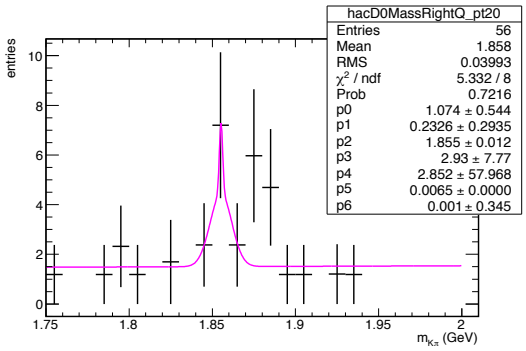

(d) $20 \leq p_{\mathrm{T}} < 30$

Figure 139: D^0 mass distributions in bins of p_{T} (GeV/c) for the 2010A dataset.

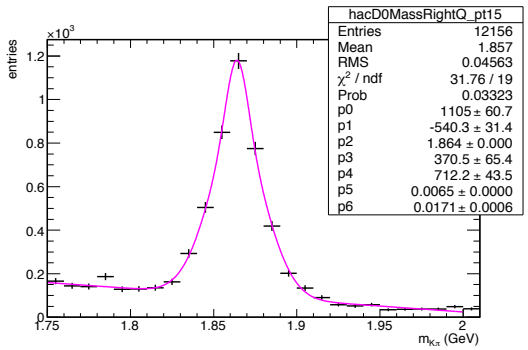

(a) $15 \leq p_{\mathrm{T}} < 20$

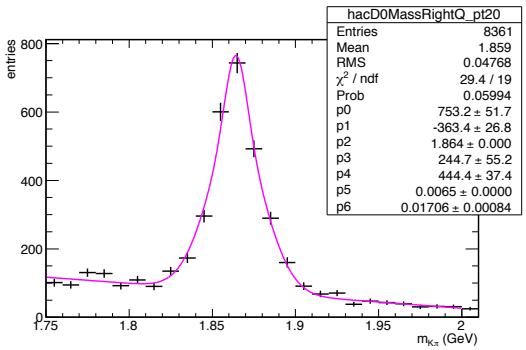

(b) $20 \leq p_{\mathrm{T}} < 30$

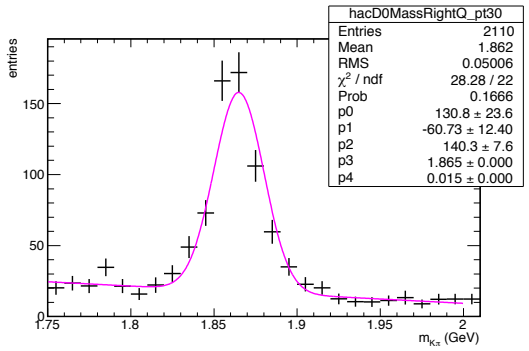

(c) $30 \leq p_{\mathrm{T}} < 50$

Figure 140: D^0 mass distributions in bins of p_{T} (GeV/c) for the 2010B dataset.

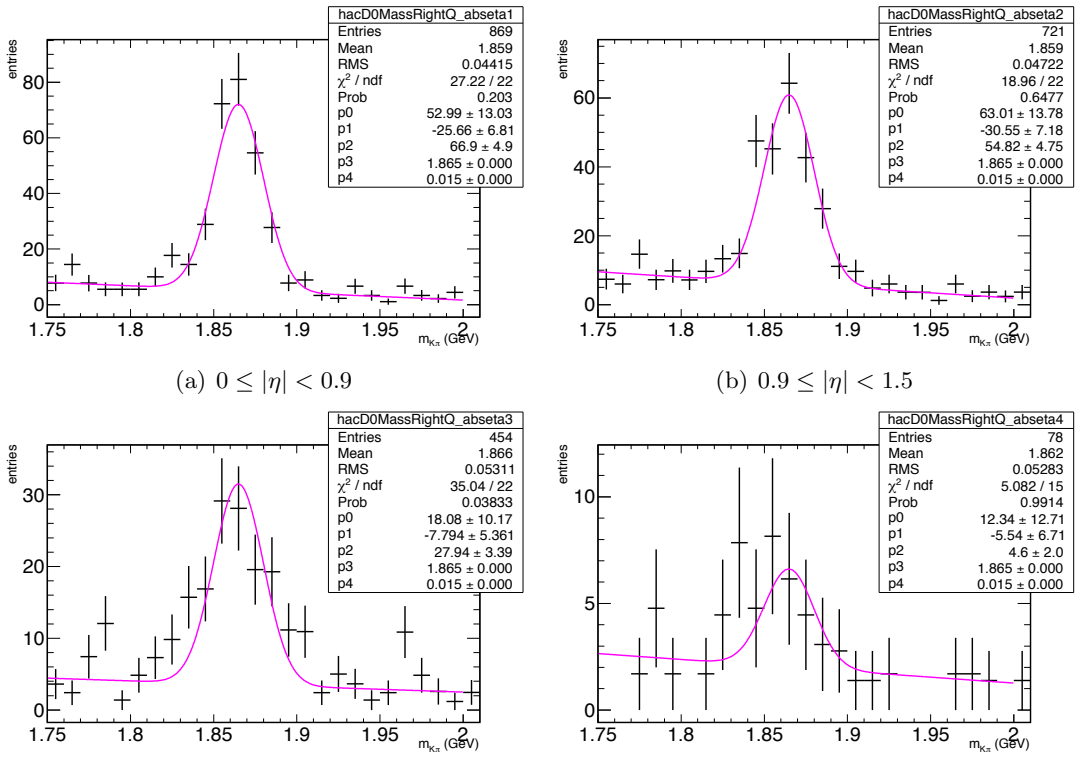

(a) $0 \leq |\eta| < 0.9$

(b) $0.9 \leq |\eta| < 1.5$

(c) $1.5 \leq |\eta| < 2.1$

(d) $2.1 \leq |\eta| < 2.4$

Figure 141: D^0 mass distributions in bins of $|\eta|$ for the 2010A dataset.

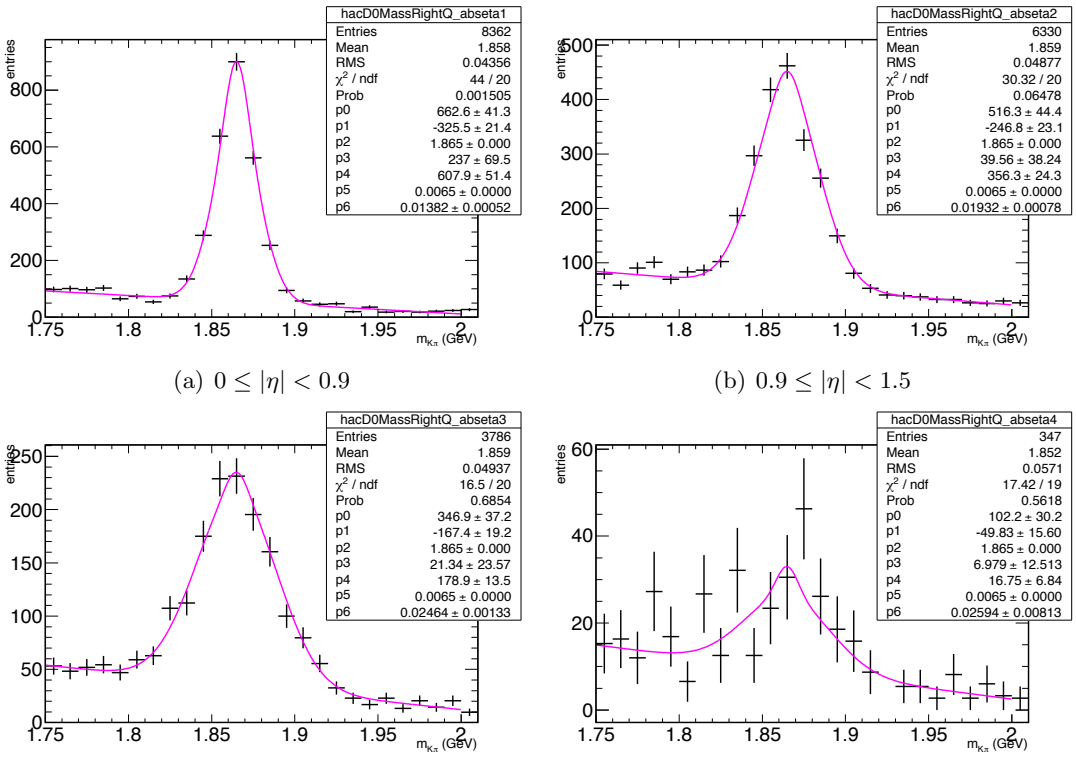

(a) $0 \leq |\eta| < 0.9$

(b) $0.9 \leq |\eta| < 1.5$

(c) $1.5 \leq |\eta| < 2.1$

(d) $2.1 \leq |\eta| < 2.4$

Figure 142: D^0 mass distributions in bins of $|\eta|$ for the 2010B dataset.

F.3 Wrong Charge Correlation Distributions

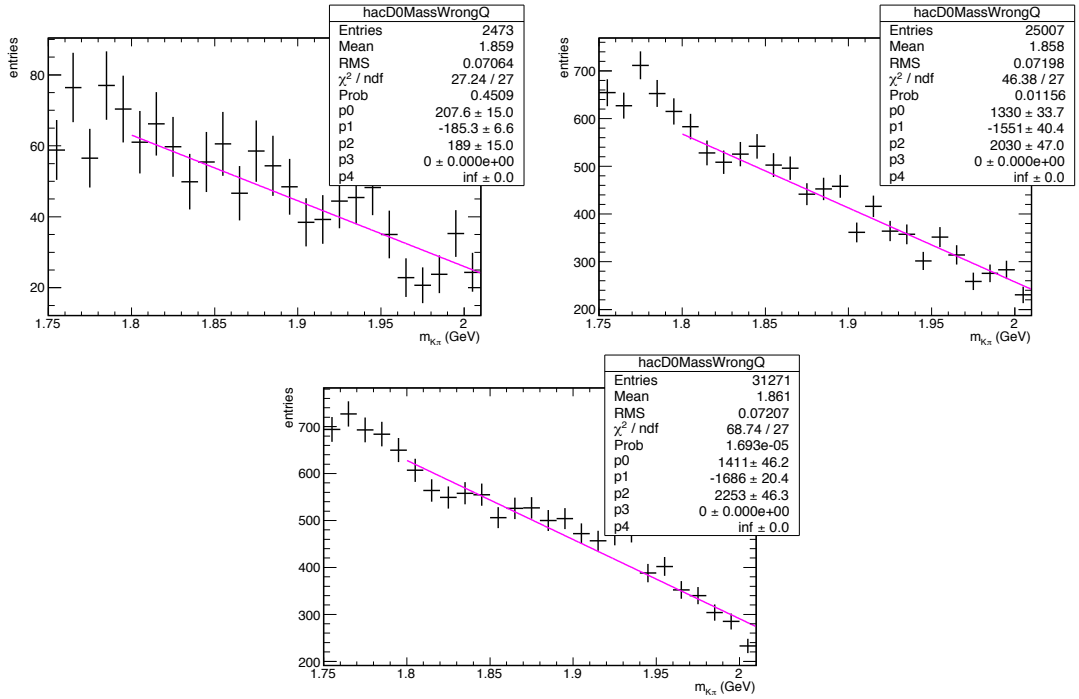

Figure 143: D^0 mass distribution of the wrong charge correlation candidates for the whole p_{T} and η range for the 2010A data (top left), 2010B data (top right), and Monte Carlo events (bottom).

F.4 Systematic Uncertainties

The systematic uncertainty due to the trigger efficiency is found by varying the trigger efficiency up and down, and checking the effect on the final cross section in each bin. The uncertainty for each bin resulting from the error on the trigger efficiency is shown in Tables 28.

The systematic uncertainty due to the selection efficiency is found by varying the selection efficiency by the error on the efficiency. This is the dominant uncertainty in this analysis, due to the low statistics in the Monte Carlo. The uncertainty for each bin resulting from the error on the selection efficiency is shown in Tables 30 and 31.

As in the case of using bins of the μD^0, the total bin-independent systematic uncer-

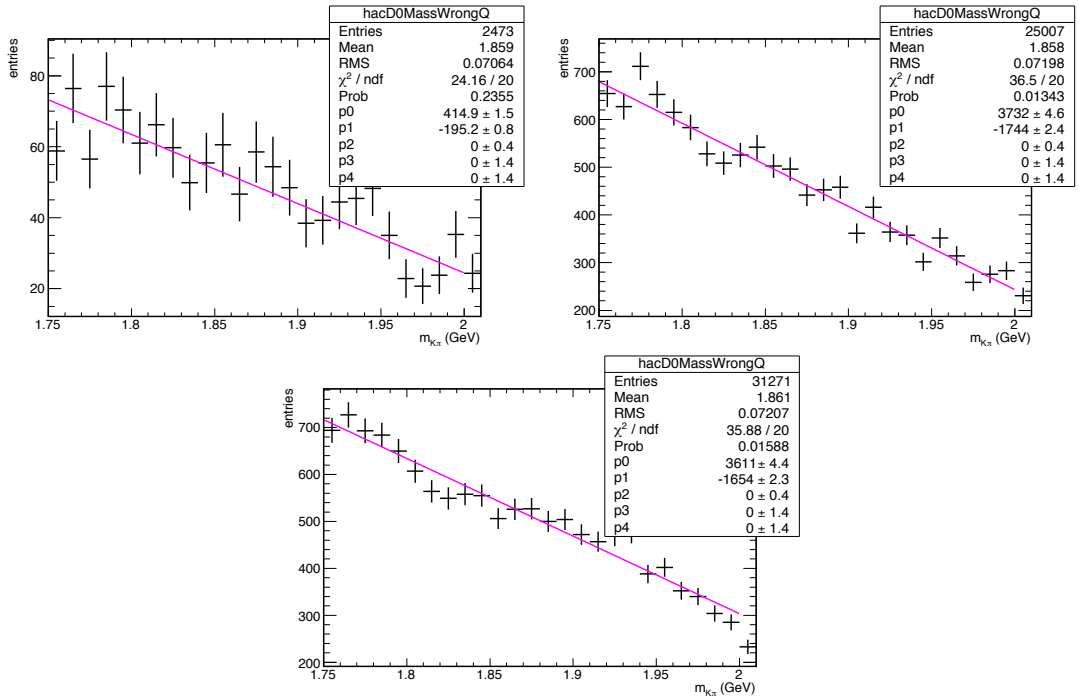

Figure 144: D^0 mass distribution of the wrong charge correlation candidates for the whole p_{T} and η range for the 2010A data (top left), 2010B data (top right), and Monte Carlo events (bottom). Fits assume background only.

tainty is 7.4%.

F.5 Results

The results are shown in Figure 145 as a function of p_{T} (μ), and in Figures 146 and 147 as a function of $|\eta(\mu)|$. The Monte Carlo cross section is calculated using the number of generated signal events and an efficiency of 1.

The cross section in each bin is listed in Table 32 as a function of p_{T} , and in Table 33 as a function of $|\eta|$.

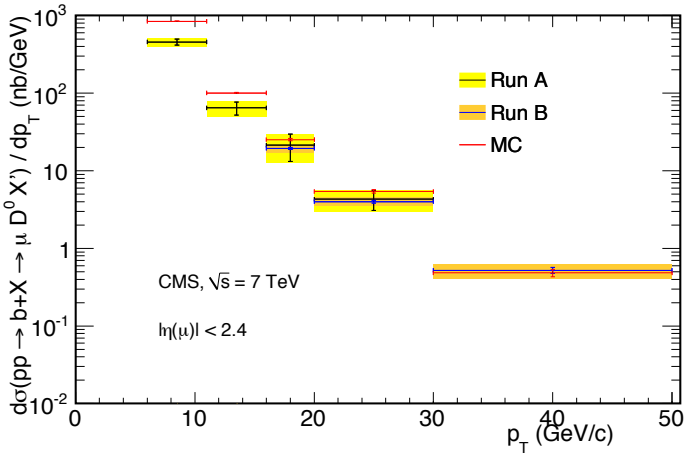

Figure 145: Cross section as a function of $p_{\mathrm{T}}(\mu)$ for Run A (black), Run B (blue), and Monte Carlo (red) events. Error bars show the statistical uncertainty, and the colored bands show the combined statistical and systematic uncertainty.

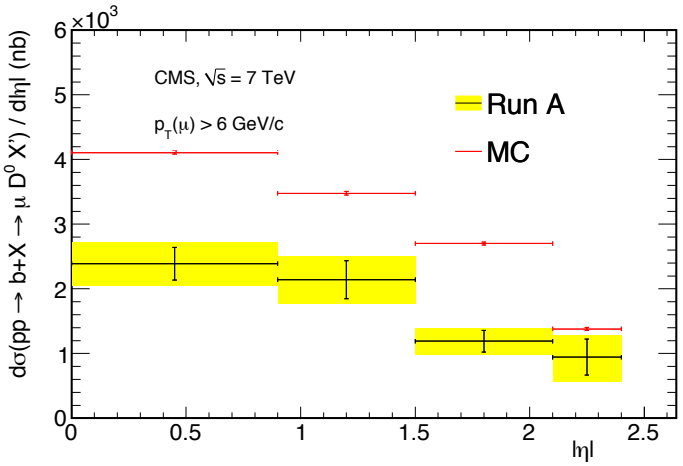

Figure 146: Cross section as a function of $|\eta|(\mu)$ for Run A (black) and Monte Carlo (red) events. Error bars show the statistical uncertainty, and the colored band shows the combined statistical and systematic uncertainty.

Table 28: Systematic uncertainty due to the error on the trigger efficiency in each bin.

Trigger	p_{T} (μ)	Cross Section (nb)	Cross Section (nb) Trig. eff. up	Cross Section (nb) Trig. eff. down	Uncertainty Trig. eff. up	Uncertainty Trig. eff. down
HLT_Mu5	6 - 11 GeV	457.5 ± 39.6	444.3 ± 37.9	475.6 ± 41.2	2.9%	4.0%
	11 - 16 GeV	64.7 ± 12.5	62.4 ± 12.5	68.7 ± 13.1	3.6%	6.2%
	16 - 20 GeV	21.4 ± 8.2	20.1 ± 8.2	23.3 ± 7.6	6.1%	8.9%
	20 - 30 GeV	4.3 ± 1.2	4.1 ± 1.2	4.5 ± 1.2	4.7%	4.7%
HLT_Mu15_v1	16 - 20 GeV	19.5 ± 0.6	19.3 ± 0.7	19.7 ± 0.7	1.0%	1.0%
	20 - 30 GeV	4.00 ± 0.2	3.96 ± 0.17	4.04 ± 0.18	1.0%	1.0%
	30 - 50 GeV	0.52 ± 0.05	0.51 ± 0.05	0.53 ± 0.05	1.9%	1.9%

Table 29: Systematic uncertainty due to the error on the trigger efficiency in each $|\eta(\mu)|$ bin.

Trigger	$\|\eta(\mu)\|$	Cross Section (nb)	Cross Section (nb) Trig. eff. up	Cross Section (nb) Trig. eff. down	Uncertainty Trig. eff. up	Uncertainty Trig. eff. down
HLT_Mu5	0.0 - 0.9	2391 ± 252	2339 ± 246	2462 ± 258	2.2%	3.0%
	0.9 - 1.5	2142 ± 295	2063 ± 285	2240 ± 295	3.7%	4.6%
	1.5 - 2.1	1192 ± 167	1147 ± 156	1248 ± 167	3.7%	4.7%
	2.1 - 2.4	945 ± 280	805 ± 245	1190 ± 280	14.8%	25.9%
HLT_Mu15_v1	0.0 - 0.9	46.1 ± 1.4	45.6 ± 1.3	46.6 ± 1.4	1.1%	1.2%
	0.9 - 1.5	41.1 ± 1.7	40.7 ± 1.7	41.6 ± 1.7	1.2%	1.2%
	1.5 - 2.1	4.3 ± 0.7	3.9 ± 0.7	4.8 ± 0.7	9.4%	12.3%
	2.1 - 2.4	–	–	–	–	–

Table 30: Systematic uncertainty due to the error on the selection efficiency for Run A.

	Bin	Generated	Fit	Efficiency	Syst. Uncertainty
p_{T} (μ)	6 - 11 GeV	34426	7736	(22 ± 0.3)%	1.4%
	11 - 16 GeV	4114	1343	(33 ± 0.9)%	2.7%
	16 - 20 GeV	824	303	(37 ± 2)%	5.4%
	20 - 30 GeV	442	200	(45 ± 3)%	6.7%
	30 - 50 GeV	79	33	(42 ± 6)%	14.3%
$\lvert\eta(\mu)\rvert$	0.0 - 0.9	30188	4808	(16 ± 0.2)%	1.3%
	0.9 - 1.5	17047	2678	(16 ± 0.3)%	1.9%
	1.5 - 2.1	13243	1835	(14 ± 0.3)%	2.1%
	2.1 - 2.4	3380	298	(9 ± 0.5)%	5.6%

Table 31: Systematic uncertainty due to the error on the selection efficiency for Run B.

	Bin	Generated	Fit	Efficiency	Syst. Uncertainty
p_{T} (μ)	16 - 20 GeV	824	303	(37 ± 2)%	5.4%
	20 - 30 GeV	442	200	(45 ± 3)%	6.7%
	30 - 50 GeV	79	33	(42 ± 6)%	14.3%
	50 - 80 GeV	7	4	(57 ± 29)%	50.9%
$\lvert\eta(\mu)\rvert$	0.0 - 0.9	852	278	(33 ± 2)%	6.1%
	0.9 - 1.5	435	130	(30 ± 3)%	10.0%
	1.5 - 2.1	347	112	(32 ± 3)%	9.4%
	2.1 - 2.4	100	20	(20 ± 4)%	20.0%

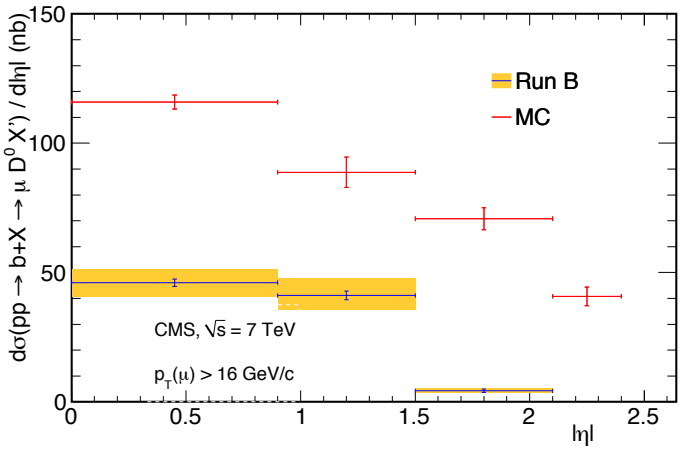

Figure 147: Cross section as a function of $|\eta|(\mu)$ for Run B (blue) and Monte Carlo (red) events. Error bars show the statistical uncertainty, and the colored band shows the combined statistical and systematic uncertainty.

Table 32: The cross section in each p_{T} (μ) bin.

Bin	2010A	2010B	Monte Carlo	MC15
$6 \leq p_{\mathrm{T}} < 11$	457.5 ± 39.6 (stat.) ± 36.9 (sys.)	–	843.0 ± 4.5	–
$11 \leq p_{\mathrm{T}} < 16$	64.7 ± 12.5 (stat.) ± 5.6 (sys.)	–	100.7 ± 1.6	–
$16 \leq p_{\mathrm{T}} < 20$	21.4 ± 8.2 (stat.) ± 2.4 (sys.)	19.5 ± 0.6 (stat.) ± 1.8 (sys.)	25.2 ± 0.9	25.2 ± 0.9
$20 \leq p_{\mathrm{T}} < 30$	4.3 ± 1.2 (stat.) ± 0.5 (sys.)	4.0 ± 0.2 (stat.) ± 0.4 (sys.)	5.4 ± 0.3	5.4 ± 0.3
$30 \leq p_{\mathrm{T}} < 50$	–	0.52 ± 0.05 (stat.) ± 0.10 (sys.)	0.48 ± 0.05	0.48 ± 0.05

Table 33: The cross section in each $|\eta(\mu)|$ bin.

Bin	2010A	2010B	Monte Carlo	MC15
$0 \leq \|\eta\| < 0.9$	1595.9 ± 607.3 (stat.) ± 125.1 (sys.)	1699.1 ± 133.9 (stat.) ± 162.8 (sys.)	4106.9 ± 23.6	4106.9 ± 94.6
$0.9 \leq \|\eta\| < 1.5$	2161.6 ± 510.9 (stat.) ± 183.6 (sys.)	1966.4 ± 165.2 (stat.) ± 292.1 (sys.)	3478.8 ± 26.6	3478.8 ± 229.6
$1.5 \leq \|\eta\| < 2.1$	1347.9 ± 356.5 (stat.) ± 114.2 (sys.)	200.1 ± 138.1 (stat.) ± 24.2 (sys.)	2702.5 ± 23.5	2702.5 ± 163.7
$2.1 \leq \|\eta\| < 2.4$	1225.5 ± 770.3 (stat.) ± 239.3 (sys.)	–	1379.5 ± 23.7	1379.5 ± 122.6